UNIVERSITE DE LIMOGES

EMPA
Materials Science & Technology

UNIVERSITÉ DE LIMOGES

ÉCOLE DOCTORALE Science – Technologie – Santé
Faculté des Sciences et Techniques

Thèse N° 14-2006

Thèse
Pour obtenir le grade de
DOCTEUR DE L'UNIVERSITÉ DE LIMOGES

Discipline : Matériaux Céramiques et Traitements de Surface

Présentée et soutenue publiquement par
Cornelis Schreuders
Le 7 Septembre 2006

SYNTHÈSE PAR PLASMA INDUCTIF DE PARTICULES NANOMÉTRIQUES DE SILICIUM
OPTIMISATION DE LA TREMPE

Directeur de Thèse: Professeur Pierre Fauchais

Jury

Rapporteurs :	Jacques Amouroux, Professeur, Université Pierre et Marie Curie, Paris, France
	Maher I. Boulos, Professeur, Université de Sherbrooke, Canada
Examinateurs :	Pierre Fauchais, Professeur, Université de Limoges, France
	Marc Leparoux, Docteur, Empa, Thun, Switzerland
	Armelle Vardelle, Professeur, École Nationale Supérieure d'Ingénieurs de Limoges, France
Invités :	Nathalie Herlin-Boîme, Docteur, CEA - CNRS, Saclay, France
	Stephan Siegmann, Docteur, EMPA, Thun, Switzerland

This thesis is dedicated to the memory of

Professor G. Nutsch

from the Technical University of Ilmenau, who has initiated this work

Acknowledgements

The work for this thesis was carried out in the Swiss federal institute for materials science and technology (Empa), in Thun, Switzerland. I would like to thank the Empa for giving me this opportunity and the Swiss Commission of Technology and Innovation (KTI) for the financial support (TOP Nano21, #5978.2 and #6740.1).

For the scientific part of this work I would like to express my gratitude to Dr. Marc Leparoux, for his advice, help, motivation, critical remarks, patience, and many fruitful discussions. Also from the EMPA Thun, Dr. Stephan Siegmann, who was also always there for good advice, useful remarks, and interesting discussions.
Furthermore, I am very grateful to professor Pierre Fauchais, university of Limoges, France, who was willing to act as my academic supervisor, after professor Gabriele Nutsch (TU Ilmenau, Germany) had lost her fight against a severe illness. I would like to thank him for his precious time, patience, and for the useful hints and comments during the writing of my thesis.

The members of the jury are gratefully acknowledged for their precious time: reading and judging of the manuscript and their presence at the defence.

Furthermore at the EMPA, I am in great debt by Max, Gerhard, Jong-Won and Bernhard, who measured or built things for and with me. As usual there are a lot of people who are not mentioned, but also contributed to this work, by giving advice or just by offering me distraction by having some small talk and let the thoughts go free.
From the external people I have met or collaborated with at the Empa, I will just mention the following people: Olaf Benedix, TU Chemnitz, Germany for showing his C++ modelling capabilities, Yann Leconte, CEA, Saclay, France, for arranging the PCS and BET measurements and Michael Dvorak, DACS, Switzerland.

Also the group around professor S.E. Pratsinis at the ETH, Zürich, Switzerland, is acknowledged for sharing some of their knowledge about the nanoparticle synthesis and for the support I have received during XRD and BET measurements I have made there.

The work of Dr. Rodolphe Bolot from the university of Belfort-Montbéliard, France, is kindly acknowledged for his modelling work on the PL-35 torch, at different frequencies, flow rates, and injector positions. Also the modelling efforts of professor Maher I. Boulos (Tekna Plasma Systems Inc., Sherbrooke, Canada) are very much appreciated.

Auch möchte ich gerne Mandy danken für das Durchhalten in Guten, aber auch in schlechte Zeiten. Es war nicht immer einfach, aber irgendwie wird es immer eine Lösung geben. Die “Dresdner” Sippe wird auch recht herzlich bedankt für Ihre Unterstützung, auf jeder Art und Weise.

Natuurlijk wil ik mijn ouders en broer niet vergeten voor hun nooit aflatende steun en vertrouwen. Ook de mensen die de moeite genomen hebben om me eens te bezoeken in “den verre” worden bedankt, want ook dat heeft me verder geholpen.
Tenslotte is Lennart aan de beurt, want ook hij heeft geleden onder het feit dat papa niet altijd het zonnetje in huis was. Alhoewel hij als laatste genoemd wordt, komt hij eigenlijk op de eerste plaats, want mijn “ventje” is en blijft altijd iets bijzonders.

Contents

Summary

In this study the nanoparticle synthesis by an inductively coupled plasma (ICP) process is investigated in detail.
The motivation for pursuing the nanoparticle synthesis by means of ICP and also why the focus is put on the quenching process is presented in chapter 1.
The ICP is a thermal plasma with a temperature of 8000 - 10000 K which, amongst others, can be used for nanoparticle synthesis based on an evaporation – condensation process. Due to the high temperature and energy density, solid precursors can be used resulting in a higher throughput per unit time. The absence of solvents and/or stabilising groups results in purer products, as compared to liquid and gaseous precursors. Also high refractory materials, like WC (boiling temperature 6000 K) can be processed. Furthermore, the ICP process is carried out in a controlled atmosphere enabling the synthesis of oxide as well as non-oxide nanoparticles, e.g. metals or semiconducting Si.
The final size, size distribution, and chemistry of the nanoparticles are determined by the temperature and velocity profiles along the trajectories, which depend on the process parameters. These profiles can be influenced downstream (below the torch exit) by cold gas quenching. Although quenching is a very important step in the nanoparticles synthesis, the quenching process does not get the attention in the literature it deserves.
In this study, the nanoparticles synthesis by means of ICP is investigated together with the effect of several plasma parameters on this process. The synthesis process has been investigated in both modelling and experimental way, with the main focus on the quenching.

The literature review, describing the “state of the art” on the items dealt with in this thesis, is presented in chapter 2. The topics are synthesis of nanoparticles (2.1), the plasma in general and the ICP in particular (2.2). A review on modelling of the ICP is found in 2.3. The particle and gas injection, especially the difficulties, are described in 2.4. Section 2.5 deals with the plasma particle interaction. The literature on quenching, with emphasis on the cold gas quenching, is presented in 2.6. The particle growth modelling is described in 2.7 and the characterisation of the nanoparticles as well as the plasma in 2.8.

The first part of chapter 3 describes the ICP equipment used in this work (3.2), after a short introduction on the ICP process is given in 3.1. The process parameters are divided into the plasma parameters and the precursor properties (3.3). The particle sampling device, used to track on the particle growth within the synthesis chamber, is described in 3.4, followed by the applied plasma and particle characterisation methods (3.5). Chapter 3.6 deals with the approaches and assumptions of the used plasma and particle growth models.

Chapter 4 deals with the results of the plasma and particle growth model. The influence of several process parameters (e.g. gas flow rates, pressure, and power level) on the temperature and velocity profiles of the plasma are modelled by a commercial computational fluid dynamics software (Fluent 6.1.18) and presented in section 4.1. The “heat source” model describes the plasma as being a heat source without the influence of the ElectroMagnetic (EM) field and has been validated with the results of enthalpy probe measurements. The estimated net power, introduced in the plasma, is 10 kW at a plate power of 15.6 kW. This results in a maximum temperature of 9200 K for a plasma gas composition of 3 slpm Ar carrier, 12 slpm Ar

central, and 80/6 slpm Ar/H_2 sheath gas. Another model, taking the influence of the EM field on the temperature and velocity profile in the torch into account, has shown that the recirculation flow, which is normally encountered, has vanished at higher frequencies and flow rates (like 13.56 MHz and the plasma gas flow rates as used in this work).
In section 4.2, several quench designs with different nozzle numbers and diameters have been modelled in 2- and 3D. A two-nozzle and several eight-nozzle designs, proposed by CFD calculations, have been built to allow experimental validations with enthalpy probe measurements and optical images of the plasma. The 3D models have found to be more realistic than the 2D models (single nozzles are converted into a surface equivalent slot), because the presence of “hot fingers” (observed in experiments) where shown in the 3D models. The behaviour of the plasma under different quench rates has been reproduced and forecasted very well by the 2- and 3D models.
The results of the particle growth model are presented in 4.3 and show that increasing pressure and power result in larger particles without quenching.

Chapter 5 gives the results of the experiments used to validate the modelling results described in chapter 4. Experiments with Silicon (Si) were carried out to assess the results of the particle growth model and the modelled quench designs (5.1). The Si experiments confirmed the trends found by the particle growth model. The results of the modelled particle size are at least within a factor two of the experimental diameter calculated from gas adsorption measurements. The improved quenching designs with the eight-nozzle angled system with a funnel in particular, as proposed and validated by the CFD model, resulted in an increased surface specific area (SSA) from 70 $m^2.g^{-1}$ for non-quench conditions to 90 $m^2.g^{-1}$ for the two-nozzle system to 145 $m^2.g^{-1}$ for the eight-nozzle design with funnel (quenched with 56 slpm Ar). The replacement of the two-nozzle by the eight-nozzle with funnel system, has brought an improvement of 60% and over 100% compared to the non-quenching conditions. By increasing the distance between torch exit and quench position the SSA could be increased to values over 200 $m^2.g^{-1}$ (56 slpm Ar), which is almost an improvement of 200% compared to the non-quenching conditions.
The experiments with tungsten carbide (WC), described in 5.2, have shown that the ICP process is able to synthesise nanoparticles from high refractory materials. These experiments also showed that quenching is able to influence the final chemistry, besides the particle size and size distribution. Also by introducing a carbon containing source in the plasma, the final phase composition could be guided.

The most important conclusions are presented in chapter 6. One of them is that the combination of modelling and experiments is an excellent tool to optimise the nanoparticle synthesis by means of ICP.

Chapter 7 provides a short outlook and directions for future work. The suggestions are given for the ICP equipment, modelling, experiments, and particle characterisation.

The abbreviations and symbols are described in chapter 8.

Appendix A describes the mathematics behind the particle growth model.

1 Motivation and scope

Nanoparticles are very attractive since they offer new potential applications, because of the altered physical and chemical properties as compared to the same bulk material. But also the current development for miniaturisation, especially in the semiconductor industry, increases the interest for nanoparticles.
Some examples of current nanoparticle applications are: Si in the semiconductor industry, Al in pyrotechnics, TiO_2 in pigments, cosmetics, photocatalysis, and SiO_2 / Pt as catalysts. The more research on nanoparticles is performed, the more potential applications (will) emerge at the horizon and come nearer to being realised.
The different properties of the nanoparticles are partially caused by a high ratio of surface to bulk atoms, which is inherent due to the small(er) size. This high ratio is very beneficial in for example catalytic applications. Furthermore the altered properties are also caused by the occurrence of new phenomena which are a consequence of the particle size being around the characteristic length scale of physical, biological or chemical processes. There is for example a change in emission of CdSe nanoparticles with changing particle size (below 5 nm) due to the quantum confinement effect.

In this study the gas phase synthesis of nanoparticles by means of an inductively coupled plasma process (ICP) is pursued.
The aim of this thesis is to better understand and then to optimise the nanoparticle synthesis by an ICP process, so tailor made nanoparticles can be produced.

In our ICP process, the nanoparticles are synthesised according to an evaporation / condensation process, in which the nanoparticles are formed from the vapour phase. The precursor, which is injected in the plasma, faces a very high temperature, up to 10,000 K, enabling the decomposition and / or evaporation of all precursors. After the precursor is evaporated, a supersaturated vapour is formed from which subsequently the nanoparticles are formed by homogeneous nucleation. The temperature and velocity profiles of the nucleated particles determine the size, size distribution, and the chemistry of the product. A way to influence these trajectories, which determine the particle growth, is to subject them to rapid cooling (quenching).

This study focuses on quenching as part of the nanoparticle synthesis process by means of an ICP. Although the great importance of quenching on the nanoparticle synthesis has been recognised (size, size distribution, and product chemistry), only a few scientific works dealing with quenching are available in the literature.
Here the influence of the quench design and quench gas flow rate on the different process parameters, like plate power, pressure, plasma gas flow rates and composition are investigated. Both modelling of the temperature and velocity profiles and experiments are being used to optimise the quenching for the ICP produced nanoparticles.

2 State of the art

2.1 Nanoparticles

2.1.1 Interests in nanoparticles

The kick-off for the nano age was given in 1959 by R. Feynman by his talk “There’s plenty of room at the bottom” [1]. However it should be kept in mind that the nano particles exist much longer than that. The Ancient Chinese already produced carbon black by combustion [2]. The Lycurgus Cup, made in fourth century by the Romans, appears green in the reflected light and red in the transmitted light, due to the presence of nanoparticles [3]. Another example is the production of artificial pearls around 1650, using 25-75 nm thick platelets of guanine and hypoxanthine isolated from fish scales [4].
Today, some of Feynman’s “visions” have come through, e.g. moving single atoms, and some remain fiction, like small scale manufacturing by master-slave devices. However, the dwarf (the meaning of nanos in Greek), due to its enormous potential, has become a giant and is still growing with respect to the number of patents issued, (potential) applications, investments and revenues [5]. But why are these nanoparticles so interesting?
Although nanoparticles are made of the same chemistry as the bulk material, they may have different properties and could be regarded as different matter [6]. Figure 2-1 shows a visual comparison between conventional WC bulk material and WC nanoparticles at nanometerscale.

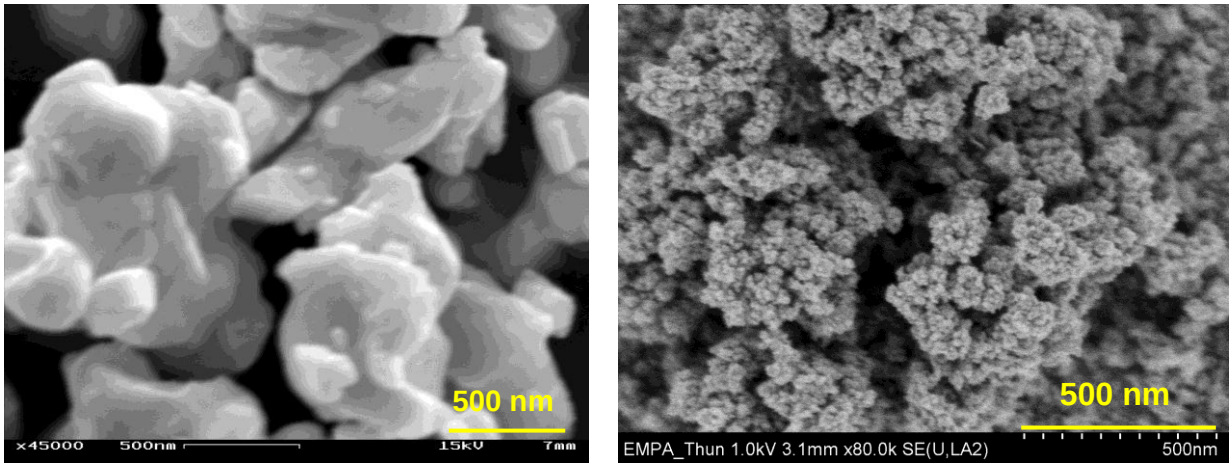

Figure 2-1: SEM pictures of micronsized WC material (left) and ICP processed WC nanoparticles (right).

The different properties observed between nanoparticles and the bulk material are caused by the size of the nanoparticles being below the characteristic length scale of the specific property and thereby affecting its nature on one hand [3], [7]. On the other hand it is due to a high ratio of surface to volume atoms [6] which leads to a dominance of the particle properties by the surface atoms. Nanostructured materials show increased mechanical properties caused by the smaller crystallite sizes which do not allow that the critical crack size is reached.

Table 2-1 shows the fraction of surface atoms as a function of the particle diameter.

Table 2-1: fraction of atoms at the surface as a function of particle diameter (d_p = 0.5 nm).

Size (nm)	Number of atoms	Fraction at surface (%)
0.5	1	
1.0	8	100
2.0	64	99
5.0	1.000	50
10.0	8.000	25
20.0	64.000	12

One of the first articles describing an effect due to the particles being nanosized was by Buffat and Borel in 1976 [8]. They found a decreasing melting temperature with decreasing size of gold particles; a large effect on the melting temperature can be found when the particle diameter is below 5 nm.
Also changes in thermal diffusivity, specific heat, and thermal expansion [9] were observed when comparing the nanoparticles (20 nm) to the bulk material (> 1μm).

Applications of nanoparticles can be found in pyrotechnics [10], fuel cells, polishing agents [11] medical applications [12], catalysts, quantum dots, gas sensors, high temperature super conductors, magnetic materials [13] to mention just a few of them. Also coating of the nanoparticles themselves [14], [15], [16] can be very desirable to avoid the formation of agglomerates or spontaneous combustion. Such a coating for example can be obtained using a condensation-evaporation process by the addition of a species with a lower solidification point. The species with the lower solidification point will nucleate heterogeneously on the surface of the already formed nanoparticles and thereby coating them.

2.1.2 Nanoparticle synthesis

Nanoparticles can be synthesised via several routes. Andrievski gives an overview of gas, liquid, and solid phase nanoparticles synthesis [17].
From these three routes, the gas phase synthesis has several advantages over the other non-gaseous techniques such as product purity, because of less manipulations which can introduce impurities, easy to separate product from residues, potential to use and produce multi-component systems, continuous processing, good process and product control (easy tuning by adjusting process parameters or addition of extra process steps) [13]. For reviews of the gas phase synthesis techniques, the reader is referred to [13], [18], [19], [20].
A schematic overview of the principle behind the gas phase synthesis is given in Figure 2-2.
The precursor is first converted into a vapour. When the temperature decreases a supersaturated vapour is formed, from which homogeneous nucleation takes place, resulting in the first primary particles. The primary particle is defined as an identifiable single particle. A high supersaturation is required to obtain a homogeneous nucleation of many small particles [21], but it also has the effect of a strong depletion of the gas phase preventing growth of the existing primary particles from the gas phase [22].

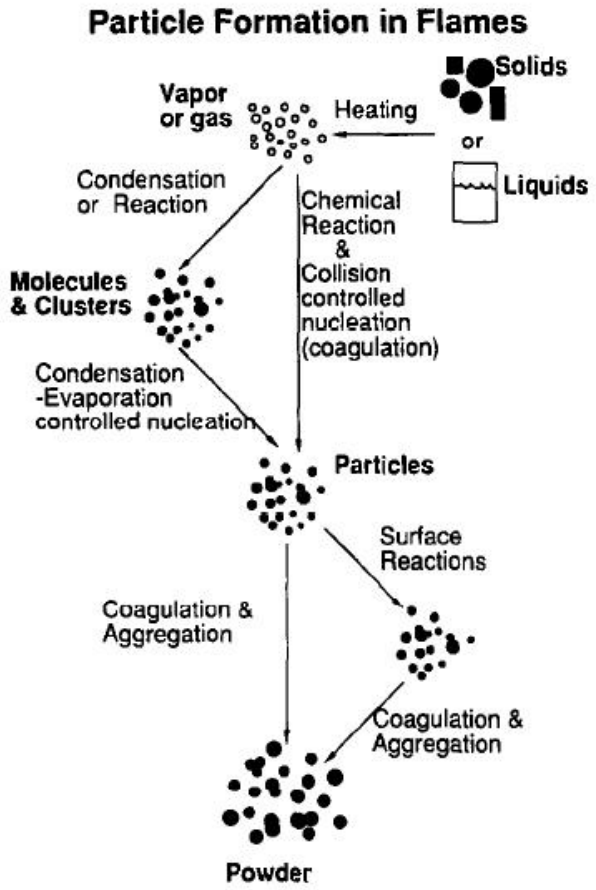

Figure 2-2: the general principle behind the gas phase synthesis ([23]).

The size of the condensed primary particles depends amongst others on the supersaturation and the temperature via the Kelvin relation [24], [25] (equation 2-1):

$$d^* = \frac{4\sigma_s \upsilon}{kT \ln S} \qquad \text{eq. 2-1}$$

This relation describes the smallest primary particle diameter d^* [m] which can serve as a stable particle, as a function of the vapour and equilibrium vapour pressure (supersaturation ratio S [-]), temperature T [K], molar volume υ [m^3], and surface tension σ_s [$N.m^{-1}$]), with k being the Boltzmann' constant 1.38×10^{-23} [$J.K^{-1}$].
The particle growth is stronger by collision with other primary particles than by condensation on the primary particles of vapour from the gas phase [22], [26]. If the temperature is still above the melting point, complete coagulation occurs after collision, resulting in the formation of one larger spherical primary particle. This can also be seen by comparing the characteristic time for collision (equation 2-2) to the characteristic time for coalescence (equation 2-3) [26].

$$\tau_c = \frac{2}{\beta N \rho_g} \qquad \text{eq. 2-2}$$

Equation 2-2 gives the characteristic time for collision [s] in which β is the collision frequency or collision kernel [$m^3.s^{-1}.\#^{-1}$], N is the particle concentration per kg gas [$\#.kg_g^{-1}$], and ρ_g [$kg.m^{-3}$] is the density of the gas phase (a function of pressure and temperature).

Equation 2-3 describes the characteristic time for coalescence (or sintering):

$$\tau_s = c_1 d_{pp} \exp\left(\frac{c_2}{T}\left(1 - \frac{d_{p,\min}}{d_{pp}}\right)\right) \qquad \text{eq. 2-3}$$

In which τ_s is the characteristic coalescence time [s]. The factors c_1 [$s.m^{-1}$], c_2 [K] and $d_{p,min}$ [m] are constants, d_{pp} [m] is the actual primary particle size and T [K] is the temperature.
Above the melting point the characteristic time for collision is much larger than that for coalescence [26], meaning that time for coalescence is much smaller than the time between two subsequent collisions. Between the melting point and a temperature of approximately 60% of this value, a collision between two primary particles does not result in the formation of one larger primary particle anymore, but instead the primary particles are connected by a sintering neck [26]. The result of this collision is the formation of a so-called hard agglomerate. In this temperature region the characteristic time for collision and coalescence are of the same other of magnitude [27]. Once below this temperature the primary particles and/or hard agglomerates are only kept together by Van der Waals forces after they collide and the soft agglomerates are formed. In this case the characteristic time for collision is much smaller than that for coalescence [26].
The hard agglomerates can be differentiated from soft agglomerates by mechanical means; hard agglomerates can, in contrast to soft agglomerates, not be separated by dissolution or ultrasonic treatment.
Due to the small size of the particles, the collected products are generally agglomerated by Van der Waals forces, even if they were dispersed in the gas phase. The temperature and residence time of the particles determine if the agglomerates are soft, hard or a combination of both [22]. In this study agglomerates and aggregates are defined as clusters of particles and are treated the same. There is only a differentiation between hard (presence of sintering necks, chemical bonding) and soft (Van der Waals forces, physical bonding).

From all the gas phase synthesis processes, three very important exponents namely inert gas condensation, flame, and plasma process are described in more detail in the following paragraphs.

2.1.2.1 Inert gas condensation and chemical vapour condensation

Inert Gas Condensation (IGC) or Gas Phase Condensation [19], [28] is described as a solid metallic or inorganic material being vaporised using heated crucibles, electron or laser beam evaporation or sputtering (Figure 2-3). The activation method depends on the melting point and vapour pressure of the precursor. The substrate material is being vaporised and as the temperature decreases the equilibrium pressure decreases and subsequently a supersaturated vapour is formed from which a homogeneous nucleation takes place.
The Chemical Vapour Condensation (CVC) or Chemical Vapour Synthesis (CVS) is very similar to the IGC process. The evaporative source is replaced by precursor(s) which is / (are) decomposed in a hot-wall reactor (for example a heated ceramic tube). The residence time, supersaturation pressure, concentration, and the temperature determine if nanoparticles or coatings are formed [19]. The latter are formed when the supersaturation is not high enough to allow homogeneous

nucleation. The advantages of the CVS process over the IGC process are a larger throughput and a wider range of precursors that can be used [22].
Also a microwave source can be used as the activation source [29], instead of a thermal heat source. The use of a microwave source has the advantage of a lower activation temperature (because of the presence of highly energetic electrons) and therefore less formation of hard agglomerates.

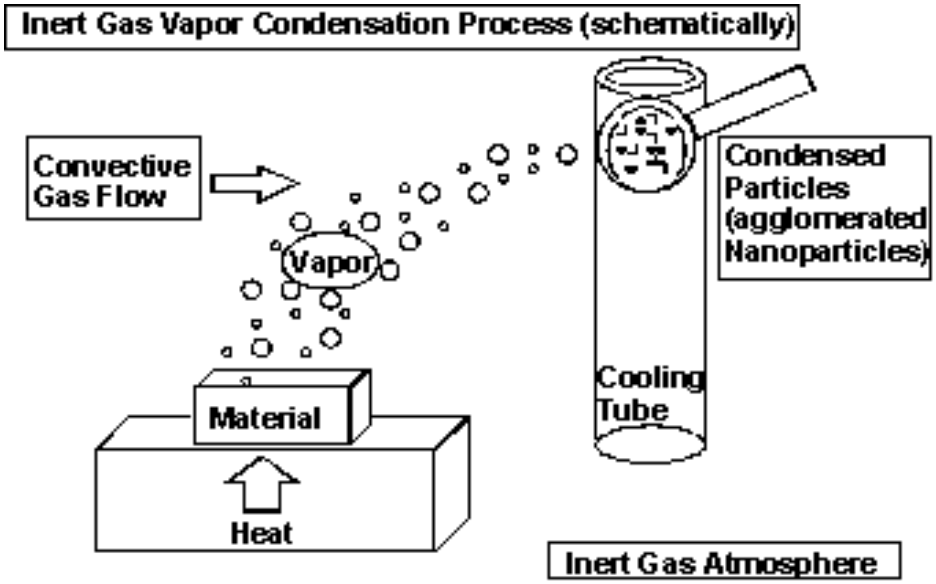

Figure 2-3: schematic representation of the IGC principle (source TU-Cottbus, D).

2.1.2.2 Flame pyrolysis

In flame processes the gaseous or liquid precursors are decomposed by the energy released by the combustion reaction of a fuel with oxygen. The need for oxygen makes the process especially suitable for the synthesis of oxides. The combustion process is well developed and is applied on an industrial scale to produce SiO_2, TiO_2, and carbon black nanoparticles [27]. Although carbon black is a non-oxide it is produced by combusting liquid aromatic oil in a natural gas – air mixture [30].
But also metals can be produced, by using a chlorine hydrogen flame [31] or a sodium metal chloride flame [16]. The by-product of the latter combustion process is NaCl, which encapsulates the metal nanoparticles preventing the metal from growing and agglomerating. The complete particles (metal with coating) will of course agglomerate. The NaCl however can be removed afterwards, resulting in only soft agglomerated nanoparticles.
One disadvantage of the atmospheric flame process is the high degree of hard agglomerates that usually are formed [16]. To overcome this problem one can use a low pressure flame (pressures around 6 kPa) [19], [32] or an expansion nozzle [33] which has a twofold function; temperature reduction and dilution of the particle concentration.
In the flame processes several different burner set-ups can be used, e.g. the premixed, diffusion, and double diffusion flame. The difference between the set-ups is the arrangement of the reacting streams. This arrangement has a strong influence on the primary particle size [23]. Figure 2-4 shows a set-up of a single and double diffusion flame burner. The double diffusion flame has two flame fronts (fuel surrounding-air and fuel-supplied air) compared to only one in the single diffusion flame. Reviews of the combustion synthesis can be found in [23] and [27].

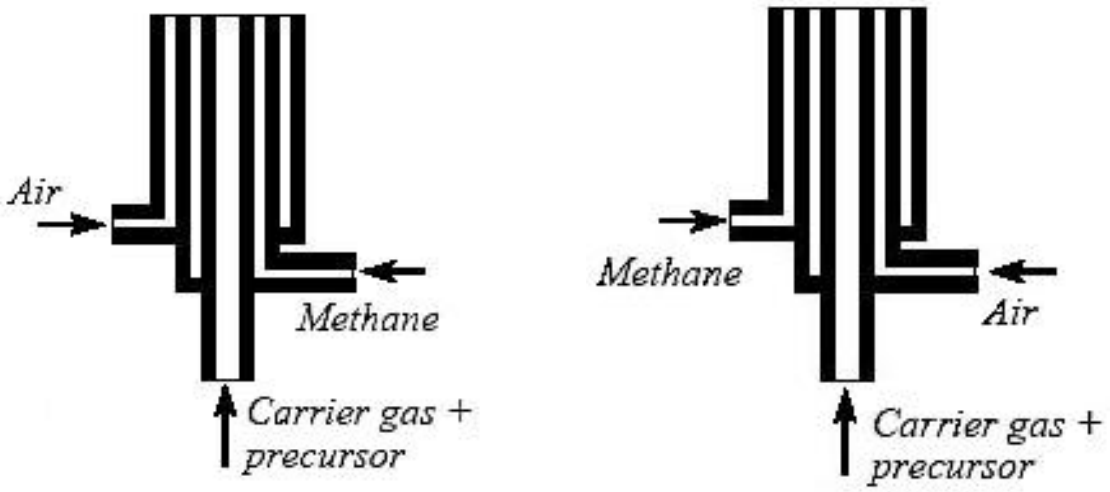

Figure 2-4: schematic drawing of a single diffusion flame (left) and a double diffusion flame burner (right) [34].

2.1.2.3 Plasma synthesis

The synthesis of nanoparticles within the plasma process is based on the evaporation / condensation principle, from which a schematic overview shown in Figure 2-2.
The precursor is injected radially or axially into the plasma and is either a gas, liquid or solid and becomes vaporised / atomised, because of the high gas temperatures in thermal plasmas. The gas phase becomes supersaturated as the temperature decreases due to a lower equilibrium vapour pressure at lower temperatures.
A high supersaturation is required to obtain many small nuclei [21], but it also has the effect of a strong depletion of the gas phase preventing growth of the existing particles [22]. The plasma process has the potential to reach these high levels of supersaturation, due to the high temperature gradient, and thus the ability to synthesise very small particles [35]. Although the conditions guarantee a homogenous nucleation, also some heterogeneous nucleation on the reactor wall can be expected [36].

There are several ways to produce a plasma: using direct current (DC plasma), microwaves (μW plasma) and radio frequency (RF plasma). Figure 2-5 shows the schematics of the DC plasma torch, DC transferred arc plasma torch, RF induction plasma torch, and microwave torch.
In [35], [37], [38], [39] the synthesis of DC plasma produced nanopowders is being described. The synthesis of nanoparticles with a microwave plasma is described in [29], [40], [41].
Papers dealing with RF plasmas and inductively coupled plasma (ICP) in particular are, [36], [42], [43], [44], [45], [46], [47], [48], [49], [50]. The whole range of oxide, non-oxide ceramic and metallic nanopowders is covered in these papers using solid, liquid or gaseous precursors.
Some of the work done on ICP synthesis of nano powders has been patented. Pirzada and Yadav [51], describe the quenching of the vapour by adiabatic expansion to produce nanoparticles, in which the vapour can be produced by an ICP source. Boulos et al. [52] synthesised metal oxide nanoparticles by quenching the vapour with gas which enters the reaction chambers from eight nozzles with a swirl

component. The plasma and quenching gases are cleaned and recycled, allowing a high quenching gas flow rate without a very high gas consumption.
Also a hybrid construction of a DC plasma combined with a RF plasma is used to produce nanoparticles. In this set-up the recirculation flow (treated in section 2.3.2), which is commonly found in the RF plasma caused by the electromagnetic field, is absent [53].

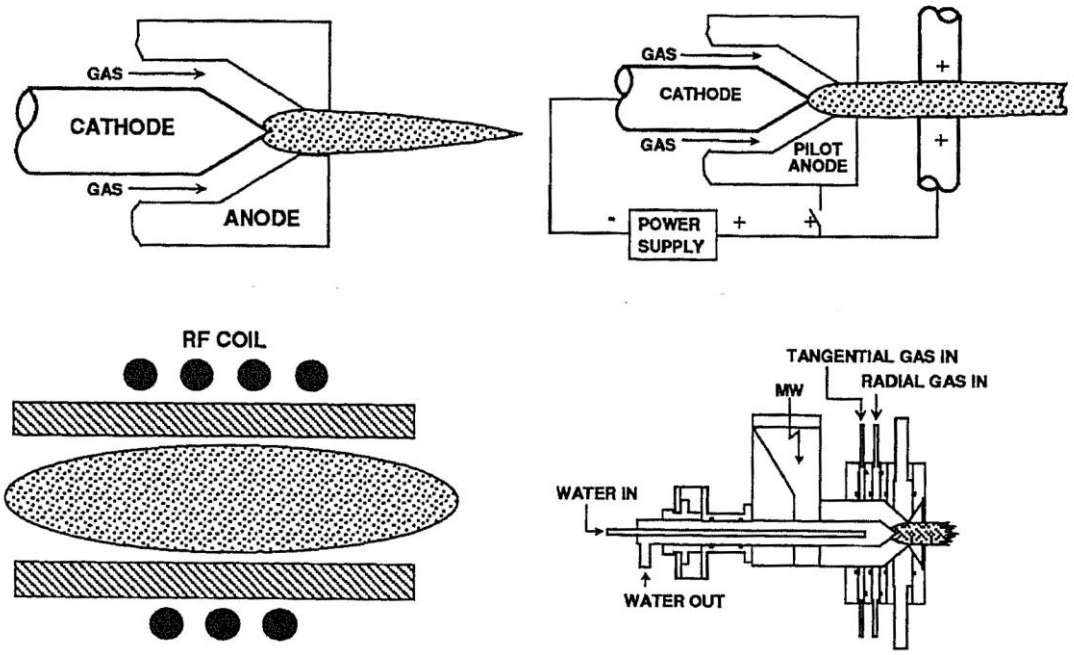

Figure 2-5: top left: d.c. plasma torch. Top right: d.c transferred arc plasma torch. Bottom left: r.f. induction plasma torch. Bottom right: microwave torch. Source: Kong et al. [54].

The advantage of the plasma synthesis over the other gas phase techniques is the high temperature and energy density enabling a high throughput [35]. An additional advantage of the operation at high temperatures is that the use of expensive gaseous and liquid precursors is no longer required; the use of much cheaper and more common solid precursors is allowed [36]. Even the synthesis of nanoparticles from high refractory materials is feasible [55].
The plasma processes can be carried out in a pure and controlled atmosphere, which reduces contamination and allows working in a reducing, inert or oxidising atmosphere [56].

The ICP process has the advantage over other plasma processes that no electrodes are required for operation and the products are therefore free from contaminants originating from the electrodes as is the case for DC plasmas. Also, it allows the use of aggressive precursors and gases [57]. The precursors have a relative long residence time in the plasma as compared to DC plasma processes [58].
A disadvantage of the (ICP) plasma synthesis route is the relative low efficiency in the plasma system due to cooling and energy conversion processes. However this can be compensated by synthesis of more complex, purer and/or “exotic” systems which can not be made by other techniques [42], [59].

Articles mentioning nanoparticle production by thermal plasmas are given by Kong and Lau [54], Waldie [60], Taylor and Pirzada [56], Young and Pfender [57], Fauchais et al. [61], Boulos [62], and Kong and Pfender [63].

2.1.2.4 Other synthesis techniques

Besides the above mentioned gas phase techniques, also a lot of other techniques producing nanoparticles are topics of research, e.g. sputtering [64], laser [65] [66], dynamic shock compression [67], spark source [68], exploding wire [69], expansion-cooling [70], precipitation [71], spraying [72], sol-gel processes [73], and mechanical milling [74], [75]. This list is by no means complete and is just presented to give some examples of techniques that are able to synthesise nanoparticles.

2.1.3 Silicon nanoparticles

Si is well investigated and is a model species for many studies, resulting in a lot of information on chemical and physical properties [76], [77]. Silicon (Latin silex, silicis meaning flint) was first identified by Lavoisier in 1787. The boiling point of Si is 3505 K [76], although also values of 2873 K (NIST, USA) and 2628 K (NASA, USA) are mentioned. The melting point of bulk silicon amounts 1683 K. Si exists as a cubic phase and has a specific density of 2.33.

The main applications of Si are in the semiconductor industry and photonics. When Si is being doped with boron an N-type semiconductor is obtained and when doped with phosphorus a P-type semiconductor is obtained. Also nano Si is used for application in pyrotechnics [10].

Nano-Si can be synthesised from the decomposition of trimethylsilane (TMS) or other Si containing precursors, which are in the gaseous or liquid phase. Some of the techniques to synthesise nano-Si are laser [77], DC plasma [35], hot-wall reactor [78] and microwave [79] synthesis.

Desilets et al. [80] already carried out synthesis of Si nanoparticles by an ICP process, using gaseous $SiCl_4$ as precursor. In their work they also combined (CFD and particle growth) modelling with experiments, but the quenching process was merely mentioned and not described in detail.

2.1.4 Tungsten carbide nanoparticles

Within this work a lot of attention has been given to the synthesis of nano WC, which was discovered in the late 1890's. WC is a high refractory material with a boiling point of around 6000 K and a very high density (around 15.6). Tungsten carbide exists as a hexagonal δ-phase: WC, as a cubic γ-phase: WC_{1-x} (sub-stoichiometric), or as hexagonal β / β' / β'' phase: W_2C [81]. Figure 2-6 shows the W-C binary phase diagram with the phase transitions.

Microstructured WC is very attractive due to its physical properties, especially its high hardness: 2200 HV_{50}, and high thermal resistivity: 0.012 $m.K.W^{-1}$. Due to these properties WC is often used for wear resistant coatings and reinforcements.

Since 1929 it is known that grain size reduction can positively influence the mechanical properties of the cemented carbides [82]: alloys containing more smaller WC (around 1 μm) particles had higher hardness than alloys containing more larger WC particles. Around the same time it was discovered that the addition of carbides of vanadium, tantalum, chromium can act as grain growth inhibitor for WC [82]. The current trend for WC alloys is the reduction of the grain size to the nanometer range in order to obtain better physical properties [81], [83].

For mechanical applications, besides the size and size distribution, is the chemistry also very important. Pure WC should be used and none of the sub-stoichiometric species, since both W_2C and WC_{1-x} will promote brittleness and degrade wear resistance [84].

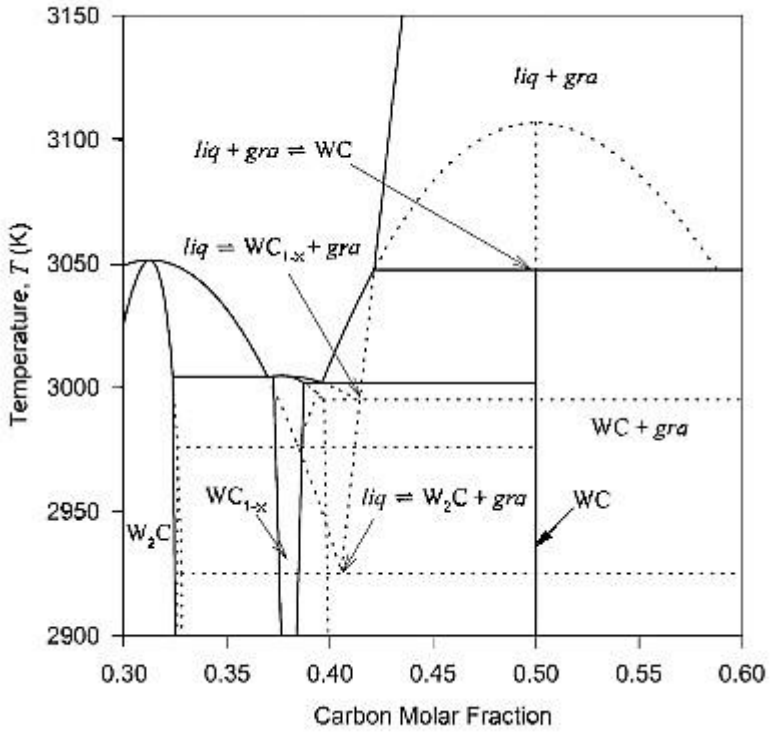

Figure 2-6: Binary phase diagram of W-C [84]. The solid lines represent the computed equilibrium phase diagram, while the dotted lines represent the computed metastable phase diagram.

Besides the problems of controlling the phase composition, also the synthesis of the WC nanoparticles seems not to be so straightforward. Schubert et al. [83] described the limits of conventional ultrafine WC powder synthesis. In which conventional synthesis means the reduction of a tungsten oxide precursor to metallic tungsten and subsequent carburisation of the metal. In this article it is stated, based on experience, that the minimal WC particle size obtained during conventional synthesis is approximately 150 nm.
No articles have been found so far describing the synthesis of WC nanoparticles using an ICP process. Boulos et al. [85], [86] published some articles dealing with tungsten carbide coatings, in which the tungsten precursor is carburised in-situ by addition of methane. In [85] a SEM picture and an X-ray diffractogram (XRD) of particles extracted before deposition on the substrate are given, but these particles were micronsized and consisted out W and W_2C (XRD). The spheroidisation of a WC / W_2C mixture by means of an ICP process is being described in [87], [88]. The products however showed a lesser carbon content than the precursor [87].

2.2 Inductively Coupled Plasma Technology

2.2.1 Plasma in general

The previous section described some of the main routes to synthesise nanoparticles via the gas phase with some of their advantages and disadvantages. In this work,

the nanoparticles have been synthesised by means of the inductively coupled plasma (ICP) process, able to synthesise nanoparticles via the evaporation / condensation principle, see section 2.1.2.3.
The ICP also has the flexibility to be operated with different plasma gases and is therefore able to deal with precursors in any physical state [47]. The high temperature (up to 10,000 K) and high energy density of the plasma allow the nanoparticle synthesis of metals and ceramics with a high boiling point.
A short introduction about plasmas with the main terminology is given below. A much more extensive view on the plasma fundamentals is given in [89].

A gas is called a plasma when it is (partially) ionised meaning that charged particles in the form of electrons and ions are present [89]. Plasma is very common, since most of the universe consists out of plasma. Perhaps the most famous example within the universe is the sun. On earth, these examples would be lightning and flames.
The gases are ionised by introducing energy to create charge carriers which make the gas electrical conductive, this process is called electrical breakdown [89], [90]. The absorbed energy is distributed among the particles by collisions between electrons and particles. The energy gained by electrons, in the electric field between subsequent collisions depends on the mean free path length (λ or mfp). The mfp is the average distance between two subsequent collisions and is a function of temperature, pressure and the collision diameter (equation 2-4):

$$\lambda = \frac{kT}{\sqrt{2}\pi\sigma_c^2 p} \qquad \text{eq. 2-4}$$

In which λ is the mean free path length [m], k the Boltzmann constant 1.38×10^{-23} [$J.K^{-1}$], T the temperature [K], σ_c the collision diameter [m], and p the pressure [Pa]. The mfp amounts around 65 nm at room temperature and atmospheric pressure, 160 nm at room temperature and 40 kPa and 4.5 µm at 8000 K and 40 kPa.
The energy gain of the electrons in the electric field can be described by the mfp multiplied by field strength. So, for a small value of E/p, a low electrical field or high pressure, the electrons will not gain much energy between the collisions. The energy increase can only be transferred equally among all species by elastic collisions with other particles (it takes over thousands of collisions between electrons and “heavy” species before the energy is equilibrated). In this case the ratio of the electron temperature (T_e) to the heavy species temperature (T_h) will be close to unity, which is one of the conditions for a thermal plasma (other conditions like a Maxwellian distribution, elastic collisions are dominating the thermal excitation and ionisation processes have to be fulfilled as well [89]).
If E/p is large, there will be no balancing of the energy between the electrons and “heavy” particles: a non-thermal plasma prevails ($T_e/T_h >> 1$).
A review about the thermal plasma technology is given by Fauchais and Baronnet [59], Boulos [62], and Pfender [91]. Conrads and Schmidt for instance give a review on plasma generation and plasma sources [92].

2.2.2 Inductively Coupled Plasma (ICP)

There are several ways to produce thermal plasmas by using an electrical discharge or another energy source like laser, shockwaves, etc. [89]. The most well-known

electrical discharges are arc, microwave, and inductively coupled (IC) high-frequency discharges. Reviews of the ICP technique are given by Eckert [90] and Boulos [93], [94].

The IC discharges can be divided into capacitive coupling in which the discharge is maintained by electrical field (E discharge) and inductively coupling in which the discharge is maintained by magnetic field (H discharge) [95]. The E discharge is generally related to non-equilibrium plasmas at low pressure, whereas the H discharge is related to thermal plasmas.

There are several inductor geometries [95], from which the helical coupler is the most frequently used. The coil, surrounding the plasma generation region, induces an azimuthally electrical field with closed loops in the plasma. The magnetic field is directed parallel to the central axis of the coil. Figure 2-7 shows a schematic drawing of a helical ICP torch and of the gas inlets in the torch.

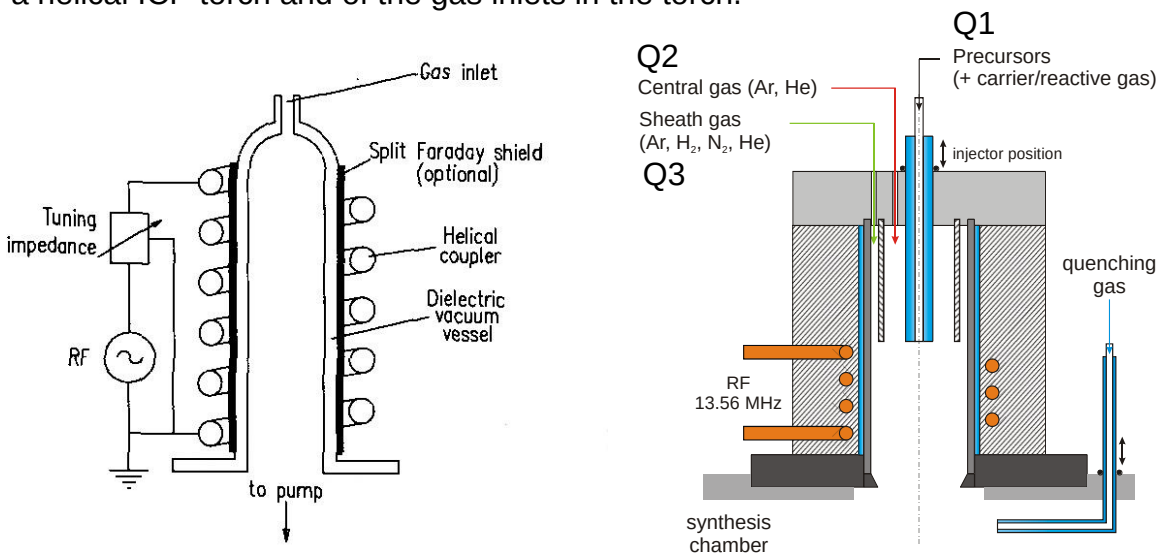

Figure 2-7: Schematic drawing of the helical ICP torch [95]. Right: Schematic drawing of an ICP torch [96]. In which d_x, L_x, R_x, r_x, and s_x are dimensions and Q_x is denoting the gas flow rates and marking the gas inlet position.

The plasma is generated by introducing energy in the plasma by ohmic dissipation. The region in which the energy is in troduced into the plasma is not the entire gas volume inside the coil region, but the skin depth [92] (which is going from wall to core), see equation 2-5:

$$\delta_c = \sqrt{\frac{1}{\pi \xi_0 \sigma f}} \qquad \text{eq. 2-5}$$

In which δ_c is the skin depth [m], ξ_0 the magnetic permeability of the plasma $4\pi x10^{-7}$ [Hy.m^{-1}], σ the electrical conductivity [mho.m^{-1}], and f the frequency [Hz] of the power supply [93].
The skin depth is a degree for the penetration of the RF field, since the electrical conductivity of the plasma prevents the alternating magnetic field from penetrating the plasma: a distance of one skin depth means a decrease of the field by a factor of e^{-1} (0.37). A large skin depth (low frequency and low electrical conductivity (function of gas composition and temperature)), will favour a more homogeneous energy distribution [93]. The skin depth thickness of an ICP is usually of around 10^{-3} - 10^{-2} m

and decreases at higher frequency and temperature. An Ar plasma, at atmospheric pressure, a frequency of 3 (13.56) MHz and a temperature of 10000 K has a skin depth of 5.3 (2.5)x10^{-3} m and increases to 9.2 (4.3)x10^{-3} m at 8000 K.

The history of the Inductively Coupled Plasma (ICP) torch dates back to 1947 when Babat carried out his experiments, using a ring discharge, which was established at low pressures but could be maintained at atmospheric pressure [93].
In 1961, Reed [55] was the first to describe an induction-coupled plasma torch operating at atmospheric pressure in an open tube with streaming gas. Although Reed mentioned that it was still too early to talk about the capabilities and limitations, some potential was already revealed and recognised by growing single crystals of stabilised zirconia, sapphire and niobium [97].
Current applications of the ICP discharge are spectrochemical analysis, aerospace research (testing of thermal shields for example), plasma materials processing (for example spheroidisation) and waste material treatment [94]. Currently, the plate power supplied to the commercial torches ranges from several kilowatts up to 400 kW [42].

The torch configuration, as shown in the right picture of Figure 2-7, has three inlet positions. The inlet in the middle, Q1, is the carrier gas or plasma gas inlet which supplies the plasma gas and the precursor. The flow rate of the carrier gas used should be sufficient enough to introduce the precursor in the plasma [98], but as small as possible to prevent that too much energy has to be used for heating the carrier gas [93], [99] and also to avoid a strong decrease of the residence time [100]. The position of the water cooled injection tube can be varied in axial direction. It can even be introduced in the discharge region [93], [101], since there is a non-coupling of the tube with the coil, because of the small skin depth.
The carrier gas can also be used to introduce a chemically active species forming a so called reactive plasma. Guo et al. [45], for instance, introduced methane in the plasma to synthesise SiC from metallic silicon.
The second inlet introduces the central gas Q2 to the torch, usually with a swirl component [102]. The function of the central gas is to act as plasma gas and to stabilise the plasma. Reed already observed that tangentially introducing the central gas had a stabilising effect on the plasma allowing higher gas velocities [55].
The inlet Q3, closest to the torch wall, supplies the sheath gas to the torch. The sheath gas is used for cooling the ceramic tube [93]. To improve the cooling a molecular gas (H_2, N_2, ..) is usually added; the higher thermal conductivity allows faster heat transfer and the molecular gases have a higher heat capacity than argon. The sheath gas also shields the ceramic tube between the coils and plasma from being coated by the precursor and thereby changing the coupling behaviour.

The effect of the several parameters on the temperature and flow fields in the plasma has been the topic of many investigations. Parameters like gas flow rates and compositions, pressure, injection position and mode, plate power, etc. have been investigated by several authors (Table 2-2).

Table 2-2: the work of several authors has been grouped by the studied parameter. The main effects of the parameter on the concentration, temperature, and velocity profile are mentioned. The references are divided into experimental, *theoretical*, or experimental and theoretical work.

Parameter	Main effects on the concentration, temperature and velocity profiles	Author
Torch / injector geometry	Better mixing for axial injection than radial. Natural convection has a negligible effect on discharge region, but has an influence on the free streaming jet.	Allemand and Barnes [100], Soucy et al. [101], [103], Boulos et al. *[102]*
Coil geometry	2D modelling of different coil geometries hardly shows an effect on the profiles. 3D modelling show asymmetric effects for non-symmetrical coil geometries.	Bernardi et al. *[96]*, *[104]*, Xue et al. *[105]*
Gases	Increase of the carrier gas will reduce the mixing of the axial injected gas (reduction of recirculation) and locally decrease the temperature on the axis (only heat transfer by conduction from the skin depth). Increase of the swirl velocity and/or carrier gas flow rate reduces the reflow around the top turn of the coil caused by magnetic pinch effect (EM field). The existence of a second reflow around the last turn of the coil has been shown, which loses strength with increasing total gas flow rate. Injecting molecular gases instead of Ar as carrier gas decreases the maximum plasma temperature, because of the higher specific heat. The temperature decreases as He is introduced in sheath gas (higher specific heat and lower electrical conductivity, see eq. 2.5), but increases as He is introduced as carrier gas (due to the higher thermal conductivity). The introduction of a molecular gas in the sheath reduces the temperature, because of the higher specific heat and higher thermal conductivity. The power necessary to sustain a plasma increases with increasing specific heat and thermal conductivity. Addition of molecular gases leads to a lower maximal temperature in the plasma, but results in a larger hot temperature area.	Boulos [93], Bernardi et al. *[96]*, Mostaghimi *[99]*, Soucy et al. [101], [103], Boulos et al. *[102]*, Boulos *[106]*, Barnes et al. *[107]* [108], Sesi et al. [109], Cai et al. *[110]*, Nishiyama et al. *[111], [112]*, Rahmane et al. [113], [114], Girshick and Yu [115], Désilets et al. [116]
Pressure	The mixing of radial and axial injected gas is slower with lower pressure. Higher pressure reduces the maximum temperature at the axis. The minimal power for sustaining a plasma is lower for reduced pressures.	Boulos [93], Soucy et al. [101], [103], Rahmane et al. [113], [114], Paik and Pfender [117], Paul and Sakuta *[118]*, Mostaghimi et al. *[119]*

Injection position / mode	The axial injected gas (Q1) mixes slower with other gases for deeper injection position. Radial injected gas mixes much faster than axially injected gas.	Soucy et al. [101], [103], Njah et al. [120], *[121]*, Davies and Soucy [122], Meubus [123]
Power	Mixing of axially and radially injected gas is faster with decreasing temperature. Increasing power at a constant gas flow rate increases the radiation heat loss	Bernardi et al. *[96]*, Mostaghimi et al. *[99]*, Soucy et al. [101], [103], Barnes and Nikdel *[107]*, Nishiyama et al. *[111], [112]*, Rahmane et al. [113], [114]
Frequency	The reflow, caused by the EM, is decreased at increasing frequency. The maximum temperature is closer positioned to the torch wall at higher frequency, due to smaller skin depth. A lower maximal temperature is obtained with increasing frequency, due to decreasing electric conductivity. The plasma diameter reduces with increasing frequency. The minimal power for sustaining a plasma is reduced with increasing frequency (1/f)	Boulos [93], Bernardi et al. *[96]*, Mostaghimi and Boulos [124], Shigeta et al. *[125]*
Up-scaling criteria	Scaling laws have been established.	VandenAbeele and Degrez *[126]*, Rahmane et al. [127]
Energy balance	Increase of the total gas flow rate increases the energy at the torch exit and lower losses at the torch wall. Approximately 60% of the plate power ends up in the plasma for a PL-35 torch.	Dundas and Thorpe [42], Reed [55], Boulos et al. *[102]*, Boulos *[106]*, Barnes and Nikdel *[107]*, Merkhouf and Boulos [128], Miller and Ayen *[129]*
Quenching	Reactive quenching with NH_3 enables nitridation of metals. Introduction of an expansion nozzle reduces the particle diameter. The penetration depth of a radial injected gas is a trade off between nozzle number and diameter for a fixed total inlet area. Influence of quenching on chemistry	Pirzada [51], Boulos et al. [52], Soucy et al. [103], Davies and Soucy [122], Johannessen [130], Wegner et al .[131], Sundström and DeMichiell [132], Hansen et al. [133], Stratton et al. [134]

Note: radial injected gases are introduced at or below the torch exit.

In the next paragraph a short overview of the theoretical work found in the literature on computational fluid dynamics (CFD) modelling of the ICP (process) is given. Modelling is a very important tool to predict the behaviour of a system when system parameters are changed. It also enables the visualisation of the temperature and flow fields and physical phenomena within the system. Possible weak and critical points in the system can be identified. Furthermore CFD can be used to accelerate

the development of new processes and equipment, since the behaviour of prototypes can be predicted without having the necessity to build them.

2.3 CFD Modelling

2.3.1 Introduction to CFD modelling

A model is the simplified theoretical description of real process and describes it by solving numerical equations. The goal of the model is to give a good representation of the “reality” and the ability to predict the influence of parameters on a process.
The equations in the models that have to be solved no longer require supercomputers and/or clustered workstations. Current computational fluid dynamics (CFD) software like Phoenics, FEM-Lab or Fluent are able to solve relative complicated systems on a normal personal computer within a reasonable time. Patankar describes the industrial importance of modelling by giving some examples of problems like tunnel ventilation, chemical vapour infiltration, refining hearths, and cement kilns [135]. The strong point of CFD is the ability to predict the behaviour of system on changes without the need for carrying out additional experiments. Even if the model does not predict the results exactly, it will at least pick up the trends, which allows better understanding of the process.

The combination of CFD with monitoring techniques (laser, optical emission spectroscopy, Fourier transformed infrared spectroscopy, etc.) is a very powerful tool for better plasma process control [136]. Deviations of the process can be detected in real time by the in-situ monitoring and non-intrusive techniques allowing a quick response to restore the optimal / defined process conditions.
Since usually both CFD and monitoring techniques are available for research, they can be used for understanding and guiding the experiments.

Even though modelling is a very useful and powerful tool to predict and describe the “reality”, its results should always be treated with care, because each model is based on approximations and assumptions.

2.3.2 CFD modelling of the ICP process

There has been a vast amount of literature published on modelling of ICP processes, ranging from modelling of the plasma itself (plasma properties) to predicting the effects of a modified torch design [100]. Some of these works are described below.

As Reed measured the temperature profile by optical spectroscopy within a torch (26 mm outer diameter) in 1961 [55], the presence of “hot spots” due to the energy dissipation in the skin depth was not observed. Also a possible influence of magnetohydrodynamic (MHD) forces caused by the electromagnetic (EM) field on the fluid flow within the torch was not mentioned. These forces can cause a reflow in the torch, around the top of the induction coils, depending on the frequency and gas flow rates. Later, calculations by Soshnikov and Trekhov [137] showed the presence of MHD forces, although they claimed that the forces were too small to exert influence on the plasma (at atmospheric pressure and a frequency of 50 MHz). The first to mention that the MHD forces were strong enough to cause a reflow within the torch was Chase in 1969 [138].

In the second half of the 1970's Boulos started with modelling of the ICP's fire-ball [106] and paid more attention to the influence of the electromagnetic field on the fluid flow in the torch. Figure 2-8 shows the temperature profile in the torch as calculated by Boulos [106]. The temperature maximum is off-axis, which is a consequence of the partial penetration of the EM-field into the torch caused by the skin-depth (equation 2-4, page 18). Reed [55] did not find this maximum because of errors in his spectroscopic work [129].
The influence of the EM field seems to be reduced or even negligible when a large swirl velocity in the central gas is being used [102], [124], [138], which causes a low pressure region overwhelming the upward flow caused by the EM-field [138]. Also operating the torch at high frequencies (13.56 MHz) reduces the reflow [124] or even let the reflow vanish [125]. The reduced reflow is also observed when an increased swirl velocity and frequency are combined [96].

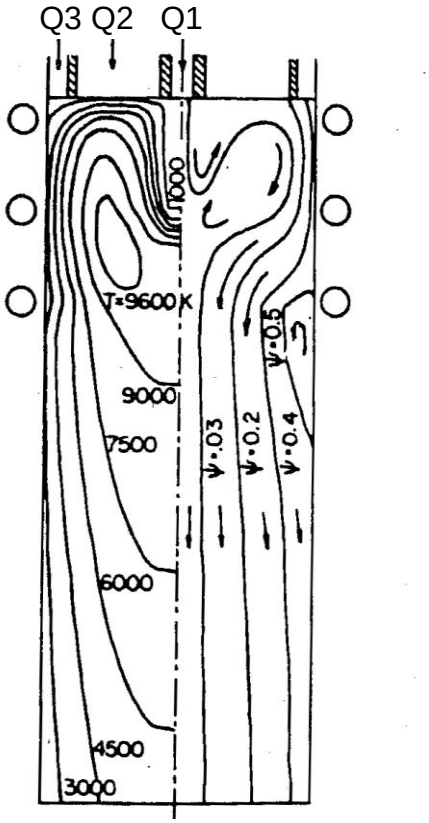

Figure 2-8: temperature profiles in the ICP torch as calculated by Boulos [106].

Although Boulos was not the first to notice the reflow in the ICP torch caused by the EM field [138] (30 mm diameter), he was the first to notice the second reflow at the end of the coil [106] (28 mm diameter). The influence of frequency, power and flow rates on the temperature and flow fields in the torch was investigated by Mostaghimi et al. [99] (50 mm diameter), Boulos et al. [102] (30 mm diameter), and Boulos [106]. In these models the EM field was assumed to be 1D. They found a reduced or even vanishing reflow in the coil region with increased swirl velocity and carrier gas flow.
In the work of Mostaghimi et al. [99] a comparison between an argon and nitrogen plasma was made; a lower temperature maximum (2000 K) was found for the nitrogen plasma, although the plate power amounted 10 kW for nitrogen and only 3 kW for argon. Furthermore, it was shown in this work that an increasing carrier gas flow rate reduces the temperature at the axis.

A further improvement of this model was the introduction of a second dimension for the EM field by Mostaghimi et al. [139] in a 50 mm torch using a pure Ar plasma. This standard 2D model offers the possibility to account for the influence of the coil geometry on flow and temperature fields. It also gives a better representation of EM fields at higher frequencies. This refinement resulted in hardly any difference on the temperature profile. The reflow caused by the MHD forces however was reduced.
Nishiyama et al. [111] also dealt with 2D EM field modelling of the plasma in a 50 mm diameter torch. They investigated the influence of plasma parameter variations like power and He (carrier) gas injection on amongst others the temperature and flow field of an Ar plasma using a Ar/He mixture as sheath gas [111], [112]. They found that an increased He carrier gas flow rate decreased the plasma temperature at the axis and the introduction of a swirl component in the central gas increases the temperature at the top of the coil.
Shigeta et al. [125] modelled the influences of the frequency, 0.5 and 13.56 MHz on the plasma velocity and temperature fields of an Ar plasma (8 kW plate power and a 50 mm torch diameter) and found the absence of the recirculation flow at 13.56 MHz. Also a slower particle evaporation was found for 13.56 MHz, meaning the evaporation of smaller particles as compared to 0.5 MHz.
Park and Hong [140] calculated the temperature and flow fields for an argon-nitrogen plasma with a 2D EM model, see Figure 2-9. They investigated an Ar plasma in which nitrogen was added to the sheath or carrier gas, in a 44 mm inner diameter torch, operating at 3 MHz and 100 A current. When nitrogen was used as a sheath gas, their simulations did not show an off-axis temperature maximum. When nitrogen was added as a carrier gas, an off-axis maximum was found, but this was due to the cooling effect of the nitrogen.

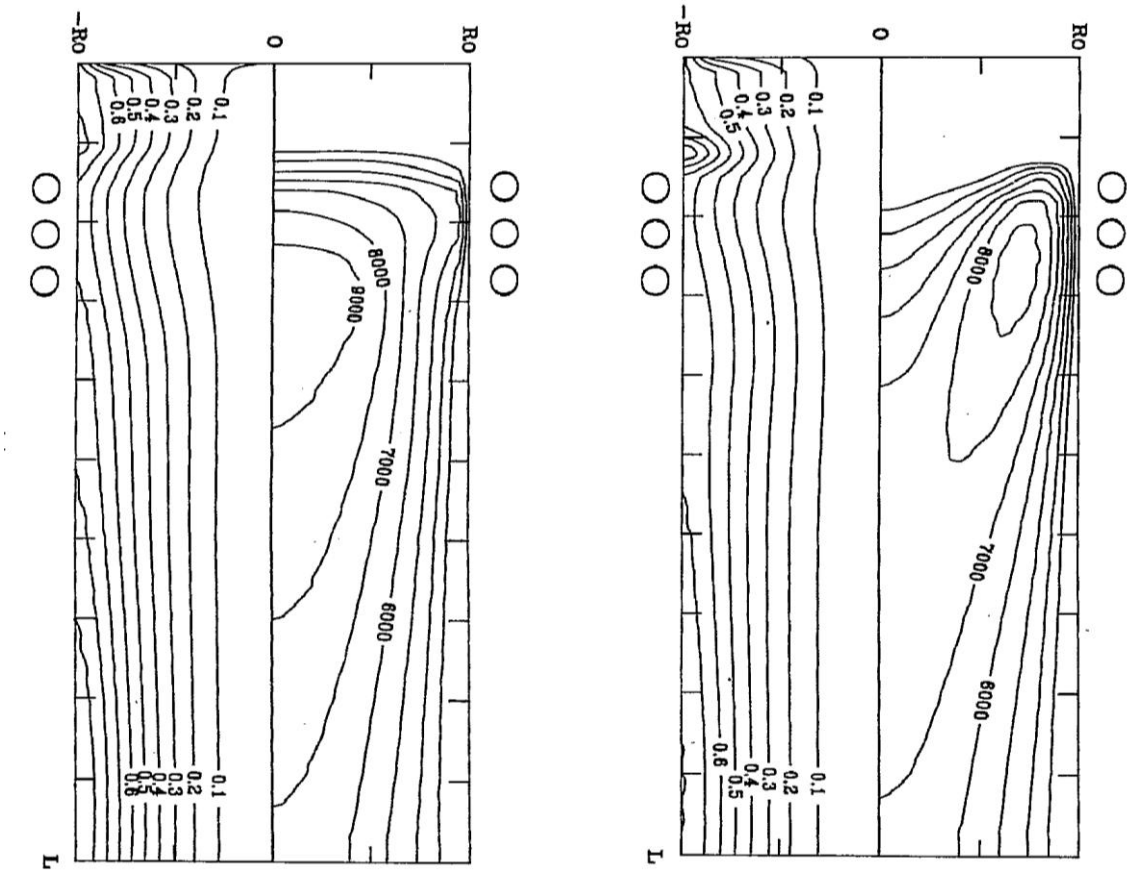

Figure 2-9: streamlines and isotherms in the torch as calculated by Park and Hong [140]. Left side: N_2 used as sheath gas. Right: N_2 used as carrier gas.

A further improvement to the model by Xue et al. [141] was the extension of the EM field outside the torch; meaning in the torch body, see Figure 2-10. The torch had a 50 mm diameter, was operated at 3 MHz and the Ar plasma had 5 kW net input). This extended field model allowed simpler boundary conditions for the EM field, which results in a better stability and easier convergence of the calculations. The extended field model also yields a more realistic EM field around the coil region and can predict the effects of the coil geometry on the EM, flow and temperature fields even better than the standard 2D model presented by Mostaghimi et al. [139].

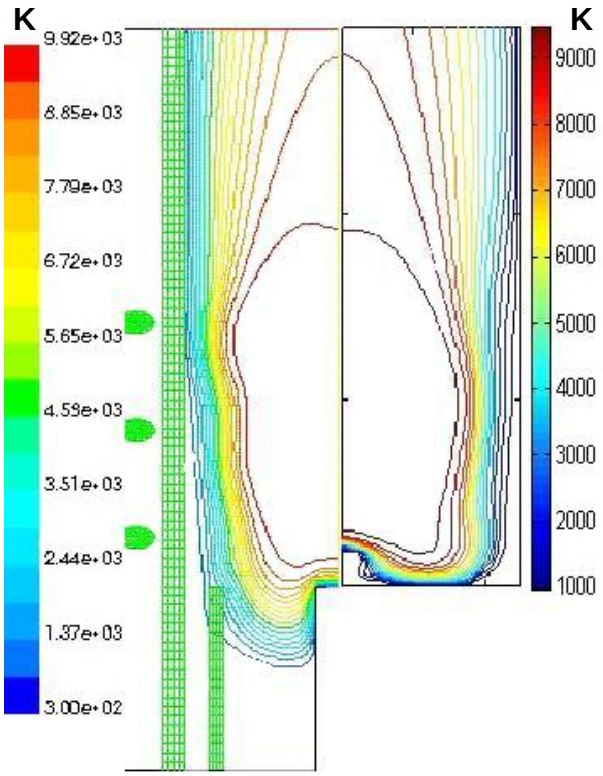

Figure 2-10: difference of the calculated temperature profiles in the ICP torch between the extended field approach (left side) and the standard 2D model (right side) [141]. Plasma is flowing from bottom to top.

Xue et al. [105] modelled the coil geometry as being asymmetric (a real turned coil) and not as flat coil rings. For small inclinations of the coil (around 4 degrees) the influence on the temperature and flow field can be neglected.
Bernardi et al. [96], [104], and [142] also showed that the 3D effects caused by the coil and play an important role on the characterisation and (non-) symmetry of the discharge.

he influence of the frequency and pressure on the local thermal equilibrium (LTE) conditions was modelled by Mostaghimi et al. in [119] and [124] respectively. The results showed a larger deviation from LTE conditions with higher frequency (modelled 3, 13, 26, and 40 MHz) and lower pressure (modelled 0.3 and 1 atmosphere).

Merkhouf and Boulos [128] also determined the electrical and energy balances for the torch and power supply. These measured balances were used to validate an integrated mathematical model. It was found that for a PL-35 torch about 60% of the plate power ends up in the plasma.

2.4 Particle and gas injection into a plasma

Before the nanoparticle formation by nucleation can occur, the precursor has to be first introduced in the plasma and then evaporated. The precursor particle injection is therefore very important. The importance of the injection system in general for any kind of application, is underlined by the presence of firms offering a wide range of special injection nozzles, like Lechler GmbH, Germany and Spraying Systems Co., USA. The nozzle is defined as the outlet of the injection system.

The injection of precursor particles into a plasma jet has been very well described for plasma spraying where the precursor particles are generally injected radially into the plasma. The influence of the precursor size distribution, carrier gas flow rate, injector geometry and position, etc. on the precursor trajectories in the plasma has been the subject of many papers [143], [144], [145]. Fauchais et al. [61] mention some of the problems which can be expected when injecting particles into a thermal plasma (e.g. a radial velocity distribution of the precursor after injection, cooling of the plasma by the carrier gas). Vardelle et al. [146] have published a review on experimental and analytical techniques on the powder injection system efficiency in plasma jets used for spray coatings.

The main problem for a uniform particle injection into a plasma is the necessity of certain momentum to penetrate the plasma. Since only the mean momentum can be adjusted and the precursor particles usually do not have monodisperse size distribution, several particles will have a different momentum, which will especially affect the trajectories of radially injected particles.

In case of the axial injection the main problems caused by the particle injection are the cooling of the precursor entrance region close to the centre line and the presence of a large recirculation caused by the MHD forces causing repellence of the particles and thereby give rise to different trajectories [61].

The importance of the precursor particle injection in the ICP process has already been recognised by Chase and Van Ruyven [98], who found that a minimum carrier gas flow rate was necessary to introduce all the precursor particles into the plasma. A lower carrier gas flow rate would result in some of the particles flowing around the plasma edge [98], [147], and thus in different trajectories of the precursor particles meaning different thermal histories. Too much carrier gas however cools the plasma along the axis [99]. This means that the precursor particles could not be completely vaporised or even melted, resulting in produced particles with a size in the same order as the precursor in the product. Boulos [148] approached this effect from a theoretical side and found that precursor particles can follow different trajectories depending on initial injection position and injection velocity. Also the influence of the precursor size on the trajectory was investigated; particles smaller than 10 µm are able to follow the streamlines.

Also Reed emphasised the proper choice of the precursor particle size [97]. Not only the precursor particle size, also the precursor feeding rate is of importance [149]. A too high precursor loading will eventually result in extinguishing of the plasma.

Another important parameter is the injector position, Figure 2-11 shows a schematically representation of ICP torch configurations with different injector arrangements.

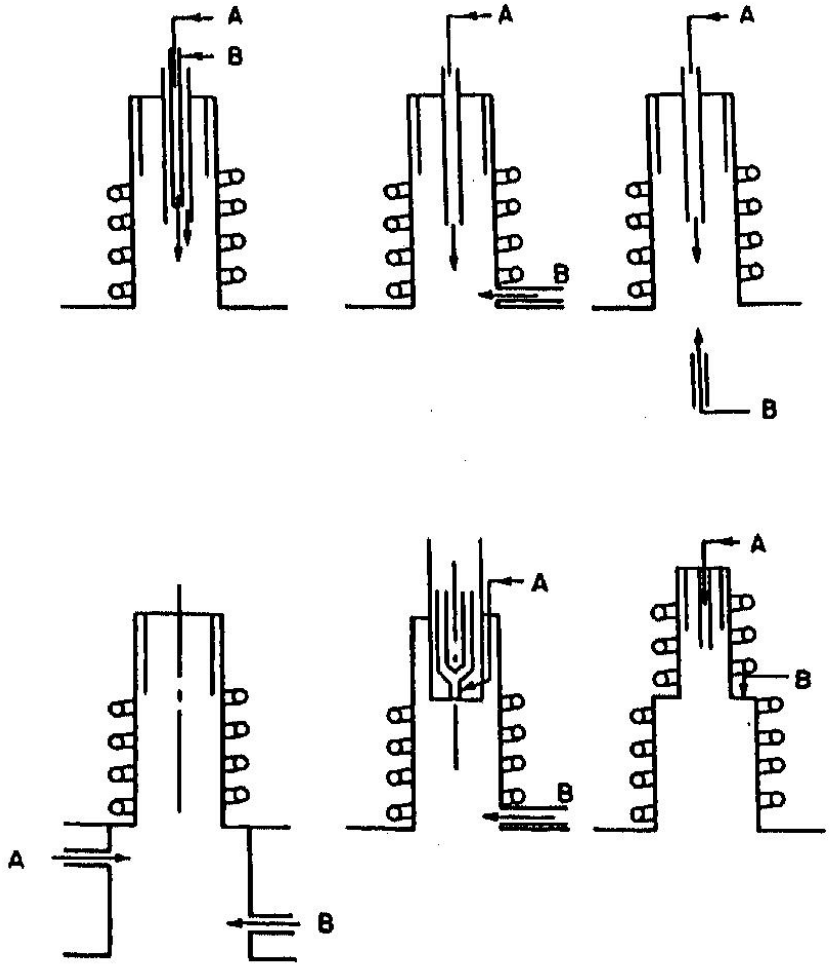

Figure 2-11: six schematic representations of different injection configurations, when a second flow is to be introduced, are shown [94]. The reactor set-ups at the bottom middle and right are DC-RF and RF-RF hybrid reactors, respectively.

Thursfield and Davies [149] determined the influence on the ICP decomposition of $MnSiO_3$ (in MnO and SiO_2) of four different injector positions, see Figure 2-12. Positions 2, at the upper edge of the plasma, and position 3, just below the last coil, gave the best conversion to MnO. Proulx et al. [150] also confirmed that the injector position in the middle of the coil region (below the recirculation zone) gave a higher liquidised fraction compared to an injection position just above the first coil, due to a lesser amount of carrier gas necessary to penetrate the plasma.
Park and Hong [140] have carried out similar experiments for the reactive synthesis of AlN from solid aluminium particles and nitrogen. However, they demonstrated that a radial particle injection below the coil region is to be preferred above axial particle injection; the cooling due to the injected particles would disturb the plasma stability in the torch. In this work they also found that nitrogen in the sheath gas is more favourable for nitridation than nitrogen in the carrier gas (they only indicated a coil current of 100 A and no power).

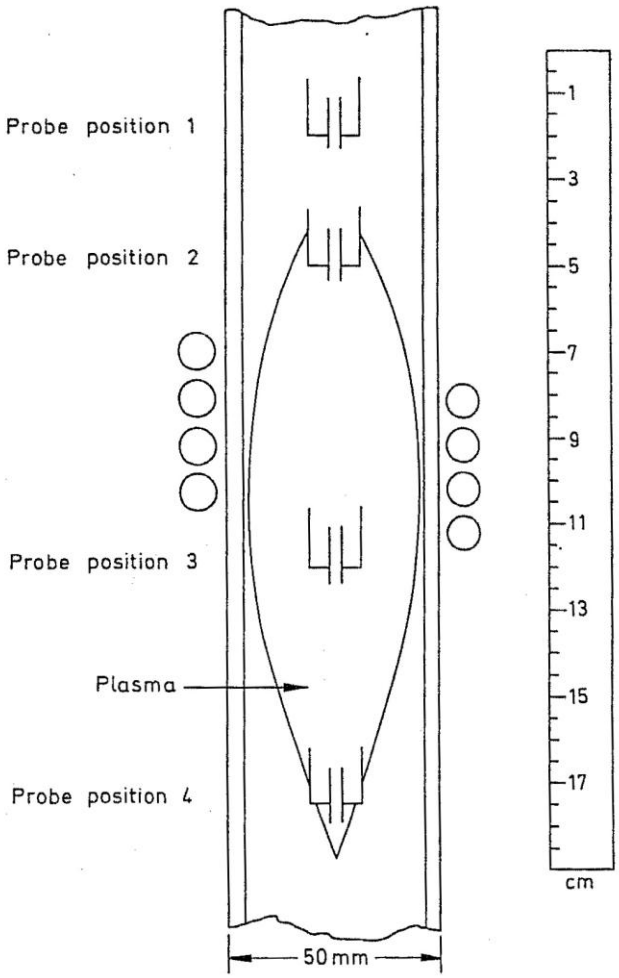

Figure 2-12: different precursor injection positions within a RF plasma torch [149].

The influence of the injection position on the carrier gas – plasma gas mixing was investigated experimentally by Soucy et al. [101] (without precursor particles). They found that mixing took place earlier when the injector was placed at the first coil as compared to a position at the last coil. Also, the gas mixing is much slower under plasma conditions as compared to the cold gas mixing due to the lower viscosity at room temperature.
Rahmane et al. [113], [114] investigated the axial injection of a cold carrier gas in the plasma. The concentration of the injected gas in the plasma, the temperature and velocity profiles of the plasma were modelled and measured as a function of the kind of plasma gas and flow rate at several heights in the torch. They found a much slower gas mixing under plasma conditions, a cooling effect on the plasma caused by the injection of a cold carrier gas, which shows a stronger effect when the injected gas is molecular. The cooling effect at the axis amounts around 4000 K between 0 (8000 K) and 8 slpm N_2 (4000 K) carrier gas at a plate power of 20 kW and a pressure of 33 kPa.

Because of the importance of a well designed injection system on the process, CFD can be an important development tool, since the new injectors can be treated theoretically and do not have to be built first and tested. Modelling has also been applied to find optimal nozzles designs, for DC spraying nozzles [151] and ICP nozzles [100].

2.5 Plasma – particle interaction

After the solid precursor particles have been injected into the plasma they have to be completely vaporised. The interaction between the plasma and the precursor determines the melting and vaporisation rate. From this rate one is able to determine the optimal residence, feed rate, and matching precursor size for complete vaporisation [152]. Reviews on the particle - plasma interaction both theoretically and experimentally are given by Waldie [153] and Pfender [154].
Pfender et al. [155], [156] described the particle dynamics and particle heat and mass transfer in thermal plasmas. Influence of variable plasma properties on transfer and drag coefficients, thermophoresis, particle shape, non-continuum effects, Basset history term, evaporation, turbulent dispersion, radiation and internal conduction, unsteady conditions, and particle charging were investigated.

Boulos [148] calculated the trajectories, temperature, and diameter of particles as a function of the heat transfer from the plasma by taking melting and vaporisation into account. The main assumptions were neglecting the particles' influence on the temperature and flow fields under low loading conditions, the absence of temperature gradients in the particle itself, and neglecting the effects of the vapour around the particle on the heat transfer. The trajectories and temperature histories were calculated for different particle sizes and inlet conditions and depended on the size, initial injection position and velocity.
The influence of vapour on the temperature profiles has been modelled by Proulx et al. [147], [157] and Essoltani et al. [158]. They found that the presence of only a small concentration of vapour increases the radiative energy loss by a substantial amount and therefore decreasing the temperature and the particle evaporation. A temperature decrease on the axis over several thousand degrees, depending on the loading, was reported as a consequence of these effects.
Proulx et al. [147] investigated the effect of particle load, size and size distribution, material properties on the plasma temperature. They found a decreasing temperature of the core region caused by an increased particle load and a by an increased electrical conductivity as a consequence of the vapour presence. The physical properties of the precursor particles were also influencing the plasma temperature; the same mass feed rate of alumina absorbed more energy than copper (higher specific heat, higher latent heat of melting and boiling for alumina). Furthermore, Proulx et al. [147] also found that powders with many small particles absorbed more energy than the same mass feed rate with larger particles. The smaller particles also showed a larger cooling effect than the larger particles, which is mainly due to a faster evaporation of the smaller particles.
Chen et al. [159] investigated the influence of the vapour on the heat transfer to a copper particle. They found that evaporation can greatly reduce the heat flux from the plasma to an evaporating particle.

Bernardi et al. [160] modelled the particle size, velocity, and temperature for different materials, diameters, and plasma conditions in an ICP process. They also calculated the particle dispersion by 3D modelling for different injection positions and swirl components of the gas flows. A smaller deviation of the original trajectory was found for heavier particles, but they did not validate their results with experiments.

2.6 Cold gas quenching

Besides the particle injection also the temperature during processing has a huge influence on the synthesis process. It is well-known that quenching, i.e. fast cooling, slows down or even stops the particle growth [22], [58], [161], [162], but also enables the preservation of metastable products down to room temperature [57], [163].

Quenching results in a significant decrease of the gas phase temperature (and particle temperature), causing a highly supersaturated vapour from which small nuclei (nanoparticles) are obtained. The supersaturation influences the amount and size of the synthesised nanoparticles [22]; a high supersaturation results in more and smaller particles than with a lower supersaturation [21].

Quenching can be carried out by using for example an expansion nozzle [51], [131], in which the cooling is achieved by adiabatic expansion of the gas, or by using a cold surface on which the particles deposit and are scraped off [19]. Borgianni et al. [164] used a movable “cold finger” (a cold surface) in their experiments to investigate the phase composition at different axial positions.

Sundström and DeMichiell [132] analysed some other possibilities to extract heat relatively fast from gases, like a gas mixing, cold wall, fluidised bed, liquid spray, etc.. They found that the cold gas mixing and fluidised bed gave the fastest quenching rates. The quenching techniques mentioned here are able to obtain cooling rates of 10^6 K.s^{-1}, see Figure 2-13. The natural temperature gradients in the plasma are in the order of 10^3 K.mm^{-1} [165].

From all these methods the gas injection seems to be the most flexible one: easy to position, variable quench rate, use of reactive quench gas. Quenching rings consisting out of several nozzles introduce cold gas into the plasma [52], [130], [133]. The drawback of using gas quenching systems is a high gas consumption. The costs however can be reduced by using a quench gas recycling system. The introduction of the quench gas has also another advantage meaning the formation of smaller particles as a consequence of the dilution [166].

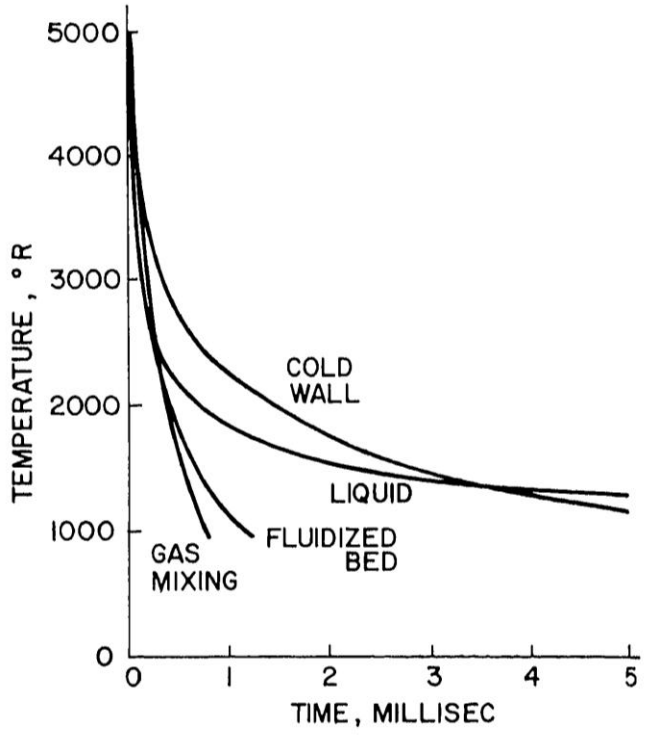

Figure 2-13: temperature as a function of time for different quenching methods [132]. The slope of these curves represents the quenching rate. (1°R = 1.8 K)

Although quenching is a very important step in the particle growth process, it is usually just mentioned that quenching has been carried out [22], [43], [58], [161], without giving many details concerning quenching position, flow rates, diameter, etc..
Only a few articles describe the quenching process in more detail, in which quenching is defined as the radial mixing of cold gas with a plasma gas.
Davies and Soucy [122] used a four-nozzle quenching ring (nozzles equidistant without axial or tangential component, position 5 mm above the torch exit) in their experiments to decompose NH_3 in the tail flame of an IC plasma. They found that the radially injected gases need a sufficient amount of kinetic energy to penetrate the plasma, depending on pressure, power, and gas flow rates. The cooling effect gets more pronounced with increasing radial gas flow rate.
Soucy et al. [103] measured the influence on the mixing of a radially injected cold gas within the plasma as a function of the number of nozzles (the nozzle diameter was kept constant, ring diameter 41 mm (9 mm above the torch exit) and 62 mm (6 mm below the torch exit and 45° upward angle). The penetration depth was inversely related to the number of nozzles for a constant flow rate, meaning a decreased penetration for an increased number of nozzles (lower velocity). Furthermore, they also found an increasing penetration depth with increasing flow rate, a faster mixing in the cold mixing case (without plasma), and the existence of a critical velocity to penetrate the plasma. It was also noticed that at very high radial gas flows, the mixing occurs further upstream, especially for the multi nozzles configurations. In [103] also an experiment with a three-nozzle design, having a radial component of 45° in upward direction, was carried out. This design resulted in a mixing further upstream, so that the radial injection position can be located further downstream as compared to the mixing without a radial angle.

Proulx and Bilodeau [166] described the effect of quenching on the Fe nanoparticles produced by an ICP process. They found a decreasing particle diameter with increasing quench gas flow rate (1 mm slot having a 70 mm inner diameter, positioned 100 mm below the torch exit with 0 - 50 slpm Ar quench gas) and decreasing iron concentration. Also a maximum particle size was observed in the radial direction, between axis and torch wall. In a further work of the same authors [80] on Si (decomposition of $SiCl_4$) they found that quenching resulted in a more homogeneous particle size distribution.
Ishigaki et al. [167] used an eight-nozzle (1 mm diameter, perpendicular to the torch axis) quench system to quench a plasma stream containing TaC just below the torch exit. They found that He used as quenching gas is more effective than Ar for the same amount of gas.
Njah et al. [120], [121] used 2D and 3D CFD simulations to investigate the influence on mixing, velocity, and temperature profiles as a function of the number of nozzles (inlet area is kept constant, ring diameter 50 mm, quench positions 33 and 50 mm below the torch exit). The 3D model used the results of the 2D model for the inlet boundary conditions. This works shows that the optimal number of nozzles in a mixing design is a compromise between the penetration strength (momentum) and the mixture ability of each nozzle.
Stratton et al. [134] described the quenching of a plasma, which was generated with a PL-35 torch, for the synthesis of ozone. The influence of single nozzles with different diameter, angles with respect to the plasma, and nozzle exit configuration on the ozone synthesis was investigated. Depending on the nozzle position and

geometry, differences in the synthesis yield and optimal quench gas flow rate were found.

Johannessen [130] used a moveable quench ring with five equidistant nozzles (ϕ 1 mm, without radial or tangential component, positioned 30 mm above the flame arrestor) to investigate influence of the quench ring height and gas flow rate on the primary particle size made by flame synthesis. The experiments were supported with 2D CFD simulations; the nozzles were replaced by a slot (the surface of the slot was chosen to obtain the equal kinetic energy for the same volumetric flow rate). The deviations caused by modelling 2D instead of 3D were found small enough to prefer the 2D model above the more elaborate and time consuming 3D model.
Hansen et al. [133] improved this quenching ring by using 2D CFD modelling. The improvement resulted in an eight-nozzle quenchring (against five in [130]), with each nozzle having a 1 mm diameter, a downward angle of 20° with respect to gas inlets and a 10° swirl component (positioned at 17 mm above the flame arrestor). The new design resulted in a more stable flame and less perturbed particle trajectories, see Figure 2-14. The left picture in Figure 2-14 shows in fact the upstream mixing as described in by Soucy et al. for their 45° angled nozzle [103].

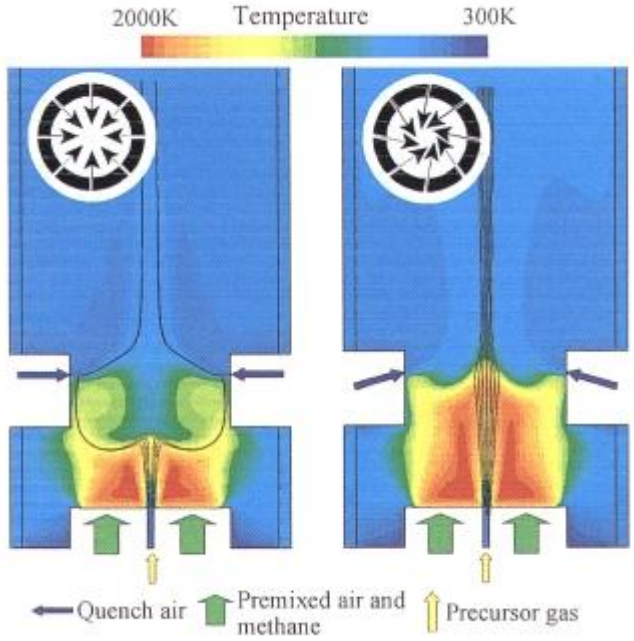

Figure 2-14: comparison of the temperature fields between a slot without (left) and with (right) an axial and tangential component. [133]. The black lines represent the average flow field of massless tracers.

A quenching ring, consisting of 16 nozzles (1.5 mm inner diameter), perpendicular to the plasma flow but with swirl component (positioned at 160 below the torch exit), used to produce metal oxide nanoparticles is described by Boulos et al. [52]. The results show a faster quench rate with increasing quench gas flow rate due to the increased turbulence.

Yoshi et al. [168] investigated the effect of quenching on particle formation and growth in thermal plasma synthesis for the reaction of Zn vapour in an Ar plasma with O_2 in the quench gas. They found that a single- and multiport injection of the quench gas (30 – 40 slpm Ar + 10 mole% O_2) resulted in more and smaller particles at 40 slpm, while fewer and larger particles were found at 30 slpm. They concluded

that the controlled distribution of the quench gas gas provides the possibility to enhance the particle size and size range.
Soucy et al. [169] used N_2 and NH_3 quenching gas to nitridate $MoSi_2$. They found the presence of a threshold quenching gas rate to penetrate the plasma in order to obtain cooling and good mixing, which is different for each type of quench gas. Also an optimum amount of quenching gas was observed, because of the trade-off between penetration and reactivity (temperature).

The quenching gas can also be used to achieve chemical reactions, in addition to cooling [163]. By using gases like NH_3 or CH_4 instead of Ar or He, nitrides or carbides may be synthesised. The quenching efficiency of the reactive quenching gases can be much higher than that of inert quenching gases since the reactive gases have to be dissociated which consumes additional energy besides the normal heating as compared to a mono atomic gas.
Munz et al. [170] and Baba et al. [171] injected NH_3 perpendicular to the plasma flow to obtain AlN from metallic Al. Pavlovic et al. [172] used a counterflow injection (see Figure 2-11 top right) of ammonia and propane-butane to carry out reactive quenching of metallic silicon to form SiC and Si_3N_4 nanoparticles respectively.

2.7 Particle growth modelling

As the quenching influences the particle growth it would be very useful to have a model able to predict the particle size development as a function of the quenching rate. But also the ability to describe the influence of other parameters on the particle growth, as there are initial concentration, temperature and velocity profiles and physical properties, would be of great interest.

After nucleation, an aerosol is formed, which is defined as a suspension of particles in the gas phase. The discipline dealing with changes in particle size distribution in space and time (as for example in case of the nanoparticle synthesis) is called aerosol dynamics (AD). Bandyopadhyaya et al. [173] give an overview of this discipline in which the history and future developments are described. The foundations of aerosols dynamics are well described in the books of Friedlander [24] and Hinds [25].
The size distribution or population balance of the aerosol is a function of coalescence, coagulation, nucleation, reaction, etc. of the particles. These parameters in turn are a function of the (initial) concentration, temperature and velocity profiles, and particle properties like atomic diameter, melting point, sintering behaviour, surface tension, etc..

There are several models describing population balances, like a monodisperse model, one-dimensional or two-dimensional sectional models each with different assumptions and complexity [174].
The model of Kruis et al. [77] is a growth model describing the volume and surface area evolution of the primary particles and aggregates under coagulation and coalescence at non-isothermal conditions, under assumption of a monodisperse primary particle and aggregate size. In which an aggregate is a cluster of several primary particles. A schematic representation of the Kruis model is presented in Figure 2-15.

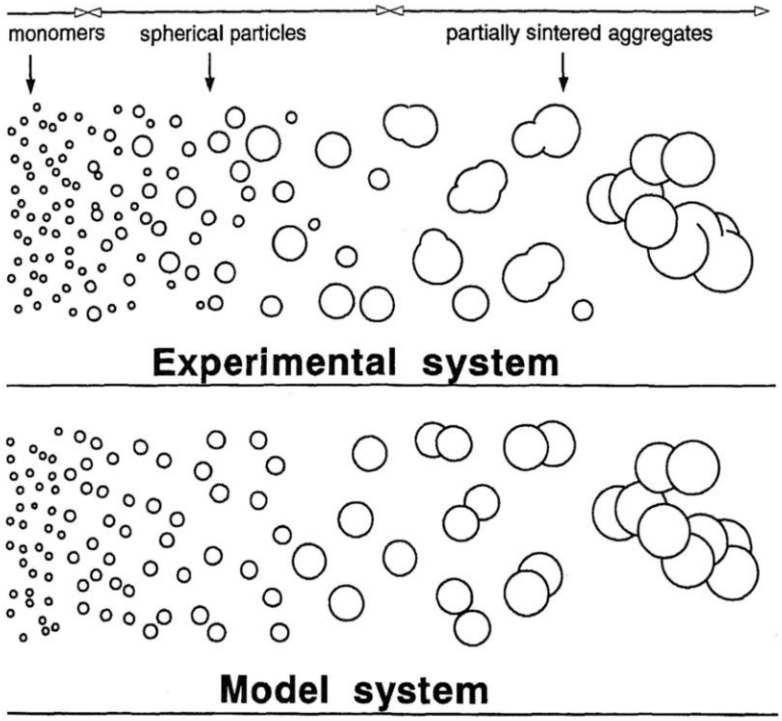

Figure 2-15: schematic representation of the aggregation sintering process and the description by the monodisperse model [77].

At high temperatures the sintering rate is high and a collision between the spherical particles results in the formation of one larger spherical particle before the next collision occurs. As the temperature decreases the sintering rate becomes lower and a collision between two spherical particles does not result in the formation of single spherical particles before the next collision occurs; the formed particles get slightly larger and are not spherical anymore. The particles are bonded with a sintering neck and hard agglomerates are formed. If the temperature has decreased to such an extent that the sintering rate gets very low, a collision between two spherical particles causes no changes in the particle size and shape; soft agglomerates are formed.
The coagulation coefficient accounts for the particles being smaller as the mean free path by using the Cunningham slip correction. Also the influence of the (increasing) collision radius on the coagulation coefficient has been introduced by using a fractal dimension which describes the aggregate structure (a fractal dimension of one means the aggregate is a line and three means a sphere).
The advantage of this model is its simplicity with reasonable good accuracy as compared to other better, but more complex models [77], [174]. The Kruis model also requires not so much CPU time and can therefore be carried out on a standard PC. The Kruis model was originally applied to model the particle growth of silicon particles by laser synthesis in an aerosol reactor [77]. Later on it has been successfully applied for modelling of flame processes and microwave processes in combination with commercial CFD software [30], [79], [175] .

Schild et al. [175] modelled the nanoparticle production of TiO_2 by the oxidation of $TiCl_4$ in a premixed aerosol reactor by implementing the Kruis model into a commercial CFD software. They found the combined model to be a very effective tool to simulate the particle formation process in complex reactor geometries and under authentic production conditions. There was no (published) comparison made to experiments.

Giesen et al. [79] modelled the nanoparticle production of Si in a microwave reactor by combining the Kruis model with a commercial CFD software. A result from this model is shown in Figure 2-16. They found the main relations of the particle size on the parameters like concentration, pressure and power to be described correctly by the model (e.g. an increasing particle size with increasing concentration). The absolute particle size was also found to be in good agreement with experimental results (3.3 nm found for the model to 5.0 nm in the experiments).

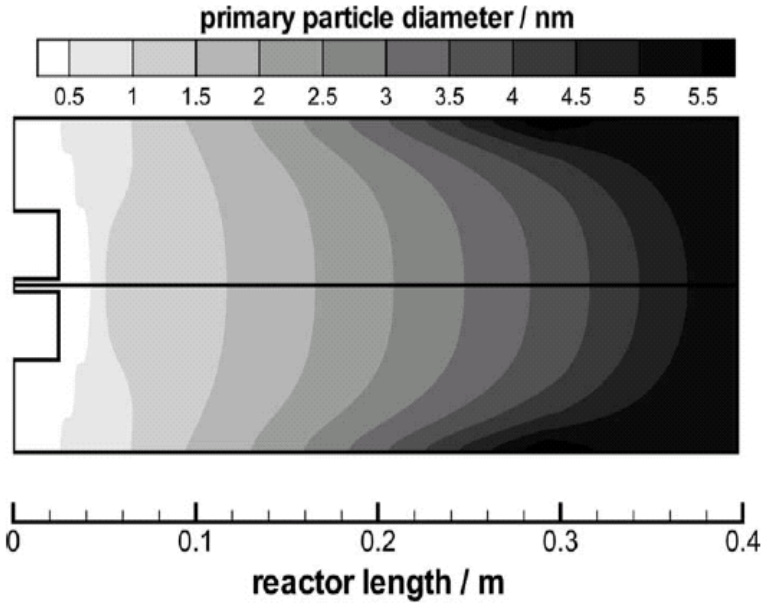

Figure 2-16: plot of the primary particle diameter as calculated by the Kruis model in a commercial CFD code [79].

Other particle growth models have also been combined with modelling of the ICP process.
Girshick et al. [44] described the synthesis of iron nanoparticles with an ICP process at atmospheric pressure. They developed a two dimensional momentum model, which calculated the temperature and velocity profiles, accounted for heating and evaporation of the solid iron precursor, modelled the particle nucleation and growth and particle transport by convection, diffusion, and thermophoresis. The modelling results were found to be in good agreement with experimental results (the average modelled diameters were within 6 nm of the experimental ones). The modelled size distribution was found to be smaller than the experimental one.
Shigeta et al. [161] modelled the nanoparticles synthesis as a function of material properties, quenching gas flow, and powder feed rate. They used a 1-dimensional growth model, which described the homogeneous nucleation and growth by collision and condensation from the vapour phase. Their calculations showed more and smaller particles with increasing quench rate and decreasing feed rate. The material properties had a significant influence on the number density and particle diameter.

The models sofar accounted for agglomeration, but did not discriminate between soft and hard agglomerates. A hard agglomerate is formed when a collision between two primary particles results in two primary particles connected by a sintering neck [26]. This is the case when the characteristic time for collision (see eq. 2-2) and for coalescence (see eq. 2-3) are of the same other of magnitude [27].
If the characteristic time for collision is much smaller than that for coalescence [26], then the particles or agglomerates are only kept together by Van der Waals forces

and soft agglomerates are formed. Hard agglomerates are formed when the characteristic coalescence time slowly passes the characteristic collision time, see Figure 2-17.
Windeler et al. [176] compared the growth process for three metal oxides with different sintering coefficients. The particles with a large diffusion coefficient yielded larger particles, while particles with a low diffusion coefficient formed smaller. The large diffusion coefficient is coupled to a small characteristic coalescence (sintering) time. As long as the characteristic collision time is larger than the coalescence time the particles sinter and thus grow faster than they collide (particle growth).

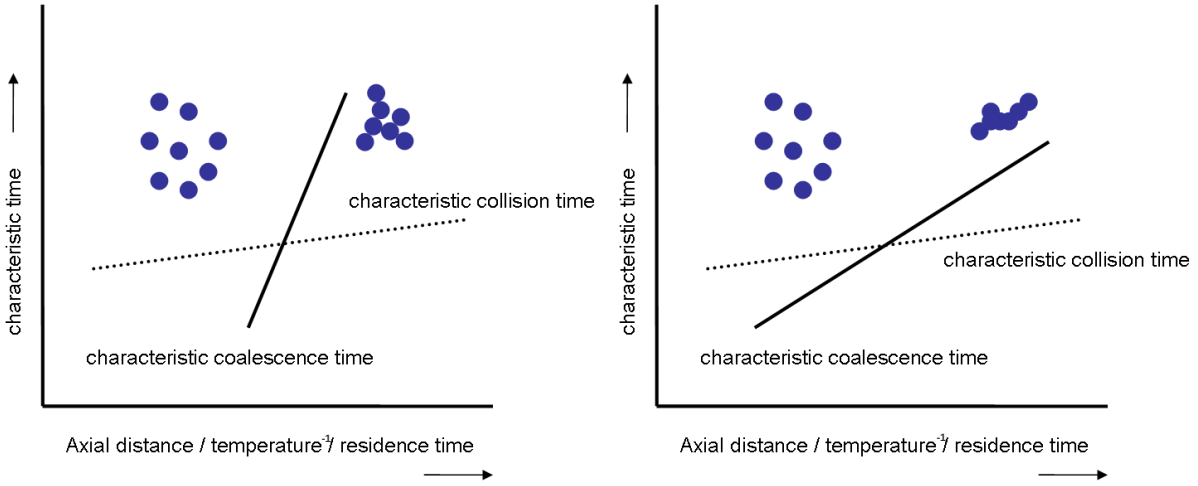

Figure 2-17: influence of the characteristic times on the aggregate formation (after Windeler et al. [176]). If the coalescence time increases much faster than the collision time (meaning a slower coalescence), then soft agglomerates are formed.

Since the characteristic coalescence time depends much stronger on the temperature than the characteristic collision time, quenching can therefore be an important tool to control the kind of agglomeration.
Tsantilis and Pratsinis [26] have modelled the effect of quenching on the formation of hard and soft agglomerates based on the Kruis model. They investigated the influence of temperature, residence time, initial concentration, and cooling rate. They defined the onset of the hard agglomerate region where the collision diameter is 1% larger than primary particle diameter. The onset for the end of the hard agglomerate region is defined where the primary particle diameter reaches 99% of its final value. A high quenching rate resulted in small primary particle diameters with increased soft agglomerate collision diameters. An example of their results is shown in Figure 2-18, it should be noted however that they also included some chemistry by introducing the dissociation of $SiCl_4$. The dissociation results in the monomer formation which is shown in Figure 2-18 by the increasing number concentration (N) at the beginning.

After all the models have been described and the experiments are carried out, the results of both have to be compared to each other. This comparison will give a better process understanding and will be used for validation of the model.

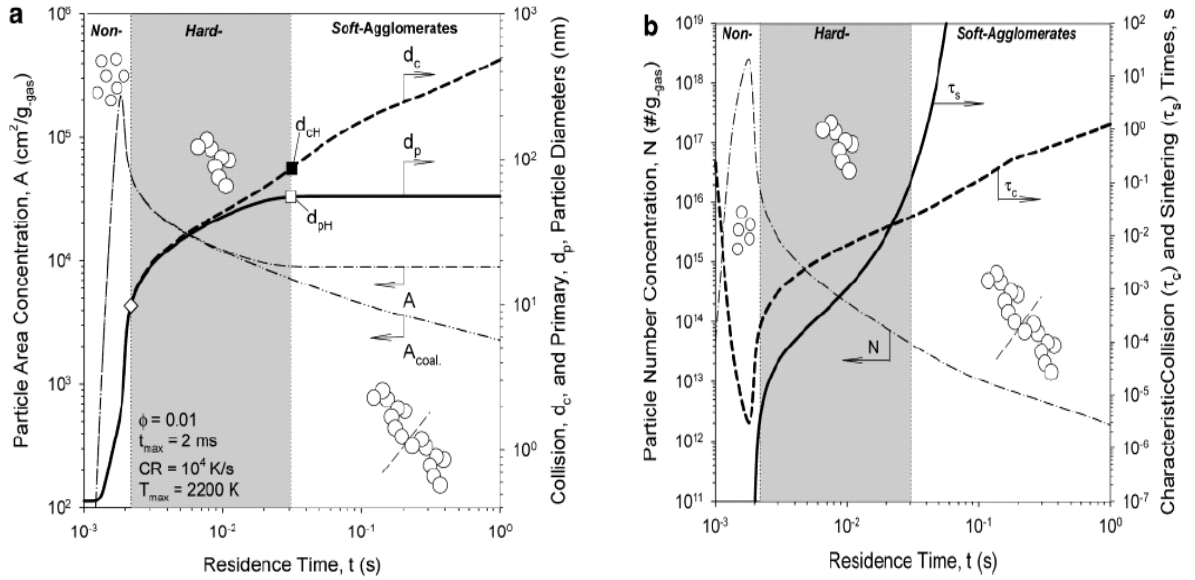

Figure 2-18: left: particle area concentration and particle diameters as a function of the residence time. Right particle number concentration and characteristic times as a function of the residence time [26]. In which ϕ = particle loading, CR = cooling rate, d_{cH} = hard agglomerate collision diameter, d_c = collision diameter, d_{pH} = hard primary particle diameter, d_p = primary particle diameter, τ_s = characteristic sintering time, τ_c = characteristic collision time.

2.8 Characterisations

2.8.1 Plasma characterisation

The plasma can be characterised by different quantities (like electron temperature, gas phase composition, plasma gas enthalpy and velocity, …) using several characterisation techniques. There are intrusive techniques, like enthalpy probe, Langmuir probe, etc, and non-intrusive techniques like spectroscopy, tracers, etc.. Some examples of techniques to characterise the thermal plasma flows with and without particles are given by Boulos [165] and Proulx and Trassy [136].

The enthalpy probe combined with a mass spectrometer (MS) is a very commonly used technique. The enthalpy probe is able to measure local pressure and enthalpy of the plasma [177]. A measurement consists out of measuring two modes; the “tare” mode, in which heat load on the probe measured in the absence of gas sampling and the “sampling” mode in which the same is done but now with gas sampling.
The (local) pressure is converted into a velocity (measurement in the tare mode), using the Bernouilli equation (equation 2-6):

$$v = \sqrt{\frac{2(p_0 - p_a)}{\rho(T)}} \qquad \text{eq. 2-6}$$

In which p_0 is the stagnation pressure [Pa], p_a is the ambient pressure [Pa], and $\rho(T)$ is the plasma density at the (local) plasma temperature [kg.m^{-3}]. This equation is valid for incompressible flows at low Mach numbers (equation 2.7):

$$Ma = \frac{v_{gas}}{\sqrt{\gamma R_s T}} \qquad \text{eq. 2-7}$$

in which v_{gas} is the plasma gas velocity [m.s^{-1}], γ is the ratio of the specific heats ($C_p\ C_v^{-1}$) [-], R_s is the specific gas constant which is defined as the universal gas constant divided by the mole weight) [J.kg^{-1}.K^{-1}], and T is the temperature [K].

The local enthalpy is calculated from an energy balance on the temperature difference of the incoming and outgoing cooling water, see equation 2.8:

$$h = h_e + \frac{\dot{m}_w}{\dot{m}_g} c_p \left(\Delta T_{sampling} - \Delta T_{tare}\right) \qquad \text{eq. 2-8}$$

In which h_e is the specific enthalpy at the probe exit [J.kg^{-1}], $\dot{m}_w$ is the mass flow rate of the cooling water [kg.m^{-3}], $\dot{m}_g$ is the gas flow rate of the sampled gas [kg.m^{-3}], c_p is the specific heat of water [J.kg^{-1}.K^{-1}] and $\Delta T_{sampling}$, ΔT_{tare} represents the temperature difference between the incoming and outgoing cooling water in the sampling mode and tare mode respectively.
MS measurements result in information on the local gas phase composition from which the plasma temperature can be determined. Section 3.5.1 gives a further explanation on the enthalpy probe measurements.

Rahmane et al. [113] used an enthalpy probe combined with a mass spectrometer to determine the diffusion of He and N_2 injected axially in an Ar/H_2 plasma generated in a PL-50 torch. The influence of these gases on the plasma temperature and velocity profiles were measured and compared to a model.

2.8.2 Particle characterisation

2.8.2.1 Particle collection and sampling

After synthesis of the nanoparticles in the gas phase, they have to be collected and characterised. Although the retention of the nanoparticles is very important, it is usually treated as something straightforward. The purpose of the nanoparticle filter is to hold back as many particles as possible from gas phase, since nanoparticles are the high value product. Usually, the collection methods are described for sample extraction [24], [25] of a small amount of particles, and not for particle collection itself. Leparoux and Siegmann [178] developed a filtration unit adapted to an ICP reactor. Johnson et al. [179] described the collection by using the thermophoretic effect to attract the nanoparticles to a cold wall from which the particles are scraped off. Thermophoresis is the movement of small particles to a colder region due to the existence of a temperature gradient. The velocity caused by the thermophoresis effect is independent of the size (for particles much smaller than the mfp).
It can be very important to get information on the particles when they still are in gas phase and not on the filter, to study for example the particle growth and morphology [180]. To get an idea about the particle size distribution in the gas phase, Dobbins and Megardis [180] used a thermophoretic sampling device. The aim was to get a

representative sample, without disturbing the gas phase too much and without having a high particle loading on the sample causing particle – particle interactions. The sampling device consisted of a rod with TEM grids mounted at its end. The size is kept as small as possible to minimise the disturbance of the flow, caused by insertion of the sampling device in the gas phase. Since the particles just after nucleation are normally much smaller than mfp, resulting in the same thermophoretic velocity, the sampling will not be size-selective [180]. Besides being used for particle sampling in atmospheric flames [180], [181], this technique has also been successfully applied for a low pressure microwave plasma [182].

2.8.2.2 Characterisation: BET measurements

After the particles are collected and sampled, they must be characterised. As already mentioned in [183], [184], the determination of the size distribution is a more challenging task as it seems. Especially, the extraction of a representative sample, the presence of agglomerates and the lack of optical properties for techniques based on light scattering are making the exact determination of the size distribution difficult.

The particle size distributions and average diameters can be measured with a lot of techniques like laser scattering, microscopy, adsorption, etc.. The question is how one can compare these average diameters. Although each method is giving the "real" mean particle diameter, it is only specific to that particular characterisation method and can not be compared to others. Therefore, the mean diameter should always be accompanied with the applied characterisation method. So, a volume averaged diameter will favour larger particles, since this diameter is calculated from the third power of the particle diameter to only the first power in a number mean average diameter.
In a technical paper, released by Malvern Instruments Ltd. (UK) [185] the differences between the several mean diameters are explained and it also describes which mean diameter is determined by some of most common size analysers.

Frequently used to determine the size of nanoparticles is the so called specific surface area (SSA) or BET analysis [186]. In which BET is the abbreviation of the inventors names of this technique, Brunauer, Emmett, and Teller. This technique measures the total surface area of a sample, which in turn can be converted into a BET equivalent diameter by assuming a monodisperse, spherical distribution with a known (usually theoretical) density. Therefore should the BET diameter be compared to image of electron microscopy to get an idea about the real particle size and the morphology. Equations 2-9 shows the relationship between the SSA and the BET equivalent diameter.

$$SSA = \frac{6}{\rho_p d_{BET}} \qquad \text{eq. 2-9}$$

In which SSA is the specific surface area [$m^2.g^{-1}$], ρ_p the particle density [$g.m^{-3}$], and d_{BET} the BET equivalent mean diameter [m].

3 Experimental

3.1 Introduction to the experiments

In this work an ICP process is used to synthesise nanoparticles. This route has been picked up because of its advantages (see section 2.1.2, page 10) over the other nanoparticle synthesis routes, such as other gas phase (flame, DC plasma), liquid phase (solid-gel), or solid (milling) processes.
In the ICP process the synthesis takes place via an evaporation – condensation mechanism. The precursor is vaporised / atomised and subsequently the nanoparticles are formed from condensation of the vapour phase. The plasma process combines a top-down and a bottom-up approach into a single step. Top-down means that larger particles are fragmented into smaller ones; like solid precursors which are more favourable because of economic and safety issues. A bottom-up approach is desirable since then the products are formed from the atoms and therefore enables the synthesis of very small particles.
The ICP process is the high energy density and high temperature of the inductively coupled plasma permitting the processing of high refractory materials. Also the ability to synthesise the products in an inert or reactive atmosphere and thereby controlling the chemistry is an advantage.
The used set-up is described in section 3.2.

3.2 Description of the ICP equipment

The ICP set-up as currently being used at the EMPA, Thun, Switzerland is shown in Figure 3-1.

Figure 3-1: overview of the ICP equipment. 1) torch, 2) RF power supply, 3) gas control unit, 4) synthesis chamber, 5) T-junction, 6) micron powder collector, 7) nano- particle sampling filter, 8) production filter, 9) production collector, 10) filter control unit, 11) water cooling control unit.

The plasma is generated in a PL-35 plasma torch (1, in Figure 3-1), which has been commercialised by Tekna Plasma Systems Inc., Canada. The torches are available in different sizes, see Figure 3-2, from which the smallest PL-35 torch is well suited for research applications. The torch has a four turn coil. The radio frequency power supply (Elgotec AG, Switzerland), connected to the plasma torch, delivers an electrical power also called plate power of 36 kW at a frequency of 13.56 MHz (2, in Figure 3-1).

Figure 3-2: from left to right: PL-70, PL-50, and PL-35 plasma torch from Tekna Plasma Systems Inc., Canada.

The gases required for the plasma process operation (e.g. carrier -, central - and sheath gas) are being supplied and controlled by the gas manifold system (3, in Figure 3-1). The plasma gas flow rates are controlled by using Tylan, type PC-261, mass flow controllers and a Brooks 8500 mass flow controller for the quench gas. The precursor, which is introduced axially in the torch together with the carrier gas, is being evaporated/fragmented/atomised in the plasma, and transferred by forced convection into the synthesis chamber (4 in Figure 3-1). The water cooled synthesis chamber, made of Inconel, consists out of a three segments, all having an internal diameter of 320 mm. Each segment is equipped with view ports allowing *in-situ* monitoring and on-line sampling. The total height of the synthesis chamber amounts 1450 mm. The last segment, forming the end of the synthesis chamber, is conical with a height of 550 mm, a final internal diameter of 63 mm and ends in a T-junction (5, see Figure 3-1). The tube leading to the filters has a 50 mm diameter. Depending on their momentum, the particles are (un)able to follow the gas stream around the bend. In case the inertia is too high, the particles are unable to follow the 90° bend and get trapped in the “micron” collector (6 in Figure 3-1). This would for example be the case when the plasma is used to spheroidise powders with a size of several tens of microns

The particles with a low inertia are able to follow the gas flow around the bend into filter unit. This will especially be the case for nano particles. To get an idea about the size of the particles being able to follow the gas flow, equation 3-1 was applied, normally used to calculate the efficiency of impactors [25].

$$Stk_{50} = \frac{\rho_p d_p^2 v C_c}{9 \mu d_{nozzle}} \qquad \text{eq. 3-1}$$

In which Stk_{50} is the Stokes number [-], which is in the order of 0.2 – 0.6, ρ_p the specific mass [$kg.m^{-3}$], d_p the spherical equivalent diameter [m], v the average jet velocity [$m.s^{-1}$], C_c the Cunningham correction factor [-], μ the viscosity of the gas phase [$kg.m^{-1}.s^{-1}$] and d_{nozzle} the nozzle inner diameter [m].

The left side of Figure 3-3 shows a schematic drawing of the set-up around the T-junction. The right side shows the schematics of the simplified impactor model [25].

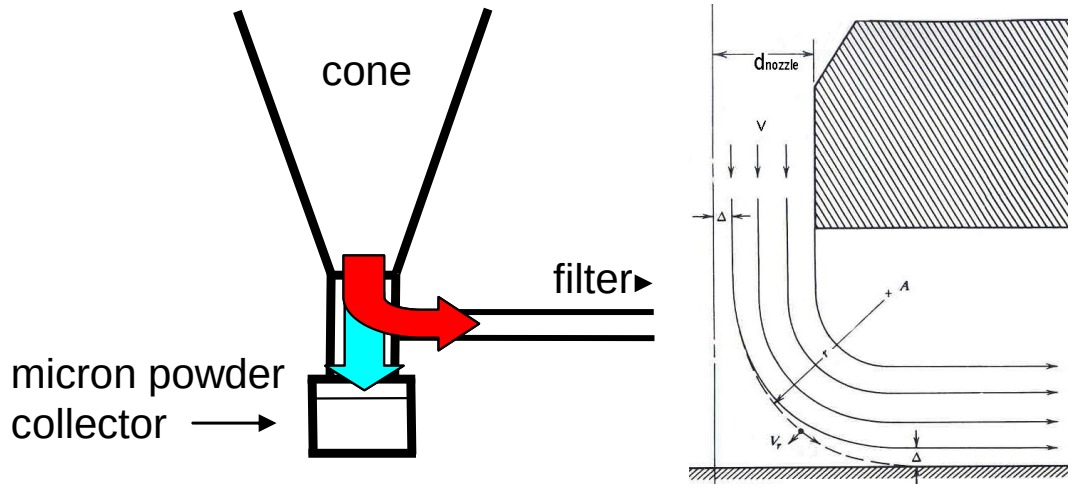

Figure 3-3: schematic drawing of the T-junction (left) and schematics of the simplified impactor model [25] (right). In which A represents the centre of the stream lines, v the particle velocity, d_{nozzle} the tube diameter, v_r the radial velocity, and Δ the radial displacement.

Table 3-1: upper particle diameter which is able to follow an Ar gas flow around a 90° bend as a function of velocity and temperature at 40 kPa. The particles are assumed to follow a trajectory closest to A in Figure 3-3 (right).

$\rho_{particle}$ [$kg.m^{-3}$]	v_{gas} [$m.s^{-1}$]	T [K]	$d_{particle}$ [μm]	$\rho_{particle}$ [$kg.m^{-3}$]	v_{gas} [$m.s^{-1}$]	T [K]	$d_{particle}$ [μm]
2000	10	800	16	2000	10	1000	17
4000	10	800	11	4000	10	1000	12
15000	10	800	5	15000	10	1000	6
2000	5	800	22	2000	10	600	14
4000	5	800	16	4000	10	600	10
15000	5	800	8	15000	10	600	5

Under assumptions of a velocity of around 10 $m.s^{-1}$ and a temperature of 800 K in the junction, WC particles (density 15,700 $kg.m^{-3}$) having a diameter smaller than 5 micrometer are able to follow the gas flow, this diameter is around 16 micrometer for Si particles (density 2330 $kg.m^{-3}$). This diameter is the 100% cut-off diameter only in the ideal case.

The filter unit, evaluated in-house [178], is built up out of a small sampling filter (7, see Figure 3-1) and a larger production filter (8 in Figure 3-1), with a filtration area of 2 m^2 and can be regenerated by Ar pulses, and the released powder is collected in the production collector (9 in Figure 3-1). The sampling filter allows extraction of powder during processing without having to stop the process. The filter control unit (10 in Figure 3-1) controls the valves which direct the flow through to the production or sampling filter.

The total system is connected to a waterring pump which allows the system being operated at pressures ranging from 15 up to 80 kPa. The torch, the synthesis chamber, and a part of the pipe leading to the sampling unit are water cooled.
The torch, (1) in Figure 3-1, is schematically drawn in the left side of Figure 3-4. The plasma torch consists out of a four turn induction coil, a water cooled ceramic tube and another ceramic tube separating the central gas (Q2) from the sheath gas (Q3).

The stainless steel injection probe (3 mm inner and 10 mm outer diameter) can be replaced by another injection probes (such as a SI-792-230 Tekna Plasma Systems Inc., Canada) consisting out of two concentric tubes, see Figure 3-4. The smaller tubes have an inner diameter of 1.7 mm and 1.9 mm outer diameter. The larger tube has an inner diameter of 3.7 mm and an outer diameter of 7.9 mm. As the injector, described in Figure 3-4, got easily clogged with particles under the used process conditions, it was decided to remove the inner tube. The precursor injector is positioned axially into the torch between z = - 79 to - 62 mm. The default position was at z = -62 mm, which is 6 mm above the middle of the coil region.

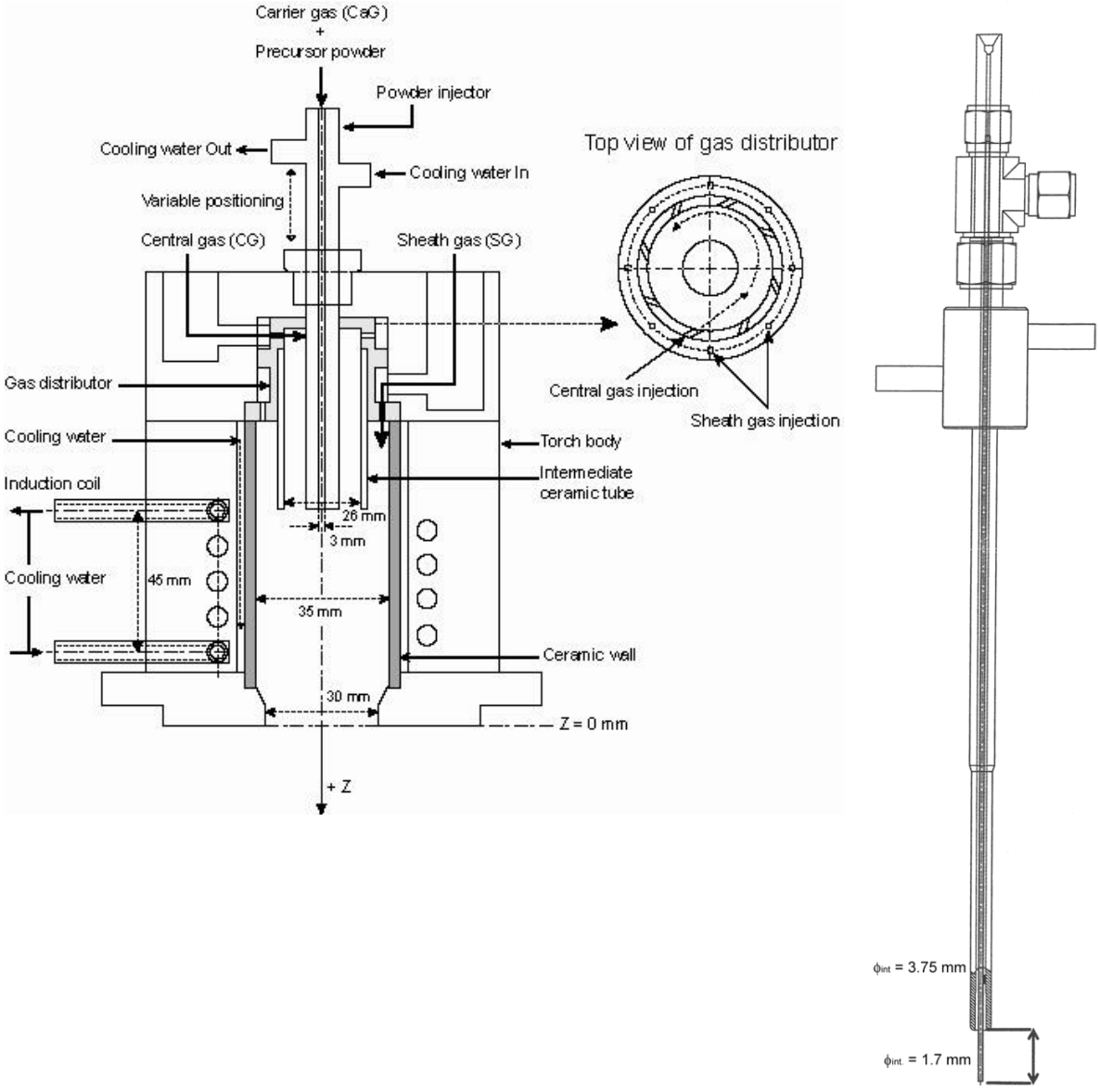

Figure 3-4: left: schematic drawing of the used ICP torch with some characteristic sizes. Right: schematic drawing of the SI-792-230 injection probe consisting out of two concentric tubes (Tekna Plasma System Inc., Canada).

The precursor, which can be a gas, a liquid or a solid, is introduced into the centre of the torch by a carrier gas (Q1). In some cases, a reactive gas (e.g. CH_4 or NH_3) may be added to the carrier gas, with the aim to influence the chemistry. The axial position of the injector can be varied easily without opening the torch, whereas changing the length of the intermediate ceramic tube is only possible by replacing the ceramic tube, which requires opening of the torch.

The central gas is introduced with a swirl into the torch and serves two purposes: it acts as a plasma gas and stabilises the plasma. The sheath gas, consisting of Ar and a molecular gas, is used to cool the ceramic tube of the torch and prevents it from being coated. The role of the molecular gas in the sheath gas is to lower the electrical conductivity and thereby keeping the plasma away from the wall.
The plasma is ignited and established between the coils (circles in Figure 3-4). The exact position, size and energy of the plasma depends on several parameters such as for instance power, frequency, pressure, nature and flow rate of the plasma gases.

3.3 Process parameters

3.3.1 Precursor powder

3.3.1.1 Powder dosage systems

Depending on the plasma parameters used, only solid precursors up to a distinct size can be fed to obtain full evaporisation. When the(se) precursors are non-flowable powders, the common conventional feeders run into problems. Therefore the IMPAKT feeding system ([187] DACS, Thun, Switzerland) has been used to feed the precursor particles. This system uses pneumatic conveying and is able to feed precursor particles with a precursor load to carrier gas ratio which is about 10 times higher than conventional systems. Figure 3-5 shows the principle of the IMPAKT system. The powder conveying cells are filled with powder by opening the valves connected to a vacuum. After the cell has been filled the valves connected to the vacuum are closed and the other valves are opened allowing the powder to be transferred to the process by a pressure boost. The continuity of the precursor flow can be controlled by using a battery of cells with a distinct phase shift and by changing the frequency of the powder filling-releasing process.

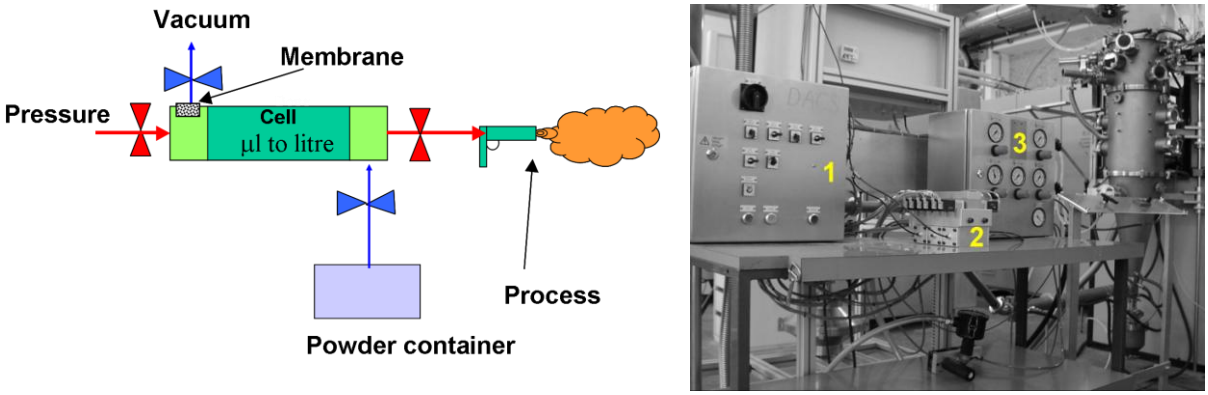

Figure 3-5: left: schematic drawing of the IMPAKT feeder. Right: photograph of powder feeder Impakt. The system consists out of three modules: 1) electrical control unit, 2) conveying unit, 3) gas control unit.

The powder feed rate can be controlled by changing the frequency, vacuum, the size of the powder conveying cell, and the diameter of the line used to convey the powder. The feed rate ranged between a few grams per hour to a few hundred grams per hour.

3.3.1.2 Silicon precursor

Figure 3-6 shows SEM images of the Si precursor (Brodmann, FlowMaster powder-44+16 µm). The precursor has a broad size distribution (ranging from sub-micron to several tens of microns) and has a flake-like shape. This powder could not be conveyed by a volumetric conventional feeder (e.g. Twin 10-2, Sulzer Metco, Switzerland) and therefore the IMPAKT feeding system was used.

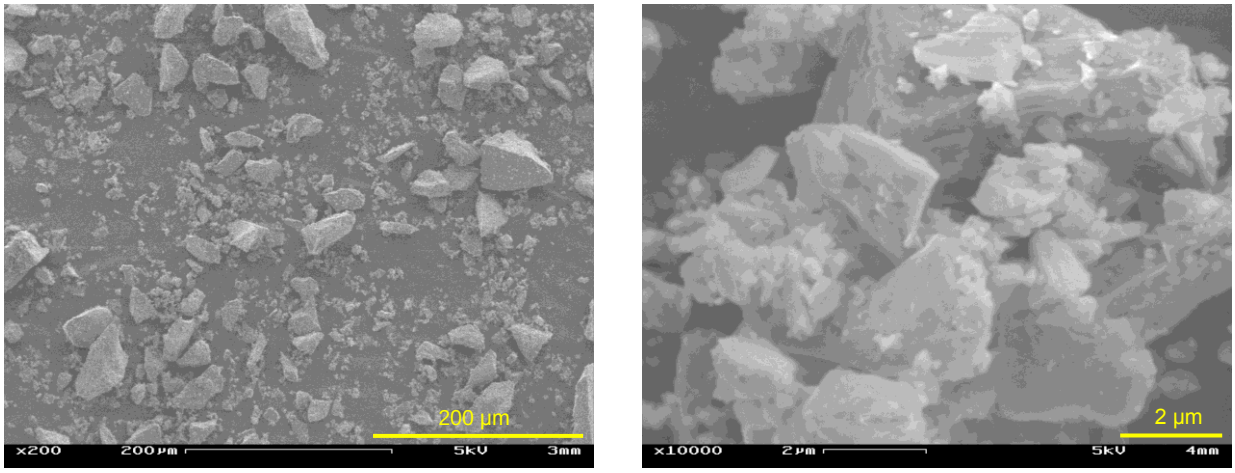

Figure 3-6: SEM pictures of the silicon precursor (Broadman, FlowMaster -44+16 µm) at different magnifications.

The size distribution has also been measured with Powdershape ® [188], an image analysis software in which the surface of the particle is recalculated into a sphere equivalent. Powdershape uses scanned images from a 5400 dpi scanner. The samples for the scanner are prepared by distributing powder on a crystal clear scotch tape. This sample preparation will show a preferred orientation on the sample, i.e. the particles will exhibit more frequently the flat side on the sample. This will result in the overestimation of the actual particle size in case of flake-like shaped particles. But also laser scattering will result in an overestimation of the particle size since the intensity of the scattered light is proportional to the sixth power of the diameter.
The results of these measurements are shown in Figure 3-7. Besides the number and volume mean average particle size, also information on the particle size distribution and shape can be found. The mean average diameter on volume basis [185] amounts 60 µm with a d_{10} of 28 µm and a d_{90} of 93 µm. The number mean diameter amount 21 µm which fits well in the -44+16 µm (sieve) distribution from the supplier. As shown in Figure 3-6, the Si precursor particles have a flake-like shape and therefore a high surface to thickness ratio.

Resultate:

Anzahl gezählter Partikel: 34121

Korn		arith.mittel	σ	unteres Limit	oberes Limit
Größe µm	nb %	20.84	14.70	5.00	1000.00
Größe µm	vol%	60.39			
Elliptizität		1.6266	0.5284		
Kristallinität		1.1316	0.0665		
Rauheit:		6.6119	3.6861		

aspect ratio	0.5823
roundness	0.8780

Max. gefunden zwischen: 64.00 und 75.00 [µm]

Korngrösse		Delta µm		Limit 1	Limit 2	Limit 3	Limit 4	Limit 5
9.19	200.74	11.00	%	10.00	25.00	50.00	75.00	90.00
Min	Max	vol%	µm	27.67	45.59	62.83	78.15	93.47
207.00		0.00	µm	28.35	66.66	104.96	143.27	181.58
196.00	207.00	0.79	%	10.38	54.11	95.65	99.21	99.21
185.00	196.00	0.00	%	89.62	45.89	4.35	0.79	0.79
174.00	185.00	0.00						
163.00	174.00	0.00						
152.00	163.00	0.00						
141.00	152.00	0.00						
130.00	141.00	0.23						
119.00	130.00	0.49						
108.00	119.00	1.24						
97.00	108.00	5.37						
86.00	97.00	8.15						
75.00	86.00	14.19						
64.00	75.00	18.64						
53.00	64.00	17.99						
42.00	53.00	11.30						
31.00	42.00	9.80						
20.00	31.00	6.95						
9.00	20.00	4.87						
	9.00							

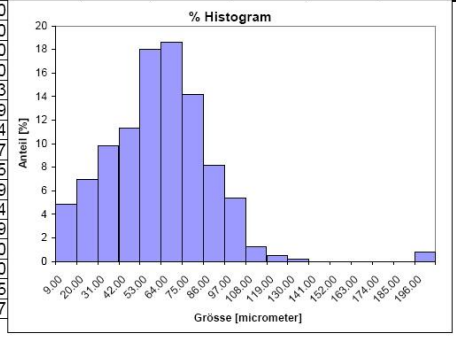

Figure 3-7: particle size distribution as measured with Powdershape image analysis software. The d_{10} amounts 28 µm, d_{50} 63 µm, and d_{90} of 93 µm.

All other characterisation methods have their distinct advantages and disadvantages and will end up in a different mean size for the same powder [185].
Some of the advantages of the Powdershape image analysis to characterise the particle size distribution are the low price, short measurement times, easy sample preparation, and calibration.

It is very important to know the size of the precursor, because all the precursor particles have to be evaporated in order to obtain a narrow nano particle size distribution. Partially evaporated precursor particles trap monomers or clusters resulting in a broad size distribution, from nanosized to the size of the partially evaporated precursor.

The crystalline phases within the precursor were characterised by X-ray diffraction (XRD). The recorded XRD spectrum of the Si precursor shows only the presence of cubic Si, see Figure 3-8. The crystallite size has not been determined by XRD.

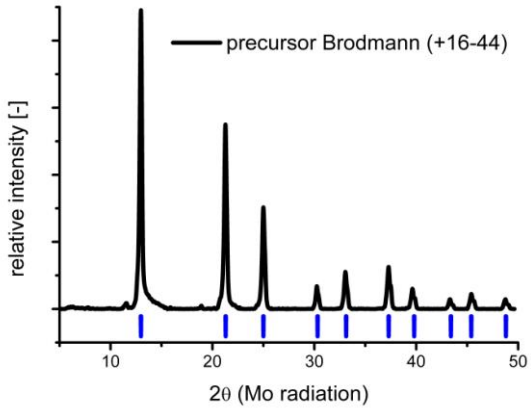

Figure 3-8: XRD spectrum of the silicon precursor (Brodmann, Flowmaster). The small lines at the bottom represent the theoretical peak positions of cubic silicon (JCPDS card 27-1402).

3.3.1.3 Tungsten carbide precursor

Figure 3-9 shows SEM images of the WC precursor (CT-1.0, Ceratizit, Luxembourg, d_{50} 1.0 µm). The precursor had a specific surface area of 0.79 $m^2.g^{-1}$. The particles have a sphere like appearance as can be seen from the SEM images.

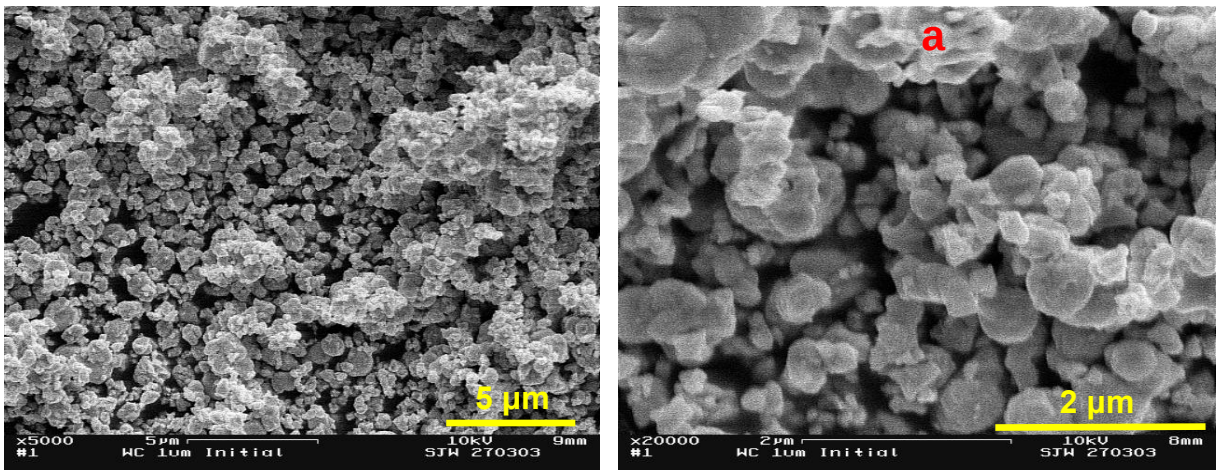

Figure 3-9: SEM pictures of the CT-1.0 WC precursor (Ceratizit, Luxemburg) at different magnifications. “a” in the right picture represents an example of an agglomerate.

Although the primary particles in Figure 3-9 are smaller than 1.0 µm, the laser diffraction measurements result in a d_{10} of 0.7 µm and a d_{90} of 2.7 µm. One of the reasons is the presence of hard agglomerates, which connects the primary particles via sintering necks, see “a” in the right image in Figure 3-9. This results in the detection of larger particles, although the partially sintered primary particles still can be identified by electron microscopy as being single particles.

The complete size distribution for WC, as measured with laser diffraction (Malvern Mastersizer X), is shown in Figure 3-10.

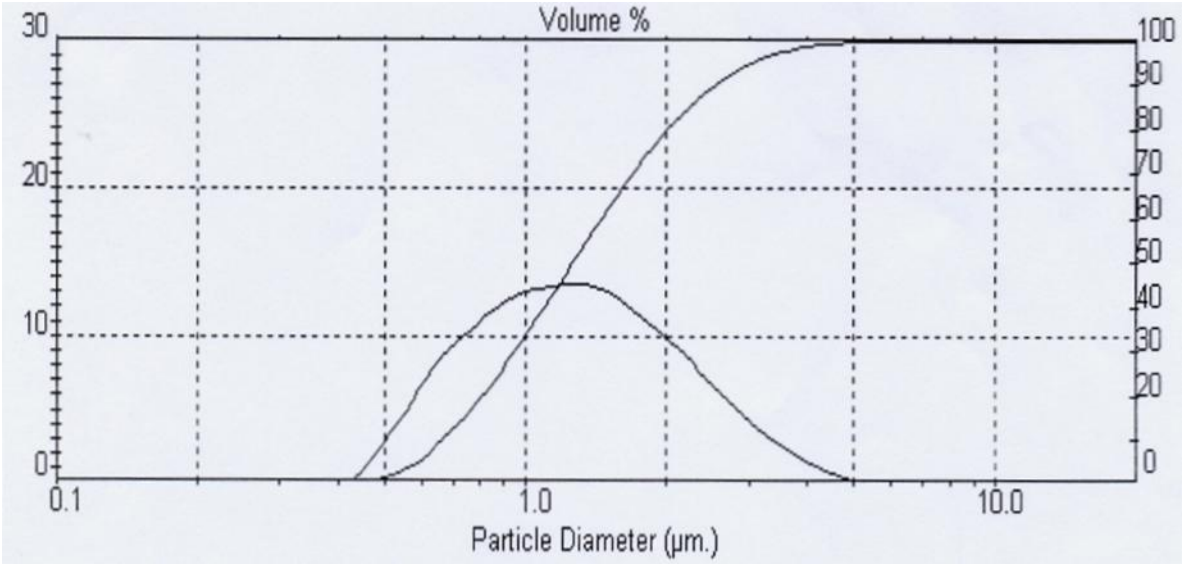

Figure 3-10: particle size distribution of WC CT-1.0 (Ceratizit, Luxembourg) as measured by laser diffraction.

The WC precursor was also characterised by X-ray diffraction (XRD). The XRD diagram, Figure 3-11, shows the presence of hexagonal WC. The peak around 19° 2θ is caused by the k_β radiation.

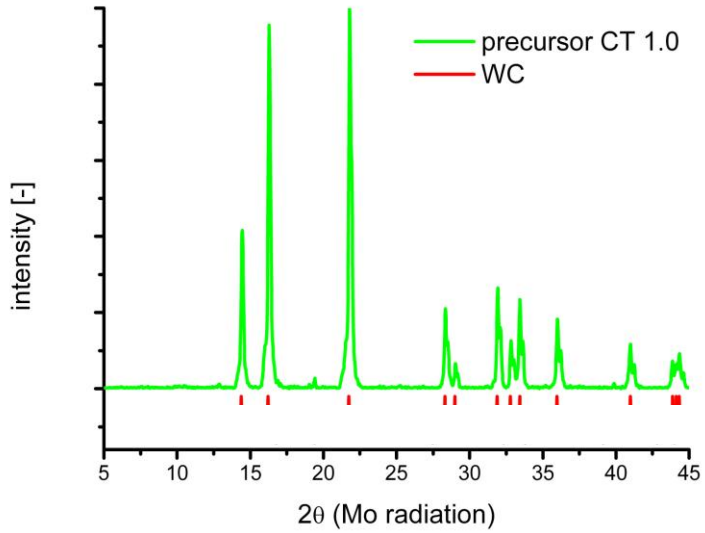

Figure 3-11: XRD diffractogram of the tungsten carbide precursor. The red lines represent the position of the theoretical peak positions of WC (JCPDS 25-1047). The spectrum has been recorded without $k_{\alpha 2}$ correction, causing the shoulders at higher 2θ values.

3.3.2 Plasma parameter window

The plasma parameters used within the experiments are described in Table 3-2. The torch and function of the used gases is described in section 3.2.

Table 3-2: plasma parameter window as being used during the experiments.

Parameter	Species	Range
Carrier gas* (Q1)	Ar, CH_4, H_2	1 — 10 slpm
Central gas*,** (Q2)	Ar	4 — 27 slpm
Sheath gas* (Q3)	Ar / H_2, N_2	60 — 100 slpm
Quenching gas*	Ar, N_2, CH_4	0 — 84 slpm
Plate power		16 — 30 kW
Process pressure		15 — 80 kPa
Injector position		z = -62 — -79 mm ***
Frequency		13.56 MHz

* Purity: Ar 4.8, CH_4 4.5, H_2 4.5, N_2 4.5

** Comprises a swirl component (60° tangential angle)

*** z = -79 mm is equivalent to the top of the first coil, while z = -62 mm is equivalent to the middle of the second coil.

Figure 3-12 shows two photographs of the plasma operated at 40 kPa, with 3 slpm Ar carrier gas, 12 slpm Ar central gas, 80/6 slpm Ar/H_2 sheath gas, and 28 slpm Ar quenching gas. A plasma flow without precursor particles is shown on the left side and a Si particle laden plasma flow on the right side. The photographs are taken from the upper viewport, at z = 110 mm. The main visible differences are the changed colour of the plasma and the presence of a glow outside the plasma region, due to the emission and radiation of the silicon vapour and/or tiny silicon particles.

Figure 3-12: left: plasma without particles. Right: plasma with Si particles. In both cases the plasma conditions were the same. The pictures show the quench ring and the transition from torch to synthesis chamber at the top. In both cases the plasma flows from top to bottom. Distance top plasma to quench ring amounts 121 mm.

3.4 Particle sampling device

The sampling device used in this work is based on the one used by Dobbins and Megaridis [180]. They used a thermophoretic sampling device to determine the morphology of soot made by combustion. Thermophoresis causes particles to move under the influence of a temperature gradient [25]. The thermophoretic velocity is almost independent of the size for nanoparticles. Under the used conditions the convective velocity can not be neglected, because of the high gas velocity (up to 200 $m.s^{-1}$).

The current sampling device has been adapted to non-atmospheric plasma conditions, the schematics are shown in Figure 3-13. It should be noted that the sampling device and the sampling filter, which is mentioned in section 3.2., are not the same. The device consists of a rod with a TEM grid holder mounted at its end. Three TEM grids can be placed behind each other, allowing radial sampling over the plasma jet in one measurement. The sampling device can be attached to the several view ports of the synthesis chamber allowing sampling at different axial positions. Its introduction in the plasma is assumed to have no influence on the plasma flow and particle trajectories, due to short residence time (order of ms) and small size of the sampling device.

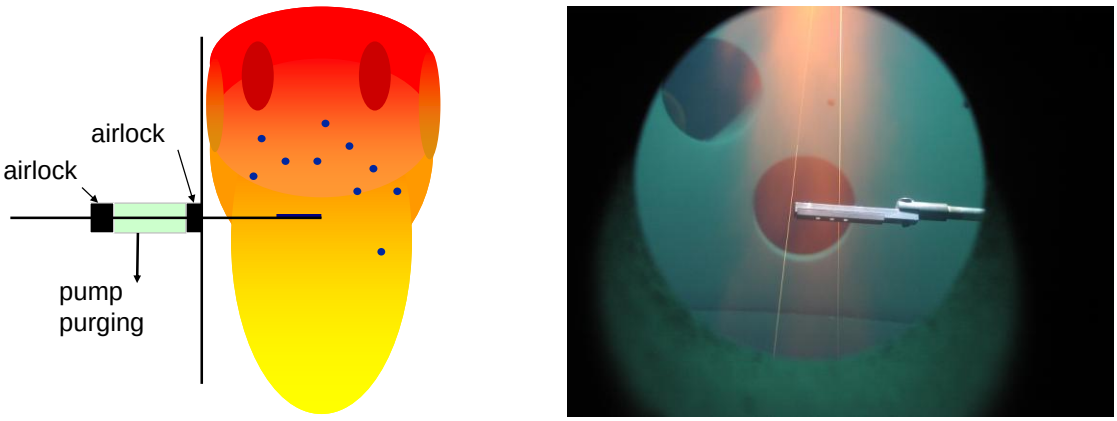

Figure 3-13: left: schematic drawing of in-line sampling device. Right: photograph of TEM grid holder inserted in the plasma taken at a view port at z = 260 mm. The solid lines show the trajectories of two larger particles.

The left side of Figure 3-13 shows a schematic drawing of the on-line sampling device. On the right side, a photograph is shown of a powder being extracted from the particle laden plasma flow with the particle sampling device. The two red lines are glowing particles, which appear as lines due to the exposure time of the camera.

The images in Figure 3-14 show SEM pictures of an empty plasma treated nickel (Ni) TEM grid.

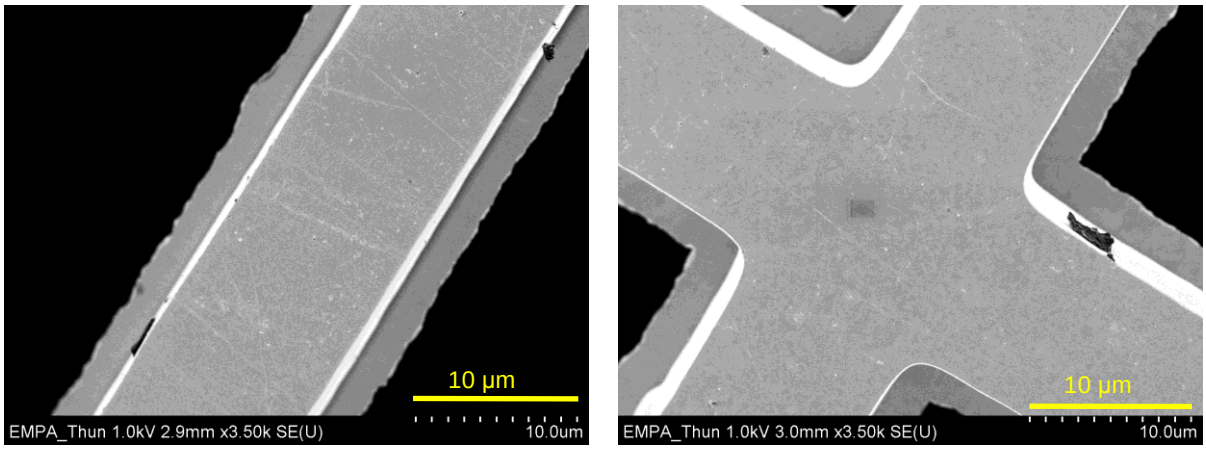

Figure 3-14: SEM pictures of an empty plasma treated Ni TEM grid (Athene, M300) at different magnifications under powder free conditions.

Figure 3-15 show SEM pictures of Ni TEM grids covered with nano silicon particles. The left image shows a TEM grid covered at a low degree with particles, while the right image is completely covered.

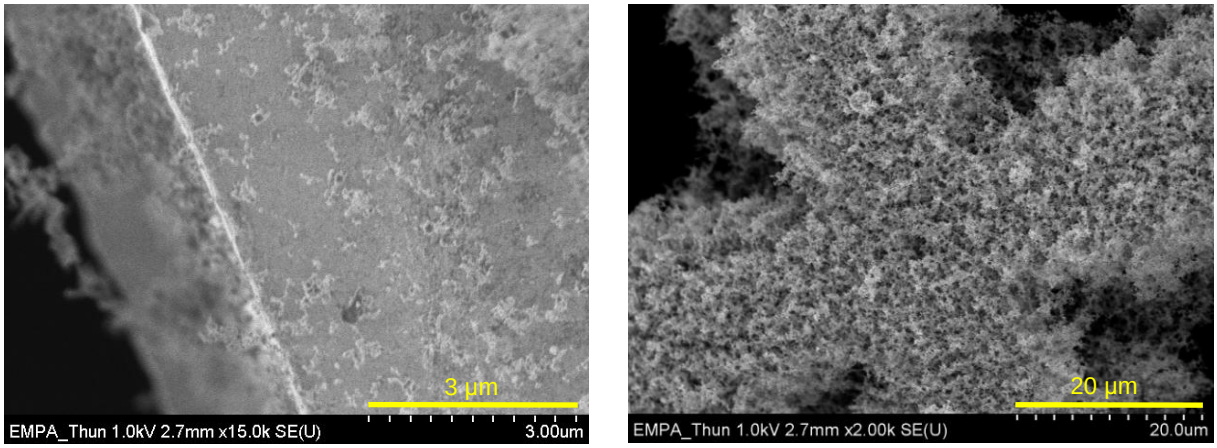

Figure 3-15: SEM images of Ni TEM grids (Athene, M300) covered with Si nanoparticles after sampling.

3.5 Characterisations

3.5.1 Plasma characterisation

The enthalpy and velocity of the plasma were measured with an enthalpy probe device (Tekna Plasma Systems Inc., Canada) under powder free conditions. A mass spectrometer (Prisma from Balzers, Liechtenstein) was connected to the enthalpy probe to determine the gas phase composition. From the gas phase composition and

the enthalpy, the temperature of the plasma can be calculated. The principle of the enthalpy probe is shown in Figure 3-16 and explained below in more detail.

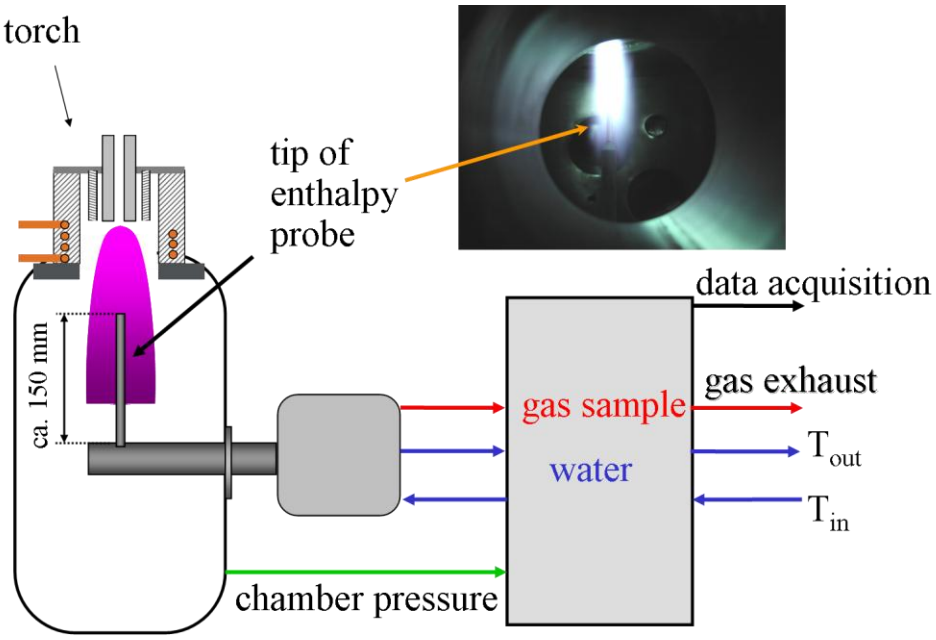

Figure 3-16: schematic drawing of enthalpy probe set-up. The photograph shows the enthalpy probe tip in a Ar/H_2 plasma

The principle of the enthalpy probe is based on the temperature difference between the incoming and outgoing cooling water in the probe tip.
The enthalpy probe tip has a hollow water cooled tube with a defined opening of around 1.5 mm diameter and is connected to a pump which causes the plasma gas to flow through the probe. By interrupting the gas flow through the probe tip, the gas flow in the probe stagnates. A measurement made under these conditions is called a "tare" measurement. In this measurement mode, the heat flux (calculated from temperature difference between incoming and outgoing cooling water) originating from the surrounding is measured. The "sample" measurement is made when the plasma gas is flowing through the tube. Again the temperature difference between the incoming and outgoing cooling water is used to calculate the heat flux. This time heat flux from the surrounding and sampled plasma gas is being measured. By subtracting the "tare" from the "sample" measurement the enthalpy of the plasma can be calculated. Equation 3-2 is the rewritten form of equation 2-8 (page 39).

$$\dot{m}_g\left(h - h_e\right) = \dot{m}_w c_p \Delta T_{asmpling} - \dot{m}_w c_p \Delta T_{tare} \qquad \text{eq. 3-2}$$

The velocity is calculated by using the difference between stagnation and static pressure of the tare and sample measurement (see equation 2-6, page 38).

A more detailed description and information on the enthalpy probe's accuracy and sensitivity is given by Rahmane et al. [177]. The influence of the particles on the plasma flow can not be measured by this technique [169], since the particles will clog the probe.
The temperature obtained from the enthalpy probe measurements is a mass averaged "heavy species" temperature, whereas spectroscopic methods (like infrared spectroscopy for example) measure the vibrational and rotational

temperature. In case of local thermal equilibrium (as is the case for the ICP) these temperatures are assumed to be the same.

In the current work, the enthalpy probe measurements are used to quantify the influence of different flow rates (Q1, Q2, and Q3) on the temperature and velocity profiles at different axial and radial positions. The enthalpy probe set-up is shown in Figure 3-17.

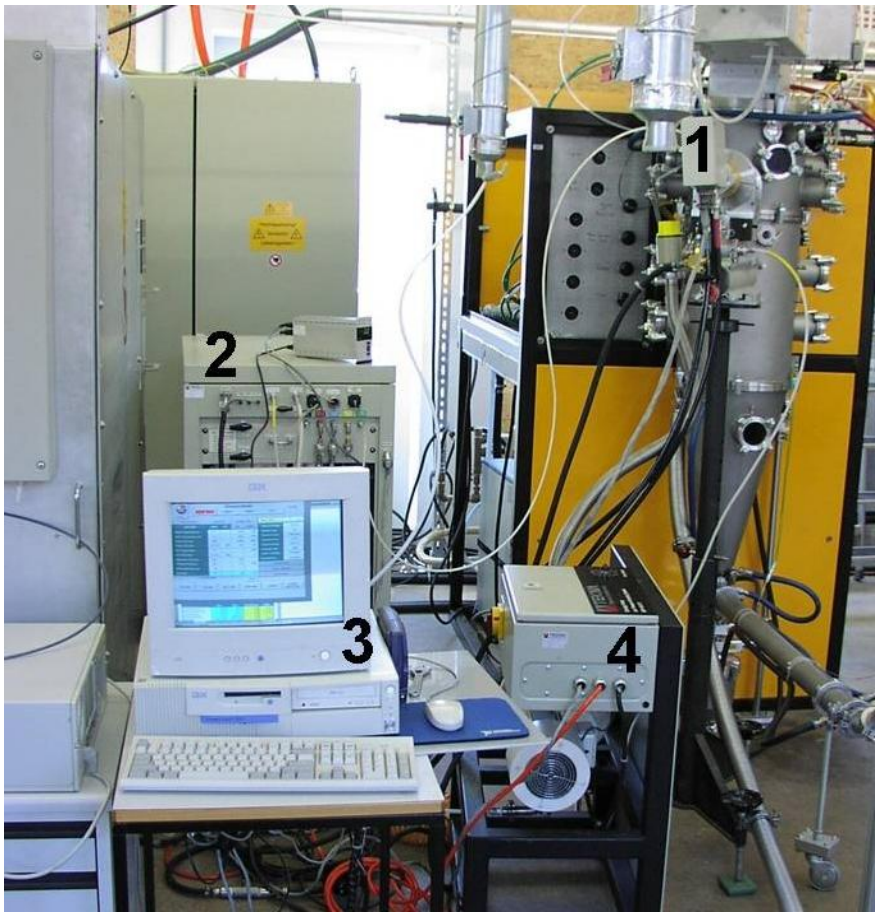

Figure 3-17: Picture of enthalpy probe set-up: 1) bulk head, 2) console, 3) computer with special software, 4) pump.

The enthalpy probe tip (see Figure 3-16) is mounted on a displacement arm, which is introduced in the synthesis chamber via a viewport. The displacement arm is connected to the bulk head (1 in Figure 3-17), in which thermo elements measure the temperature of the in- and outgoing cooling water. The console (2 in Figure 3-17) controls the cooling water flow rate, gas extraction / sampling, and measures the chamber pressure by sensors. The measured data are processed by the computer (3 in Figure 3-17), which is equipped with a special software. The pump (4 in Figure 3-17) enables sample extraction from the plasma via the probe tip.

3.5.2 Powder characterisation techniques

The precursor and synthesised nanopowders were characterised by electron microscopy to obtain information on the particle size, size and shape distribution. Three different electron microscopes were used in this work: a Zeiss, type DSM 962, scanning electron microscope (SEM), a high resolution scanning electron microscope (HR-SEM) from Hitachi, type S4800, and a transmission electron

microscope (TEM) from Philips type CM 30. The HR-SEM was equipped with an energy dispersive X-ray (EDX) detector from EDAX/Ametek for element analysis.
Furthermore, a Malvern Mastersizer X, Powdershape image analysis software, and Photon Correlation Spectroscopy (carried out at CEA, France) were used.
A Bruker, AXS D8 Advance, diffractometer operating with Cu radiation and a Siemens, Diffraktometer D5000 operating with Mo radiation were used to measure X-ray diffraction (XRD) patterns for determination of the crystalline phases. Quantitative phase determination of the XRD patterns were performed using the Bruker Topas 2 software based on Rietveld analysis.
Surface specific area (SSA) measurements [186], also called BET measurements were carried out using a Beckmann Coulter TA 3100. A small tube is filled with a few tenths of a gram of sample and heated for 2 hours at 200 °C to remove the water. The tube is cooled in liquid nitrogen and evacuated. Nitrogen gas is introduced in the tube and the pressure decrease due the nitrogen adsorption at the sample surface is recorded. By measuring at several pressures the SSA can be calculated. The SSA can be correlated to a BET average diameter under the assumption of a monodisperse distribution of spherical particle (see section 2.8.2). This average diameter is a weight based mean.

3.6 Modelling

3.6.1 Introduction

The modelling within this work has been divided into two parts: modelling of the plasma and quenching design with a commercial CFD software and modelling of the particle growth by a C++ code.

3.6.2 CFD modelling

3.6.2.1 Boundary conditions

The modelling of the plasma flow field and quenching designs, was carried out using Fluent 6.1.18, a commercial CFD software. The designs were constructed and meshed with Gambit, which is a part of the Fluent software.
The plasma process has been treated as a steady state process, with the plasma being modelled as a simple heat source, meaning without using the EM field. This assumption has been used as a first approach, since only the flow field outside the plasma torch has been investigated and the influence of the EM field is assumed to be negligible here. Thus only the balances for mass, momentum, and energy were solved, where as the Maxwell's equations do not have to be solved.

The heat source is a square in the 2D and a cylinder in the 3D model with a homogeneous power distribution. Furthermore, the plasma is assumed to be optically thin and incompressible sub-sonic, which is the case if the Mach (Ma) number is well below 0.3 (see equation. 2.7, page 39). For a temperature of 9000 K, a velocity of 150 $m.s^{-1}$ and an Ar plasma, the Mach number would amount 0.09.

A realisable k – ε model has been used to model the turbulence (hint from Fluent, GmbH, Germany). The walls have a temperature of 300 K, as a result of the water cooling, and have a "no slip" condition, meaning a zero velocity at the wall. Viscous heating was neglected due to the expected small effect on the temperature and viscosity (small Brinkman number $\mu v^2/k\Delta T$ in the order of 10^{-3}-10^{-2}). The energy loss

by radiation has been neglected, since the temperature outside of the plasma torch is well below 8000 K. The swirl component of the central gas has been neglected since its effect on velocity and temperature field was found to decrease rapidly outside the torch [113]. This allows the use of an additional simplification of the model.
The inlets were assumed to be ring shaped instead of separate holes for the 2D models (axi-symmetric). The 2D models describe the set-up from the gas inlets in the plasma torch to the outlet near the filter unit. The 1000 mm tube leading from the T-junction (5 in Figure 3-1) to the filter has been assumed to be connected to the synthesis chamber without the 90° bend.
The quenching designs have been investigated in 2D and 3D. Depending on the amount of quenching nozzles that were modelled, zero, one, or two symmetry planes have been applied. Since the 3D model would consist out of too many cells to be handled with a single computer, only a part of the synthesis chamber has been modelled. The new created inlet can be fed with data obtained from the 2D model.

The 2D grid consisted out of quadrilateral cells. The 3D grid consisted out of hexahedral and tetrahedral cells. The number of cells varied on the dimension and the refinement necessary to obtain a constant solution. In Figure 3-18 an example of a 2D model of the synthesis chamber with funnel, as created and meshed with Gambit, is shown. The right picture shows a 3D model of a three-nozzle design.

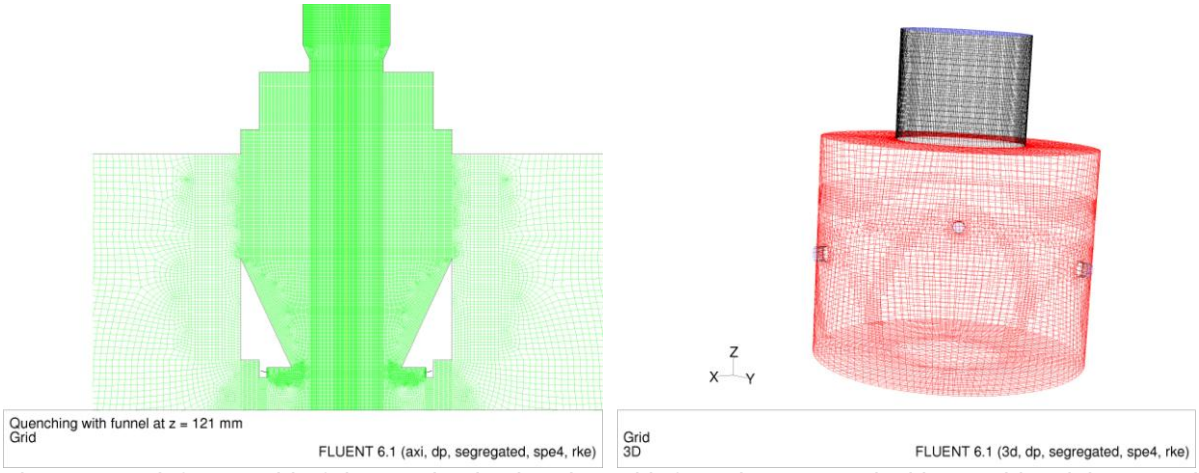

Figure 3-18: left: 2D grid of the synthesis chamber with funnel as created with Gambit. Right: 3D grid of a three-nozzle design.

3.6.2.2 Gas properties

The pressure and temperature dependence of the gas properties (like density, viscosity, specific heat, and thermal conductivity) were obtained from [89] and [189] and converted into a polynomial functions. The density of the mixture was calculated using the volume weighted mixing law, the specific heat using the mixing law. The mixture's thermal conductivity and viscosity were calculated using the mass weighted mixing law. The diffusion coefficients (mass and thermal) were calculated by the kinetic theory approach using the Lennard-Jones parameters (Ar: 3.41 Å, 120 K, H_2: 2.92 Å, 38 K, N_2: 3.62 Å, 97.5 K, and He: 2.56 Å, 10.2 K).
Figure 3-19 shows the calculated specific heat as a function of the temperature for two different pressures. From this figure, one can deduce that a plasma gets colder at a lower pressure (40 kPa compared to 101 kPa) for the same energy input.

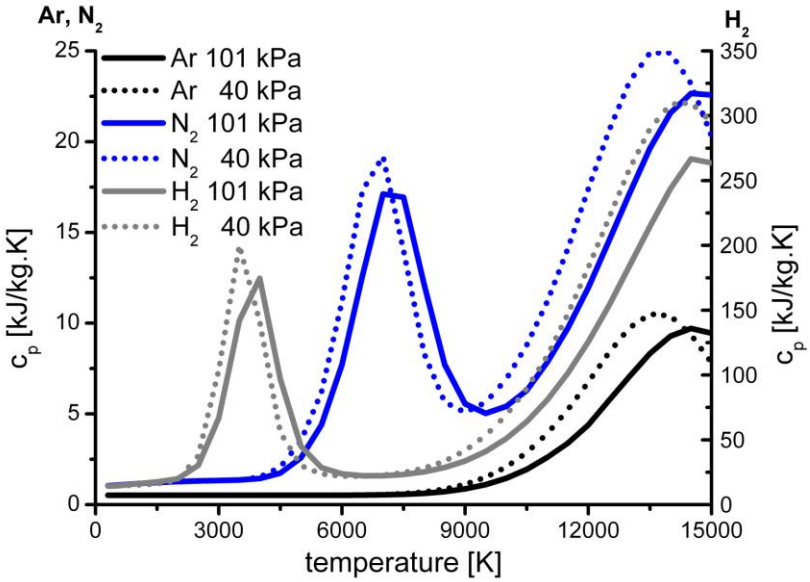

Figure 3-19: specific heat as function of temperature for Ar, N_2, and H_2 at 40 and 101 kPa. (The sharp transitions are caused by the large intervals between two consecutive points.)

Figure 3-20 shows the temperature dependency of the viscosity and thermal conductivity for 40 and 101 kPa. Only a small deviation can be found between the properties at atmospheric pressure and at 40 kPa, therefore the viscosity and thermal conductivity have been assumed to be pressure independent [89].

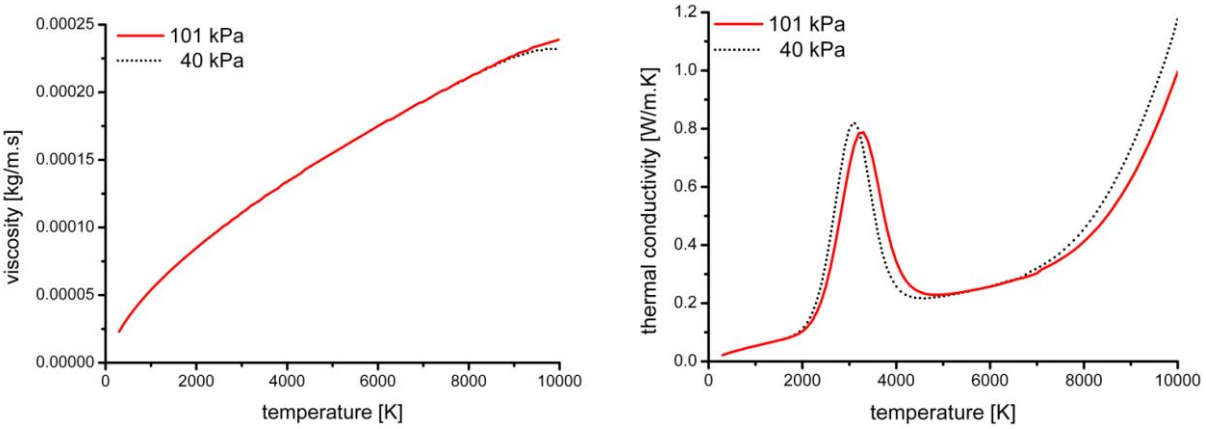

Figure 3-20: influence of the pressure on the temperature dependence of the viscosity (left) and thermal conductivity (right) for a 95 slpm Ar / 6 slpm H_2 mixture. Data from B. Pateyron, University of Limoges, France

The effects of dissociation and ionisation are incorporated into characteristics of Figure 3-19. Figure 3-21 shows the calculated density, specific heat, and viscosity of H_2. The dissociation of H_2 at atmospheric pressure starts around 2500 K and thereby influences the specific heat, which shows an increase, and the viscosity, which shows a decrease (caused by the reduction of the mass from 2 atomic mass unit (a.m.u.) to 1 a.m.u due to the dissociation). Also the steeper slope of the density versus temperature curve points out a change in the temperature region around 3000 K.

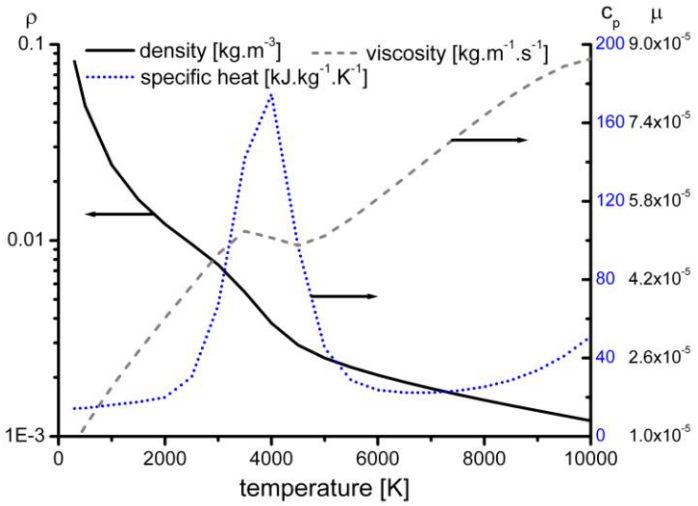

Figure 3-21: density, specific heat and viscosity of H_2 at atmospheric pressure as a function of the temperature.

3.6.3 Particle growth model

The model of Kruis et al. [77] has been used to model the influence of quenching on the particle size. The model deals with coalescence and coagulation of a monodisperse distribution. The program is fed with the temperature and velocity profiles of the CFD model.

The differential equations as described in the paper of Kruis [77] are valid for isothermal conditions and can be adapted to non-isothermal conditions, see appendix A Kruis model. The model code has been programmed in C++ using a 3rd order backward difference formula (bdf) method to solve the differential equations. The Runge-Kutta (2, 3) method has been used for the initialisation of the bdf method. The assumptions on which the growth model is based are listed below. The monomer distribution is monodispersed and homogeneous throughout the entire reactor and they are all assumed to encounter the same temperature and velocity profiles. All the seeds are single monomers and are formed by homogeneous nucleation when the condensing point has been reached. All collisions between monomers and particles are assumed to be 100% efficient. The Kelvin diameter (equation 2-1), thus the supersaturation and other kinetic effects, do not play a role. There is no particle - particle and plasma - particle interaction. The coagulation above the melting point is assumed to be immediate, meaning a very high sintering rate. Thermophoresis does not have any influence on the particle trajectories and also the influence of the particle momentum has been neglected.

The initial monomer concentration is calculated from:

$$N' = \frac{n}{V} * \frac{1}{\rho} = \frac{n}{V} * \frac{V}{M} \qquad \frac{[\#]}{[m^3]} \cdot \frac{[m^3]}{[kg]} = \frac{[\#]}{[kg]} \qquad \text{eq. 3-3}$$

In which N' is the monomer concentration [#.kg^{-1}], n the number of monomers [#], V the total volume of the gas flow [m^3], and ρ the gas density [kg.m^3]. The density has been assumed to be that of the 3-12-80/6 composition in all cases.

The validation is carried out by comparing the values obtained from this model to the literature values, which can be found in the appendix A Kruis model.

The model can be used for different species by replacing the material specific properties.

4 Modelling results

4.1 CFD: Plasma

4.1.1 Goal of the plasma modelling

In order to synthesise tailor-made nanoparticles it is very important to control the temperature and velocity of the particles in the plasma torch and synthesis chamber (as well for evaporation as for growth). By using CFD a better insight in the temperature and velocity profiles can be obtained allowing targeted actions to optimise the synthesis process. Figure 4-1 shows a schematic drawing of the torch and the top of the synthesis chamber (see also section 3.2) with the most important dimensions, z = 0 mm represents the torch exit. The values for the injector and quenching positions represent the ranges used during this work, they are however not limited to these values.

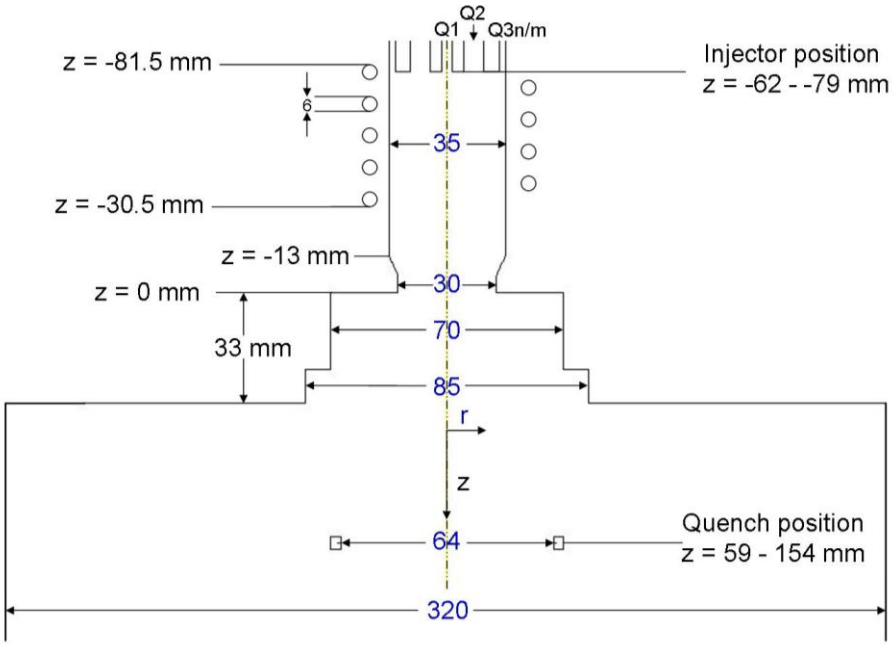

Figure 4-1: schematic drawing of the torch and top of the synthesis chamber. All values are presented in mm. n/m stands Q3n/m for noble / molecular gas.

4.1.2 Plasma modelling: heat source model

There are several approaches to model the inductively coupled plasma; among them are the heat source, the 1D and 2D ElectroMagnetic (EM), the extended 2D EM field approaches.

The introduction of the EM field in the model is necessary to describe its effect on the temperature and velocity profiles especially inside the torch (section 2.3.2). As this work is more focussed on the particle growth and quenching, which mostly occur outside the torch region, the EM field has been neglected; the plasma is simplified to being a heat source. Furthermore, the influence of the swirl component in the central gas and the radiation have been neglected. A comparison between the heat source model and extended 2D EM field approach is made in the next section. Figure 4-2 shows the position of the heat source within the torch.

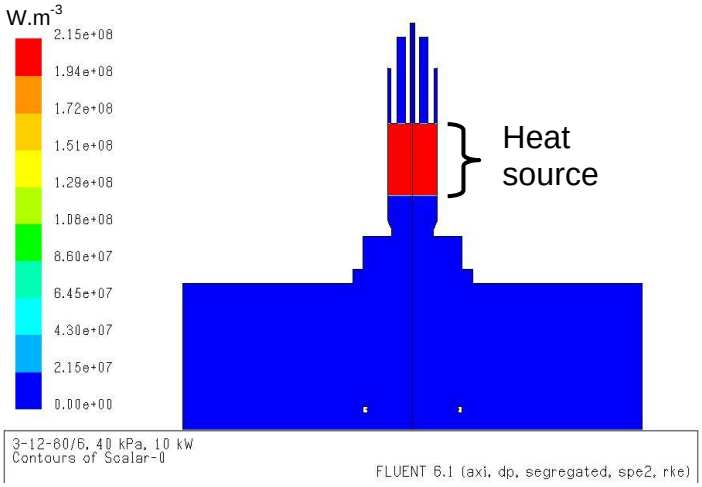

Figure 4-2: position of the heat source in the model. The parameter represents the power input with a maximal value of 2.15e8 $W.m^{-3}$, this results in a net input power of 10135 W.

The net power input of the heat source lies in the range of 8 -15 kW. The energy of the heat source, representing the net power input into the plasma, was adjusted to be in compliance with the temperature and velocity obtained from the enthalpy probe measurements (see section 3.5.1). The range from 8 – 15 kW resulted in a maximum temperature between 7500 K and 10000 K.
The literature, however, refer to the power input as being the plate power, which is defined as the power which is introduced in the torch. Around 60% of this plate power actual ends up in the plasma [128] for PL-35 torch operated at 5 MHz at 101 kPa with 0-30-70/0 plasma gas composition.
Figure 4-3 shows the temperature and velocity profiles as obtained by using the current heat source model. The gas flow rates are the same in both cases: 3-12-80/6 at 40 kPa with 10 kW net power input. The gas flow rates are described as: Q1-Q2-Q3n/Q3m. In which Q1 represents the carrier gas and Q2 the central gas flow rate. Q3n and Q3m represent the noble and molecular gas flow rate in the sheath gas (Figure 3-4). Q1, Q2, and Q3n are Ar flow rates and Q3m is a hydrogen flow rate unless mentioned otherwise. All the flow rates are given in standard litre per minute (slpm).

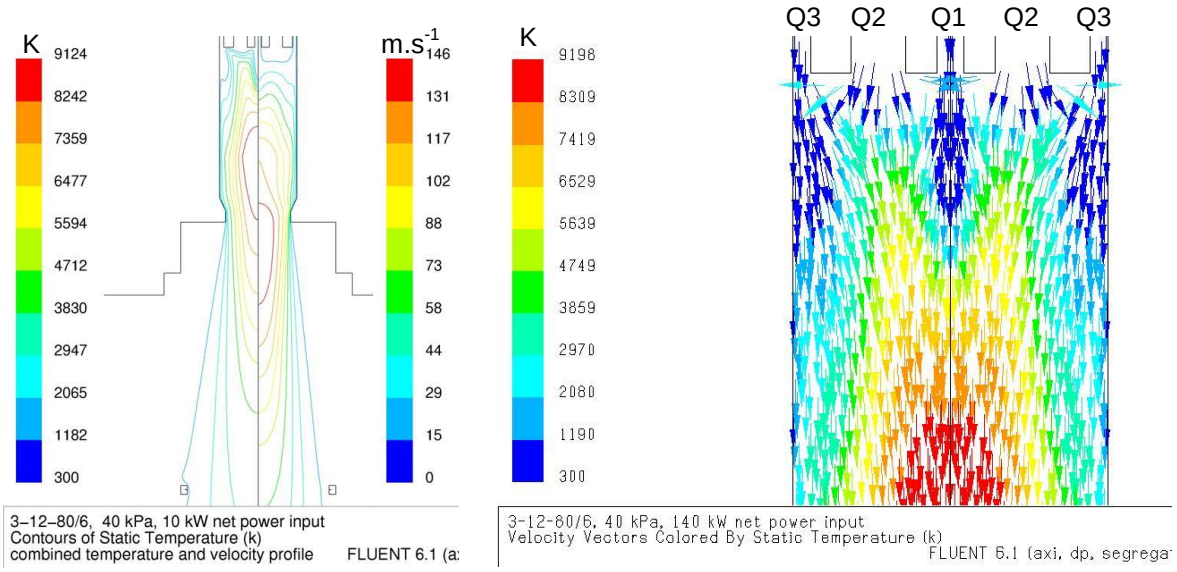

Figure 4-3: left: temperature and velocity profiles and right: velocity vectors as function of the temperature as modelled with the heat source approach as used in this work. Modelled 2D parameters: 3-12-80/6H_2, 40 kPa, 10 kW.

The plot with the velocity vectors in Figure 4-3 shows that the recirculation in the coil region is absent in the heat source model (without EM field), as where it is present in models using the EM field (see for example Figure 2-8 and Figure 4-7).

Summary of 4.1.2
A model using a heat source is used to describe the temperature and velocity profiles in the PL-35 torch and synthesis chamber. The heat source approach has been picked up because the area of interest (were the particle growth takes place) is well outside the torch region, where the effect of the EM field is expected to be negligible. The heat source model does not show a recirculation inside the torch.

4.1.3 Heat source model versus the extended 2D EM field approach

As already shown in the previous section, the heat source model does not show any recirculation in the torch region. Therefore, a comparison between the heat source and an extended 2D EM field approach model has been made.

The absence or presence of the recirculation has an effect on the particle trajectories within the torch. Normally, the coil current induces a magnetic field and causes an upward flow at the torch axis (direction opposite to the carrier gas flow). The precursor particles, which are introduced along with the carrier gas, will need a higher momentum to penetrate the plasma [106] than already required otherwise. If the particle momentum is not high enough to penetrate the plasma, the particles will "bounce off" and follow a trajectory along the plasma edge. Another consequence of the recirculation is a better mixing of the carrier gas with the central / sheath gas, which leads to the presence of carrier gas throughout the entire torch. If some of the precursor is already vaporised, this could result in coating of the torch tube (which could eventually damage the tube if the coating couples).
The recirculation however can be overcome by giving the particles a higher momentum; by using a higher carrier gas flow rate [113] and/or a smaller injector.
Figure 4-4 shows the influence of the central gas and carrier gas flow rate on the axial velocity in the torch.

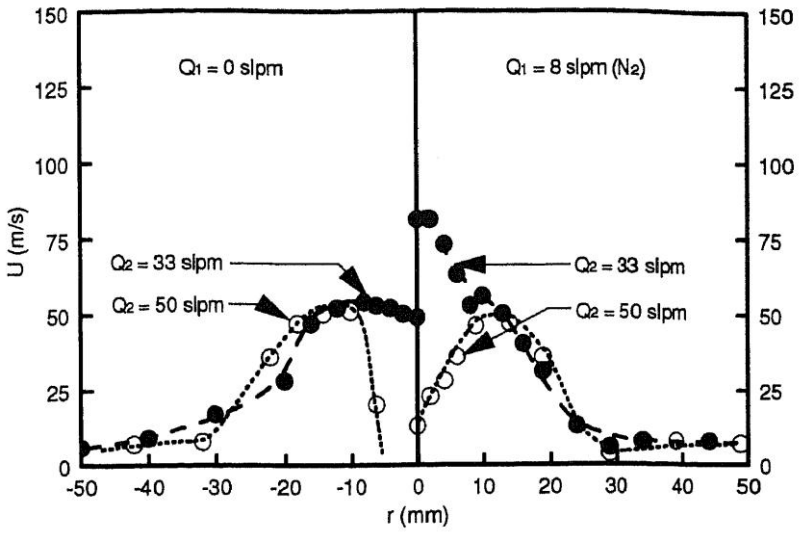

Figure 4-4: influence of the carrier gas amount on the axial velocity in a PL-50 torch (Rahmane et al. [113]). Gas flow rates; left: 0-33 or 50-71/4 and right: 8-33or 50-71/4. A high carrier gas flow (Q1) reduces the reflow caused by the EM-field. Process conditions: plate power 20 kW, 3 MHz, 33 kPa, carrier gas injector at z = -93 mm.

When a central gas flow rate with a swirl component above a certain threshold value is used, the recirculation caused by the EM-field gets stronger. The swirl component causes a pressure difference which influences the velocity profile in the centre and results in an upward velocity at the axis [113]. Figure 4-4 also shows that increasing the carrier gas flow, thus velocity, reduces the recirculation effect and even let is vanish.
Boulos et al. [102] used a 30 mm inner diameter torch, operating at 101 kPa, 3 MHz, and a plate power of 3 kW to investigate the effect of the sheath gas swirl component on the reflow for a 0-2-18/0 plasma gas composition. The recirculation is reduced with increasing swirl velocity.
Besides a reduction or even stopping the recirculation, the increase of the carrier gas flow rate also has another effect on the plasma temperature and velocity profile. A higher carrier gas flow rate results in a stronger cooling of the plasma along the axis and in a higher velocity, especially just below the injection point. As a consequence the axially injected precursors face less energy which can be used for evaporation. Figure 4-5 shows the carrier gas effect as observed in a real plasma. The left photograph shows the plasma, as seen from below, with a 1 slpm Ar carrier gas flow. Underneath each picture is a schematical representation of the situation. The right photograph shows the plasma for the same conditions, but with 10 slpm Ar carrier gas flow rate. The bright edges are the high temperature zone caused by the coupling of the EM field, resulting in a concentrated power dissipation in that region as a consequence of the skin depth (equation 2-6). As the skin depth is very small at high frequencies (2.5 mm for pure Ar at 13.56 MHz and 10000 K), the heat transfer to the middle of the plasma has to result from conduction. At low carrier gas flow rates the heat transfer from conduction and convection (only when a recirculation is present) is much higher than at higher carrier gas flow rates. Another important factor is that at lower gas flow rates, less energy is wasted to heat up the cold carrier gas. The effect of these factors can be seen by less emission (a larger darker region) in the centre of the plasma at a higher carrier gas rate.

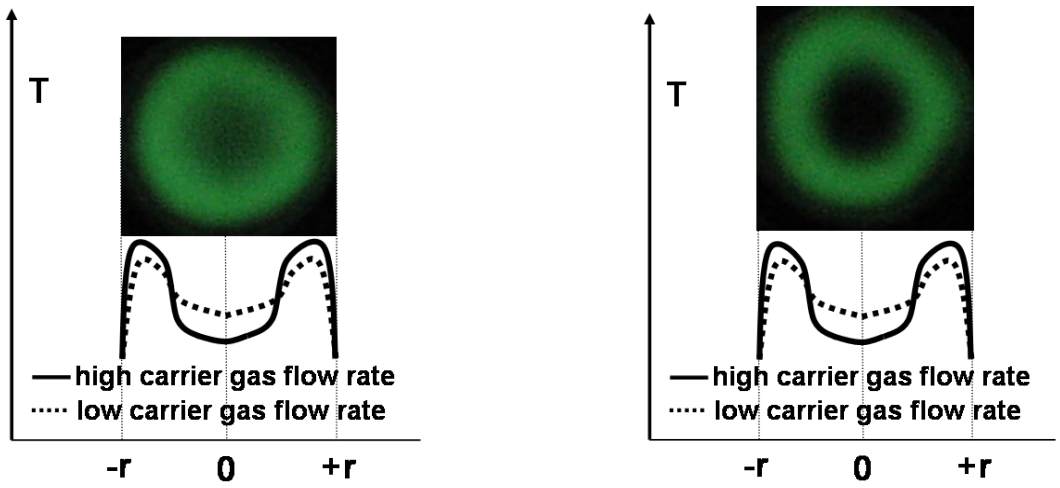

Figure 4-5: visual appearance of the plasma cross section with different carrier gas flow rates. These observations (current work) were made with a mirror. The green colour of the plasma is caused by the use of a filter to reduce the light intensity. A schematic drawing of the situation is placed underneath the pictures. Left: plasma conditions: 1-12-80/6, plate power 22.5 kW, and 60 kPa. Right: plasma conditions: 10-12-80/6, plate power 22.5 kW, and 60 kPa.

The same effect has been predicted by the heat source model, as shown in Figure 4-6. The left picture shows a “homogeneous” temperature distribution when the carrier gas flow rate is low, while a high carrier gas flow has the maximum

temperature off-axis as is shown in the right picture. By comparing Figure 4-5 and Figure 4-6 the same trends are found, despite the absence of the EM-field in the heat source model. Although the modelled conditions are not the same as for the experimental ones, the trends remain the same.

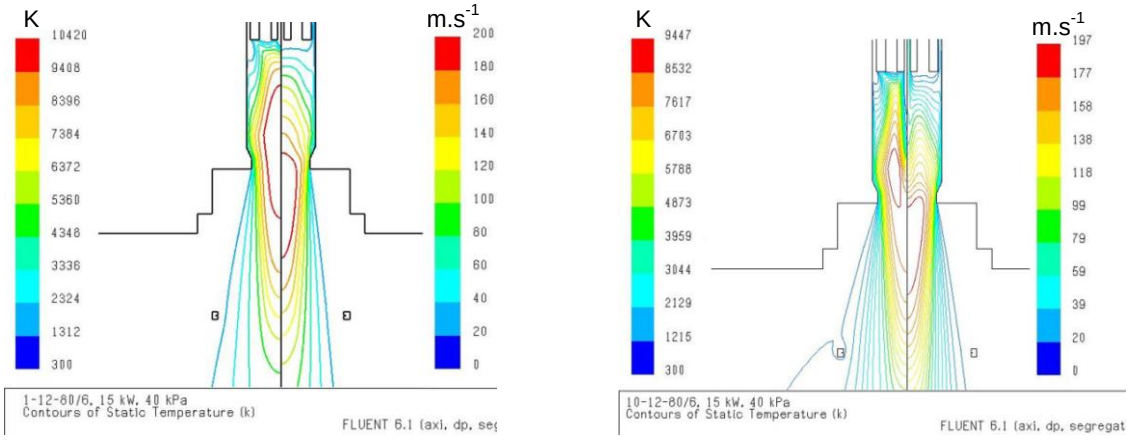

Figure 4-6: Influence of the carrier gas amount on the temperature at the axis. Left: 1 slpm Ar carrier gas. Right: 10 slpm Ar carrier gas. Modelled conditions: Q1-12-80/6, 40 kPa, and 15 kW power input.

Another possibility to circumvent the injection problem caused by the EM field, is by lowering the injection position so that the particles are injected below the recirculation zone [150]. Also the use of an increased torch frequency reduces the effect of the recirculation caused by the EM field. Shigeta et al. [125] state that the recirculation flow vanishes with increasing frequency. In their work they compared the velocity profiles in a 50 mm diameter torch operating with frequencies of 0.5 MHz and 13.56 MHz. A 10-10-25/0 plasma gas composition was used at a pressure of 101 kPa and a net power input of 8 kW.
Figure 4-7 shows the calculated velocity vector profiles for torch frequencies of 0.5 MHz and 13.56 MHz, and the radial course of an axially injected copper particle [125] (20 µm diameter, only the dotted line is of interest).

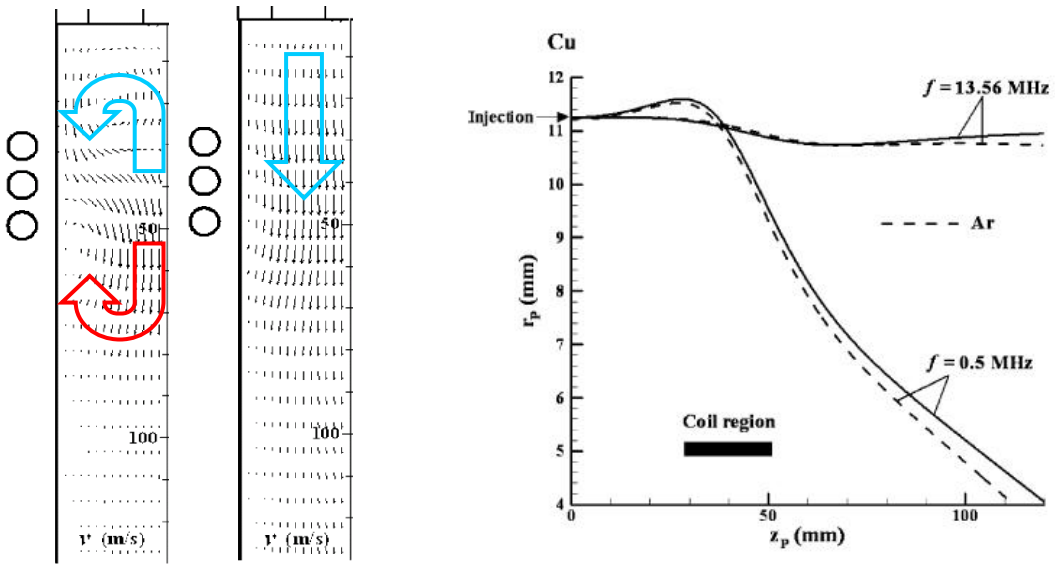

Figure 4-7: Left: velocity vectors in torch region for a coil frequency of 0.5 MHz (large arrows were not present in the original image) and a coil frequency of 13.56 MHz (middle). Right: radial course of a 20 µm Cu particle injected axially at 11.2 mm from the torch axis for 0.5 and 13.56 MHz. (The solid lines should be ignored.) Figures from Shigeta et al. [125]. Plasma conditions: 10-10-25/0 slpm Ar, net plasma power 8 kW, pressure 101 kPa, torch diameter 50 mm.

The images show different velocity profiles and particle trajectories around the coil region for different torch frequencies. Operating the ICP at a higher frequency is beneficial for obtaining a plasma flow field without a recirculation caused by the EM field. This means that a particle needs less momentum (e.g. less carrier gas) to penetrate the plasma and the axial injected particle remains on its original trajectory parallel to the axis.

In the current work a frequency of 13.56 MHZ is being used, which could mean that, according to Shigeta et al. [125], there will be no recirculation. To confirm this, the torch geometry and plasma conditions as used in this work, have been modelled with the extended 2D EM field approach, by R. Bolot [190]. Figure 4-8 shows the results for a PL-35 torch using a 3-12-80/6 plasma gas composition at 40 kPa, with swirl component.
The velocity vectors show the absence of the reflow in the coil region caused by the EM field. The reflow that is present is caused by the swirl component of the central gas Q2.
The absence of the reflow would be very beneficial for the introduction of a solid precursor into the plasma, since the precursor particles of different size will follow more or less the same trajectories, which is not the case at lower frequencies (3 MHz), see Figure 4-7. Furthermore, less carrier gas is necessary to penetrate the plasma. This means that less energy is required to heat up the carrier gas and more energy is available for the evaporation.

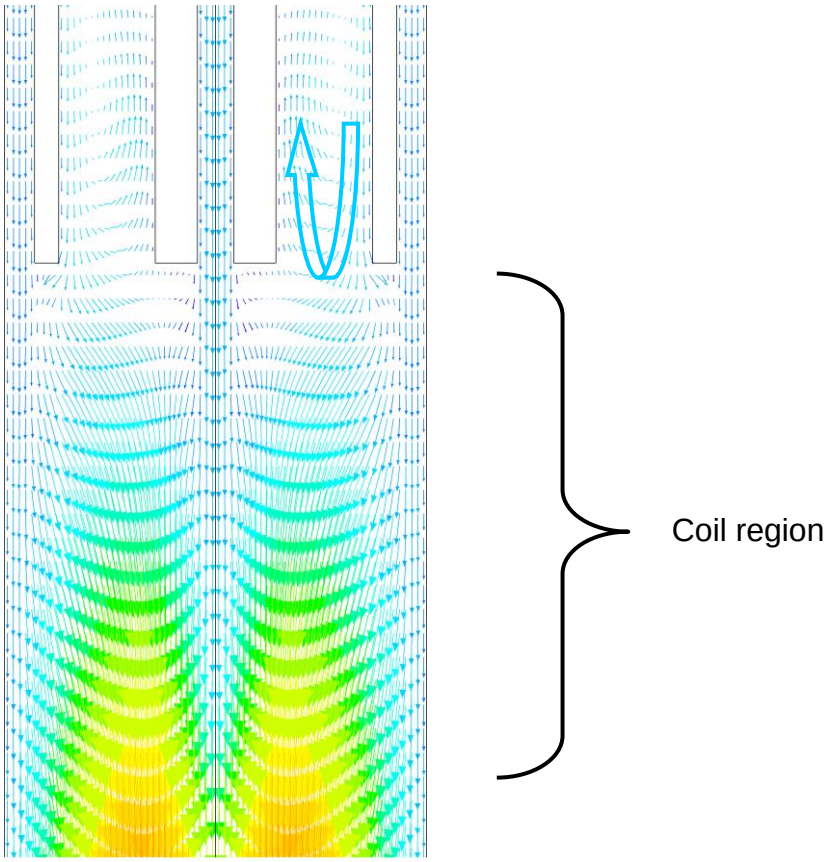

Figure 4-8: axial velocity presented by velocity vectors inside the PL-35 torch. The model was created by R. Bolot [190] for the set-up used in this work and was based on the extended 2D EM field approach as suggested by Xue et al. [141]. Modelled 2D conditions: 3-12-80/6, 40 kPa, 13.56 MHz, 12.6 kW net power input.

The absence of the reflow has also been confirmed by M. Boulos [191]. The same torch and reactor geometry as used in this work were modelled for 40 kPa and 16.25 kW plate power (about 10 kW into the plasma) and a 3-12-80/6, 5-27-80/6, and 3-12-80/6N_2 composition.
Further results of preliminary investigations [190] are suggesting that the frequency is probably less important than the carrier gas velocity and the pressure in order to reduce the reflow.

Figure 4-9 compares the temperature and velocity along the axis for the 2D EM field and the “heat source” model.

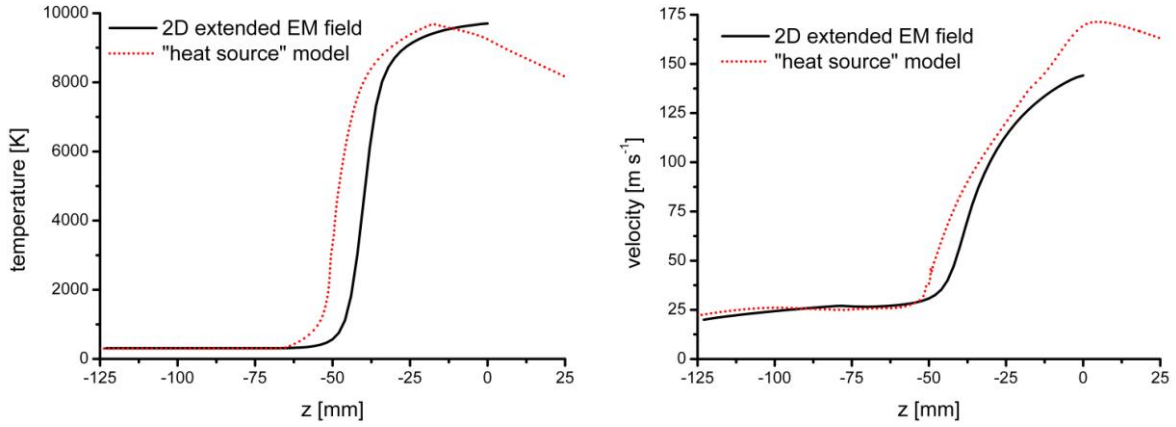

Figure 4-9: comparison of the temperature and velocity along the axis for the extended 2D EM field approach by Bolot [190] and the current “heat source” model. Modelled conditions: 3-12-80/6, 40 kPa, 12 kW net power input.

Due to the fact that the power is only dissipated in the skin depth, the maximum temperature and velocity at the axis are reached later in the extended 2D EM field approach as compared to the “heat source” model. Because the heat has to be transferred by conduction and convection to the axis, whereas as in case of the “heat source” model, the power is dissipated over the whole radius and therefore does not have to be transferred.
The skin depth also causes a difference between position and magnitude of the temperature maximum. As most of the heat is dissipated in the skin depth, this leads to a higher energy density than compared to the homogeneous distribution of the heat source model. The result is a temperature maximum which is about 1500 K higher and positioned off-axis (about 10 mm away from the axis). The maximum velocity along the axis shows some differences between the models. This is due to the fact that the current extended 2D EM field approach model does not comprise the compression part at the torch exit.

Summary of section 4.1.2
The heat source model results in the absence of a recirculation commonly found in the ICP torch when modelled with for instance an extended 2D EM field approach. These models are however used applied to torches with a larger diameter, lower gas flow rates, and lower frequencies. This recirculation, induced by the EM field, can also be reduced and even stopped by increasing either the carrier gas flow rate (Q1), the swirl component in the sheath gas (Q3) [102] or by reducing the central gas flow rate (Q2). A reduced recirculation has a positive effect on the particle injection, because the particles will face “homogeneous” trajectories and less momentum is needed to introduce the particle in the plasma. It also means a lower carrier gas flow

rate can be used and therefore less cooling of the plasma along the axis will occur, which is beneficial for the evaporation process.

The torch used in this work has a 35 mm diameter and is operating at a frequency of 13.56 MHz with a 3-12-80/6 plasma gas flow rate. The results of an extended 2D EM field approach of this set-up and process parameters have shown the absence of a recirculation. Further results of this preliminary model are suggesting that the absence of the recirculation is probably a consequence of the high plasma gas velocity in torch, due to the small diameter and high gas flow rates, and to a lesser extent due to the frequency.

4.1.4 Experimental validation of the heat source model

Besides a qualitative validation via comparison between observations and the results of other models, as described in the previous section, the current model has also been validated quantitatively via comparison to the results of enthalpy probe measurements [192], see section 2.8.1 and 3.5.1. Several measurements with different plasma gas flow rates and compositions, power, and pressure levels were made. The mass spectrometer, used to determine the gas phase composition, has been calibrated with a well-defined Ar/H_2 mixture (5 vol% H_2), which is close to the hydrogen concentration of the plasma compositions used in this work.
Figure 4-10 and Figure 4-11 show the comparison between the model and enthalpy probe measurements obtained at z = 22 mm and z = 75 mm respectively. These measurements have been carried out in the absence of quenching (defined as 2.8 slpm Ar (at z = 63 mm)). The modelled power input of the heat source has been adapted to obtain a good fit with the enthalpy probe measurements.

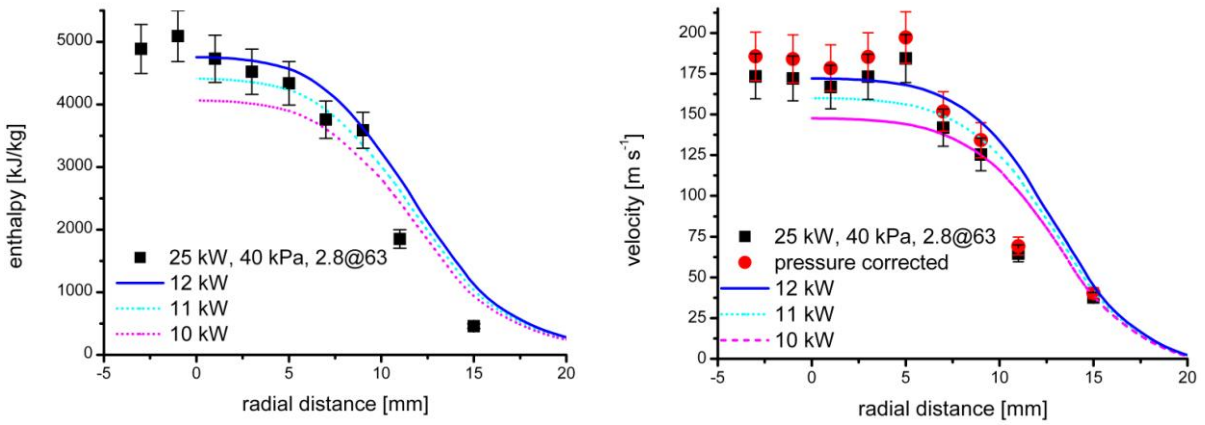

Figure 4-10: left: comparison of the measured (points) and calculated (lines) enthalpy as a function of the radial distance. Right: idem for the axial velocity. Experimental parameters: 5-27-80/6, 40 kPa, plate power 25 kW, enthalpy probe tip at z = 22 mm. Modelled parameters: 5-27-80/6, 40 kPa, 10 - 12 kW power input.

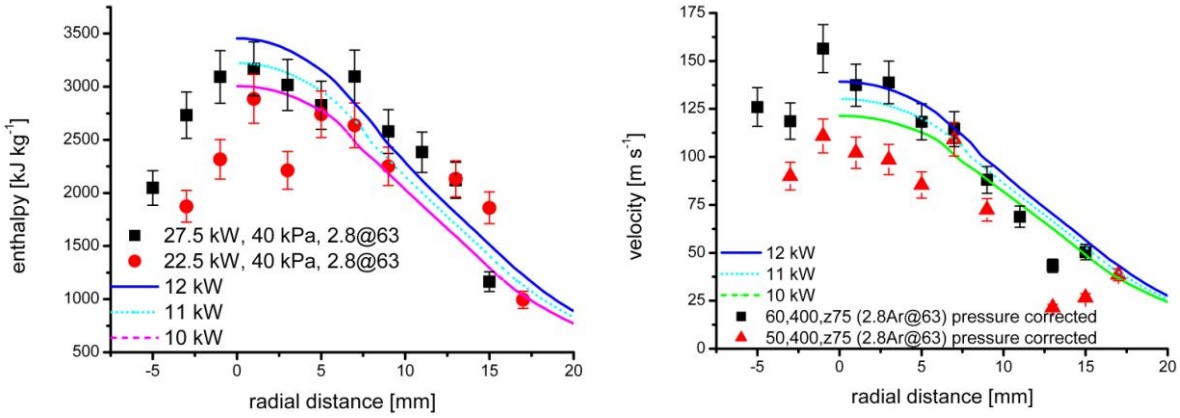

Figure 4-11: comparison of the measured (points) and calculated (lines) enthalpy (left) and axial velocity (right) as a function of the radial distance. Experimental parameters: 5-27-80/6, 40 kPa, plate power 22.5 kW and plate power 27.5 kW, enthalpy probe tip at z = 75 mm. Modelled parameters: 5-27-80/6, 40 kPa, 10-12 kW power input.

The modelled values are displayed until the symmetry axis (radial distance of 0 mm), whereas the enthalpy probe measurements have been displayed over the symmetry axis, as the measurements show an a-symmetric behaviour. This a-symmetric behaviour has already been confirmed experimentally by other authors (e.g. [193]) and theoretically by Bernardi et al. [104]. Also a (small) misalignment of the probe tip or probe arm could contribute to this effect.
The heat source model shows a good agreement with the enthalpy probe measurements for a net input power of 11 kW, when the plate power amounts 25 kW. This results in an efficiency of ca. 45%, whereas Merkhouf and Boulos [136] found an efficiency of 60% for PL-35 torch operating at atmospheric pressure and a frequency of 5 MHz (plasma gas composition 0-30-70/0). They however had an additional term (power loss in coil inductor) which is not included in this number of 60% and would reduce the efficiency below 60%. As the radiation is not included in the heat source model (slightly larger than 1 kW [190]), it will increase the efficiency to about 50%.

The temperature has been measured at z = 965 mm and z = 2500 mm with a thermo-element for different process parameters. The results are shown in Figure 4-12, Table 4-1 and Table 4-2.

Table 4-1: temperature measured at z = 965 mm and z =2500 mm for different plasma parameters. The quenching ring consisted out of 8 x ϕ 1.5 mm nozzles (angled), had a 63 mm internal diameter, and was positioned at z = 121 mm.

Plasma gas composition	Plate power [kW]	Pressure [kPa]	Quench gas Ar [slpm]	Temperature [K]* z = 965 mm	z = 2500 mm
1-12-80/6	15.6	40	2.8 / -	865	350 / - -
10-12-80/6	15.6	40	2.8 / 56	843	355 / 538 330
1-27-80/6	15.6	40	2.8 / 56	835	352 / - 331
5-27-80/6	15.6	40	2.8 / 56	829	360 / 543 334
5-27-80/6	18.5	40	2.8 / 56	983	381 / 958 403
10-27-80/6	15.6	40	2.8 / 56	818	360 / 543 334
3-12-80/6	15.6	40	2.8 / 56	861	357 / 552 332
3-12-80/6	15.6	30	2.8 / 56	864	360 / 553 335
3-12-80/6	15.6	60	2.8 / 56	845	342 / 534 323
3-12-80/6	13.0	40	2.8 / 56	718	338 / 479 321
3-12-80/6	18.5	40	2.8 / 56	980	377 / 871 395

* $\pm$ 7 K

The results show an increasing temperature at z = 2500 mm with either increasing plate power, increasing gas flow rate, or decreasing pressure. These effects result in a higher gas velocity carrying the heat further downstream.
When a quench gas flow rate of 56 slpm Ar is used, a decrease of the temperature is found compared to the non-quench (2.8 slpm Ar) condition. This is not the case for a high plate power, because then the temperature even rises with quenching by 56 slpm Ar. This is probably due to a complete penetration of the plasma with 56 slpm Ar at 15.6 kW plate power, which is not the case at 18.5 kW. The higher plate power results in higher temperature and viscosity, which makes the penetration by the quench gas more difficult. When the plasma is not (completely) penetrated the quench gas acts as a confinement and prevents the entrainment of cold(er) gas from the environment. It also increases the velocity and thereby transferring the heat further downstream.
At z = 965 mm the temperature increases with either increasing plate power, decreasing plasma gas flow rate, decreasing quench gas flow rate, or decreasing pressure.
The plasma gas flow rate has an opposite effect at this height compared to the z = 2500 mm case, although the effect at z = 2500 mm is less pronounced. A higher gas flow rate means that the energy has to be distributed over a larger mass and therefore will result in a cooler plasma. The temperature at z = 965 mm decreases with increasing quench gas flow rate to temperatures well below 800-900 K. This is of importance for the Si particle growth, since 800-900 K is the temperature range at which no particle growth occurs and only soft agglomerates are formed.
The measured temperature, as presented in Table 4-1, have been compared to the temperature predicted by the heat source model, see Figure 4-12.

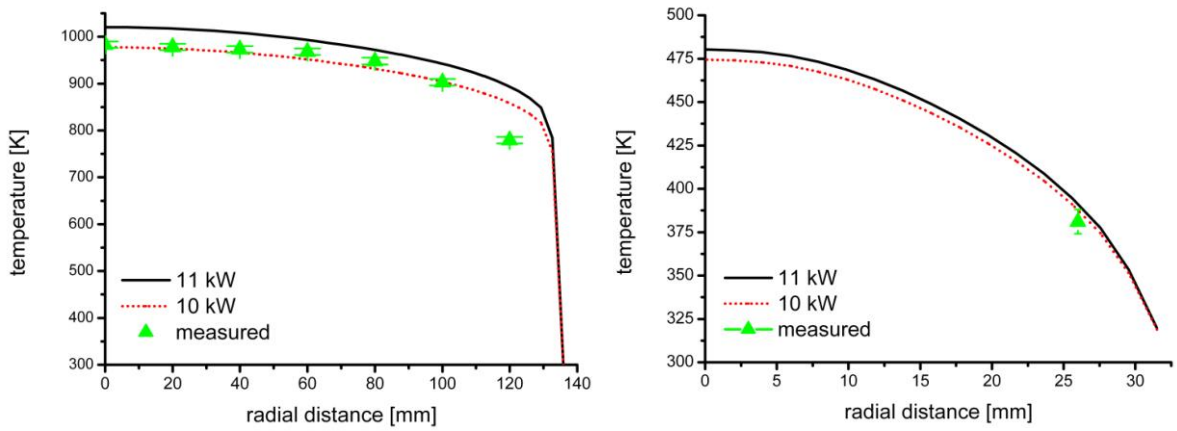

Figure 4-12: x-y plots of the temperature at z = 985 mm and z = 2500 mm as a function of the radial position. Modelled process conditions: 3-12-80/6, 40 kPa, 10 and 11 kW net power input.

From these results the net power input in the plasma has been estimated to be around 10 kW for a plate power level of 18.5 kW, resulting in an efficiency of ca. 55%.
The efficiency obtained by comparing the modelled power to the plate power in Figure 4-12 differs from Figure 4-10 and Figure 4-11. This is caused by reduced sensitivity of the temperature at high z values. The temperature difference between 10 and 11 kW net power input is 500 K at z = 22 mm, whereas it is only 30 K at z = 965 mm. The thermoelement accuracy (± 7 K) makes it therefore more difficult to determine the net power input from the temperature profiles at higher z values.

Table 4-2 shows the effect of the quenching position, pressure, and plate power on the temperature measured at z = 2500 mm for the 3-12-80/6 plasma gas composition when quenched with an 8 x ϕ 1.5 mm (angled, 15° downward).

Table 4-2: comparison of the effect of plate power, pressure, quench position and Ar quench gas rate on the gas temperature measured at z = 2500 mm for 3-12-80/6 plasma gas composition. The quenching position (8 x ϕ 1.5 mm, angled) was 53 mm and 121 mm (italics).

Plate power [kW]	Pressure [kPa]	Quench gas [slpm]	Temperature [K]* 53 mm *121 mm*
15.6	30	2.8 / 56	360 *354* / 335 *387*
15.6	40	2.8 / 56	357 *348* / 332 *364*
15.6	60	2.8 / 56	342 *341* / 323 *355*
13.0	40	2.8 / 56	338 *330* / 323 *338*
18.5	40	2.8 / 56	377 *367* / 395 *404*
15.6	40	2.8 14 28 42 56 **	*357* *362* *374* *378* *332*

* ± 7 K
** no results for z = 53 mm

The trends at z = 2500 mm show an increasing temperature with either decreasing pressure, increasing quench gas flow rate (up to 42 slpm Ar), or increasing plate power. It is interesting to see that the temperature rises with increasing quench gas flow rate and drops drastically after quenching with 56 slpm Ar (last row of Table 4-2), which indicates a complete penetration, thus cooling instead of guiding the plasma. The temperature profile has been visualised in Figure 4-13 .
The maximum in the temperature measured at z = 2500 mm depends on the quench gas flow rate. The same explanation as for the results of Table 4-1, the quench gas acting as a confinement for the plasma, is valid here.

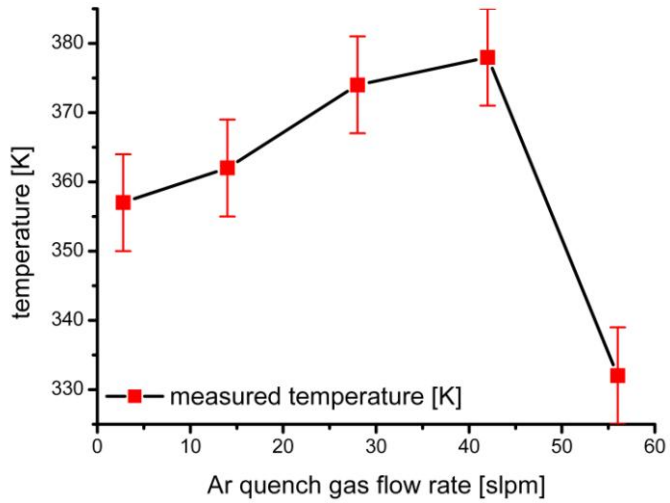

Figure 4-13: measured temperature, at z = 2500 mm and r = 26 mm, as a function of the Ar quench gas flow rate. Plasma parameters: 3-12-80/6, 15.6 kW, and 40 kPa. Quenched at z = 121 mm, with 8 x ϕ 1.5 mm (angled).

The measured trend at z = 2500 mm with increasing quench gas flow rate is in agreement with the heat source model. Figure 4-14 shows modelled temperature at z = 2500 mm as a function of the quench gas flow rate N_2.
The effect of Ar and N_2 quenching gas is the same, a decreasing temperature with increasing flow rate, except for the absolute difference, which is caused by a different heat capacity. As the c_p for molecular N_2 is higher than for Ar, it also means that N_2 is more efficient, but cools down slower.

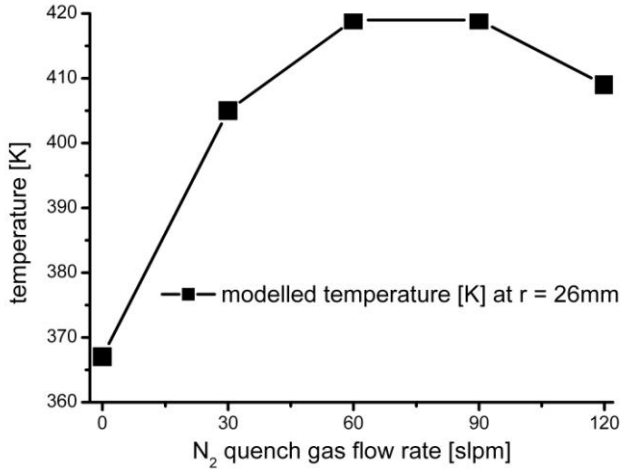

Figure 4-14: modelled temperature at z = 2500 mm and r = 26 mm, as a function of the N_2 quench gas flow rate. Modelled parameters: 5-27-80/6, 10 kW, 40 kPa, quenched at z = 63 mm (quench surface angled and equivalent to 8 x ϕ 1.5 mm).

The temperature at z = 2500 mm increases with increasing quench gas flow rate until a maximum is reached for 60 slpm N_2 and subsequently decreases with a further increase of the quench gas flow rate.

Summary of section 4.1.4

The heat source model (11 kW net power input) shows a good agreement between the calculated and measured (enthalpy probe) temperatures and velocities between z = 22 and z = 75 mm for the 5-27-80/6, 40 kPa, 25 kW plate power conditions. Also is the heat source model in compliance with thermoelement measurements at higher z values (965 and 2500 mm). Approximately 50% of the total plate power is available for the plasma. This is in agreement with the 60% found by Merkhouf and Boulos [136] for the same torch as used in the current work, but operating at 5 MHz, when the loss into the inductor coils are taken into consideration.

The quenching efficiency can be found in the temperature at z = 2500 mm. A complete penetration is found to result in a lower temperature than compared to lower degrees of penetration (lower quench gas flow rates).

4.1.5 Heat source model: parameter study

The heat source model has proven its validity with respect to qualitative and quantitative validation. The model has further also been checked on “common sense” by comparing the gas diffusion behaviour for plasma and non-plasma conditions. In Figure 4-15 the radial concentration profiles of N_2, which was injected axially, at different heights are shown for the presence (right) and absence (left) of plasma.

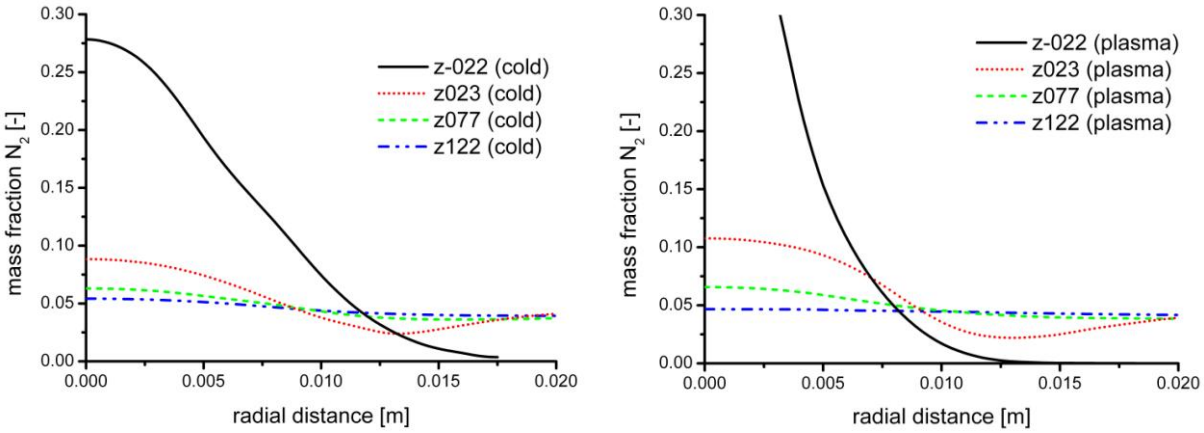

Figure 4-15: N_2 mass fraction as a function of the axial distance z for "cold gas" conditions at 300 K (left) and plasma conditions (right). Modelled conditions: $8N_2$-33-71/6, net power input 15 kW, 40 kPa.

The modelled diffusion behaviour shows the expected behaviour, meaning N_2 diffuses slower in the plasma gas than in the "cold" case, because of the high viscosity of the plasma. The diffusion coefficient for N_2 in Ar amount 5 x 10^{-5} $m^2.s^{-1}$ at 300 K and 40 kPa and around 8 x 10^{-3} $m^2.s^{-1}$ at 6000 K and 40 kPa (obtained from modelling). The results of Figure 4-15 are in agreement with the results of Rahmane et al. [113] for almost similar conditions.

The influence of substituting Ar by other gases in carrier and sheath gas on the temperature and velocity profiles has also been investigated. Figure 4-16 shows the modelled temperature profiles of two cases comparing Ar and N_2 used as carrier gas.

When Ar is substituted by N_2 as carrier gas, a decrease of the maximum temperature is seen (due to the different c_p characteristics), which is also found by Rahmane et al. [113]. Furthermore is the cooling of the plasma outside the plasma torch slower when N_2 is being used; a smaller temperature gradient (3.7 x 10^5 to 5.5 x 10^5 $K.m^{-1}$ for Ar). Both the lower temperature and gradient are caused by the higher specific heat of N_2 per slpm carrier gas (including the dissociation of N_2 around 7000 K). The temperature difference between the modelled temperature maxima in Figure 4-16 amounts approximately 2000 K.

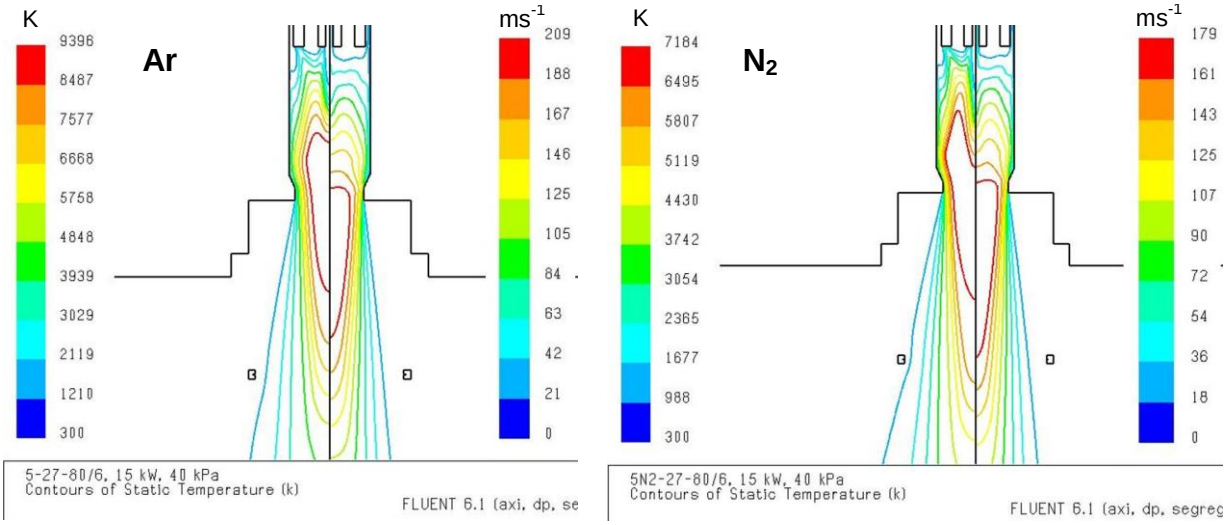

Figure 4-16: comparison of the plasma temperature of 5-27-80/6 plasma gas composition. Left: Ar carrier gas. Right: N_2 carrier gas. Net power input 15 kW, pressure 40 kPa.

The influence of different process parameters on the maximum gas temperature and residence time, as calculated by the model, is shown in Table 4-3 to Table 4-5. The

residence time, important for the evaporation is defined as the time the plasma gas spends in the temperature zone above 3500 K (boiling point of Si). Table 4-3 shows the influence of the carrier and central gas flow on the plasma temperature.

Table 4-3: modelled maximum temperature, length of region in which temperature is above 3500 K, matching residence time, and maximal velocity as a function of the plasma gas flow rate. Pressure 40 kPa, 15 kW net power, and injection position z= -79 mm.

plasma gas flow rate	maximum temperature (off)	axis [K]	z [mm] (> 3500 K)	τ [ms] (>3500 K)	v_{ax} [m s^{-1}] (maximum)
1-12-80/6		10419	-60 – 144	1.71	200
1-27-80/6		9916	-58 – 140	1.57	210
3-12-80/6		10273	-52 – 140	1.54	201
5-12-80/6		10028	-43 – 143	1.49	201
5-27-80/6	**9397**	9381	-39 – 139	1.26	208
10-12-80/6	**9447**	8912	-25 – 141	1.23	197
10-27-80/6	**9026**	8060	-18 – 137	1.06	202

An increasing plasma gas flow results in general in a reduction of the maximum temperature, residence time, and length of the “T > 3500 K” region. Furthermore is the initial 3500 K position shifted towards the end of the torch (z = 0 mm) with increasing carrier gas flow rate. The decrease of the axial velocity by the reduced temperature is stronger than the increase as a consequence of the increased flow rate. The maximum temperature is shifted from the axis when the carrier gas flow is increased from 1 to 5 slpm Ar. A larger residence time at higher temperatures (over 3500 K) can be obtained by reduction of the total gas flow rate. A broad high temperature region is very beneficial for the precursor evaporation, since it can not be expected that all the precursor particles introduced by the injector (3 mm diameter) will follow the trajectory along the axis, which is fulfilled for all the plasma gas compositions.

Table 4-4 shows the influence of adding other species to the plasma gas composition on the temperature and length of the “T > 3500 K” region.

Table 4-4: modelled maximum temperature, length of region in which temperature is above 3500 K plasma gas composition, matching residence time, and maximal velocity as a function of the plasma gas composition. Pressure 40 kPa, 15 kW net power, and injection position z = -79 mm.

plasma gas composition	maximum temperature (off)	axis [K]	z [mm] (> 3500 K)	τ [ms] (>3500 K)	v_{ax} [m s^{-1}] (maximum)
5-27-80/6	**9397**	9381	-39 – 139	1.26	208
5-27-80/10		9387	-39 – 129	1.18	203
5H_2-27-80/6*	**5307**	4018	0 – 103	0.93	119
5N_2-27-80/6	**7184**	6674	-30 – 149	1.37	178
5-27-80/6N_2		8427	-39 – 160	1.42	196
5N_2-27-80/6N_2*	**6840**	6575	-30 – 170	1.54	180
5He-27-80/6	**9200**	9139	-42 – 135	1.18	218
1H_2-27-80/6	**9129**	9082	-46 – 138	1.55	204
1$H_2$4Ar-27-80/6	**8891**	8467	-32 – 137	1.18	201

* not able to form a plasma under the modelled conditions, as the temperature is well below 7500 K.

Replacement of Ar by other gases in the carrier gas reduces the highest temperature and results in a temperature maximum which is off-axis. Furthermore, the substitution of H_2 by N_2 in the sheath gas results in a cooler plasma, but in a longer residence time at T > 3500 K. As the c_p for N_2 per slpm is higher than per slpm H_2,

the gas mixture remains hotter than 3500 K for about 20 mm more. Since the velocity does not differ so much, the residence time for the N_2 sheath gas is longer.

Table 4-3 and Table 4-4 have shown the influence of the plasma gas flow and composition on the maximum temperature and region, whereas Table 4-5 does the same for other process parameters, like pressure and power.

Table 4-5: modelled maximum temperature, length of region in which temperature is above 3500 K, matching residence time, and maximal velocity as a function of the plasma parameters for the 3-12-80/6 composition. Pressure 40 kPa, 10 kW net power, and injection position z = -79 mm, unless mentioned otherwise.

plasma parameters	maximum temperature axis [K]	z [mm] > 3500 K	τ [ms] >3500 K	v_{ax} [m s^{-1}] (maximum)
3-12-80/6	9211	-47 – 105	1.41	152
3-12-80/6 15 kW	10273	-52 – 140	1.54	201
3-12-80/6 30 kPa *	9213	-47 – 107	1.07	203
3-12-80/6 60 kPa *	9212	-47 – 106	2.13	102
3-12-80/6 -10**	8844	-36 – 108	1.28	151
3-12-80/6 funnel***	9212	-47 - 113	1.54	152
3-12-80/6 swirl****	9198	-53 – 105	1.57	149

* c_p, κ have been assumed to be the same as for 40 kPa
** injection position of carrier gas lowered by 10 mm (z = -69 mm)
*** a funnel has been introduced in the reactor to guide the plasma flow (see section 4.2.3.2)
**** swirl component of the central gas taken into account

This table shows that an increasing power results in a higher maximum temperature and a longer high temperature region (T > 3500 K). The introduction of the swirl component increases the length of the high temperature region. An increase of the working pressure results in an increase of the residence time in the high temperature region. The shift of the precursor injection position towards higher z values (closer to the torch exit) results in a reduction of the temperature and residence time. The funnel set-up increases the residence time as compared to the situation without, due to the decrease in velocity caused by the convergence in the funnel.

The plasma gas composition that will be used for the nanoparticle synthesis has to fulfil several criteria, with respect to system requirements, residence times, costs, powder transport and injection, etc..
A high temperature and energy density are required for the evaporation of refractory materials. The plasma should have a high thermal conductivity and a long residence time at high temperatures to allow the evaporation of larger and/or more precursor particles, in order to obtain a high synthesis rate. Also should the high temperature region be wide enough to allow all the precursor particles to face a high temperature necessary for evaporation, to account for the fact that the injector already has a 3 mm diameter and thus not all the particles follow the trajectory along the axis. The carrier gas flow should give the precursor enough momentum to penetrate the plasma, but should be as low as possible to prevent cooling of the plasma and reduction of the residence time. The operation conditions require certain minimum and maximum gas flow rates and gas compositions; a minimal amount of sheath gas is necessary to avoid overheating of the torch. It is desirable to keep the costs of the used gases (Q1-Q3) as low as possible.
The addition of methane or ammonia to obtain a reactive atmosphere, in order to synthesise carbides and nitrides, should be possible without any hazards (an O_2 / H_2 mixture for example is not allowed). A drawback of these gases is the stronger

cooling of the plasma after introduction in comparison to Ar or N_2. This is not only caused by the higher specific heat, but also by the high amount of energy required for the dissociation (92000 and 69000 $kJ.kg^{-1}$ for methane and ammonia respectively to 34000 $kJ.kg^{-1}$ for nitrogen). Of course, the dissociation temperature has to be considered.
Since some of the criteria are counteracting, a trade-off has to be made. The best compromise was found to be the 3-12-80/6 composition.

Summary of 4.1.5
Several process parameters have been modelled and been evaluated on the residence time above 3500 K (boiling point of Si) and other criteria like costs, safety issues, …. The 3-12-80/6 plasma gas composition has been found to be the best compromise to be used in the nanoparticle synthesis. Of course, the plasma gas composition should be adjusted to the targeted particles, for example should N_2 be used instead of H_2 in the sheath gas if a non-reducing atmosphere is required.

4.2 Quenching design and optimisation

4.2.1 Goal of the quench modelling

Now the best compromise for the plasma gas composition has been found from the modelling, how can the size, size distribution and chemistry of the final products be tailored. The answer is found in controlling the temperature profiles of the seeded particles, by assuming that the evaporation process has no influence. By using quenching, which is the rapid cooling of the gas phase, the temperature profiles can be adjusted. If, for example, the temperature region where the particles sinter (ranging from melting point to approximately 60% of the melting point) could be crossed very rapidly, only soft agglomerates can be obtained (see section 2.7). Also the kinetics can be changed by quenching resulting in the synthesis of species which are not thermodynamically stable at room temperatures [52].

4.2.2 Quench gas efficiency

From the several options to quench, see section 2.6, the addition of cold gases has been chosen, because of its suitability and flexibility.
As the main purpose of quenching is the reduction of the plasma gas temperature, it is important to know how effective (temperature decrease per unit gas) the used quench gas can be. Figure 4-17 shows the calculated temperature as a function of the energy content of the plasma (3-12-80/6) for several quench gas flow rates. This figure gives an idea about the minimum temperature which can be achieved for a hypothetic case; immediate and perfect mixing of the plasma and the quenching gas and immediate heat transfer. The temperature is calculated by distributing the plasma energy over the total of the plasma and the quench gas.

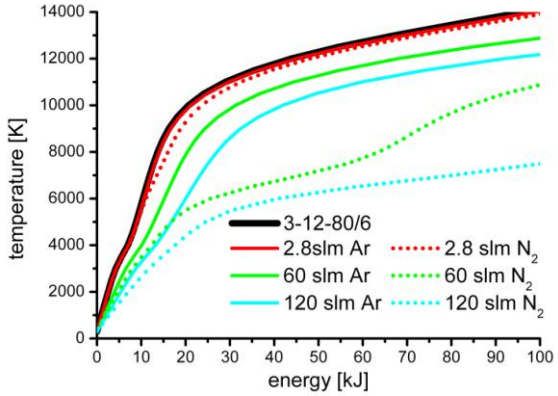

Figure 4-17: calculated temperature as a function of the energy content for different quench gas flow rates under assumption of perfect mixing and immediate heat exchange. Plasma gas: 3-12-80/6.

A stronger cooling with increasing quenching gas flow rate is predicted. Quenching with N_2 will lead to a stronger quench effect as compared to Ar. This is caused by the higher heat capacity of N_2, which will compensate for the lower mass flow as compared to a same gas flow rate of Ar. Especially at temperatures over 5000 K, where the N_2 starts to dissociate, the efficiency of quenching with N_2 becomes more pronounced. This can be seen by the larger temperature difference between the Ar and N_2 curve for same quench gas flow rates. The 60 slpm N_2 curve shows a steeper slope around 7000 K, because here the c_p of N_2 decreases and any additional energy will result in a faster temperature increase. This point for 120 slpm N_2 is beyond 100 kJ and therefore not visible in this curve.
Although N_2 is more effective than Ar (see Figure 4-17), it is not always better to quench with N_2; it depends on the nanoparticles that are synthesised and the quenching temperature. Whereas Ar is inert, N_2 can show some reactivity, especially at high temperatures (formation of N radicals due to dissociation of N_2).
It is to be expected that the assumed immediate heat transfer and perfect mixing will not occur. This will especially be observed at low quench gas flow rates, as a certain momentum density is required to penetrate the hot (plasma)gas. This aspect would (slightly) favour the use of Ar over N_2 as a quenching gas because of its higher density and therefore higher momentum density at the same gas flow rate.

The graph in Figure 4-18 shows the calculated plasma gas temperature (3-12-80/6) for different energy contents as a function of the Ar quench gas flow rate. The temperature has been calculated by dividing the available energy over the total gas distribution.

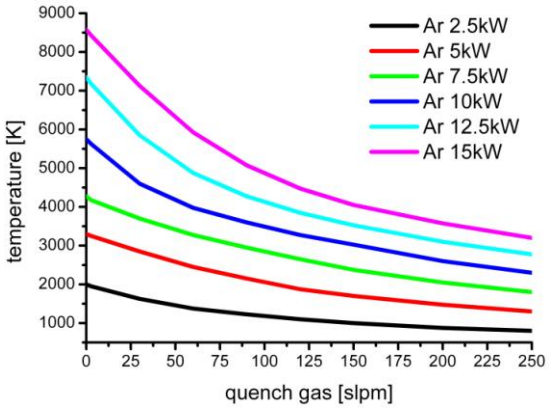

Figure 4-18: temperature of the plasma and quench gas mixture as a function of the quench gas flow rate for different energy contents. 0 slpm quench gas represents the pure plasma gas: 3-12-80/6.

The figure shows that the quenching efficiency is high for very low quench gas flow rates and when the quenching is carried out at high temperatures, which is shown in the gradients of the curves.

Table 4-6 presents the maximal quench rate as a function of the energy content of a 3-12-80/6 plasma gas composition (see Figure 4-18) under the assumption of ideal mixing and immediate heat transfer. It also shows the amount of quench gas required to reduce the temperature below 1000 K.

Table 4-6: maximum temperature, quench rate in $K.slpm^{-1}$, and quench gas flow to reach a temperature below 1000 K as a function of energy content of a 3-12-80/6 mixture at 101 kPa.

Energy content	T_{max} [K]	Quench rate Ar	slpm Ar T < 1000 K	Quench rate N_2	slpm N_2 T < 1000 K
2.5 kW	2000	20 $K.slpm^{-1}$	150	25 $K.slpm^{-1}$	100
5.0 kW	3300	20 $K.slpm^{-1}$	400	25 $K.slpm^{-1}$	275
7.5 kW	4275	35 $K.slpm^{-1}$	675	45 $K.slpm^{-1}$	450
10.0 kW	5750	45 $K.slpm^{-1}$	950	110 $K.slpm^{-1}$	625
12.5 kW	7350	65 $K.slpm^{-1}$	1175	265 $K.slpm^{-1}$	800
15.0 kW	8575	65 $K.slpm^{-1}$	1425	360 $K.slpm^{-1}$	950

The table confirms the data of Figure 4-17 and Figure 4-18; higher quenching rates can be achieved at higher temperatures and by using N_2 instead of Ar. The table also shows that although the quenching rate for N_2 at 8575 K is about 14 times than quenching at 2000 K, additional 850 slpm N_2 is required to reduce the temperature below 1000 K.
Although Figure 4-18 and Table 4-6 show that quenching is more effective at higher temperatures and with low quenching rates, it is not the main objective to reach a high quenching efficiency. It is the optimal temperature conditions for the particle growth after quenching (preferably no growth) and the amount of available quenching gas which are of major importance.

Summary of section 4.2.2
Quenching at higher temperatures is more effective than quenching at lower temperatures with the same quench gas flow rate. N_2 is a more effective quench gas than Ar, especially at high temperatures when the N_2 dissociation consumes a lot of energy. The advantage of Ar over N_2 is its inertness, particularly at high temperatures. The decisive question with respect to the quenching is the (desired) final temperature and how the residence time evolution will be like as a function of the temperature.

4.2.3 Modelling of the quench design

4.2.3.1 Two-nozzle system

The previous section showed us that the targeted temperature after quenching is the decisive question for where to quench. The next question is with what kind of device the hot gas will be quenched in the best way.
The first quenching design was a two-nozzle system (Figure 4-19). The nozzles had a 4 mm inner and a 6 mm outer diameter. The distance between the nozzle exits amounted 100 mm.

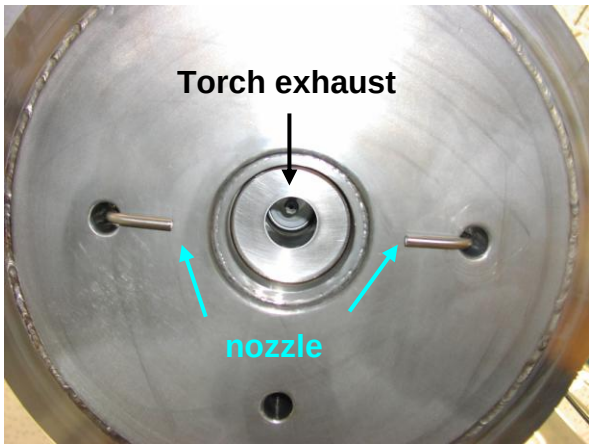

Figure 4-19: top view of the two-nozzle system.

Figure 4-20 compares the results of a 3D model to a real plasma. The 3D model only described the part of the reactor within a 35 mm diameter. The inlet boundaries conditions for the 3D models were obtained from the mass flux, temperature, and mass fraction profiles at z = 0 mm as calculated by the 2D model (5-27-80/6, 10 kW net power input, 40 kPa).

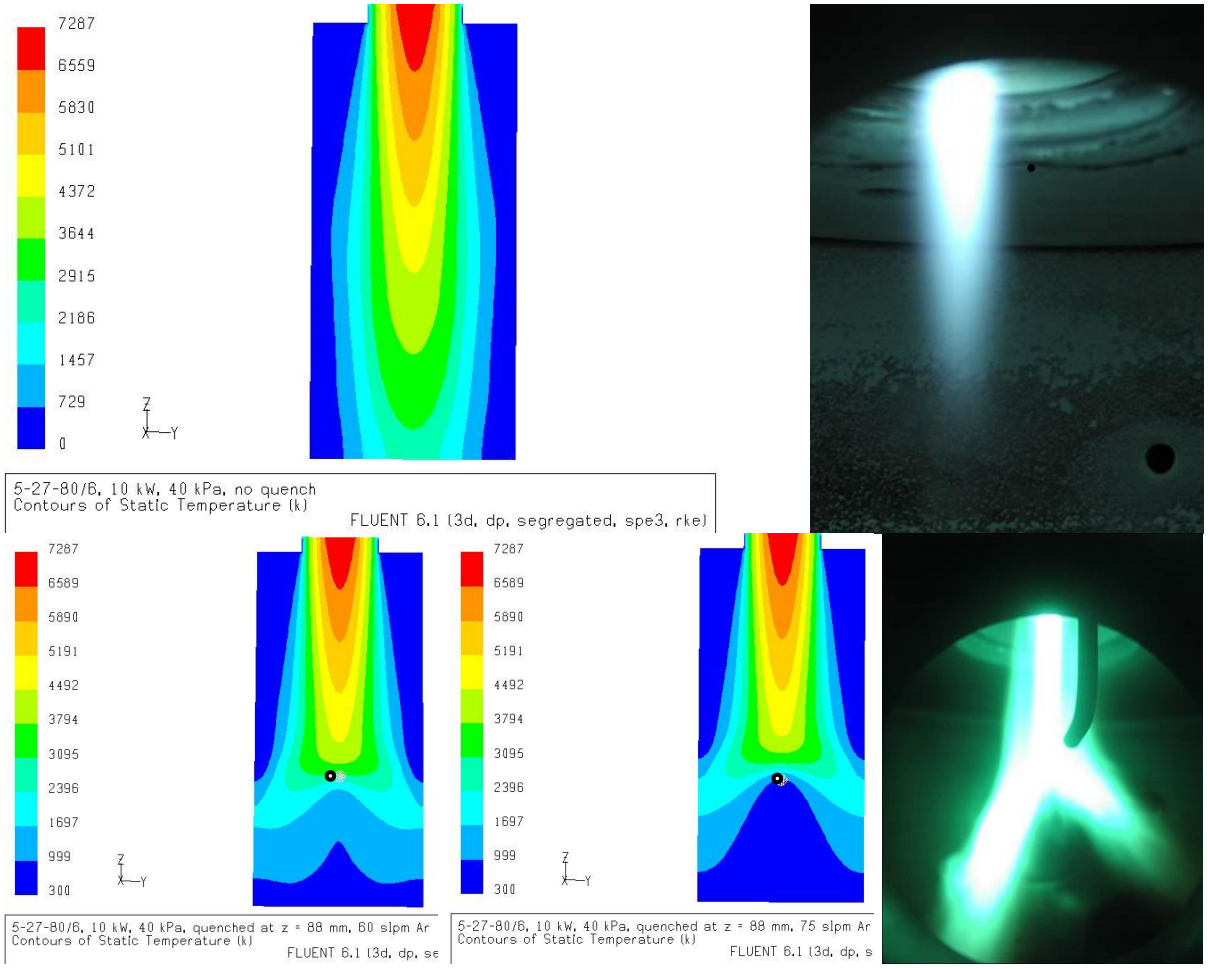

Figure 4-20: Top left: 3D model without quenching. Top right: plasma without quenching. Bottom left and middle: 3D model, quenched with 60 and 75 slpm Ar at z = 88 mm. Bottom right: plasma quenched with 56 slpm at z = 88 mm (2 x ϕ 4 mm nozzles), the second nozzle is behind the plasma (not visible). 3D inlet boundary conditions obtained from 2D model (5-27-80/6, 10 kW, 40 kPa) at z = 0 mm. The black spot in the CFD images represents the nozzle position. Plasma conditions (5-27-80/6, 15.6 kW plate power, 40 kPa).

As already shown in the previous section 4.1, the current heat source model is able to predict and describe the trends very well outside the torch, which is confirmed by Figure 4-20. The model predicts a comparable behaviour with increasing quench gas flow rate as for the real plasma. The a-symmetry in the right photograph is caused by a small misalignment of the two nozzles. This picture also shows that a two-nozzle design is not suitable to obtain a homogeneous temperature distribution, since the plasma is split in two tails where the temperature is not cooled efficiently.
The quantitative agreement, in the sense of quench gas flow rates, is not as good as the qualitative agreement. The modelled quench flow rate amounts 60 - 75 slpm Ar to obtain a splitting of the plasma as compared to 56 slpm for the real plasma. The model overestimates the actual required quench gas rate by about 30%. There are three factors contributing to the overestimation of the quench gas flow rates by the 3D model.
Of course there are some errors introduced by the assumptions and simplifications of the model itself, which contribute to this difference. The plasma radiation for example, has been neglected and would lead to a lower temperature and therefore easier quenching.
Furthermore is the gas entrainment from the environment, as a consequence of the turbulence at the edges, not taken into consideration. The entrainment results in additional cooling of the plasma, which makes quenching easier.
The plasma is modelled as being stable and non-fluctuating, which is in reality not the case [165]. During the experiments the plasma power is fluctuating (maximal 3%) and therefore not always as hot and viscous as for steady operation.

Summary of section 4.2.3.1
A two-nozzle system is not the best way to quench a hot plasma gas with respect to the nanoparticle synthesis, since the plasma is divided in two hot tails, which does not allow homogeneous cooling.
The “heat source” model has proven its ability to predict and reconstruct observed phenomena occurring during quenching. The quantitative agreement of the model is not as good as the qualitative agreement and overestimates the actual gas flow by about 35%.

4.2.3.2 Ring design

As the two-nozzle quenching shows a strong inhomogeneous temperature profile, quenching by means of a multi-nozzle design was applied. The following describes the contemplations and approach to optimise the geometry. Some parameters of the design are the number and size of the nozzles.

Under assumption of a constant surface for the quench gas outlet, the amount of nozzles is a trade-off between the penetration depth (defined here as the distance that the maximal velocity is kept upright) and the momentum density (ρv^2). The number of nozzles will be a compromise and lies somewhere between the two extremes: a single nozzle (strong penetration) and a slot (good radial homogeneity of the quench gas flow). This is further explained in Figure 4-21 in which the momentum of a 4 mm diameter nozzle is compared to that of a 1.5 mm diameter nozzle. The first comparison corresponds to a situation in which both quench rings have an equivalent surface area (e.g. 9 x ϕ 4 mm and 64 x ϕ 1.5 mm nozzles), thus the gas at each nozzle has the same velocity at the nozzle exit for a constant total flow rate. The second case represents the case in which both rings consist out of the

same number of nozzles and have the same flow rate flowing through each nozzle (e.g. 9 x ϕ 4 mm and 9 x ϕ 1.5 mm nozzles). The radial profiles of the momentum at 0, 25, and 75 mm from the nozzle exit are shown.

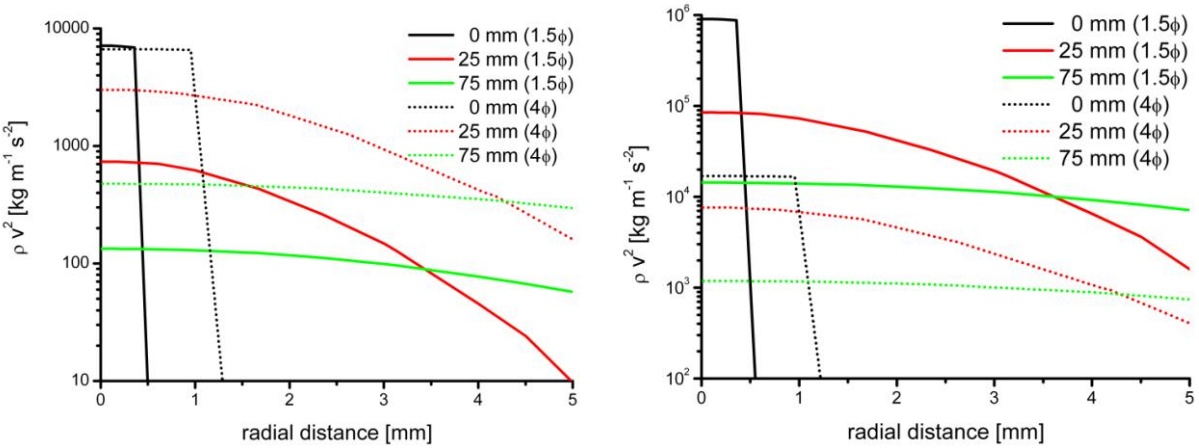

Figure 4-21: comparison of the modelled (3D) momentum density of a 4 mm diameter nozzle to a 1.5 mm diameter nozzle as a function of the radial distance for different axial distances: 0 (nozzle exit), 25, and 75 mm from the nozzle exit. Left: for equivalent surface (9 x ϕ 4 mm and 64 x 1.5 ϕ mm). Right: for equivalent number (9) of nozzles.

Thus, a small nozzle has a high velocity and therefore a high momentum, but a low penetration depth and vice versa for a large nozzle.
It is shown that the momentum is decreasing over the distance, especially for small nozzles. This will favour the use of large nozzles. On the other hand a certain amount momentum is necessary to penetrate the plasma, which favours smaller nozzles because of their higher velocity compared to larger nozzles (same flow rate per nozzle) and therefore higher momentum.
Thus depending on the nozzle-plasma distance, required momentum, and available flow rates, the number and size of the nozzles have to be chosen.

If the homogeneity of the temperature profile has to be considered as well then more nozzles are favourable. In which more nozzles will eventually end up in a slot and result in a more homogeneous temperature distribution, see Figure 4-22.

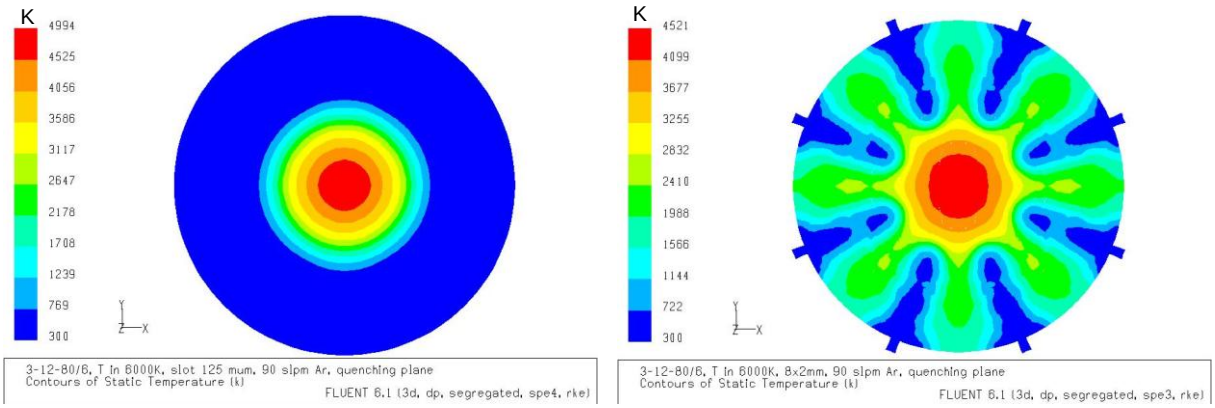

Figure 4-22: comparison of a 3D model of a ring (slot width 125 µm) to a 3D model of an eight-nozzle (ϕ 2 mm) quench ring. The surface of the quench gas outlet and nozzle – axis distance (32 mm) is the same in both cases. Modelled parameters: homogeneous gas mixture of 3-12-80/6 at 40 kPa with an inlet temperature of 6000 K, quenched with 90 slpm Ar at the same position.

The slot results in a homogeneous temperature distribution, whereas the eight-nozzle ring shows the presence of regions where hot gas flows in between of two adjacent cold jets. On the other hand, the eight-nozzle ring shows a lower maximum temperature. So there is a trade-off between homogeneity and efficiency, which determines the number and size of the quench nozzles.

From these observations, several ring designs, 8 x ϕ 2 mm and 8 x ϕ 1.5 mm (with and without an axial angle) were subject to more modelling. The top graph in Figure 4-23 shows the modelled temperature along the axis as a function of the quench flow rate, whereas the right side shows the axial velocity for the same conditions for an 8 x ϕ 2 mm quench ring. The region from z = -50 to 500 mm is zoomed in additionally, in which z = 63 mm is marked with a straight solid line.

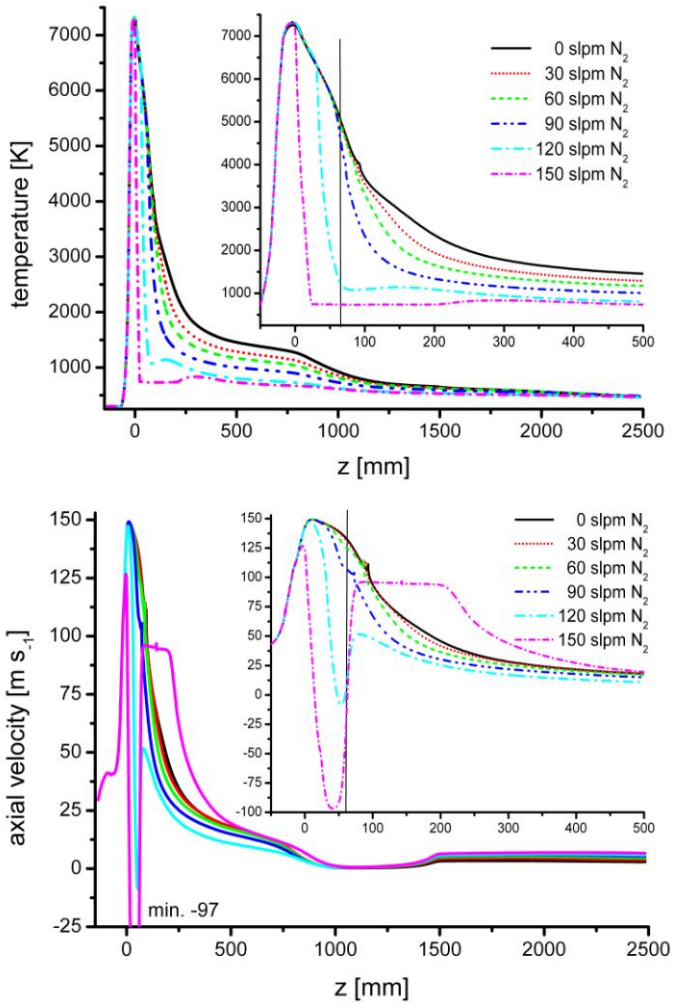

Figure 4-23: top: modelled temperature as a function of the axial position and bottom: modelled axial velocity as a function of the axial position for different quench gas flow rates. Modelled (2D) plasma parameters: 5-27-80/6, 40 kPa, 10 kW, quenched at z = 63 mm (quench surface equivalent to 8 x ϕ 2 mm → slot height of 0.125 mm at a 32 mm radius).

The behaviour of the temperature profile is straight forward; a lower temperature is obtained with an increased quench gas flow rate. However, it is more complicated for the velocity profile.
The behaviour of the velocity profile is dependent on the quench gas flow rate. As the quench gas rate increases the velocity of the plasma gets more and more disturbed. At a certain point, the quench gas (around 120 slpm N_2) will become so

powerful that the plasma stream is pushed back, expressed by a negative axial velocity.
The peak in the velocity curve is caused by a small jump in the density function at 4000 K, which is artificial (a jump in the interpolation of the density of Ar).
The situation gets more complicated around the quenching position with increasing quench gas flow rate, because of the appearance of a “dip” in the velocity profile. This “dip”, indicating a decreased velocity, is positioned above the quenching point (lower z). These decreased axial velocities, when quenched with 120 and 150 slpm N_2, are explained by the ring symmetry of the quench design. As the quench gas from one side collides with quench gas from the opposite side, it flows partially upward and downward. This upward flow of the quench gas is directed opposite to the plasma and decelerates the plasma. The stronger the quench gas collides in the middle of the ring, the stronger the upward flow gets and the more pronounced the deceleration gets and even results in a change of direction (see 120 and 150 slpm). This is the case for higher quench gas rates and cooler plasma (higher z value or deeper quenching position).
Figure 4-23 shows the presence of an optimal quench gas flow rate between 90 and 120 slpm (5-27-80/6H_2, 10 kW net power input, and 40 kPa). In which optimal means that the pathlines along the axis do not change direction and do not decelerate too much in order to keep a short residence time, but encounter a high temperature gradient.
This optimal quench gas flow rate is a function of pressure, plasma gas flow rate and composition, and of the temperature (quenching height).
Figure 4-24 compares the actual gas trajectory to the trajectory along the axis for quenching with 120 slpm. In case the gas would not be disturbed by the quench gas, the actual tracer trajectory and the trajectory along the axis would be the same. The x-axis in the right figure is the path length and is defined as the actual length along the trajectory. Only in case the trajectory goes along the axis the z value is equal to the path length.

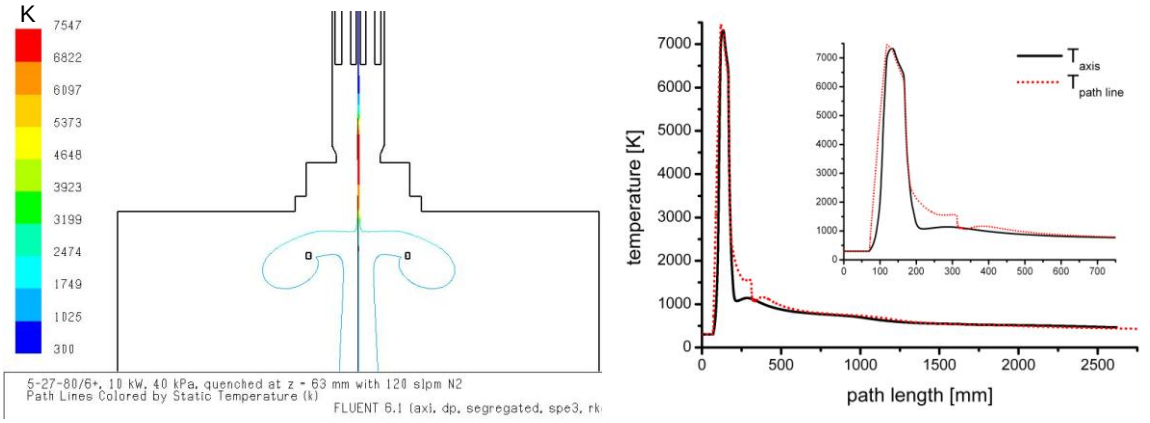

Figure 4-24: comparison of the particle trajectories between a tracer released from the precursor inlet for 120 slpm N_2 quenching and a particle which travels along the axis. Right: comparison of the temperature profiles along these trajectories. Region between z = 0 – 750 mm is zoomed additionally. Modelled conditions: 5-27-80/6, 10 kW, 40 kPa, quench position z = 63 mm (8 x ϕ 2 mm) with 120 slpm N_2.

Figure 4-24 shows a difference between the actual trajectory and the ideal trajectory (along the axis), with respect to temperature and path length. The actual trajectory takes the gas around the quenching nozzles and results in a less controlled cooling and will also travel a longer way in comparison to the trajectory along the axis.

This will influence the final particle size, as will be shown in section 4.3.4.4. The particle following the trajectory around the nozzle will spend a longer time in a temperature zone in which sintering occurs. Thus the particles will get larger, before they reach the end of the synthesis chamber. Figure 4-25 compares the temperature profiles for quenching with 90 and 120 slpm N_2. Although the left graph in Figure 4-25 seems to suggest that quenching with 120 slpm N_2 is better when the temperature profiles are regarded as a function of z. However, it is the opposite when the two are compared versus the residence time. When the temperature profiles along the trajectories are compared to each other, it is the residence time in a distinct temperature region which is decisive and not the path length, since the growth processes are governed by time and not by distance.

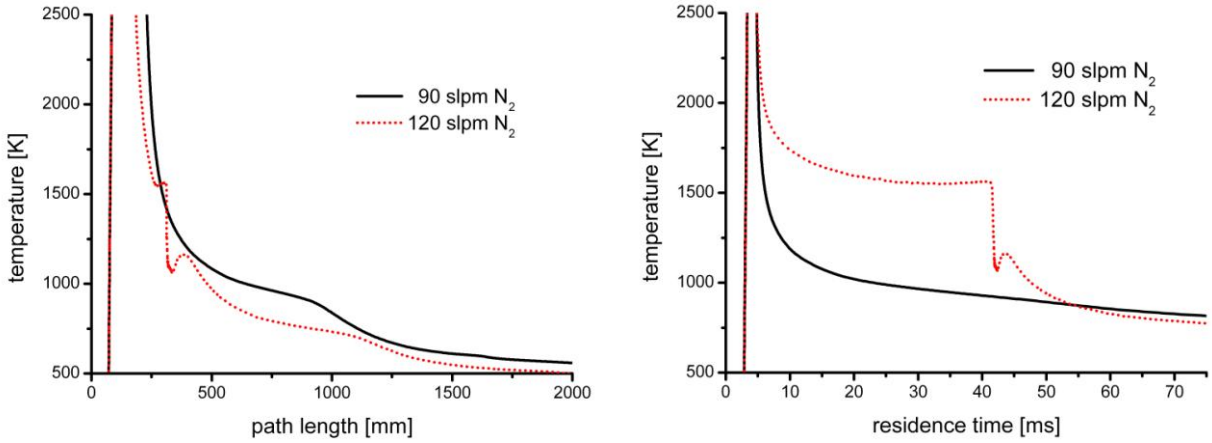

Figure 4-25: temperature as a function of the path length (left) and residence time (right) for 90 and 120 slpm N_2 quench gas. Modelled parameters (2D): 5-27-80/6, 40 kPa, 10 kW, quenched at z = 63 mm (surface equivalent to 8 x ϕ 2 mm).

Figure 4-26 represents the results of Figure 4-23 by showing the temperature and velocity profiles in contour plots for 5-27-80/6, 40 kPa, 10 kW as a function of the quench gas flow rate.

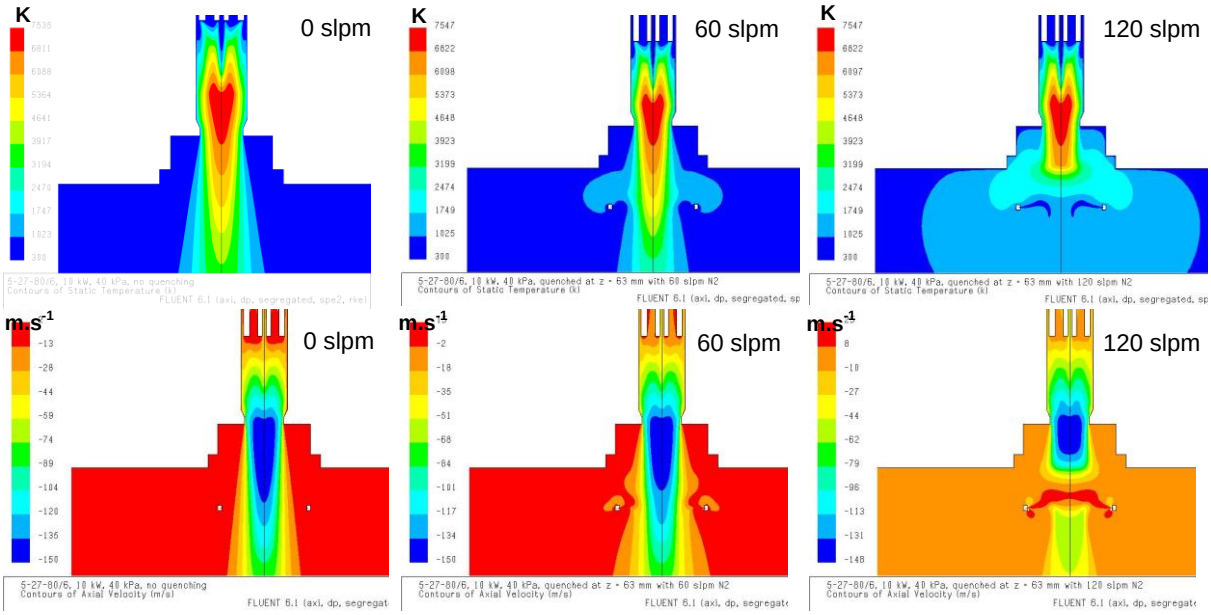

Figure 4-26: top: modelled temperature profiles. Bottom: modelled axial velocity profiles. From left to right: quench gas flow rate 0, 60, and, 120 slpm N_2 respectively. Parameters (2D): 5-27-80/6, 40 kPa, 10 kW, quenched at z = 63 mm (surface equivalent to 8 x ϕ 2 mm)

The value of 120 slpm quenching gas is too high to maintain an ideal (gas) flow, which would result in homogeneous trajectories for all particles, as already shown in Figure 4-24 and Figure 4-25. The quench gas causes the plasma gas flow to stagnate and forces the plasma gas flowing around the ring (the entire region within the quench ring has a velocity which is directed opposite to that of the plasma).

With respect to controlling the temperature profiles not only the quench gas flow rates are of great importance, also the quenching height is a very important parameter. The quenching height, which is determined by the temperature and the energy content of the plasma, will influence the minimal final temperature that can be reached after quenching (the plasma temperature is decreasing with increasing z).
Figure 4-27 shows the influence of the quenching height on the plasma's temperature and velocity profiles.

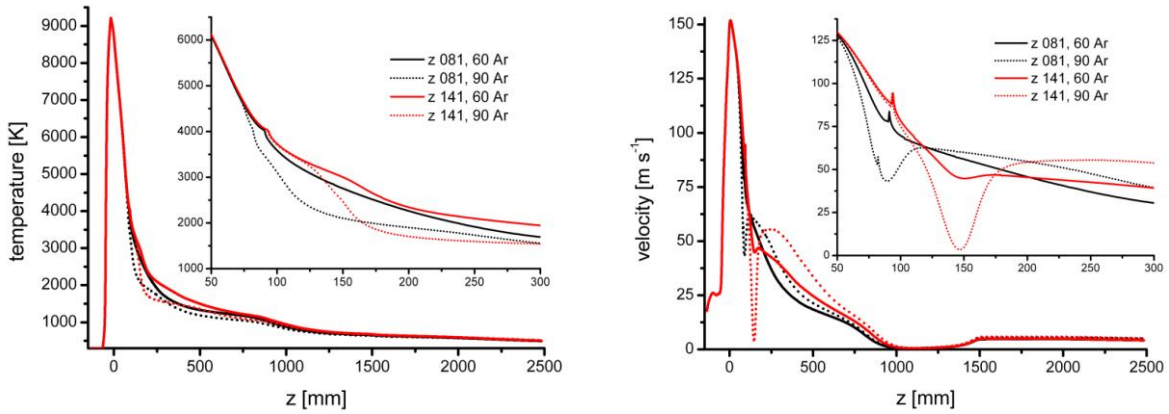

Figure 4-27: modelled temperature (left) and axial velocity (right) as a function of the axial position for different quenching heights. Modelled (2D) parameters: 3-12-80/6, 40 kPa, 10 kW, 8 x ϕ 1.5 mm, 15° angle in positive z-direction.

The temperature curve versus z shows that lower temperatures can be achieved by quenching with a higher quench gas flow rate. Furthermore, the temperature gradient for quenching at z = 81 mm is much steeper than at z = 141 mm. The maximum quench rate for quenching at z = 81 mm amounts $10x10^4$ $K.m^{-1}$ for 60 slpm Ar and $17x10^4$ $K.m^{-1}$ for 90 slpm to $6.9x10^4$ $K.m^{-1}$ and $7.3x10^4$ $K.m^{-1}$ at z = 141 mm for 60 and 90 slpm Ar respectively.
Quenching with 90 slpm Ar results in a better penetration at z = 141 mm, since the velocity profile shows a stronger decrease (axial velocity close to 0) as compared to z = 81 mm. A value of the axial velocity of 0 means a complete cutting of the plasma. The position of the minimal velocity also points out a stronger quenching effect for z = 141 mm. The minimum is positioned 9 mm below the quench gas outlet at z = 81 mm and only 6 mm at z = 141 mm. The velocity minimum is a consequence of the quench jet momentum and of the cooling effect of the quench gas (contraction of the gas). The presence of the small peak in the velocity at 4000 K is an artefact due to a small jump in the Ar density.
A conclusion which can be drawn from the results of the CFD is that there is a maximum quench gas flow rate with respect to the controlled trajectories.

From the considerations on nozzle number and diameter, two quench rings were constructed. The first ring consisted out of eight nozzles (ϕ 2 mm, equivalent to the surface of the two-nozzle system) which were divided symmetrically over the ring and were positioned perpendicular to the plasma jet. The ring itself had a 64 mm

diameter and was made of a hollow tube with a 12 mm outer diameter and an 8 mm inner diameter (see Figure 4-28 left photograph).
A second quench ring was constructed and consisted out of eight nozzles as well, with a 1.5 mm diameter, which had a 15 °angle directed downstream. The quench ring, which had a modular construction for simple replacing of the nozzle inserts, had a 124 mm outer and a 64 mm inner diameter. The total height of ring amounts 24.5 mm and the centre of the 1.5 mm diameter nozzles is positioned at 10.5 mm from the bottom of the ring (see Figure 4-28 right photograph).
A tangential component or swirl would be beneficial to get rid of the “hot fingers” as shown in Figure 4-22, but has the disadvantage that the middle of the plasma jet can not be reached and therefore not cooled. The extent of these effects depends on the swirl angle.

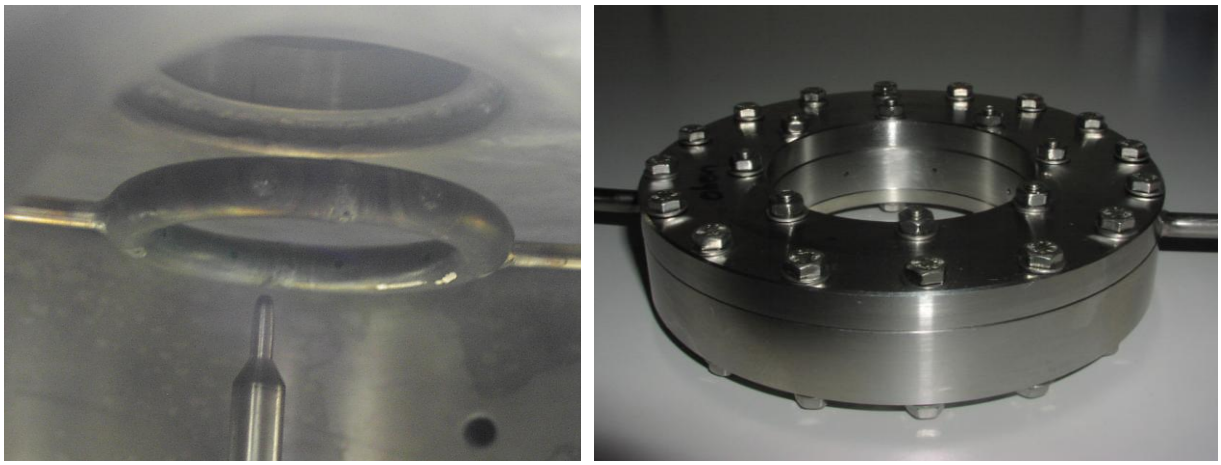

Figure 4-28: left: eight-nozzle quench ring (8 x 2 mm) with enthalpy probe tip just below the ring. Right: eight-nozzle quench ring (8 x 1.5 mm, angled).

The angle of the nozzles with respect to the plasma axis was expected to give a small “water jet pump” effect, resulting in a more directed plasma flow and allowing the use of a higher quench gas flow rate before the plasma is pushed back, see Figure 4-29.

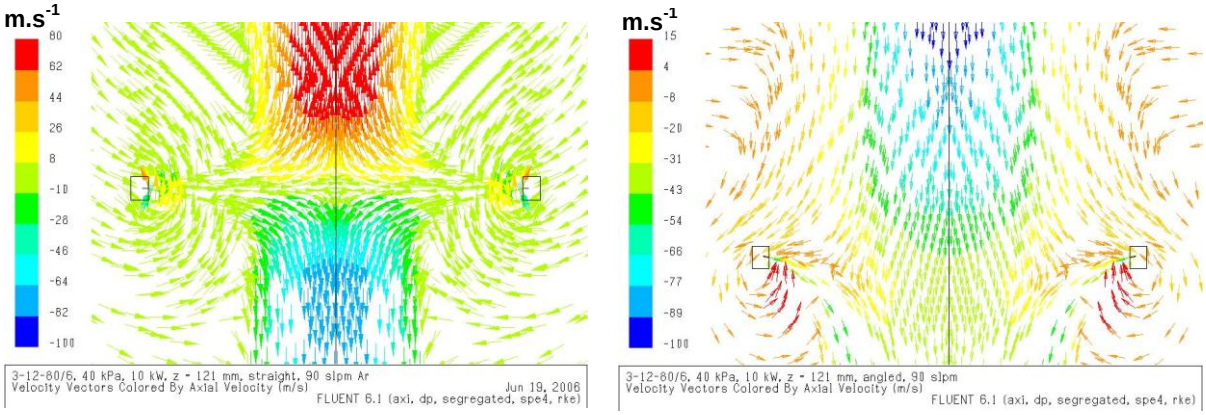

Figure 4-29: 3-12-80/6, 40 kPa, 10 kW quenched at 121 mm with 90 slpm Ar. Left: 8 x ϕ 1.5 mm straight. Right: 8 x ϕ 1.5 mm angled.

The results, for the same conditions, show that in case of straight nozzle configuration (first design) the plasma is completely penetrated, whereas it is not the case for the angled nozzle configuration (second design). In which the latter has a more controlled gas flow with respect to the residence time of the trajectories.

The photographs in Figure 4-30 and Figure 4-31 show the two different quench ring designs under plasma conditions and different quench gas flow rates.

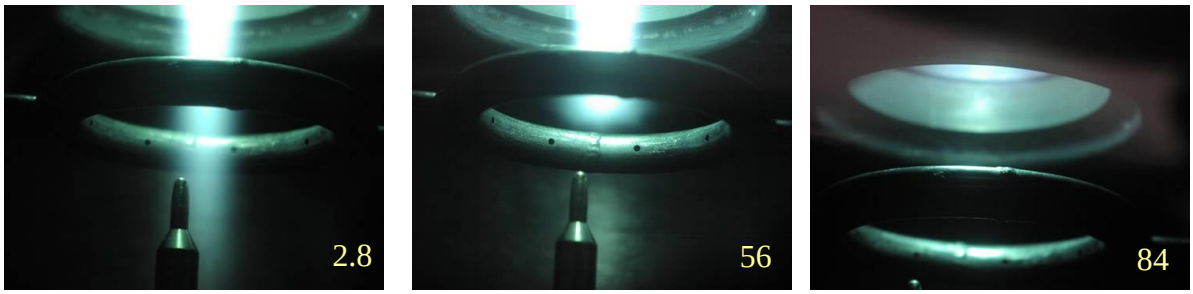

Figure 4-30: from left to right. Plasma (5-27-80/6, 15.6 kW plate power, 40 kPa) with increasing amount of Ar quenching gas respectively. Position quench ring (8 x ϕ 2 mm): z = 88 mm.

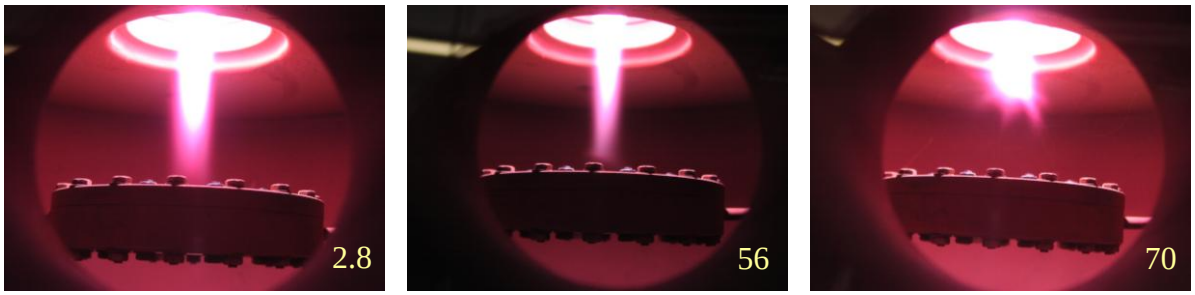

Figure 4-31: from left to right. Plasma (3-12-80/6, 15.6 kW plate power, 40 kPa) with increasing amount of Ar quenching gas respectively. Position quench ring (8 x ϕ 1.5 mm, 15° angle): z = 121 mm.

These figures show the upward shifting of the plasma as has been predicted by the model, which is shown in Figure 4-23 and Figure 4-26. The right photograph in Figure 4-31 also shows the presence of “hot fingers”, which were also predicted and shown in the model (Figure 4-22 right).

In the current work it has not been attempted to obtain a turbulent quenching as being described in a patent of Boulos et al. [52]. In this patent, an ICP process (PL-35 torch) was used to produce nano TiO_2. A multi-nozzle ring (16 x ϕ 1.5 mm) with a tangential component was used to inject 225-375 slpm Ar, in order to reduce the temperature of the plasma gas by gas quenching. The stagnation point of the plasma, caused by colliding with the quench gas, causes a deflection of the gas flow. The plasma gas is then mixed in recirculations with the vast amount of quench gas, see Figure 4-32. The result is cooling and dilution of the plasma gas and the formed nanoparticles.

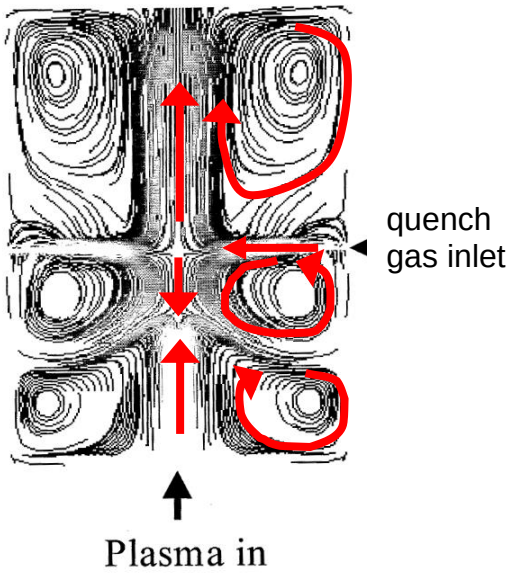

Figure 4-32: recirculations caused by the introduction of a vast amount of quenching gas. The recirculations result in a cooling and dilution of the plasma gas and formed nanoparticle. The arrow at the right represents the axial position of the quench gas inlet. Source: Patent WO2004 052778, by Boulos et al. [52].

Furthermore, a large quench gas flow rate will result in pushing the plasma back into the torch (see Figure 4-30), which will have a negative effect on the life-time of the torch.

In order to guide the plasma through the ring and avoid deflection of the plasma gas around the quench ring, a funnel has been placed on top of the quench ring (Figure 4-33). The funnel has an 84 mm diameter at the top and a 44 mm diameter at bottom. The funnel is 40 mm high and its bottom is positioned at 15.5 mm above the ring bottom. The effect will be demonstrated in Figure 5-13 (page 126) when Si is introduced in the plasma.

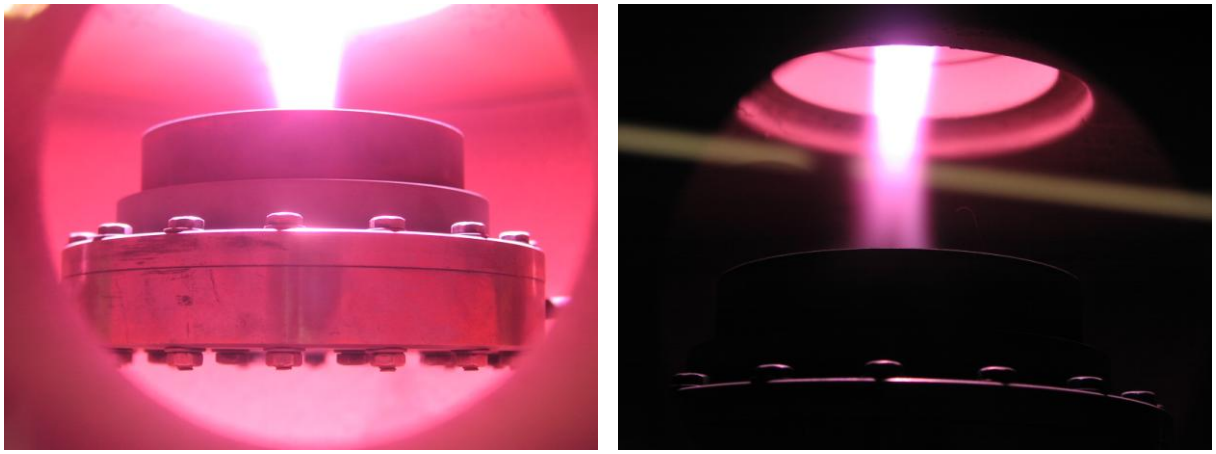

Figure 4-33: left: plasma without particles quenched with 2.8 slpm Ar. Right: plasma without particles quenched with 56 slpm. Plasma parameters: 3-12-80/6, 40 kPa, 15.6 kW plate power, quench ring at z = 121 mm (8 x ϕ 1.5 mm, 15° angle).

Summary of section 4.2.3.2

The choice of the nozzle size and number in a quench ring is dependent on the required momentum and on the desired homogeneity of the temperature distribution. Although a slot results in a more homogeneous temperature distribution, it could be

better to quench with a few nozzles since then a better quenching effect (better penetration as a consequence of the higher momentum) can be achieved.
The heat source model has shown that, under a certain threshold quench flow rate, the gas flow remains “undisturbed” and the temperature decreases along the axis with increasing quench gas flow rate.
At a quench flow rate above the threshold value this is not the case. The temperature decrease along the axis becomes larger, but the gas flow becomes disturbed and follows uncontrolled trajectories. Therefore, a high quench gas flow rate (120 slpm Ar for the current conditions) is not always beneficial with respect to the temperature and velocity distribution within the synthesis chamber. Besides the quench gas flow rate also the quench height plays an important role on the final temperature. Quenching at lower temperatures (higher z value) is more effective.
The introduction of a funnel has a positive effect on the particle dispersion, within the synthesis chamber from an optical point of view, compared to the two-nozzle and eight-nozzle ring (without funnel) quenching, as will be shown in Figure 5-13.

4.2.4 Experimental validation of the quench modelling

The quenching model has been validated quantitatively using the enthalpy probe (see section 3.5.1) coupled to a mass spectrometer. The latter has been calibrated by measuring the gas phase composition of a well defined Ar / H_2 (95 / 5 vol%) mixture which is close to the H_2 concentration of the used plasma gas compositions.

Figure 4-34 shows the measured enthalpy, at z = 75 mm, as a function of the radial distance for different quench gas flow rates and plate powers.

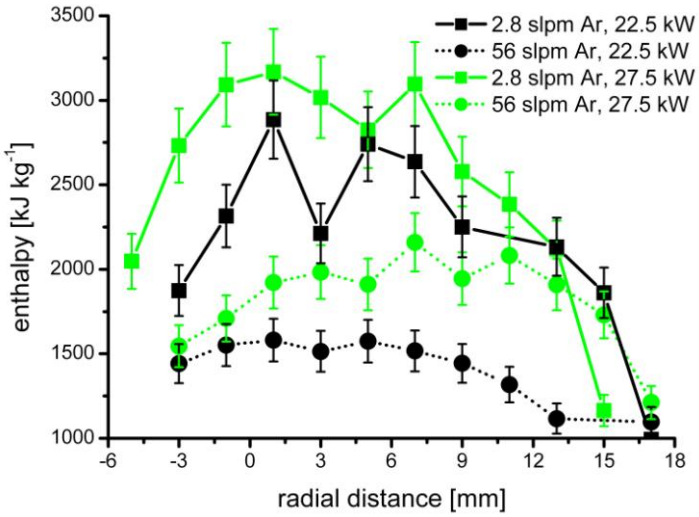

Figure 4-34: measured enthalpy as a function of the radial distance for different quench gas flow rates and plate powers. Plasma parameters: 5-27-80/6, 40 kPa, quench ring (8 x ϕ 2 mm) at z = 63 mm. Enthalpy probe tip at z = 75 mm.

This figure shows that the enthalpy increases with plate power. Increasing the quench gas flow rate reduces the enthalpy.

Figure 4-35 shows the enthalpy of the plasma / quench gas mixture after quenching as a function of the radial distance for different quench gas rates and compositions.

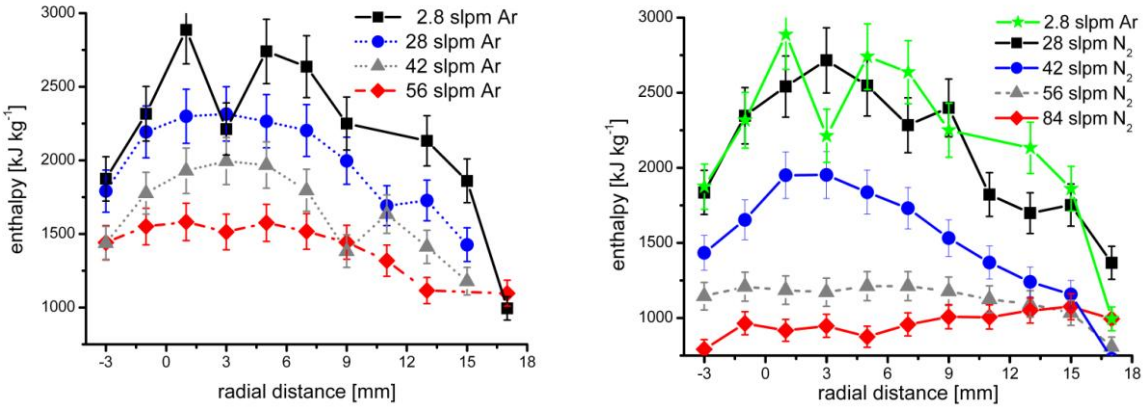

Figure 4-35: measured enthalpy as a function of the radial distance for different quench gas flow rates. Left: Ar and right: N_2. Process parameters: 5-27-80/6, 40 kPa, eight-nozzle quenchring (8 x ϕ 2 mm) positioned at z = 63 mm, enthalpy probe tip at z = 75 mm. In the 2.8 slpm Ar curve, the 3 mm point seems to be an outlier.

For the current investigated process conditions a penetration of the plasma tail can be achieved by a quench flow rate of 28 slpm Ar (Figure 4-35). The criteria for penetration have been set to be a strong deviation (15%) from the "zero" quenching (2.8 slpm Ar) case and a flattening of the profile.
Applying such criteria in the N_2 quenching case is more difficult. Although the enthalpy for 2.8 slpm Ar and 28 slpm N_2 are almost the same, their temperatures are very different. An enthalpy of 2850 $kJ.kg^{-1}$ represents a temperature of circa 4400 K for Ar, while the same enthalpy results in a temperature of 3950 K for N_2. This difference is due to the higher enthalpy for N_2 in comparison to Ar.
So a value of slightly more than 28 slpm N_2 can also be regarded as being enough to enable penetration of the plasma.
A complete penetration is assumed when the measured enthalpy profile becomes flat, which is by 56 slpm N_2 and over 56 slpm for Ar. It is also shown that the N_2 is more effective than Ar to reduce the temperature at 56 slpm. The temperature of such a homogeneous plasma gas - N_2 mixture amounts 2000 K, while that for 56 slpm Ar amounts 3000 K.

Figure 4-36 shows the relative volume fraction of N_2 (measured concentration divided by initial concentration) for different quench flow rates as a function of the radial distance (measured at z = 75 mm), which gives information about the mixing of the quench gas with the plasma gas.

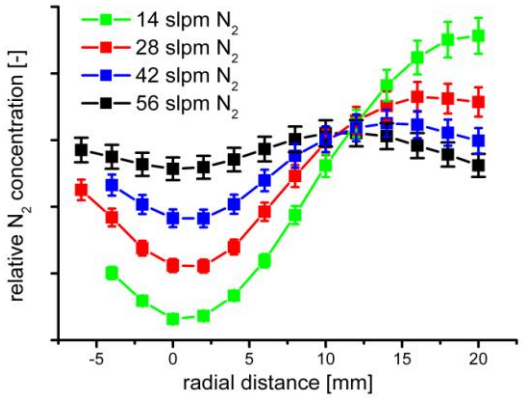

Figure 4-36: normalised N_2 concentration as a function of the radial position for different N_2 quenching gas flow rates. Plasma parameters: 5-27-80/6, 40 kPa, eight-nozzle quench ring (8 x ϕ 2 mm) positioned at z = 63 mm, concentration measured at z = 75 mm.

The curves show flatter profiles for increased quench gas flow rates. The flattening is caused by the better penetration and therefore better mixing of the plasma with the quench gas. Furthermore, the maximum of the N_2 concentration is shifted further to the axis with increasing quench gas flow rates. The maximum is positioned at the axis when the plasma is totally penetrated.

Figure 4-37 shows the modelled enthalpy and normalised N_2 concentration calculated at z = 75 mm as a function of the radial position for different N_2 quench gas flow rates for a 5-27-80/6 plasma gas composition. The quenching ring (8 x ϕ 2 mm, diameter 64 mm) was positioned at z = 63 mm.

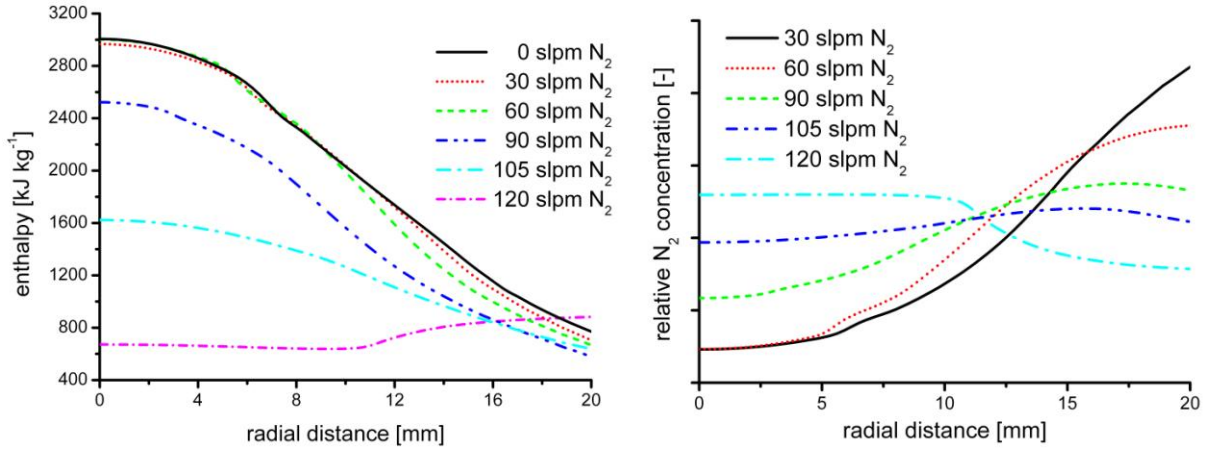

Figure 4-37: left: modelled enthalpy profiles and normalised concentration (right) as a function of the radial distance for different quench gas flow rates as calculated at z = 75 mm. Modelled parameters (2D): 5-27-80/6, 10 kW, 40 kPa, quenched at z = 63 mm (equivalent to 8 x ϕ 2 mm).

If the results of Figure 4-37 are compared to those of Figure 4-35 a good qualitative agreement is achieved. The enthalpy is reduced when the quench gas flow rate is increased and the concentration profile of the quench gas in the total mixture is flattening for an increased quench gas flow rate.
Although the model gives a good description of the experimentally observed trends, the quantitative agreement is a factor 2 off. Besides the factors already mentioned previously (assumptions of the model, gas entrainment, and plasma instability) to explain this difference, two additional factors can be introduced. First, there are errors introduced by the enthalpy probe measurements. Another factor is introduced when the modelling is carried out in 2D. The 2D model represents the eight nozzles in a slot equivalent, which has a lesser penetrating efficiency than a nozzle. This means that the actual required quench flow rate is lower than calculated by the model.

Figure 4-38 shows the influence of the inlet temperature on the 3D model. To reduce the central processing unit (CPU) time only the synthesis chamber has been modelled in 3D. The inlet boundary condition is the homogeneous mixed 3-12-80/6 composition. The temperature is set to 4500-6000 K with the velocity obtained from the 2D model at these temperatures. Quenching at different temperatures is meant to represent quenching at different heights.

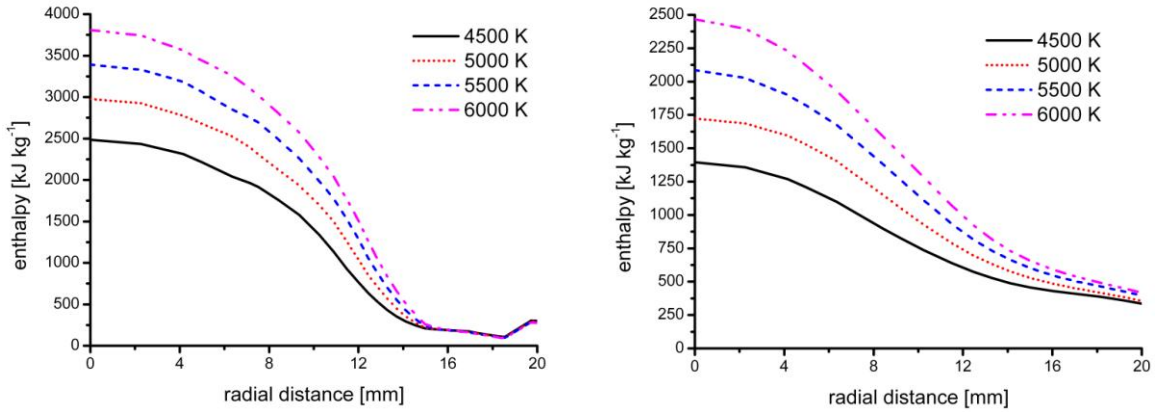

Figure 4-38: modelled enthalpy distribution at the quenching plane (left) and 12 mm below the quenching plane (right) as function of the inlet temperature along the line between two nozzles. Modelled parameters (3D): 3-12-80/6, 60 slpm Ar quenching gas, 8 x ϕ 2 mm and 40 kPa.

The enthalpy decreases as a function of the radial distance and as a function of the inlet temperature. The temperature is reduced for 6000 K inlet to 4160 K and for 4000 K to 2840 K. A higher efficiency (temperature reduction) is found for quenching at high temperatures. But if the desired temperature after quenching, for example, should be below 3000 K then the only possible way to achieve this is to wait until the plasma temperature is around 4000 K. It should be kept in mind that this statement about the optimal quench temperature is not a general one. It is depending on the process parameters (including quench design and quench gas flow rate), but also on the physical properties of the synthesised (nano)particles.

Summary of section 4.2.4

The heat source model is able to predict and confirm the trends found with enthalpy probe measurements with respect to the quenching process; a decreasing enthalpy with increasing quench gas flow rate. There is however a significant difference between the modelled (2D) and measured quench gas flow rate required to penetrate the plasma. The modelled (2D) flow rates are higher than the actual required flow rates. The difference between the model and the measurements are caused by the assumption of a surface equivalent slot instead of nozzles, the plasma having no entrainment and being stable without fluctuations, the inlet boundary conditions for the 3D model (obtained from the 2D model).

The optimal quench conditions are a function of the process parameters, quench design, quench gas flow rate, and the physical properties of the synthesised (nano)particles.

4.2.5 3D modelling of the quench design

As it is not possible to model quench rings with different numbers of nozzles in 2D (two nozzles become two slots), 3D models were made. These 3D models compared the effectiveness for different quench geometries (different nozzle number and diameter). The n umbers and diameters of the nozzles were picked to result in an equivalent surface of 2 x ϕ 4 mm (2.51×10^{-5} m^2).

Although the slot and the eight-nozzle configuration give the same result when they are modelled in 2D, they are quite different when modelled in 3D; the 2D model is not able to show the “hot fingers” (Figure 4-22).

Figure 4-39 shows the 3D models of several quench systems with equivalent quench surface (2 x ϕ 4 mm) for the same process conditions. The graphs are iso-altitude

cuts taken at the quench plane (qp) and 12 mm below the quench plane (qp+12). The input parameters were a homogeneous mixture of 95 slpm Ar and 6 slpm H_2 (3-12-80/6) with an inlet temperature of 6000 K and a velocity of 126 $m.s^{-1}$. Quenching took place at 50 mm below the inlet with 90 slpm Ar quench gas. These parameters were estimated from the 2D model. The distance of the nozzles to the centre amounts 32 mm in all cases.

quench plane	12 mm below quench plane	nozzle number and diameter
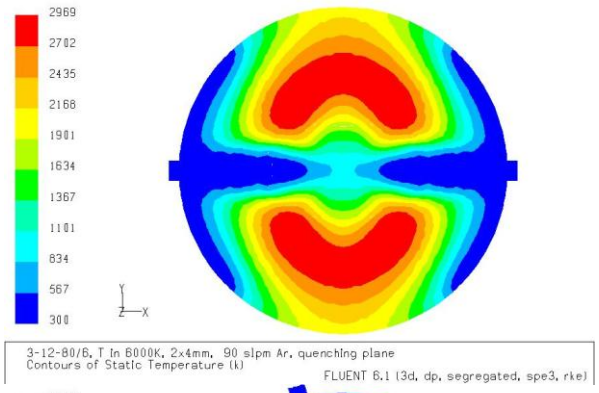	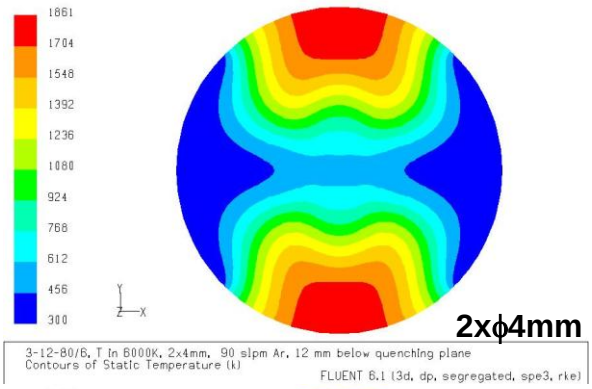	**2xϕ4mm**
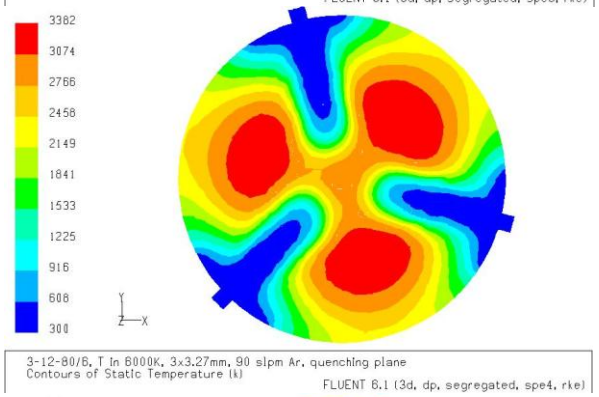	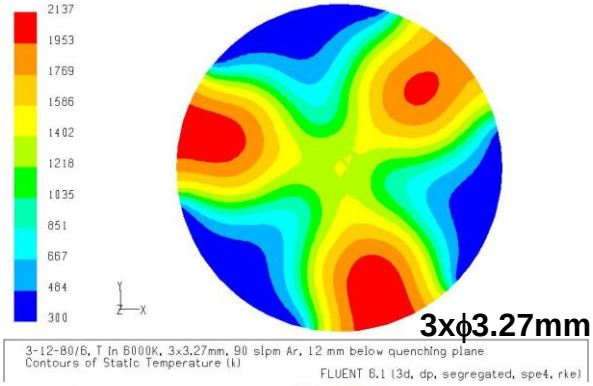	**3xϕ3.27mm**
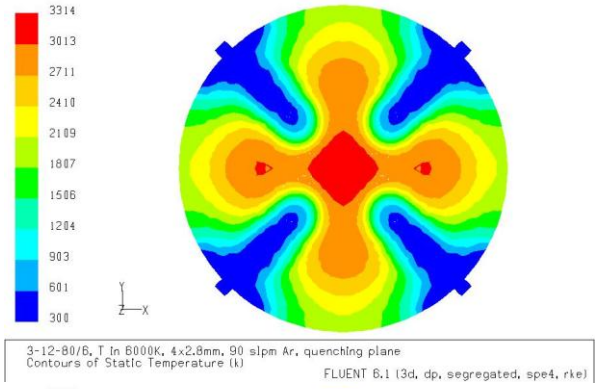	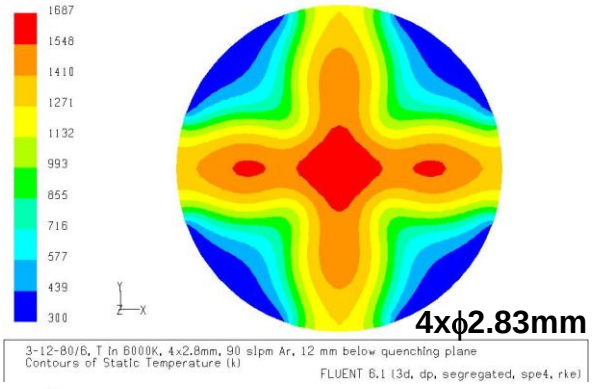	**4xϕ2.83mm**
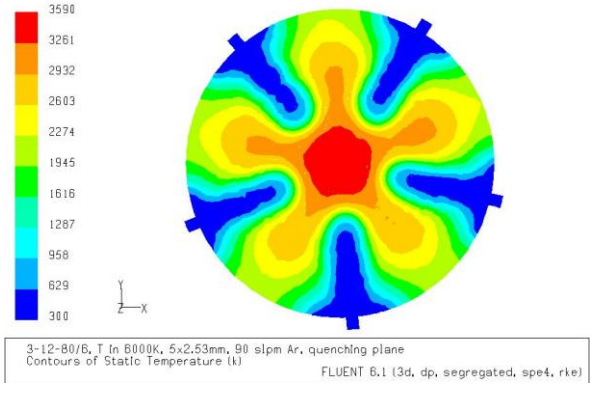	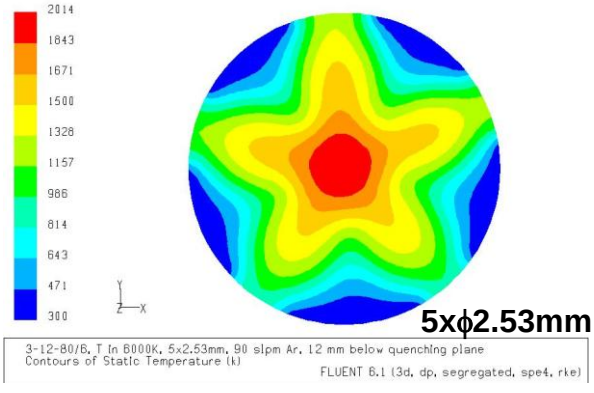	**5xϕ2.53mm**

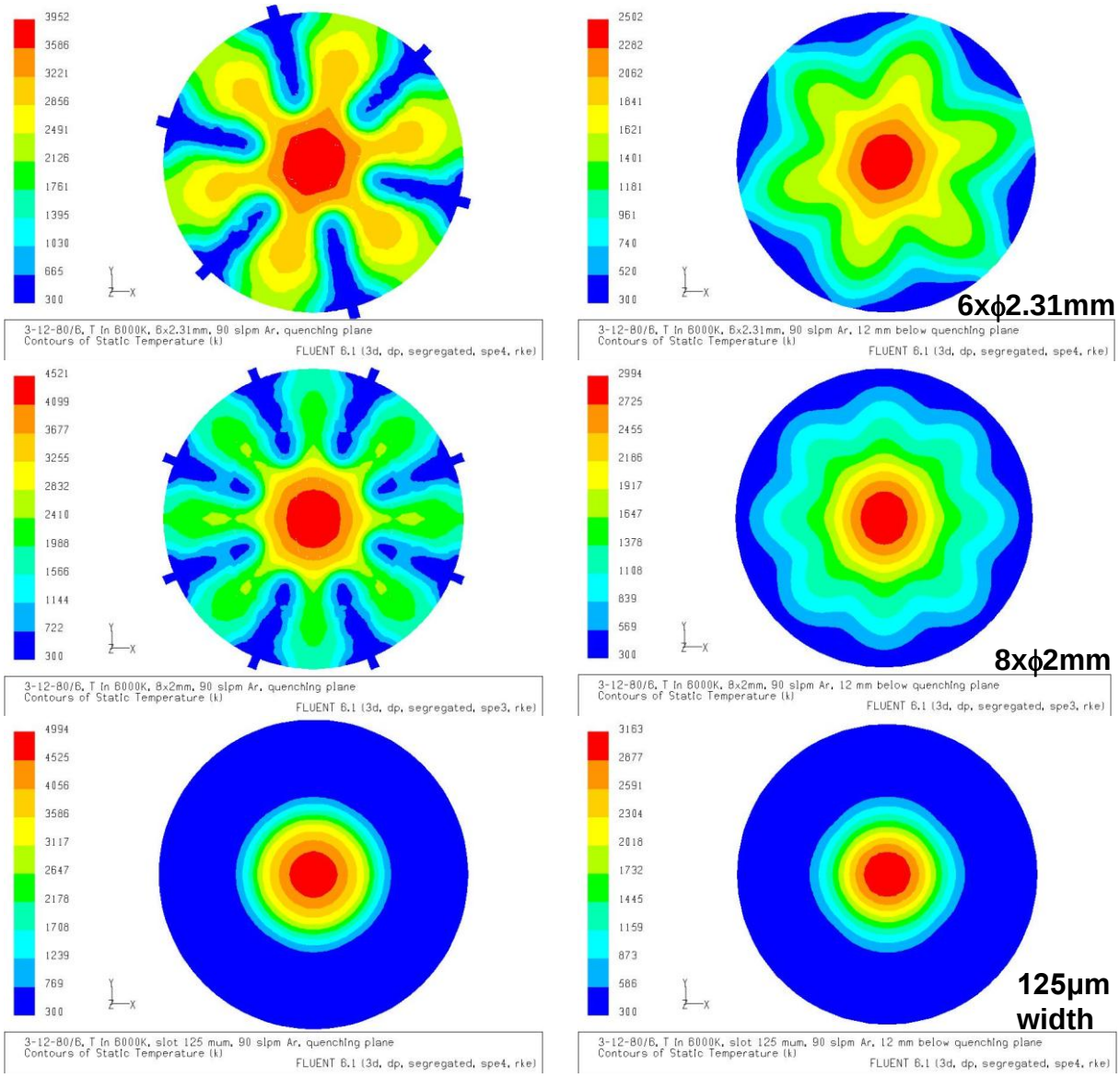

Figure 4-39: modelled temperature of a two-nozzle design. Left: quenching plane. Right: 12 mm below quenching plane. Modelled 3D parameters: 3-12-80/6, v_{in} 126 m.s^{-1}, T_{in} 6000 K, 40 kPa, 90 slpm Ar quench gas. All combinations have a surface equivalent nozzle outlet area (2.51x10^{-5} m^2).

The maximum temperature at the axis found in the quenching plane increases with increasing number of nozzles. This is explained with a smaller penetration for smaller nozzles (Figure 4-21). The two- and three-nozzle designs have temperature off-axis, which means that the quench gas is sufficient enough to completely penetrate the plasma and shows that some of the quench gas is flowing in the opposite direction of the plasma gas (Figure 4-29).
The temperature at 12 mm below the quench plane is lower for every design. The two- and three-nozzle designs have a maximum temperature at the edges, which indicates again the deflection of the plasma. The quench design with four nozzles shows the lowest temperature at 12 mm below the quench plane.
More than eight nozzles have not been modelled, because no difference would be expected (when the amount of nozzles goes to infinity, a slot is obtained). This is also seen by the temperature and temperature profiles resembling more the results of the slot design with increasing number of nozzles.
The a-symmetry occurring in some of the images is due to the meshing.

The homogeneity of the temperature profiles with respect to the particle trajectories is hard to judge. Although the two-nozzle design shows the lowest temperature difference in the quenching plane, it does not tell anything about the direction and velocity of the plasma flow (Figure 4-20, page 76 shows that the two-nozzle quenching is the optimal design with respect to the trajectories).

The modelling results of the 8 x 1.5 mm design (without and without axial angle) are shown in Figure 4-40. For allowing a good comparison on the influence of the nozzle diameter, the pictures of the 8 x 2 mm design have been included in this picture as well.

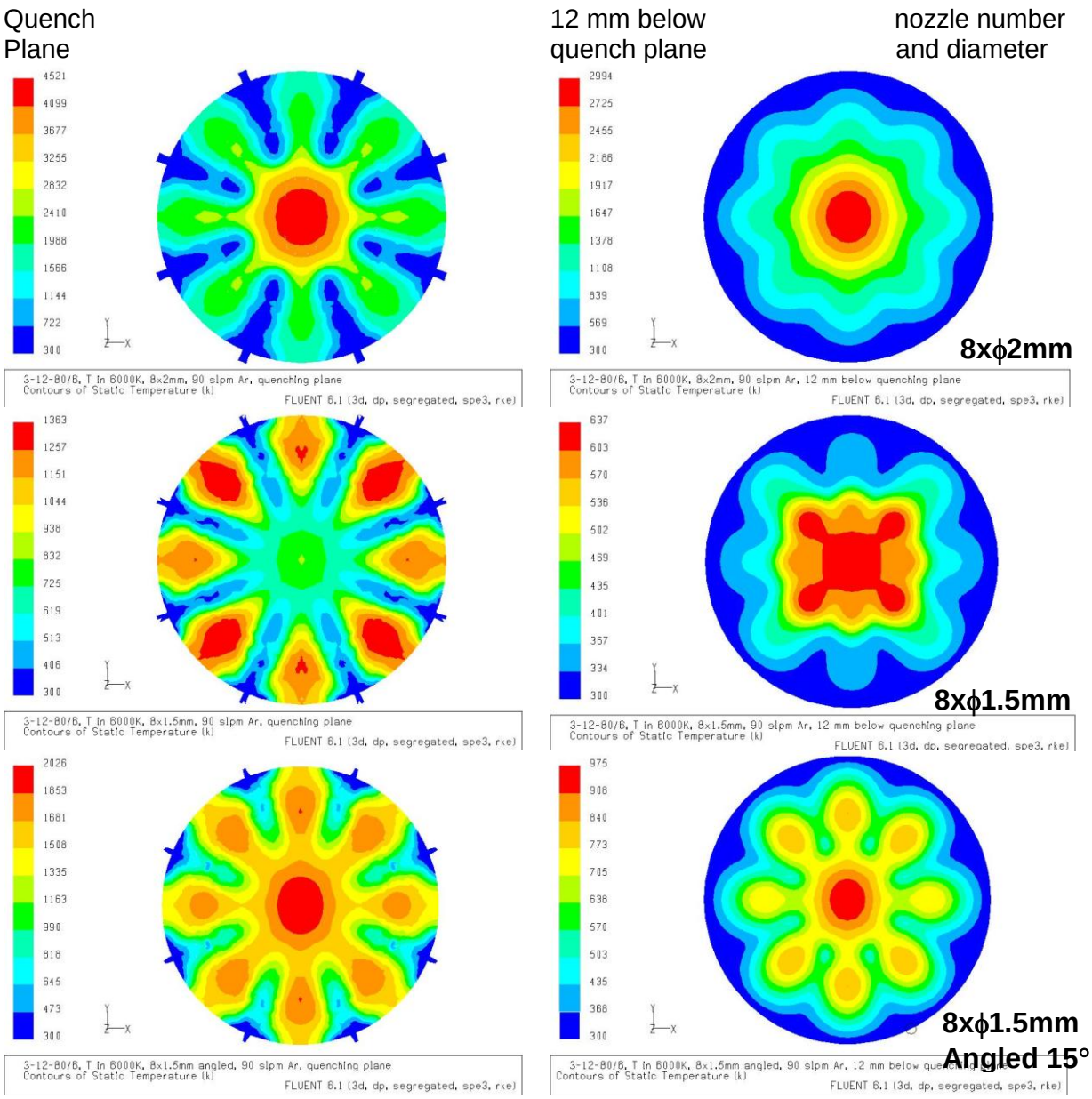

Figure 4-40: modelled temperature of an eight-nozzle design. Left: quenching plane. Right: 12 mm below quenching plane. Top: 8 x ϕ 2 mm, middle: 8 x ϕ 1.5 mm, and bottom: 8 x ϕ 1.5 mm angled. Modelled 3D parameters: 3-12-80/6, v_{in} 126 m.s^{-1}, T_{in} 6000 K, 90 slpm Ar quench gas.

The temperature distribution shows that only the 8 x ϕ 1.5 mm design is able to penetrate the plasma completely under the conditions as described in the legend of Figure 4-40. This however also means that the trajectories will flow around the ring.

The modelling shows furthermore that a reduction of the nozzle diameter results in a better penetration at the same quench gas flow rate.
The effect of the angle is shown in Figure 4-29 and allows the use of a higher quench gas flow rate before the plasma flow is diverted.
The results of Figure 4-39 and Figure 4-40 are summarised in numbers in Table 4-7.

Table 4-7: maximal temperature at the quenching (qp), 12 mm below the quenching plane (qp+12), and the temperature reduction along the axis as a function of the number of nozzles. Modelled conditions: 3-12-80/6, T_{in} 6000 K, 40 kPa, 90 slpm Ar quenching gas. The quench designs from two nozzles to the ring design have all the same quench gas inlet surface.

# nozzles	d_{nozzle} [mm]	T_{max} [K]	T_{axis} (qp) [K]	T_{max} [K]	T_{axis} (qp+12) [K]	Temperature reduction at the axis [K]
2	4.00	2969	920	1861	576	5424
3	3.27	3382	2935	2137	1408	4592
4	2.83	3314	3314	1687	1687	4313
5	2.53	3590	3590	2014	2014	3986
6	2.31	3952	3952	2502	2502	3498
8	2.00	4521	4521	2994	2994	3006
Ring	0.125	4994	4994	3163	3163	2837
6	1.50	1495	646	711	602	5289
8	1.50	1363	839	637	637	5363
8	1.50 15°	2026	2026	975	975	5025

The results show that the temperature increases with increasing number of nozzles. This is caused by a decreased momentum as a consequence of a smaller mass flow rate through a nozzle. By comparing the maximum temperature in the plane to the temperature in the centre it can be said that the two and three nozzles geometry are able to completely penetrate the plasma, because the temperature in the centre is lower than the maximum somewhere else found in the plane. Also the more nozzles are present, the more the resulting profiles resemble the slot profile.
The table also shows a huge decrease of the temperature for the 8 x ϕ 1.5 mm nozzle configuration compared to the 8 x ϕ 2 mm configuration.
The maximum temperatures for the six, eight (ϕ 1.5 mm) nozzles designs are far below the ones obtained with the four-nozzle system. This is caused by the presence of an upward flow, diverting the plasma around the edge (see Figure 4-26).

Summary of section 4.2.5
The strongest quench effect can be obtained with a two-nozzle quench system, because of the higher momentum as compared to a more nozzles system (for an equivalent quenching surface). But fewer nozzles result in a less homogeneous particle trajectory distribution.
The data in Table 4-7 only reflect the temperature reduction when the 3-12-80/6 plasma gas composition is quenched with 90 slpm Ar, however it does not say anything about the velocity profiles of the gas flow and thus the trajectories the nanoparticles will follow (see Figure 4-24). Therefore it is not possible from this table to predict the best quenching design for obtaining the smallest particle size.

4.3 Particle growth modelling

4.3.1 Goal of the particle growth modelling

The growth model of Kruis has been used to describe the particle growth within the ICP process. The mathematics, on which the model is based, is described in Appendix A. In this work the growth model has been investigated for silicon nanoparticles. The main assumptions, see also section 3.6.3 (page 57), are described below.
Only the particle vapour is considered; it is assumed that all the precursor particles are completely vaporised. The monomers are distributed homogeneously over the entire reactor and they are all assumed to encounter the same temperature and velocity profiles. Furthermore, the model does not consider the particle nucleation; all the seeds are single monomers and are formed immediately by homogeneous nucleation when the condensing point has been reached (3500 K for Si), thus the supersaturation, Kelvin diameter (equation 2-1, page 11), thermophoresis, and other kinetic effects do not play a role. All collisions are assumed to be 100% efficient. There is no particle - particle and plasma – particle interaction. The coagulation above the melting point is assumed to be immediate, meaning an infinite sintering rate.

The required material properties for the spherical Si particle are all bulk properties and size independent. Besides the physical particle properties, the collision diameter, density, and viscosity of the plasma gas are also needed to calculate the monomer density and the Knudsen number. The plasma gas properties (density and viscosity) are assumed to be the same for each plasma composition and are set to the values of 3-12-80/6. The growth model needs the temperature and velocity profiles as inputs, which are obtained from the CFD model (see sections 4.1. and 4.2).
The growth model is used to describe and predict the particle growth in the synthesis chamber as a function of different process parameters. By understanding the influence of these process parameters, the final particle size can be tailored.

The experiments show a few, not completely vaporised particles in the product (maximum diameter about 5 μm). The precursor that is not completely vaporised was either too large or followed a trajectory along the edges of the plasma. The different trajectories of the precursor particles occur as a consequence of the size distribution, velocity distribution of the carrier gas (reduced velocity towards the injector wall, and collisions of the precursor particles with the injector wall).

4.3.2 Example of the growth model with modelled profile

This section deals with an example to illustrate the growth model. As already mentioned, the model needs the temperature and velocity profiles as input. Table 4-8 gives the Si properties which are required. The solidification and condensation point are not required for the model as described in [77], they are used in the current work to define the temperatures at which the particles start to nucleate and where the sintering rate is reduced from infinity (above the melting point the particles are assumed to coagulate immediately: infinite sintering rate). These properties can be replaced by the ones of any other compound.

Table 4-8: silicon properties which are used in the particle growth model.

Melting point	1683 K	Surface tension	1.0 J m^{-2} [77]
Boiling point	3505 K [76]	Sintering coefficient	0.18 x exp(-2.3x10^5/(RT)) [77]
Density	2330 (s) 2530 (l) $kg.m^3$	Molar volume	1.205 x 10^{-5} $m^3.mole^{-1}$ [77]
Molar weight	28.05 x 10^{-3} $kg.mole^{-1}$	Boundary between two particles	2.714 x 10^{-10} m [77]
Monomer diameter	3.3689 x 10^{-10} m [77]		
Fractal dimension	1.8 [77]		

Figure 4-41 shows the temperature and velocity profiles of the 3-12-80/6 plasma composition at 40 kPa with 10 kW net power input, with the temperature region below 3500 K of interest. In the curves, z = 0 mm represents the torch exit and t = 0 ms the time at which 3500 K is reached in the cooling phase. The condensing point of Si is also assumed to be the nucleation temperature.

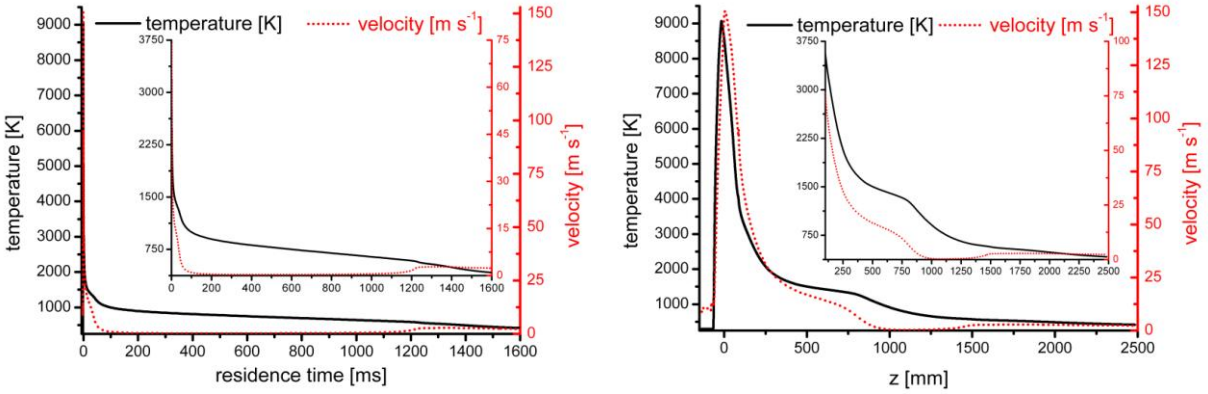

Figure 4-41: modelled temperature and velocity profiles as a function of time (left) and z (right). Modelled plasma parameters: 3-12-80/6, 40 kPa, 10 kW net power input, and no quenching.

The temperature is only a very short time above the melting point of Si (1683 K), in the order of 5 ms, which is short in comparison to the total residence time.

Figure 4-42 shows some characteristics calculated with the Kruis model as a function of time using the modelled profiles as shown in Figure 4-41. The initial monomer concentration (N_0 in the figures of appendix A) is calculated from the precursor feed rate under assumption that all precursor is vaporised and is distributed over the complete gas mixture (equation 3-2). The z position, at which Si starts to condensate: the 3500 K isotherm, depends on the process parameters like power, pressure, plasma gas composition, …. and are presented in Table 4-3 to Table 4-5 (page 71 - 72). For the 3-12-80/6, 40 kPa, 10 kW, and no quenching, this z position is situated 104 mm below the torch exit.

The sizes of the soft and hard agglomerates are represented by the aggregate diameter curve. The transition between hard and soft agglomerates is not visible in the curves, but has to be calculated. The hard agglomerates are formed when the agglomerate size is 1% larger than the primary particle size until the primary particle reaches 99% of its final size. These definitions are the same as used by Tsantilis and Pratsinis [26], and are based on experimental observations by Windeler et al. [176]. After the d_{pp} has reached 99% only soft agglomerates are formed.
The values for τ_c and τ_s are species and process parameter dependent (see eq. 2-2 and 2-3 on page 12).

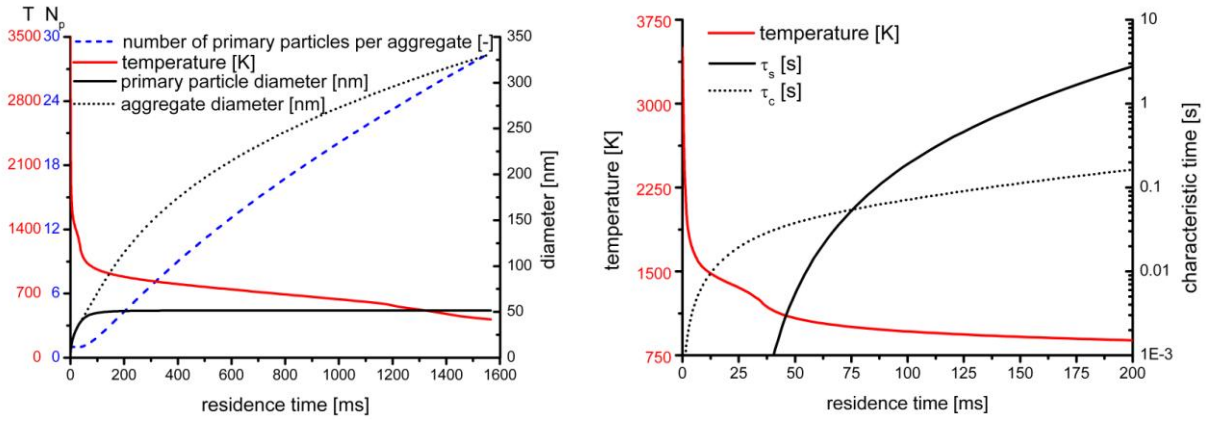

Figure 4-42: Growth model results. n_p, temperature, primary particle (d_{pp}), and agglomerate diameter (d_{agg}) as a function of time (left). Right: temperature and characteristic times of collision (τ_c) and sintering (τ_s) as a function of the residence time [26]. Modelled parameters: 3-12-80/6, 10 kW, 40 kPa, 2.0 g.min^{-1} feed rate.

The red curve in the left graph, which represents the temperature, has a high gradient at the beginning which gradually decreases. The left graph shows that the particle growth of the primary particles is fast in the beginning (high slope of the size versus time curve up to 25 ms) and slows down until a constant particle size is reached. The particle growth takes only place during approximately the first 200 ms (from t = 0 ms corresponding to z = 104 mm and 3500 K to t = 200 ms, which corresponds to z = 1020 mm and 875 K). About 83% of the primary particle growth takes place in the first 50 ms after the condensing point has been reached. The temperature of 875 K is defined as the end of the sintering region. The aggregate size increases very rapidly at the beginning to level off with increasing time. The number of primary particles per aggregate increases very slowly at the beginning (up to 65 ms).
The right graph shows the temperature curves and the characteristic sintering and collision times. Both characteristic times are increasing with decreasing temperature. The collision time is larger than the sintering time up to 75 ms and increases slower than the sintering time.

The results of Figure 4-42, left show that the final product of 3-12-80/6, 40 kPa, 10 kW, no quench, would consist out of soft agglomerates having a 331 nm diameter which are made of 28 primary particles. The hard agglomerates have a 113 nm diameter and are consisting out of 4 primary particles, which have a 51 nm diameter each (the hard agglomerates are kept together by chemical bonds, while the soft agglomerates only have the Van der Waals forces to keep them together). The primary particle (d_{pp}), hard and soft agglomerate diameter (d_{agg} and $d_{hard\ agg}$ respectively) are the same until τ_c and τ_s get in the same order of magnitude around 65 ms (z = 950 mm, 1000 K). After this time the hard agglomerates are formed until τ_s becomes about ten times larger than τ_c (around 190 ms). In the beginning where τ_c is much larger than τ_s only spherical particles are formed, which can be seen at the amount of 1 primary particle per aggregate.

However, it should be mentioned that the calculations were carried out for z values up to 2500 mm. In reality z reaches a value of 4250 mm, therefore the growth model has been extended to be in compliance with this z value. The only effect seen by comparing the results of the growth model for that of z = 4250 mm to z = 2500 mm was on the number of primary particles per soft agglomerate and the size of the soft

agglomerates. The reason is that the temperature has decreased well below the sintering temperature (875 K) in this extended zone and will therefore not exert influence the d_{pp} and hard agglomerate size.

Summary of section 4.3.2
The actual particle growth occurs only in a temperature range from 3500 K to about 875 K. This temperature range corresponds to a residence time of 200 ms and a z range from 100 to 1025 mm for 3-12-80/6, 10 kW, and 40 kPa, in which the first 50 ms account for 83% of the total particle growth.
The evolution of the characteristic collision and sintering times determine the size of the primary particles and hard agglomerates, the time before the characteristic collision time crosses the characteristic sintering time makes up for 83% of the final primary particle size.
The characteristics times are process parameter dependent and therefore different parameters will result in different particle sizes.

4.3.3 Particle growth model: parameter study

4.3.3.1 Influence of the plasma gas composition

The effect on the particle growth can be divided into process parameters which influence the temperature and velocity profiles and the physical properties of the nanoparticles. Table 4-3 to Table 4-5 (page 71 - 72) show that the different process parameters result in different residence times for T > 3500 K, which will also be the case for the residence times at T < 3500 K. Therefore, to make a comparison between the several compositions and process parameters, the n_p and d_{agg} are calculated for the same residence time (in the order of a second), with a temperature below 875 K to exclude primary particle growth and sintering.
The influence of the plasma parameters on the number of pp per aggregate, and d_{pp}, d_{agg} (agglomerate size) and $d_{hard\ agg}$ (size of the hard agglomerates) are presented in Table 4-9 to Table 4-11 (analogue to Table 4-3 to Table 4-5, pagesm 71 and 72).

Table 4-9: influence of the plasma gas flow rates on the number of pp in the agglomerate, d_{pp}, d_{agg}, and $d_{hard\ agg}$. Modelled parameters: net power input 15 kW, 40 kPa, no quenching, 2.0 g.min^{-1} precursor feed rate.

plasma gas composition	d_{pp} [nm]	n_p [-] soft	hard	d_{agg} [nm]	$d_{hard\ agg}$ [nm]
1-12-80/6	84	5.4	2.1	215	124
1-27-80/6	73	6.6	2.3	208	114
5-27-80/6	71	7.0	2.3	209	112
10-12-80/6	75	6.4	2.3	210	118
10-27-80/6	67	8.0	2.6	213	112

An increased carrier and central gas flow rate result in smaller primary particles, caused by the lower monomer concentration and the shorter residence time at higher (sintering) temperatures (for the latter see the temperature profiles in Figure 4-43). The number of soft and hard agglomerates increases with increasing gas flow rate, because the transition between τ_c and τ_s takes places earlier (shorter residence at higher temperatures, see Figure 4-43) in case of the high gas flow rates. This means that the particles have less time to coalesce and therefore start agglomerating earlier and thus resulting in a higher number of primary particles per agglomerate.

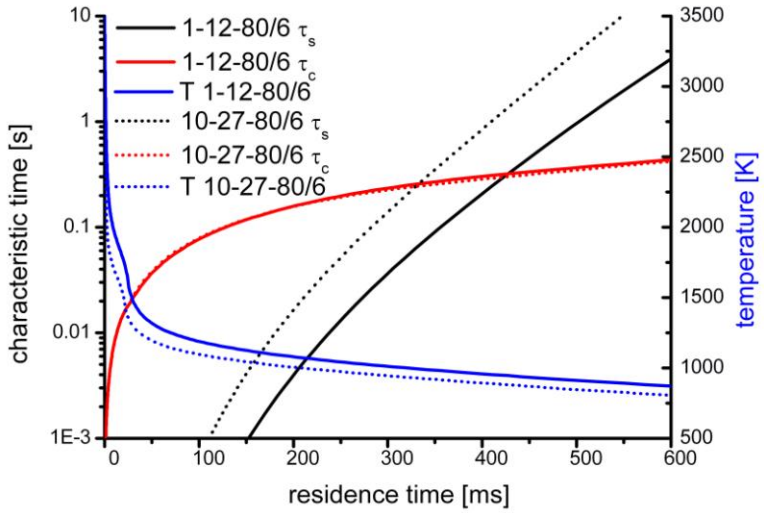

Figure 4-43: comparison of the characteristic sintering and collision times for 1-12-80/6 (solid lines) and 10-27-80/6 (dotted lines) plasma gas composition. Other modelled process parameters: 40 kPa, 10 kW, and 2.0 g.min^{-1} feed rate.

The results of the particle growth model for different plasma gas compositions are described in Table 4-10.

Table 4-10: influence of the plasma gas composition on the number of pp in the agglomerate, d_{pp}, d_{agg}, and $d_{hard\ agg}$. Modelled parameters: net power input 15 kW, 40 kPa, no quenching, 2.0 g.min^{-1} precursor feed rate.

plasma gas composition	d_{pp} [nm]	n_p [-] soft	hard	d_{agg} [nm]	$d_{hard\ agg}$ [nm]
5-27-80/6	71	7.0	2.3	209	112
5-27-80/10	71	6.6	2.3	202	111
5H_2-27-80/6	53	16.2	4.1	249	115
5N_2-27-80/6	72	6.4	2.7	210	112
5-27-80/6N_2	68	7.9	2.5	213	110
5N_2-27-80/6N_2	72	6.4	2.3	203	112
5He-27-80/6	69	7.4	2.5	209	113
1H_2-27-80/6	73	6.4	2.3	205	114
1H_2/4Ar-27-80/6	71	6.8	2.4	205	112

There is hardly any difference in d_{pp} and (hard and soft) agglomerate diameters for the different plasma gas compositions. Except for the composition with 5 slpm H_2 carrier gas which has a lower d_{pp} and a higher soft agglomerate diameter. Both are caused by faster cooling as compared to other compositions. The sooner the temperature becomes below 875 K, the sooner the particle growth stops and only soft agglomerates are formed.

The results in Table 4-11 present the influence of several process parameters on the primary particle and agglomerate diameter.

It is shown that there is hardly any difference in size between particles which followed the axis or that followed the pathlines (trajectory of a massless particle released at the edge of the precursor inlet). Furthermore, lower power levels result in smaller particles than compared to higher power levels, but also result in larger soft agglomerates. The lower power level causes a faster crossing of the temperature range in which particle growth occurs, resulting in smaller primary particles and

larger soft agglomerates in comparison to high power. Although a lower power level is detrimental with respect to the precursor evaporation.
A higher pressure results in larger particles and a lower number of pp in the agglomerates than compared to lower pressures. Although the initial concentration is lower at higher pressure, the larger particles are caused by a longer residence time at higher temperatures.
The introduction of the funnel (without any quenching) reduces d_{pp} and $d_{hard\ agg}$ according to the calculations, as the expansion after the funnel acts as a pressure sink and results in a faster reduction of the gas temperature to a temperature below the sintering region, around 875 K.

Table 4-11: influence of the plasma parameters on the number of pp in the agglomerate, d_{pp}, d_{agg}, and $d_{hard\ agg}$. The plasma properties have been assumed to be pressure independent. Modelled parameters: net power input 10 kW, 40 kPa, no quenching, unless mentioned otherwise, 2.0 g.min^{-1}.

Process parameters		d_{pp} [nm]	n_p [-] soft	hard	d_{agg} [nm]	$d_{hard\ agg}$ [nm]
3-12-80/6		51	21.1	4.2	280	113
3-12-80/6	pl*	51	22.3	4.5	283	115
3-12-80/6	15 kW	76	6.7	2.2	219	116
3-12-80/6	30 kPa	47	32.0	4.9	323	112
3-12-80/6	60 kPa	58	12.1	3.5	232	115
3-12-80/6	-10**	57	16.0	4.0	265	121
3-12-80/6	funnel ***	47	26.1	2.7	292	82
3-12-80/6	swirl ****	51	22.1	4.3	283	112

* pl means pathline, where pathline is defined as the trajectory of a massless particle released at the edge of the precursor inlet.
** injector outlet position lowered by 10 mm.
*** a funnel has been introduced in the reactor to guide the plasma flow (see section 4.2.3.2)
**** swirl component of the central gas taken into account

Figure 4-44 compares the characteristic times for the 8 x Φ 1.5 mm quenchring with and without funnel.

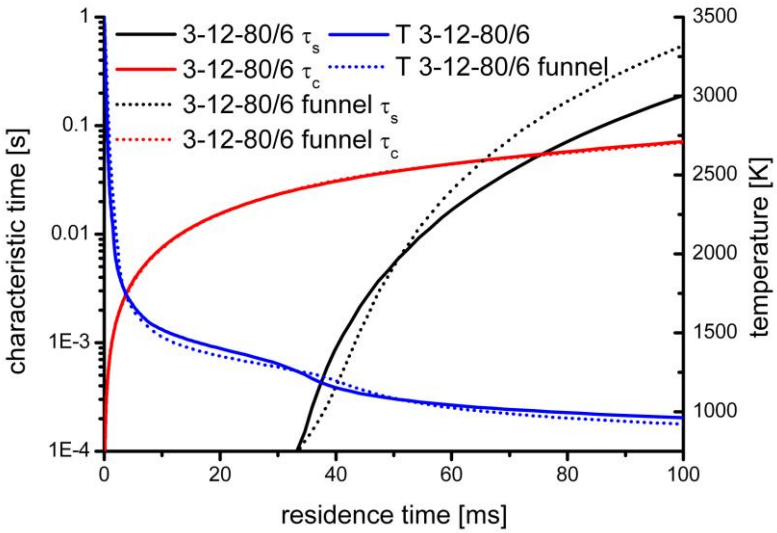

Figure 4-44: comparison of the characteristic times for 3-12-80/6 plasma gas composition with (dotted lines) and without funnel (solid lines). Other modelled process parameters: 40 kPa, 10 kW, and 2.0 g.min^{-1} feed rate.

The τ_s crosses the τ_c earlier in the funnel design and will therefore result in smaller particles. Also makes the τ_s a larger tangent with the τ_c in the funnel case, resulting in smaller soft agglomerates.

The temperature profiles for different parameters are shown in Figure 4-45. It shows that the pressure and power have a large influence on the temperature and velocity profiles, whereas the influence of the plasma gas composition is very small. This is reflected in the results of Table 4-9 to Table 4-11.

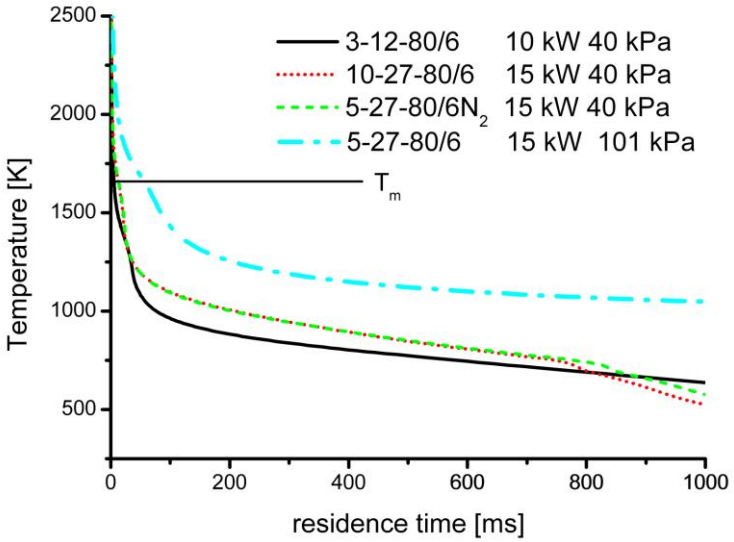

Figure 4-45: temperature on the axis as a function of the residence time for different plasma gas compositions, power levels, and pressures. The horizontal solid line represents the melting point of Si.

Summary of section 4.3.3.1

Low power levels and pressures result in smaller particles (but are detrimental for the evaporation process). The introduction of the funnel (without any quenching) reduces d_{pp} and $d_{hard\ agg}$. An increased carrier and central gas flow rate result in a smaller primary particles and hard agglomerates. The pressure and power have a huge influence on the particle growth, which increases with increasing pressure and power.

4.3.3.2 Influence of other parameters

Besides the plasma gas composition also other parameters (like the particle properties mentioned in Table 4-8, feed rate, etc.) will influence the final particle size. In the article of Kruis et al. [77], also the influence of the fractal dimension (agglomerate shape ranging from lines (dimension: 1) to spheres (dimension: 3)) and the sintering rate on the particle size are investigated. The primary particle diameter was found to decrease with increasing fractal dimension and with a lower sintering rate.

As already mentioned before, there is an uncertainty in the condensing point of Si (values found in the literature range from 2628 K to 3505 K). Table 4-12 shows the influence of the condensing point on the particle growth, this can also be regarded as a different nucleation temperature. In this table the temperature and velocity profiles of 3-12-80/6 has been used for all cases.

Table 4-12: influence of the condensing temperature on the number of pp in the agglomerate, d_{pp}, d_{agg}, and $d_{hard\ agg}$. Parameters: temperature and velocity profiles of 3-12-80/6 (10 kW net power input, 40 kPa, no quenching) at the axis with a Si precursor feed rate of 2.0 g.min^{-1}.

T_b [K]	n_p [-]		d_{pp} [nm]	d_{agg} [nm]	$d_{hard\ agg}$ [nm]
	soft	hard			
3900	28.7	4.2	53	342	117
3500	28.5	4.2	51	331	113
3000	28.3	4.3	49	317	110
2500	27.9	4.3	47	300	105

As the condensing temperature decreases, the primary particle diameter, the number of primary particles in the agglomerates, the hard, and soft agglomerate diameter decreases. This is expected since the modelled temperature for these conditions drops from 3500 K to 2500 K in less than 1 millisecond, so the total residence time is about the same for each boiling point, but the initial monomer concentration decreases by about 30% going from high to low boiling point, see the equation below (already described on page 57)

$$N' = \frac{n}{V} * \frac{1}{\rho} = \frac{n}{V} * \frac{V}{M} \qquad \frac{[\#]}{[m^3]} \cdot \frac{[m^3]}{[kg]} = \frac{[\#]}{[kg]}$$

The precursor feed rate will have also an influence on the particle growth, as it has a direct influence on the initial monomer concentration. In the particle growth model, the precursor is assumed to be completely evaporated and therefore being proportional to the initial monomer concentration. Table 4-13 shows the influence of the particle feed rate on the particle growth.

The results in Table 4-13 show an increased primary particle diameter with increasing precursor feed rate. Thus in order to obtain small nanoparticles, a low precursor feed rate should be used.

Table 4-13: influence of the precursor feed rate on the number of pp in the agglomerate, d_{pp}, d_{agg}, and $d_{hard\ agg}$. Parameters: temperature and velocity profile of 3-12-80/6 (10 kW net power input, 40 kPa, no quenching) at the axis.

feed rate	d_{pp}	n_p [-]		d_{agg}	$d_{hard\ agg}$
[g.min^{-1}]	[nm]	soft	hard	[nm]	[nm]
0.5	37	25.0	4.0	218	78
1.0	43	26.9	4.3	270	98
2.0	51	28.5	4.2	331	113
3.0	57	29.2	4.1	372	123
4.0	61	29.6	3.9	403	129
6.0	68	29.9	3.6	451	137

Summary of 4.3.3.2

The boiling point has some influence on the particle size under non-quenching conditions. The particle size decrease with 8% for the highest to the lowest boiling point of Si found in the literature (2628-3505 K). d_{pp}, d_{agg}, and, $d_{agg\ hard}$ are increasing with increasing monomer concentration (proportional to the precursor feed rate).

4.3.4 Particle growth model: influence of quenching

4.3.4.1 Introduction

Not only the plasma parameters and the feed rate are influencing the particle and agglomerate size. Also quenching with parameters, like flow rate, nozzle diameter, and quench height, are of great importance for the particle growth.

4.3.4.2 Particle growth model: influence of quench design

Table 4-14 and Table 4-15 show the influence of the nozzle diameter and quench position respectively on the primary particle and agglomerate size. The nucleation position for the process parameters: 3-12-80/6, 40 kPa, 10 kW is determined at z = 104 mm (see section 4.3.2).

Table 4-14: influence on the particle growth as a function of the nozzle diameter (8 nozzles are converted into a slot equivalent) with and without an axial component (15° downward with respect to the quench plane). Modelled process parameters: 3-12-80/6, 40 kPa, 10 kW net power input, quenched at z =121 mm, 60 slpm Ar, precursor feed rate 2.0 g.min^{-1}.

Nozzle diameter	d_{pp} [nm]	n_p [-] soft	hard	d_{agg} [nm]	$d_{hard\ agg}$ [nm]
1.5 mm	47	14.6	4.0	207	100
1.5 mm 15°	37	30.1	6.5	242	102
2.0 mm	51	11.4	3.2	196	97
2.0 mm 15°	43	19.0	4.8	220	101

Quenching with a 1.5 mm nozzle results in a smaller particle size compared to 2.0 mm nozzles with the same quench gas flow rate. The smaller nozzles have a higher momentum resulting in a better penetration of the plasma (Figure 4-21, page 78), resulting in a better mixing of the quench and plasma gas and therefore in a lower temperature. When the nozzles make a 15° angle with respect to the quench plane, the particles also get smaller in comparison to the same designs without an angle. This is due to the smaller deflection of the plasma gas by the quench gas, see Figure 4-29 (page 83). This will result in a shorter residence time at temperatures in the sintering region for the angled design and thus in smaller particles. The introduction of a nozzle results in a significant reduction of the particle size.

Summary of section 4.3.4.2

Quench designs with an equivalent number of smaller nozzles and nozzles with a (15°) downward component to the quench gas direction result in the synthesis of smaller particles.

The influence of the angle on the quenching and particle growth has not been investigated into much detail yet. It is, however, expected that there is an optimal angle, just like there is an optimal nozzle number and diameter. If the angle is too small then the plasma will be deflected and if the angle is too high, then the plasma will not be penetrated and no quenching effect will be obtained.

4.3.4.3 Particle growth model: influence of quenching height

Besides the quench design, also the quenching height determines the temperature and velocity profiles after quenching. If the quench position is closer to the torch exit, the plasma temperature is higher, resulting in a more difficult penetration, see Figure

4-27 (page 82). Table 4-15 shows the modelled particle size as a function of the applied quenching height for a 60 and 90 slpm Ar quench gas flow rate. By varying the z value, the temperature at which the quenching is carried out can be changed. The nucleation height (z value at which 3500 K (T_b of Si) is reached) is process parameter specific and amounts 104 mm under the current process conditions.

Table 4-15 influence of the quench position on maximum temperature at the quench plane (for non quenching conditions), momentum density of the plasma jet, the number of pp in soft and hard agglomerates, d_{pp}, d_{agg}, and $d_{hard\ agg}$ as calculated with the Kruis model along the pathline (trajectory of a massless particle released at the edge of the injector outlet). Modelled plasma parameters: 3-12-80/6, 10 kW, 40 kPa, quenchring at z = 121 mm (area equivalent of 8 x ϕ 1.5 mm, 15° angle), 2.0 g.min^{-1} precursor feed rate.

Position [mm]	T_{max} [K]	ρv^2 [kg m^{-1} s^{-2}]	d_{pp} [nm]	n_p [-] soft	n_p [-] hard	d_{agg} [nm]	$d_{hard\ agg}$ [nm]
z = 81							
60 slpm	4312	549	38	21.7	5.8	209	100
90 slpm	4312	549	28	44.2	7.7	232	87
z = 101							
60 slpm	3665	424	37	22.8	6.2	211	102
z = 121							
60 slpm	3311	356	36	25.6	6.9	217	103
90 slpm	3311	356	28	46.6	10.4	234	101
z = 141							
60 slpm	3054	283	39	20.5	6.3	207	106
90 slpm	3054	283	29	40.9	10.8	224	108
z = 161							
60 slpm	2808	157	43	14.2	4.4	189	98
90 slpm	2808	157	27	50.2	12.0	238	106

The table shows a decreased maximum temperature at the axis with increasing z.
At a quench gas flow rate of 60 slpm, where there is no complete penetration of the plasma, there is a stronger reduction of the plasma gas velocity with increasing quenching heights, which will result in an increased residence time. Because the plasma is not completely penetrated the temperature remains higher; the particles will have a longer time to grow. This is shown in Table 4-15 by an increased primary particle diameter.
The number of primary particles in the hard agglomerate diameter decreases because of the longer sintering time at higher temperature resulting in more spherical particles. The size of the hard agglomerates has a maximum at z = 141 mm, because of the different evolutions of the characteristic sintering and collision time curves.

Figure 4-46 compares the evolution of the characteristic sintering and collision times as a function of the residence time (after 3500 K has been reached).

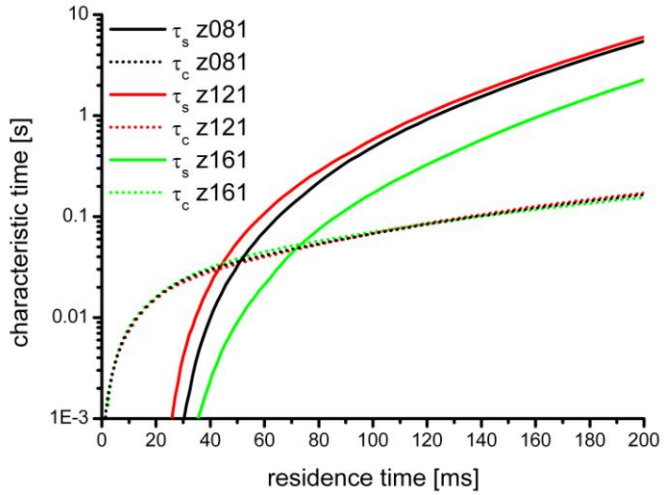

Figure 4-46: characteristic times obtained from the particle growth model different quenching heights as a function of the residence time. Modelled conditions: 3-12-80/6, 10 kW, 40 kPa, 60 slpm Ar.

The characteristic collision times increase slowly after a strong increase at the beginning. The characteristic sintering times show the same behaviour. Whereas the characteristic collision times are almost the same for all heights, the characteristic sintering times are different. The particles growth until the collision time is about 1 order of magnitude smaller than the sintering time. Thus the particles will be the smallest at z = 121 mm and largest for z = 161 mm. When the collision time is less than one order of magnitude smaller the particles sinter and the hard agglomerates are formed. Normally, the z = 161 mm case would result in the largest number of primary particles per hard agglomerate, because of the reason mentioned before. This is now however not so in this particular case because the sintering time is getting large in comparison to the residence time. The changed order of the characteristic sintering times is caused by the different temperature characteristics obtained after quenching.

With 90 slpm Ar the primary particle diameter increases to z = 141 mm to decrease again for z = 161 mm. Quenching with 90 slpm at z = 141 mm is not so efficient as could be expected from the calculated maximum temperature as compared to the values of z = 81 mm. Although quenching at z = 141 mm results in a stronger penetration and therefore in a lower temperature as compared to the temperature profile of z = 81 mm, it has a much lower velocity (thus a longer residence time) around 1200 K, which is still in the sintering region and will thus result in the synthesis of larger particles. The particle size decreases again for z = 161 mm.

Figure 4-47 shows the d_{pp} as a function of the quench height and flow rate (data are obtained from Table 4-15.

The diagram suggests the presence of an optimal quenching height when the plasma is not completely penetrated (z = 121 mm) and the presence of a less preferable quenching height when the plasma is penetrated (z = 141 mm).

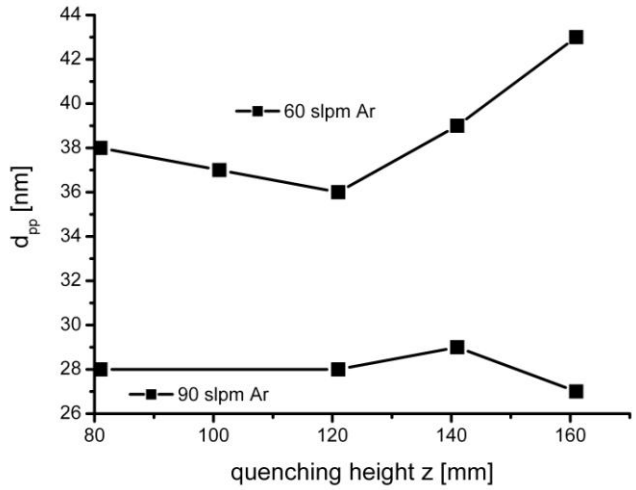

Figure 4-47: d_{pp} as function of the quenching height and quench gas flow rate.

Summary of section 4.3.4.3

The quenching height has not of large influence on the final particle size as long as the plasma is not completely penetrated (for these process conditions!), but it is absolutely an important parameter for other process conditions. Although the plasma has a decreasing temperature with increasing z position and therefore can be penetrated easier, it does not necessarily result in smaller particles.

4.3.4.4 Particle growth model: influence of quench gas flow rate

The effect of the quench gas flow rate on the particle growth is presented in Table 4-16, in which d_{pp}, n_p, d_{agg}, and $d_{hard\ agg}$ are calculated as a function of the N_2 quench gas flow rate. The quenching effect is due to two components: cooling of the gas phase and dilution of the initial monomer concentration, under the assumption of immediate and perfect mixing (in reality the dilution will not be homogeneous, it will take longer before the complete mixing takes place). These effects, however, are linked to each other and can not be separated completely. The last two columns show the particle diameter which would be obtained when only the temperature effect would be present ($d_{pp,T}$) and when only the dilution effect would be present ($d_{pp,q}$). For $d_{pp,\ T}$ the temperature and velocity profiles of the quench cases are used, without correcting the initial concentration for the extra quench gas. $d_{pp,\ q}$ uses the temperature and velocity profiles of the non- quenching case, in which the initial concentration is corrected for the additional quench gas.

Table 4-16: influence of quench gas flow rate on the number of pp per agglomerate, d_{pp}, d_{agg}, and $d_{hard\ agg}$ as calculated with the Kruis model. The last two columns show the calculated particle diameter when only the influence on temperature is included, without any dilution effect ($d_{pp,T}$) and vice versa ($d_{pp,q}$ profiles of no quenching conditions). Modelled plasma parameters: 5-27-80/6, 10 kW, 40 kPa, quenched at z = 63 mm (area equivalent of 8 x ϕ 2 mm), 2.0 g.min^{-1} precursor feed rate.

Quench gas flow rate	d_{pp} [nm]	n_p [-] soft	hard	d_{agg} [nm]	$d_{hard\ agg}$ [nm]	$d_{p,T}$ [nm]	$d_{p,\ q}$ [nm]
0 slpm N_2	51	26.8	4.8	243	120	51	51
30 slpm N_2	38	30.8	6.0	252	101	41	47
60 slpm N_2	32	41.7	4.3	257	72	37	45
90 slpm N_2	25	73.1	2.7	275	43	29	43
120 slpm N_2	26	56.0	1.0	247	26	36	42
150 slpm N_2	11	536.8	2.6	367	19	16	42

These results show that the primary particle and hard agglomerate diameter decreases with increasing quench gas flow rate. Table 4-16 also shows that the temperature effect caused by the quenching has a much more pronounced effect on the particle size than the dilution effect. Furthermore, it is also shown that an increasing quench gas amount does not necessarily result in much smaller particles, compare the particle size of 90 slpm to that of 120 slpm. The size of the hard agglomerates decreases as a consequence of the sharper transition between the characteristic sintering and collision time. When $\tau_c >> \tau_s$ the particles sinter faster than they agglomerate resulting in a particle growth and spherical particles (1 primary particle per agglomerate). If $\tau_c \approx \tau_s$ the particle growth is not so fast anymore as previously and hard agglomerates are formed (an increase of the number of primary particles per agglomerate). When $\tau_s >> \tau_c$ the particles do not grow anymore and only soft agglomerates are formed.

The size of the agglomerates becomes larger for higher quench flow rates, although the highest quench gas flow rate has the lowest initial monomer concentration, it has the highest number concentration remaining at the end of the “hard” agglomerate phase (about a factor of 4 more). The 120 slpm case is an exception because it has different temperature characteristics in comparison to the other temperature profiles (see Figure 4-48). As seen in Figure 4-48 is the temperature resulting from quenching with 120 slpm N_2 higher than the temperature achieved with 90 slpm N_2 over several milliseconds and therefore results in larger particles, even though the quench gas flow rate is 33% higher. This is caused by the upward flow of the quench gas and thereby diverting the plasma gas flow (see Figure 4-24 to Figure 4-26 on page 80 – 82).

The influence of the quench gas flow rate on the temperature profiles as a function the path length and residence time are shown in Figure 4-48. The path length is defined as the length of the pathline, which is the trajectory of a massless particle released at the edge of the injector outlet, see for an example Figure 4-24.

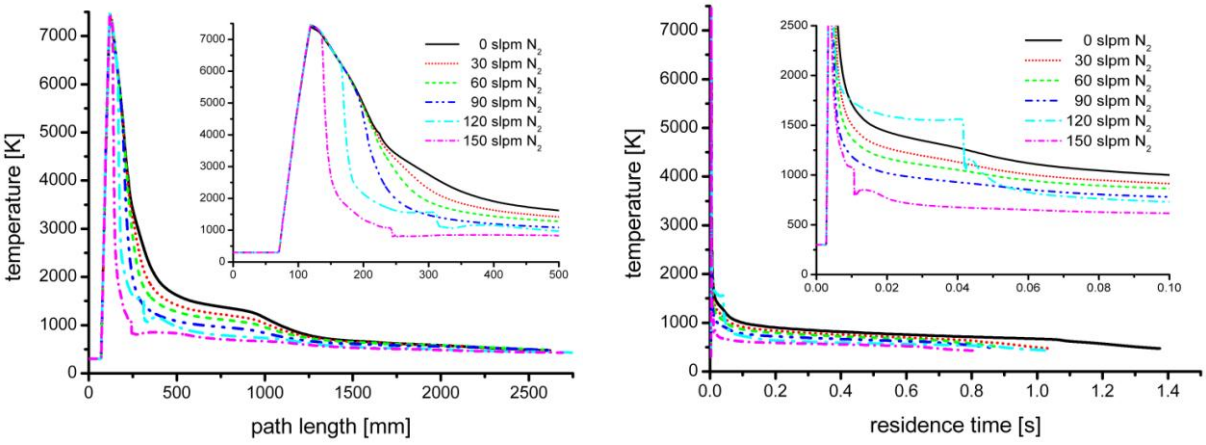

Figure 4-48: influence of N_2 quench gas flow rate on the temperature profile as a function of the path length (left) and residence time (right). The trajectories are pathlines released from the edge of the precursor inlet. Modelled conditions: 5-27-80/6, 10 kW, 40 kPa, quenched at z = 63 mm (surface equivalent to 8 x ϕ 2 mm).

The left graph shows that the temperature decreases stronger with increasing quench gas flow rate as a function of the path length. The right graph shows that the

temperature decreases stronger with increasing quench gas flow rate as a function of the residence time, except for quenching with 120 slpm N_2. If the 120 slpm case is compared to the 90 and 150 slpm cases one sees that despite the longer path length, the particles have the shortest residence time in temperature region (3500-875 K) in which the particle growth occurs, when the plasma is quenched with 90 or 150 slpm N_2.

The quench rates, calculated for the different quench gas flow rates, are presented in Table 4-17 and expressed in $K.s^{-1}$ and $K.m^{-1}$. The rates are calculated from the difference between the maximum temperature and the temperature after a certain time (Δ time) of distance (Δ z) on the pathline (released from injector edge).

Table 4-17: quench rates in $K.s^{-1}$ and $K.m^{-1}$ as a function of the N_2 quench gas flow rate and different time and size intervals on the pathlines. The rates are calculated from the difference between the maximum temperature and the temperature after a certain time (Δ time) or distance (Δ z). The columns titled with maximum represent the maximal quench rate on the pathline or axis. Modelled conditions: 5-27-80/6, 10 kW net power input, 40 kPa, quenched at z = 63 mm (surface equivalent to 8 x ϕ 2 mm).

N_2 quench gas flow rate [slpm]	Δ time $1x10^{-2}$ s $[K.s^{-1}]$	Δ time $1x10^{-3}$ s $[K.s^{-1}]$	maximum $[K.s^{-1}]$	Δ z 50 mm $[K.m^{-1}]$	Δ z 100 mm $[K.m^{-1}]$	maximum $[K.m^{-1}]$	maximum at axis $[K.m^{-1}]$
0	$5.9x10^5$	$3.9x10^6$	$1.6x10^7$	$3.2x10^4$	$2.6x10^4$	$6.0x10^5$	$8.6x10^4$
30	$6.1x10^5$	$4.1x10^6$	$1.6x10^7$	$3.4x10^4$	$2.7x10^4$	$6.0x10^5$	$8.5x10^4$
60	$6.2x10^5$	$4.3x10^6$	$1.7x10^7$	$3.5x10^4$	$2.7x10^4$	$6.0x10^5$	$1.1x10^5$
90	$6.4x10^5$	$5.0x10^6$	$1.8x10^7$	$4.4x10^4$	$2.7x10^4$	$6.0x10^5$	$2.3x10^5$
120	$5.8x10^5$	$5.0x10^6$	$3.7x10^7$	$5.6x10^4$	$4.4x10^4$	$6.0x10^5$	$4.1x10^5$
150	$6.6x10^5$	$5.6x10^6$	$6.9x10^7$	$6.3x10^4$	$1.1x10^5$	$6.2x10^5$	$6.4x10^5$

The table shows that the quench rates increase with increasing quench gas flow rate. An exception is at 120 slpm quenching gas at the largest Δtime, because of the change in the flow "regime", see Figure 4-48. Between 90 and 120 slpm is the transition where the plasma flows outside the ring (see also Figure 4-24 and Figure 4-26 on page 80 - 82).
The maximum quench rates for a Δ z are all the same, except for the highest quench rate. This means that the maximum quench rate for quench gas flow rates smaller than 120 slpm is positioned in a region where the quench gas has no influence on the quench rates, otherwise an increase with increasing quench gas flow rates would be expected. First at a quench gas flow rate of 150 slpm the maximum quench rate shifts to a position further downstream (higher z value) where it is determined by the quench gas flow rate.
The last column, which gives the maximum quench rates at the axis, has to be considered with precaution, since not all of the values are meaningful, because at high quench gas flow rates the particles do not follow the trajectory along the axis. It is furthermore shown that the magnitude of the quench rates are very much subject to the size of the picked intervals (compare for example the quench rates at Δ z 50 and 100 mm) and therefore the values in the literature should be taken with care.

Summary of section 4.3.4.4
The value of the quench rates depends very heavily on the size of the intervals. There is a threshold value of the quench rate beyond which the trajectories are

deflected to positions outside of the quenchring. An increasing quench gas flow rate does not always result in smaller particles.
The temperature effect of the quenching has a stronger influence on the particle growth than the dilution effect (reduction of the monomer concentration).

4.3.5 Particle growth model: validation of agglomeration

Figure 4-49 shows the dependence of the number of primary particles per aggregate, residence time, and temperature as a function of the axial distance.

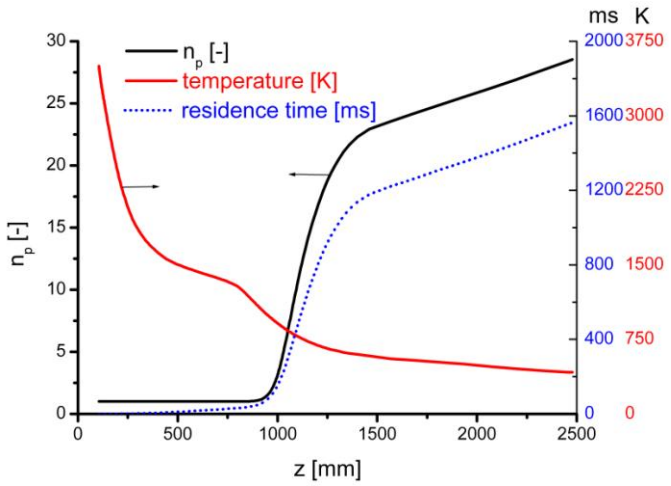

Figure 4-49: calculated number of primary particles per aggregate, residence time, and temperature as a function of z. Modelled plasma parameters: 3-12-80/6, 10 kW net input power, 40 kPa, feed rate 2.0 g.min^{-1}, no quenching.

The temperature decreases with increasing z value and experiences a stronger decrease around z = 900 mm. The residence time increases slowly up to z = 950 mm to increase very rapidly to z = 1500 mm. The number of primary particles per aggregate shows the same behaviour except for the region up to 850 mm where the number of primary particles remains constant.
Figure 4-49 shows that the agglomeration takes place in the cone part (z = 933 – 1483 mm) of the ICP equipment, see Figure 3-1 (page 41). The strong agglomeration occurs here, because of the temperature being in the sintering region combined with the long residence time (about 1100 ms). The same figure also shows that this region of the cone part is crossed very slowly for the conditions. To check this prediction, a sampling system (see section 3.4) has been used to take samples at different axial positions.

Figure 4-50 shows the particles sampled at z = 260 mm (left) and sampled close to the filter (right). From the SEM images of the synthesised products, it is clear that most of the precursor particles have been (partially evaporated), see also section 4.3.1. (Please take into consideration that the injected Si precursor particles have a flake-like shape and particle size distribution ranging from +44-16 µm according to the supplier.)

These SEM pictures clearly show the difference between the particles sampled at low and high z values. At low z values, close to the torch exit, the particles are non agglomerated, while at higher z values the sampled particles are mostly agglomerated. Furthermore, some nanowires can be found at higher z values.

The particle growth model predicted a number of 4 primary particles in the hard agglomerate and a particle size of 57 nm. In order to validate these numbers, SEM images of small agglomerates at a large magnification should be made.

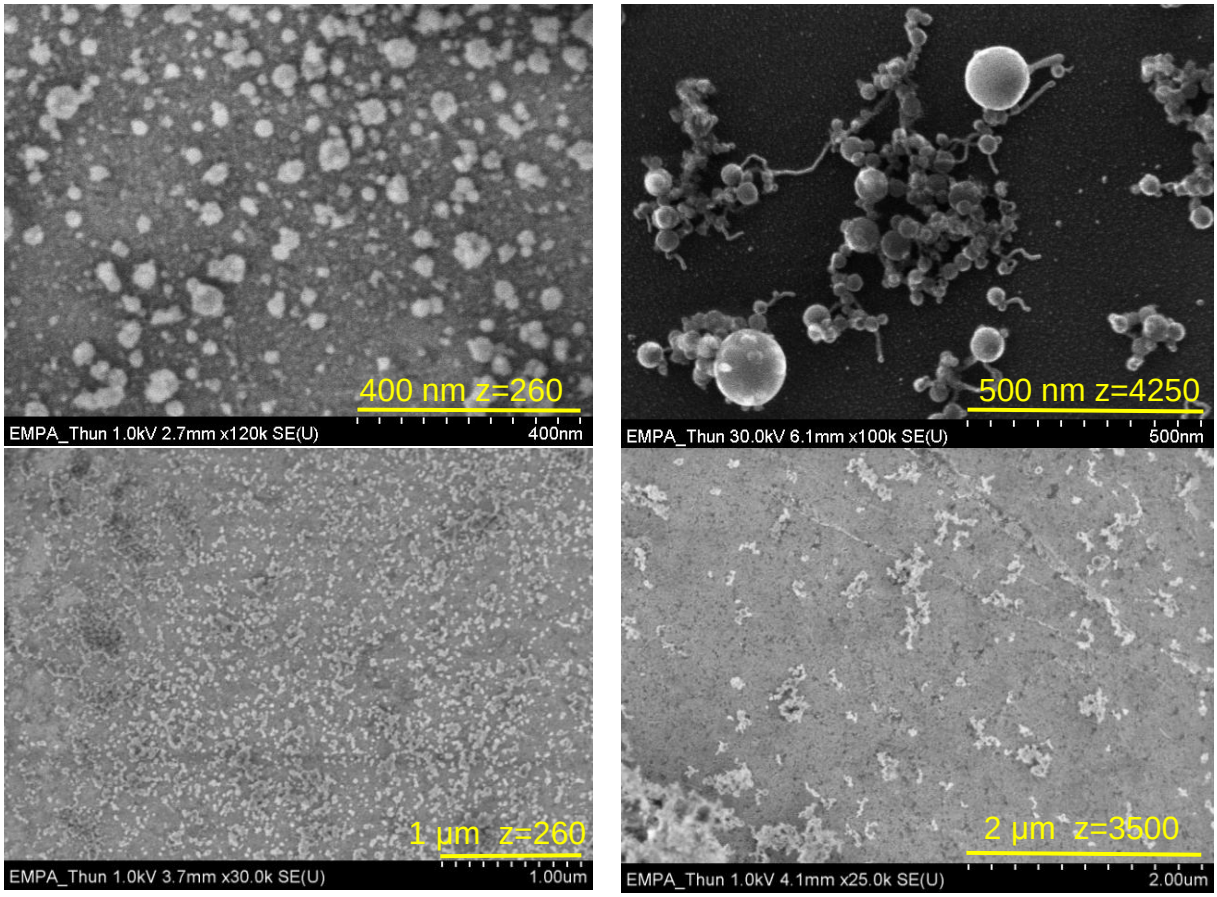

Figure 4-50: SEM pictures of Si particles extracted at different heights. Top: Si nanopowder collected at z = 260 mm (left) and at the sampling filter (z = 4250 mm, 7 in Figure 3-1, right). Plasma conditions: 3-12-80/6, plate power 15.6 kW, 40 kPa, feed rate 1.9 g.min^{-1}, quenching: 2.8 slpm Ar at z = 121 mm. Bottom: Si nanopowder as collected at z = 260 mm (left) and at z = 3500 mm. Plasma conditions: 3-12-80/6, plate power 15.6 kW, 40 kPa, feed rate 2.2 g.min^{-1}, quenching: 56 slpm N_2 at z = 121 mm.

Figure 4-51 shows such a high resolution SEM image of a small agglomerate.

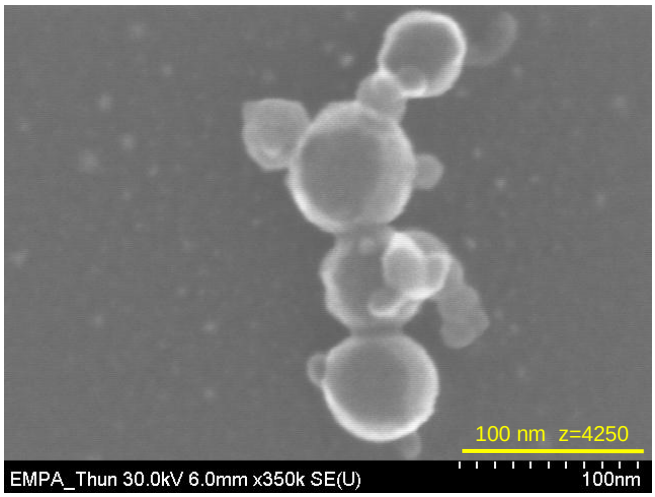

Figure 4-51: SEM image of Si nanoparticles extracted at the sampling filter (z =4250 mm). Plasma conditions: 5-27-80/6, 15.6 kW plate power, 40 kPa, feed rate 3.0 g.min^{-1}, 2.8 slpm Ar quenching at z = 121 mm.

From this SEM image it is very difficult to differentiate between hard and soft agglomerates (presence of sintering necks). The agglomerate shows some particles around 60 nm, but also particles which are much smaller.
Also images made in the Scanning Transmission Electron Microscope (STEM) mode do not give a clear differentiation (Figure 4-52, right). Although these electron microscope images were recorded at the same position, the STEM mode shows much more particles. The “extra” particles in the right image are particles which are on the back side of the TEM grid and are only visible in the transmission mode. The SEM mode has only an electron detector at one side of the grid, while the STEM mode has electron detectors at the top and bottom side of the grid.

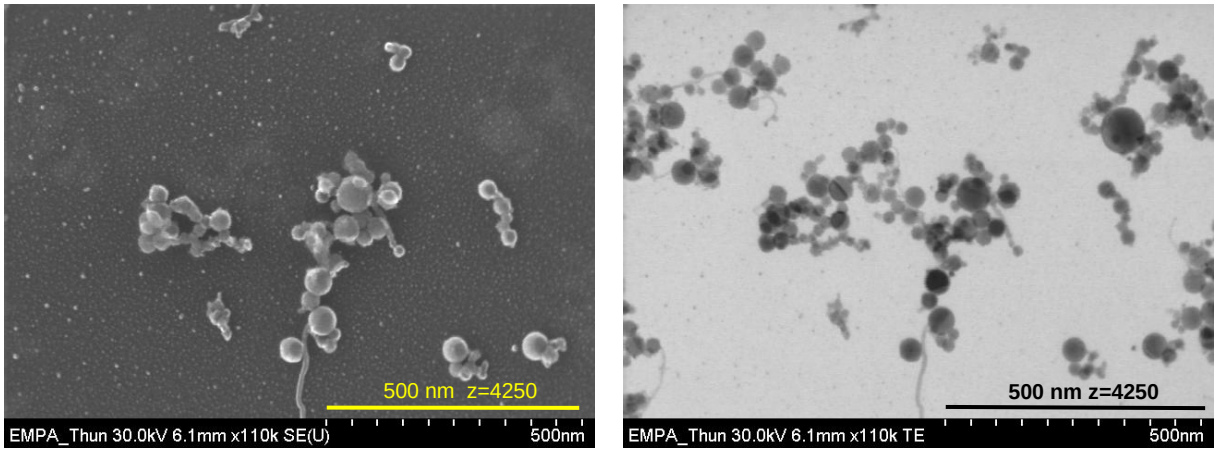

Figure 4-52: Si nanopowder as collected at the sampling filter (z = 4250 mm). Left: SEM mode. Right: STEM mode. Plasma conditions: 3-12-80/6, plate power 15.6 kW, 40 kPa, feed rate 1.9 g.min^{-1}, quenching: 2.8 slpm Ar at z = 121 mm.

Figure 4-50 to Figure 4-52 show TEM grids which are only covered to a small degree. Figure 4-53 shows two samples that were extracted at a low and high z value and which are completely covered. For a better investigation of the particle size and size distribution, the sampling time should be reduced in the order of half a second. However, this sampling time depends on the particle concentration, which is a function of the particle feed rate and sampling height.

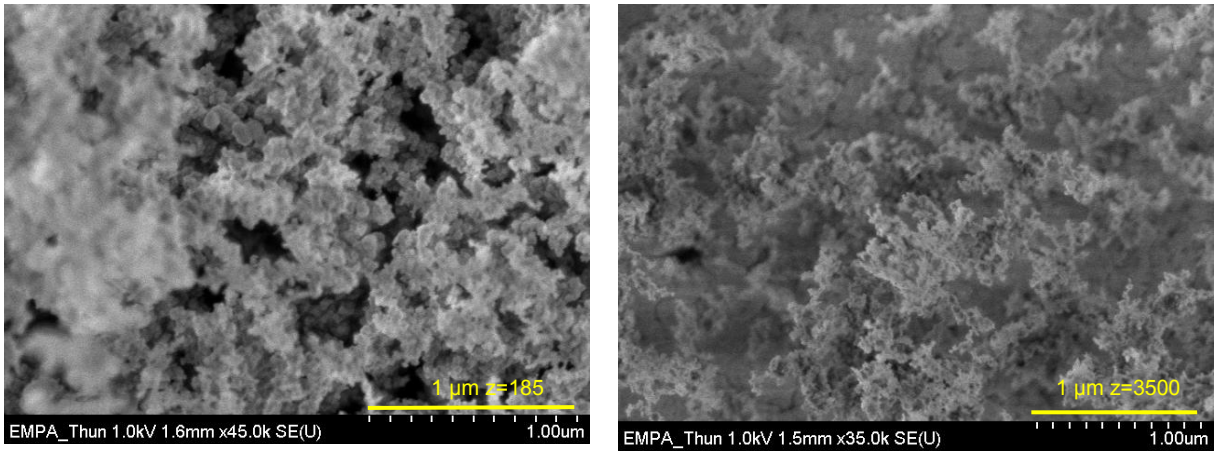

Figure 4-53: SEM pictures of Si particles extracted at different heights. Left: Si nanopowder as collected at z = 185 mm and at z = 3500 mm (right). Plasma conditions: 3-12-80/6, plate power 15.6 kW, 40 kPa, feed rate 2.6 g.min^{-1}, quenching: 2.8 slpm Ar at z = 121 mm.

By comparing samples extracted at different heights, also the difference between the different agglomeration degrees can be found. As already shown in Figure 4-49, an agglomerate is equal to just one primary particle at low z values, whereas it is built up out of many primary particles at high z values. When the plasma has a high degree of particle loading (a high precursor feed rate), the sample containing particles with a small degree of agglomeration will show a dense structure (left image in Figure 4-53), while the sample containing a high degree of agglomeration shows a more open and fluffy structure (right image in Figure 4-53).

It is also interesting to note that the particles at z =185 mm are larger than at z =3500 mm. This was not expected a priori and also not from the predictions of the growth model.
First of all it could be caused by an incomplete evaporation of the precursor particles at this height, because the CFD modelling has shown that the 3500 K isotherm is reached at z = 104 mm An incomplete evaporation would result in much larger particles downstream since the temperature at the sampling position is well below the boiling point of Si (Figure 4-49). As the vaporisation rate of the precursor is very small at this temperature, the decrease of the particle diameter can be neglected. This however means that the particles at z = 3500 mm should be at least as large as they were at z = 185 mm, which is not the case (Figure 4-53).
Figure 4-54 shows another example of a completely covered TEM grid extracted at z = 185 mm.

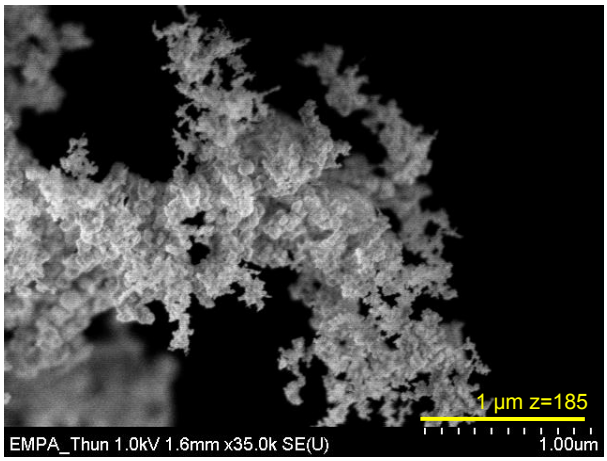

Figure 4-54: SEM picture of Si particles extracted at z = 185 mm. Plasma conditions: 3-12-80/6, plate power 15.6 kW, 40 kPa, feed rate 1.4 g.min^{-1}, quenching: 2.8 slpm Ar at z = 121 mm.

Figure 4-54 shows that at z =185 mm also much smaller particles in the agglomerates and have a more open structure than shown in Figure 4-53 can be obtained. Thus the incomplete evaporation will not be the reason for the presence of the large particles in Figure 4-53.

The other explanation is growth instead of incomplete evaporation of injected particles. By keeping the TEM grid in the plasma too long, the captured particles will heat up and therefore start or continue to sinter on the grid. Since the particles are very small it can be expected that the sintering temperature is lower than for the micro sized particles, resulting in the formation of larger particles.

Summary of section 4.3.5
With only SEM or TEM it is very difficult to differentiate between hard and soft agglomerates, therefore the results of the in-line sampling should be taken with precaution. Furthermore, the question remains how representative the sample is for the complete product.
The trends as predicted by the particle growth model concerning the agglomeration behaviour are confirmed by SEM pictures and in-situ measurements.
The growth model forecasts the main part of the agglomerate growth to happen in the cone region of the equipment, which is supported by experiments.
The comparison of the particle size aspects of the growth model (like influence of quench gas flow rate, quench design, and quench height) are made in section 5.1.

4.4 Discussion

This chapter has shown that several compromises have to be made to find an optimal process parameter set for the synthesis of nanoparticles.
It already starts with the plasma gas flow rate. A lower carrier gas flow rate does not cool the plasma that much at the axis as a higher flow rate, but gives the precursor only a small momentum, whereas a certain momentum is required to penetrate the plasma. A high central gas rate stabilises the plasma better than a low central gas rate, but more gas has to be heated up.

According to the growth model a high pressure is beneficial for the evaporation of the precursor particles, but results in the formation of larger nanoparticles. The same is true for a high power (a higher temperature). A higher precursor feed rate results in a higher throughput, but also in a stronger cooling of the plasma. The consequence will be the presence of larger particles, which have not been evaporated completely, in the product. The higher monomer concentration (assuming that all the precursors are evaporated) leads to more product, but also larger particles.
Thus the process has to be carried out with moderate carrier gas, central gas, pressure, power, and feed rate, in order to have a compromise between the evaporation and growth process.

Also compromises have to be made with regards to the optimal quench parameters. Quenching is the more effective at higher temperatures, as shown by a higher quench rate. But it also means that more gas has to be used to reduce the temperature to a specific temperature where no growth occurs, than when the quenching is carried out at already a lower temperature. Although N_2 is more efficient in reducing the temperature than Ar, it can introduce chemistry, which is not always desired. For the quench design there is also a trade-off between the number and diameter of the nozzles. The more nozzles are present, which becomes eventually a slot, the more homogeneous the temperature distribution gets. But a larger number of nozzles also mean a lower flow rate (velocity) per nozzle at a constant total flow rate and thus a smaller momentum. To avoid the smaller momentum, the diameter can be adapted to maintain the same surface, achieved by a smaller diameter for more nozzles (and vice versa) resulting in the same momentum per nozzle. However, when the nozzle gets smaller it can not hold the momentum upright for a long distance as a larger nozzle could. Consequently the quench ring diameter (not discussed in this work) would have to be adapted to the nozzle number and diameter. The ring diameter is limited to a minimal value, which depends on the thermal load the ring can withstand and which will not immediately result in a deflection of the plasma gas flow around the quench ring.

A small diameter will have a stronger quenching effect than a large ring diameter, because the nozzles are closer to plasma and will therefore not loose much momentum. The plasma could, however, be deflected earlier around the small quench ring and will result in uncontrolled trajectories, especially at higher quench gas flow rates. The higher the quench gas rate is the better the penetration and the higher the dilution, but the stronger the deflection of the plasma gets, resulting in uncontrolled trajectories, which could also lead to a broader size distribution. At very high quench rates the plasma can be pushed back into the torch and increases the costs of the process.
Furthermore is also the nozzle angle of importance on the quenching effect (only a 15° angle has been investigated); the nozzles perpendicular to the plasma will show a higher penetration than nozzles having an angle directed with the plasma flow direction. But the nozzles perpendicular to plasma will deflect the plasma earlier around the quench ring than the nozzles with an angle. The angle is also restricted to certain limits: no angle at all represents the perpendicular case, whereas the angle is set to be too parallel to the plasma flow no quenching effect will occur (only conductive heat transfer, which is not so fast as convective heat transfer).

The quenching height is also an important parameter. When the plasma is quenched close to the torch exit, i.e. at a higher temperature, it results in a lesser penetration than quenching with the same quench gas rate further away from the torch (a lower temperature). The plasma flow, however, is not deflected so early when quenched close to the torch exit.

Thus to get to the optimal parameter set for the synthesis of nanoparticles, a lot of compromises have to be made. The compromises are a function of the desired product characteristics.

The predictions from the CFD as well as from the particle growth models have been investigated experimentally. The results of these experiments are described in the next chapter.

5 Nanoparticle synthesis

5.1 Synthesis of Silicon nanopowders

The optimal plasma gas composition has been identified for the nanoparticle synthesis from the heat source and particle growth model and was said to be 3-12-80/6. The influence of the pressure, power, quench design, quench height, and quench gas flow rate on the particle size for the optimal plasma gas composition is being dealt with in this chapter. The modelled temperature and velocity profiles of the (3-12-80/6, 40 kPa, and 10 kW net power input) conditions are shown in Figure 5-1.

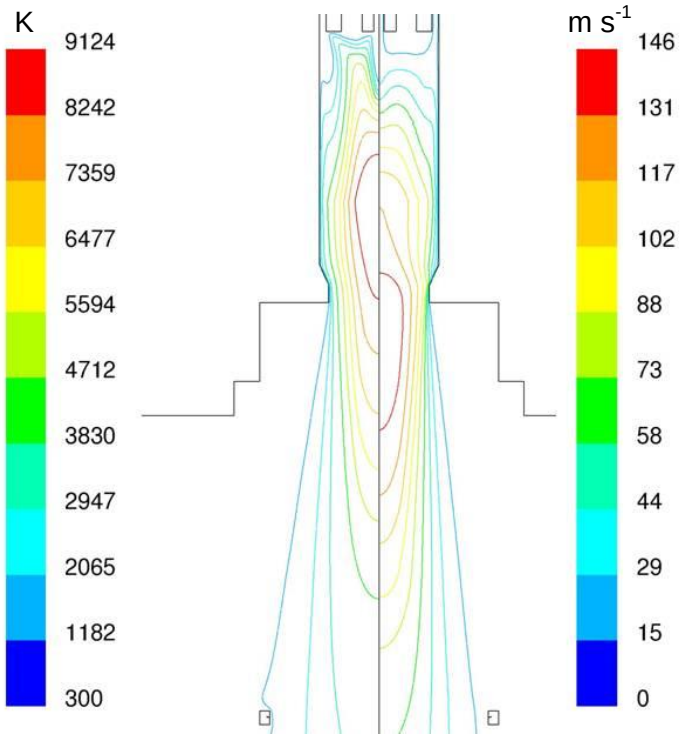

Figure 5-1: modelled temperature and velocity profiles used to determine the optimal quenching height and calculate the residence time. Modelled 2D parameters: 3-12-80/6, 10 kW net power input, 40 kPa.

5.1.1 Silicon precursor powder

The silicon precursor (described in 3.3.1.2) had a flake-like shape and the size distribution had a d_{10} of 28 µm and a d_{90} of 93 µm. When one is talking about ICP synthesis of nanoparticles, it is important to know what would be the maximal quantity and size of precursor that can be evaporated. Therefore a “back-of-the-envelope” calculation was performed, to determine the maximum precursor feed rate that could evaporated under the current conditions. The heat of evaporation for one kilogram Si amounts 13,725 kJ and the heat of fusion 1,800 kJ. Figure 5-2 shows the required energy for the complete evaporation of 1 kg solid divided into four stages. Stage 1 concerns the heating to the melting point; stage 2 is the melting of the particle, stage 3 deals with heating the material from the liquid phase to the boiling point; stage 4 is the complete evaporation.

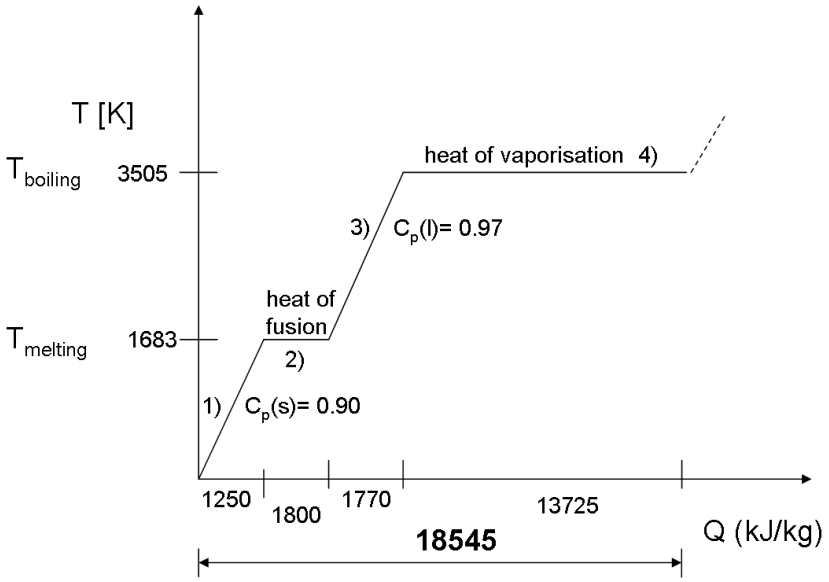

Figure 5-2: energy required for the evaporation of 1 kg of Si divided into four stages: 1) heating of the solid from room temperature to the melting point, 2) melting, 3) heating of the melt to the boiling point, 4) boiling. The average specific heat for the solid and liquid phase has been displayed. (The figure is not scaled.)

From Figure 5-2 it can be seen that the total amount of energy required to vaporise 1 kg of Si amounts 18.5×10^3 kJ. Assuming that the 10 kW net power in the plasma is solely available for the evaporation of Si, about 32 $g.min^{-1}$ can be evaporated. The energy losses caused by radiation (plasma), cooling (wall), etc., are already included in this number as this was determined with the enthalpy probe measurements, thus 10 kW is available for the evaporation process.
However, the energy of the plasma is useful as long as the temperature is above the boiling point of the precursor: the energy left in the plasma after the temperature has decreased below the boiling point is wasted. Also, the influence of the evaporating particles on the plasma temperature is not included in this calculation. Furthermore, the precursor is not distributed over the entire plasma, meaning that not all of the plasma energy is available for the particle evaporation. Taking all those factors into consideration it can be concluded that the actual evaporation rate will be much lower than 32 $g.min^{-1}$.
There were no calculations made of the particles in-flight.

5.1.2 Plasma experiments with Silicon

The synthesised nano particles were separated from the gas phase by a sampling filter, (7 in Figure 3-1) and transferred to a glove-box (Ar atmosphere; 50 ppm < H_2O and 100 ppm < O_2). Some of the samples were taken out of the glove-box for characterisation by electron microscopy, BET analysis, X-ray diffraction, and TGA/DTA measurements.

The mean particle size, as determined by BET analysis, was calculated according to equation 2-9 (page 40), in which the specific mass of the silicon nanoparticles was assumed to be 2330 $kg.m^{-3}$. The results of the BET measurements showed a maximal deviation of 12% per experiment, see page 129.

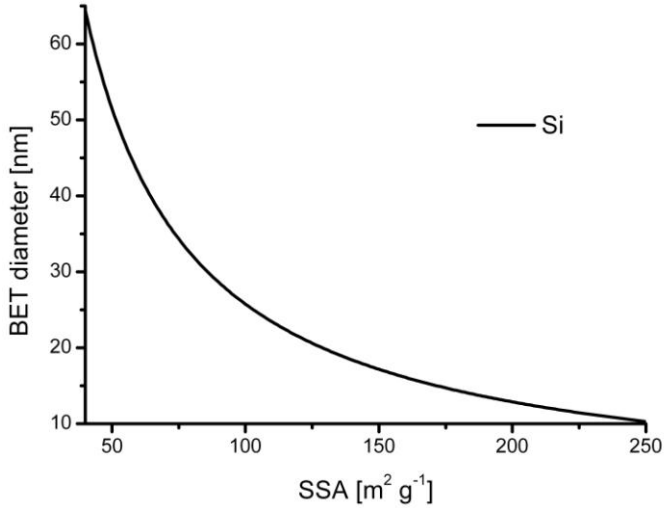

Figure 5-3: BET equivalent diameter as a function of the specific surface area (SSA) for Si.

The figure shows a decreasing BET diameter with increasing specific surface area (SSA).

Figure 5-4 shows a particle loaded plasma quenched with a two-nozzle system with 56 slpm Ar.

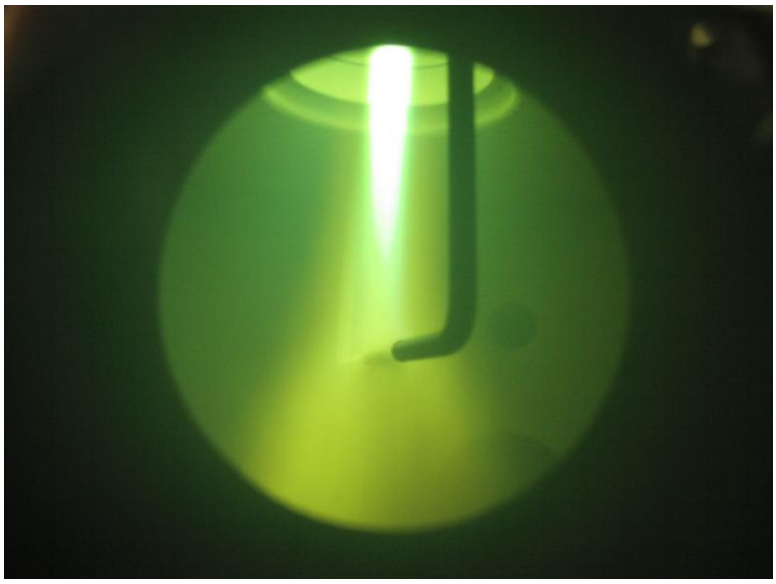
Figure 5-4: Si loaded plasma (3-12-80/6, 40 kPa, 15.6 kW plate power (around 10 kW net power input), quenched at z = 121 mm with 56 slpm Ar quenched with two nozzles (ϕ 4 mm, 64 mm distance).

The image shows the splitting of the vapour cloud and particles into two parts perpendicular to the nozzle axis. Table 5-1 shows the result of an experiment with a two-nozzle design quenched with two different quench rates.

Table 5-1: result of BET measurements for the two-nozzle design (see section 4.2.3 for the quench design). Experimental conditions: 3-12-80/6, plate power 15.6 kW, 40 kPa, quench height z = 121 mm (2 x ϕ 4 mm).

Quench gas flow rate [slpm]	Injector position z [mm]	Feed rate [g.min^{-1}]	SSA [m^2.g^{-1}]	d_{BET} [nm]	d_{model} [nm]
2.8 Ar	-62	2.6	64	40	55
56 Ar	-65	2.4	90	29	38

A higher SSA is found by quenching with 56 slpm Ar, which is in agreement with the particle growth modelling.

Figure 5-5 shows SEM images of Si nanoparticles synthesised by quenching with 56 slpm Ar with the two-nozzle quench design. The samples were extracted at z = 260 mm (top), z = 3500 mm (bottom left) and z = 4250 mm (bottom right).

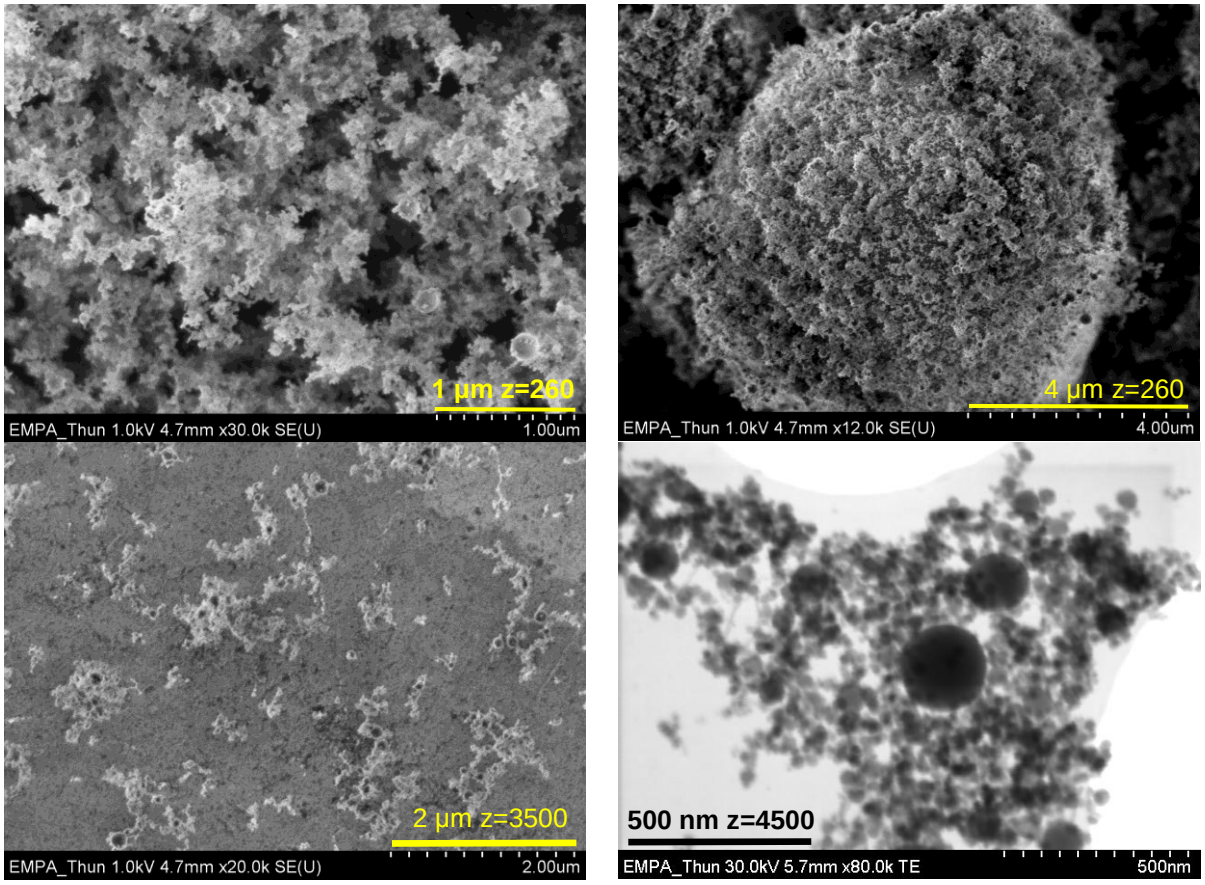

Figure 5-5: SEM pictures of Si nanoparticles extracted at z = 260 mm (top left and top right), at z = 3500 mm (bottom left) and at z = 4250 mm (bottom right). Process parameters: 3-12-80/6, plate power 15.6 kW, 40 kPa, feed rate 2.4 g.min^{-1}, quenching: 56 slpm Ar at z = 121 mm (2 x ϕ 4 mm).

All the images show a broad size distribution, with particles up to approximately 200 nm, which is inherent to quenching with the two-nozzle design (Figure 4-20), due to the different residence times. The top right image shows a partially vaporised particle encapsulated with nanoparticles. The size of the agglomerates is described in section 4.3.5.

The two-nozzle system has been replaced with an eight-nozzle system (ϕ 2 mm) with as main objectives: improvement of the symmetry of the temperature profile and the particle trajectories in order to result in smaller particles and a narrower size distribution. Figure 5-6 shows a particle loaded plasma quenched with 56 slpm Ar using the 8 x ϕ 2 mm design.

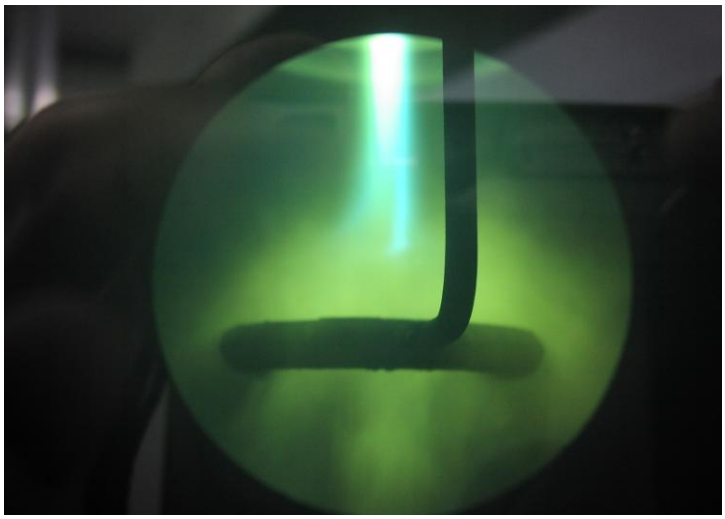

Figure 5-6: Si loaded plasma (3-12-80/6, 40 kPa, 15.6 kW plate power, quenched at z = 121 mm with 56 slpm Ar quenched with an eight-nozzle ring (ϕ 2 mm).

As with the two-nozzle design, the vapour cloud and particles follow very different trajectories at this quench flow gas rate and quench design. Some particles flow through the ring and some flow around the ring.

The BET diameters, obtained during synthesis of Si using an eight-nozzle design (8 x ϕ 2 mm, see Figure 4-28), are shown in Table 5-2 as a function of the quench gas flow rate.

Table 5-2: results of BET measurements for the eight-nozzle ring design (see 4.2.3) as a function of the quench gas flow rate. Experimental conditions: 3-12-80/6, plate power 15.6 kW, 40 kPa, quench height z = 121 mm (8 x ϕ 2 mm).

Quench gas flow rate [slpm]	Injector position z [mm]	Feed rate [g.min^{-1}]	SSA [m^2.g^{-1}]	d_{BET} [nm]	d_{model} [nm]
2.8 Ar	-73	3.0	69	37	57
2.8 Ar	-65	1.9	101	25	50
28 Ar	-65	2.1	91	28	47
42 Ar	-65	1.8	97	27	42
56 Ar	-65	1.8	123	21	36
56 Ar	-73	2.4	107	24	38
56 Ar	-65	2.6	96	27	39

The trends, as predicted by the growth model are confirmed by the experiments; the particle size decreases and the SSA increases with increasing quench gas flow rate. The model forecasts a particle diameter of 50 nm for a feed rate of 1.9 g.min^{-1} and 57 nm for 3.0 g.min^{-1} compared to the experiments where a BET equivalent diameter of 25 nm for 1.9 g.min^{-1} and 35 nm for 3.0 g.min^{-1} were found. Also the trend of a decreasing particle diameter with decreasing feed rate (Table 4-13) has been confirmed experimentally. A modelled diameter of 37 nm is found for 2.0 g.min^{-1} and 60 slpm Ar quenching gas against a d_{BET} of 21 nm for 1.8 g.min^{-1} and 56 slpm Ar. The fact that the SSA for 42 slpm and 56 slpm Ar are almost the same is caused by the difference in feed rate. The size reduction caused by the increased quench gas flow rate is countered by the higher precursor feed rate (see Table 4-13).
By comparing the diameter to the ones found in Table 5-1, it was determined that the eight-nozzle design is able to synthesise smaller particles. The SSA has been increased by almost 20% going from the two-nozzle to the eight-nozzle (ϕ 2 mm) design.

Figure 5-7 shows SEM images of nanoparticles obtained after quenching with the eight-nozzle design. These images show a narrower particle size distribution for the product (z > 3500 mm) than for the two-nozzle system (compare to Figure 5-5). This statement however, has to validated with for example photon correlation spectroscopy (PCS) experiments.
Furthermore, the comparison of the products, extracted from the sampling filter (right images in Figure 5-7), show that quenching with 56 slpm seems to result in a smaller size distribution than is the case without quenching. As the plasma jet is completely cut by quenching with the eight-nozzle system at 56 slpm Ar, all the particles encounter strong cooling. Whereas the plasma is not completely penetrated or cut-off for the two-nozzle system at 56 slpm Ar, some particles face strong cooling while others do not, which will result in a broader size distribution.

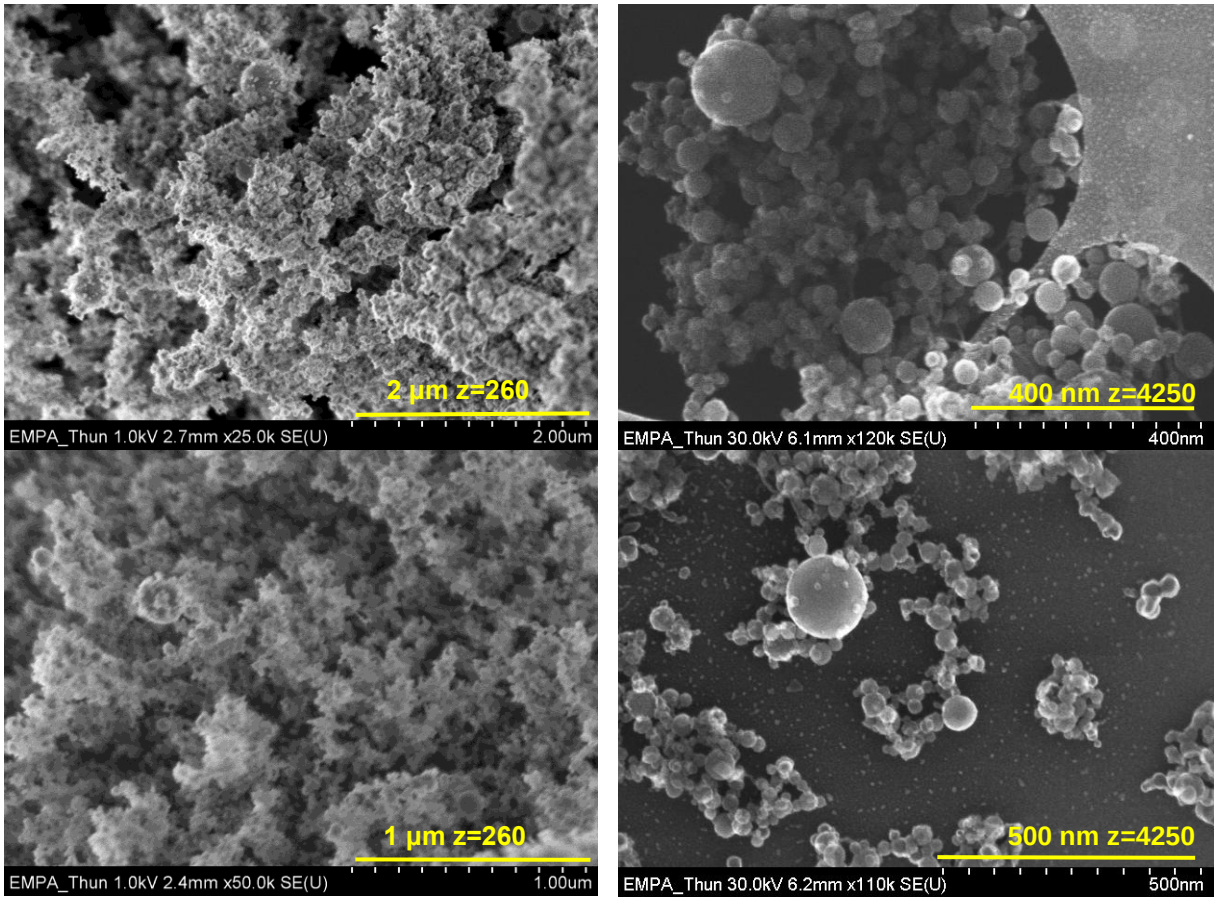

Figure 5-7: SEM images of Si nanoparticles synthesised at high and low quench gas rates. Top left: 2.8 slpm Ar and 1.9 g.min^{-1}, extracted at z = 260 mm and z = 4250 mm (top right). Bottom left: 56 slpm Ar and 1.8 g.min^{-1}, extracted at z = 260 mm and z = 4250 mm (bottom right). Process parameters: 3-12-80/6, 15.6 kW plate power, 40 kPa, quenching at z = 121 mm (8 x ϕ 2 mm).

The second experiment without quenching, described in Table 5-2, leads to a very high SSA of 101 m^2.g^{-1} (d_{BET} of 25 nm), which is higher than for many other experiments where quenching was applied. This looks peculiar, but by having a closer look to the top right image in Figure 5-7, also many particles much larger than 25 nm are found. The low feed rate (1.8 g. min^{-1}) in comparison to the other experiments is contributing to this observation. This example illustrates the disadvantage of the BET measurement, because the influence of the small particles

is overestimated in this method and no information on the particle size distribution is obtained.

To avoid the particle dispersion around the quench ring, as observed for the two-nozzle and eight-nozzle design, the nozzles in the quench ring have been giving a 15° angle in the direction of the plasma gas flow. The purpose of the angle was to let the quench gas act as a “water jet pump” and thereby sucking the particle loaded plasma gas through the quench ring. This will force all the particles to follow the same or similar trajectories

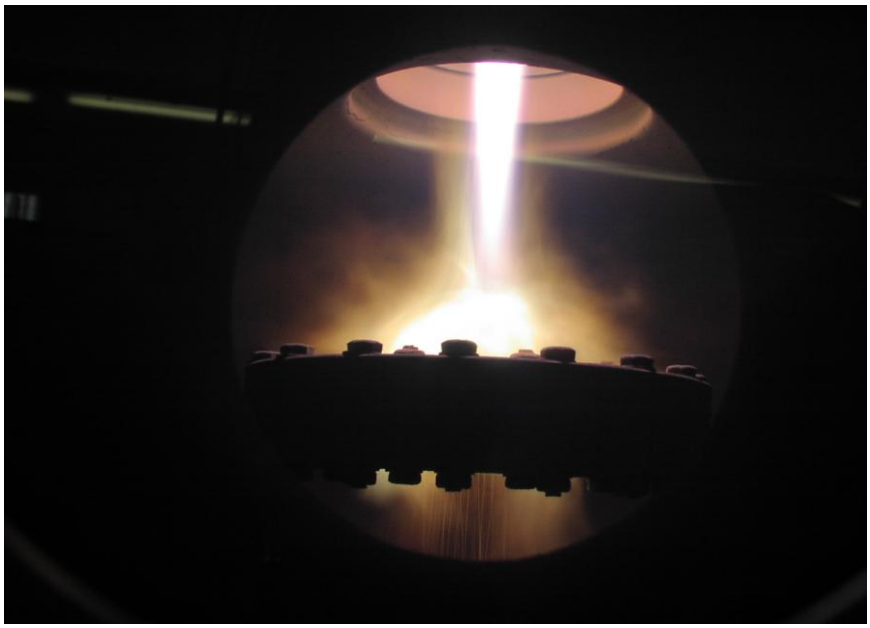

Figure 5-8: Si loaded plasma (3-12-80/6, 40 kPa, 15.6 kW plate power, quenched at z = 121 mm with 56 slpm Ar quenched with an eight-nozzle ring with angle (ϕ 1.5 mm).

The introduction of the angle has improved the situation for these process conditions, although there is still some flow around the ring.

The experiments with the eight-nozzle angled design were divided into four parts: influence of precursor feed, pressure, power, and quenching height Table 5-3 show the SSA of quenching experiments with the eight-nozzle with angle design as a function of the precursor feed rate on the SSA.

Table 5-3: results of BET measurements for eight nozzles (angled) ring design as a function of feed rate and quench gas flow rate. Experimental conditions: 3-12-80/6, plate power 15.6 kW, 40 kPa, quenching at z =122 mm (8 x ϕ 1.5 mm, angled).

Quench gas flow rate [slpm]	Injector position z [mm]	Feed rate [g.min^{-1}]	SSA [m^2.g^{-1}]	d_{BET} [nm]	d_{model} [nm]
2.8 Ar	-62	1.3	112	23	46
2.8 Ar	-62	1.5	124	21	48
2.8 Ar	-62	2.1	91	28	52
2.8 Ar	-62	2.7	82	31	55
2.8 Ar	-62	2.9	78	33	56
2.8 Ar	-62	4.8	75	34	64
2.8 Ar	-62	6.9	62	42	70
56 Ar	-65	1.8	118	22	36
56 Ar	-62	1.4	135	19	34

The trend of an increasing particle diameter with an increasing precursor feed rate, as predicted by the particle growth model, is confirmed by the experiments. The lower the feed rate, the stronger is the effect on the particle size, which causes the particle diameter to decrease to low values even without quenching as shown for the first two experiments in Table 5-3.
The SSA of the eight-nozzle (ϕ 1.5 mm) design with angle showed no increase in comparison to the eight-nozzle (ϕ 2 mm) design.

Figure 5-9 shows the SEM images of samples for different precursor feed rates.

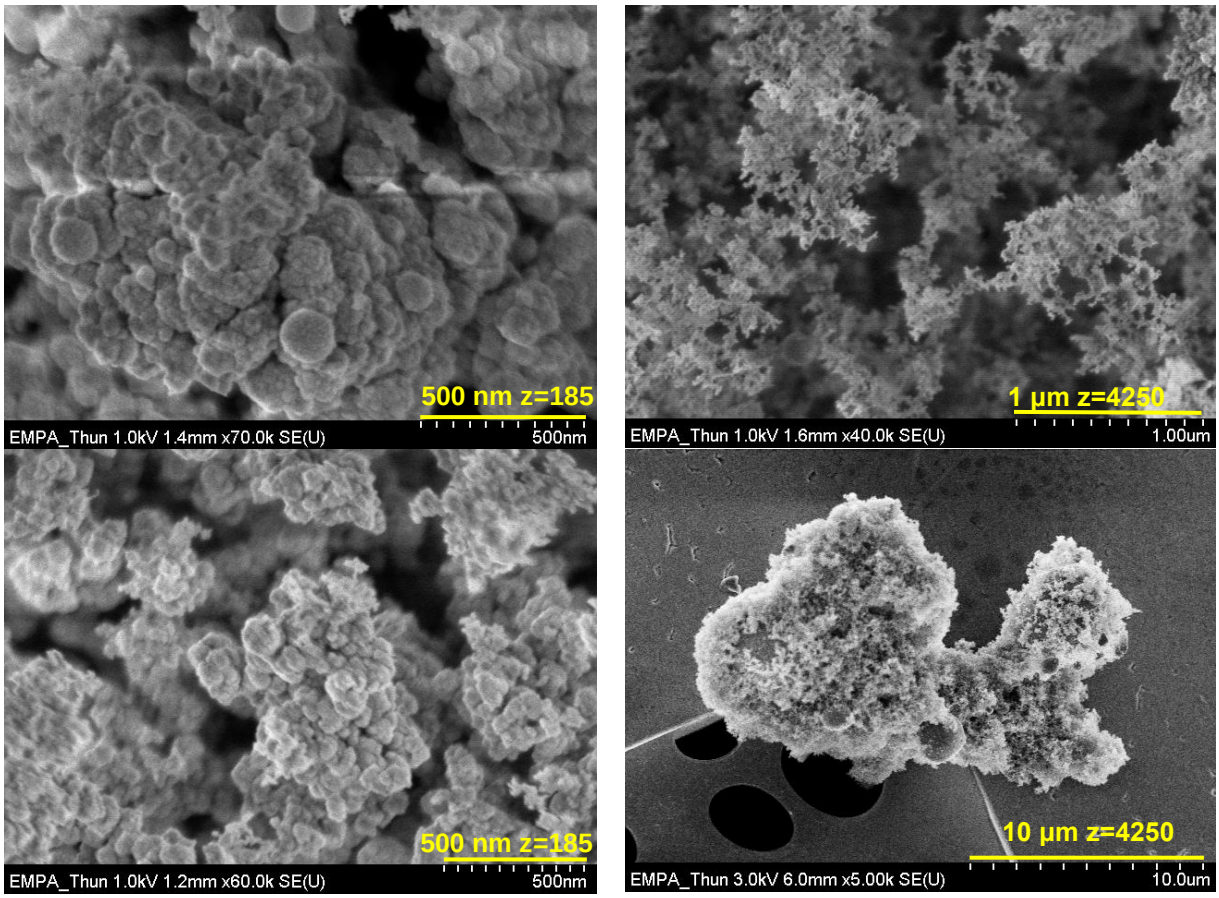

Figure 5-9: SEM images of Si nanoparticles synthesised with high and low precursor feed rates. Top left: 1.4 g.min^{-1}, extracted at z = 185 mm and z = 4250 mm (top right). Bottom left: 2.6 g.min^{-1}, extracted at z = 185 mm and z = 4250 mm (bottom right). Process parameters: 3-12-80/6, 15.6 kW plate power, 40 kPa, quenching: 2.8 slpm Ar at z = 121 mm (8 x ϕ 1.5 mm, angled).

The SEM images show smaller particles for the lower precursor feed rate (top images) compared to higher feed rates (bottom). Although the particles at the top left image seem to be larger than the particles at the comparable image at the bottom left, the latter does not show the “sub” structures visible at the top left image.
Furthermore is the amount of large incomplete melted particles found in the products lower for the smaller feed rate. This is also expected as the energy available in the plasma decreases, when the feed rate, thus the particle load, increases.
It is also assumed that the chance of particles being in the “shadow” of others rises drastically and therefore will these particles receive less heat from the plasma, resulting in a non-complete vaporisation.

The influence of the plate power on the SSA is investigated for the eight-nozzle angled design (Table 5-4).

Table 5-4: results of BET measurements for eight-nozzle (angled) ring design as a function of plate power and quench gas flow rates. Experimental conditions: 3-12-80/6, 40 kPa, quenching at z = 122 mm (8 x ϕ 1.5 mm, angled), injector position at z = -62 mm.

Quench gas flow rate [slpm]	Plate power [kW]	Feed rate [g.min^{-1}]	SSA [m^2.g^{-1}]	d_{BET} [nm]	d_{model} [nm]
2.8 Ar	13.4	1.7	149	17	44
56 Ar	13.4	1.3	171	15	29
2.8 Ar	15.6	1.3	112	23	46
56 Ar	15.6	1.4	135	19	34
2.8 Ar	18.5	1.3	129	20	56
56 Ar	18.5	1.3	109	24	47

The results show that a low plate power and quenching with 56 slpm Ar at a low plate power are beneficial for the synthesis of small particles. At a higher power level it is remarkable to see that the SSA without quenching is larger, thus a smaller particle diameter, than obtained by quenching with 56 slpm Ar. This is caused by the altered temperature and velocity profiles of the particle, due to the different plate power. By quenching at higher power levels, the residence in the growth region is prolonged and therefore results in larger particles (see also the measured temperature as presented in Table 4-1 (page 66) and Table 4-2 (page 68)).
However, when comparing the SSA's in Table 5-4, it should be considered that during the experiments the quenching height was kept constant, whereas the plasma momentum density changes with the applied plate power. Thus quenching at higher plate power can be compared to quenching closer to the torch exit (lower z), which is more difficult due the higher momentum density. Therefore, it does not mean that it is not possible to synthesise smaller nanoparticles at higher plate powers.

Figure 5-10 shows SEM images of particles sampled at low plate power (top) and high plate power (bottom).

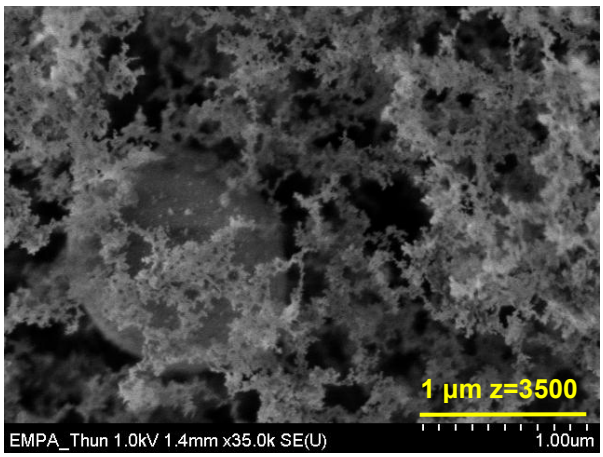

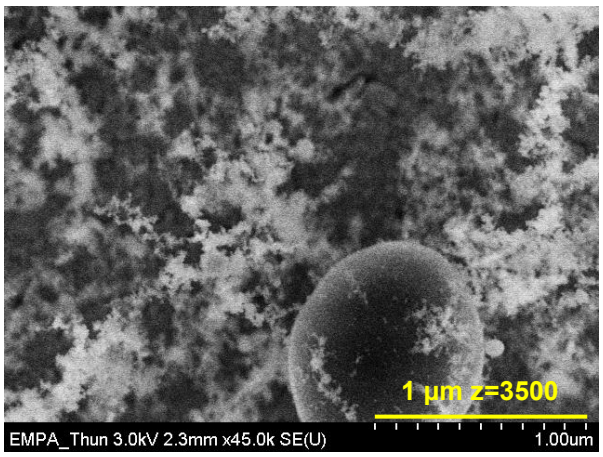

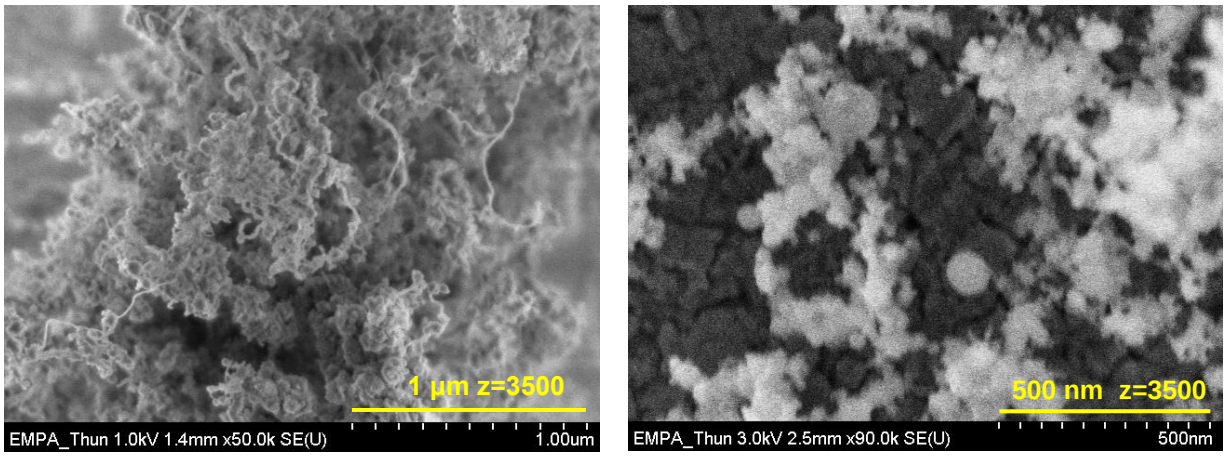

Figure 5-10: SEM images of Si nanoparticles synthesised with high and low plate powers. Top left: 13.4 kW, 1.7 g.min^{-1}, and 2.8 slpm Ar. Top right: 13.4 kW, 1.3 g.min^{-1} and 56 slpm Ar. Bottom left: 18.5 kW, 1.3 g min^{-1}, and 2.8 slpm Ar. Bottom right: 18.5 kW, 1.3 g min^{-1}, and 56 slpm Ar. Process parameters: 3-12-80/6, 40 kPa, quenching at z = 122 mm (8 x ϕ 1.5 mm, angled), samples extracted at z = 3500 mm.

The particles are smaller for lower plate power levels (at least according to the BET measurements). The lower plate power level, however, has the disadvantage that more not completely vaporised particles are present in the product.

The influence of the working pressure on the experimental SSA is summarised in Table 5-5.

Table 5-5: results of BET measurements for eight-nozzle (angled) ring design as a function of pressure and quench gas flow rates. Experimental conditions: 3-12-80/6, plate power 15.6 kW, quenched at z = 122 mm, injector position at z = -62 mm.

Quench gas flow rate [slpm]	Quench height [mm]	Working pressure [kPa]	Feed rate [g.min^{-1}]	SSA [m^2.g^{-1}]	d_{BET} [nm]	d_{model} [nm]
2.8 Ar	122	30	1.1	148	17	38
2.8 Ar	122	30	1.3	114	23	39
56 Ar	122	30	2.0	162	16	
2.8 Ar	121	40	1.3	112	23	46
56 Ar	121	40	1.4	135	19	34
2.8 Ar	122	60	1.3	76	34	57
56 Ar	122	60	1.3	135	19	

The results with regards to the SSA show that working at a lower pressure has a positive effect when small particles are desired. The low pressure decreases the initial monomer concentration (see equation 3-3), but also increases the mean free path and therefore reducing the amount of collisions; thus a slower particle growth. Furthermore, a lower pressure increases the velocity and thereby reduces the residence time.

Figure 5-11 shows SEM images of nanoparticles synthesised at low pressure (top) and at high pressure (bottom).

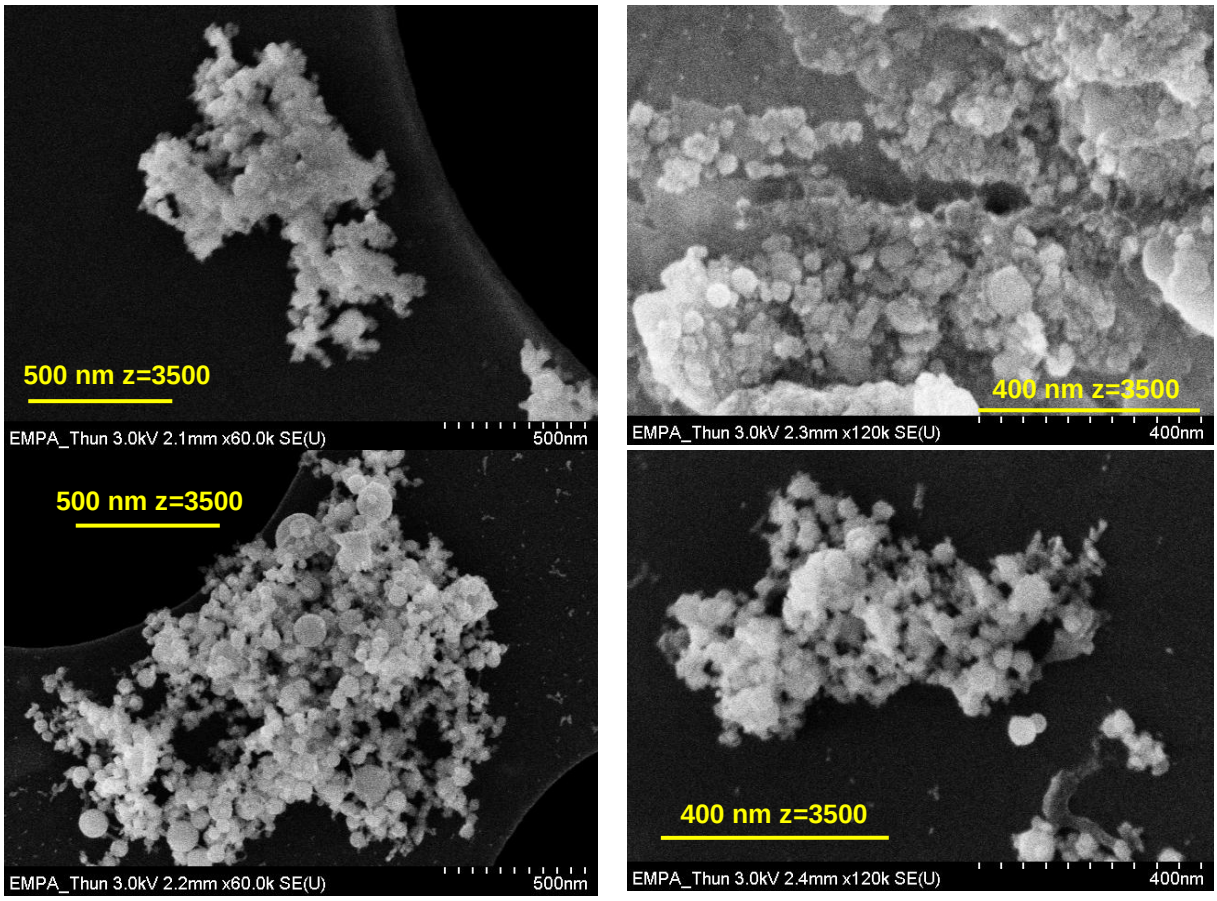

Figure 5-11: SEM images of Si nanoparticles synthesised at high and low pressures. Top left: 30 kPa, 1.3 g.min^{-1}, and 2.8 slpm Ar. Top right: 30 kPa, 2.0 g.min^{-1} and 56 slpm Ar. Bottom left: 60 kPa, 1.3 g.min^{-1}, and 2.8 slpm Ar. Bottom right: 60 kPa, 1.3 g.min^{-1}, and 56 slpm Ar. Process parameters: 3-12-80/6, 15.6 kW, quenching at z = 122 mm (8 x ϕ 1.5 mm, angled), samples extracted at z = 3500 mm.

The particles are smaller for the low pressure case, but this only really visible at low quenching rates and not so much at higher quench flow rates. The disadvantage is that a lower pressure is detrimental with respect to the maximal particle size and amount that can be evaporated (because of the shorter residence time at higher temperatures, see Table 4-5).

The influence of the quenching height for a quench gas rate of 56 slpm Ar on the SSA is shown in Table 5-6.

Table 5-6: results of BET measurements for eight-nozzle (angled) ring design as a function of quenching height and quench gas flow rates. Experimental conditions: 3-12-80/6, plate power 15.6 kW, 40 kPa, injector position at z = -62 mm.

Quench gas flow rate [slpm]	Quench height [mm]	Feed rate [g.min^{-1}]	SSA [m^2.g^{-1}]	d_{BET} [nm]
56 Ar	59	1.3	198	13
56 Ar	80	1.5	173	15
56 Ar	122	1.4	135	19
56 Ar	154	1.9	201	13

The effect of the quenching height is not so straight forward as could be expected from the temperature distribution without quenching. In the case without quenching the temperature and velocity decrease with increasing z (see Figure 5-1), thus

quenching would be easier with increasing z value because of the lower plasma jet momentum. A better penetration of the plasma results in a stronger cooling, thus smaller particles would be expected. The results of Table 5-6 show that this is not completely true.
It is partially caused by the different feed rates. But more important is the influence of the changed temperature and velocity profiles after quenching (see Figure 4-27). These profiles are not always changing in a beneficial way for obtaining smaller particles. The growth model has predicted a similar effect for the particle size after quenching at different heights (see Table 4-15, page 103 and Figure 4-47, page 105) for the 90 slpm case in which a complete penetration of the plasma is achieved.
It should also be noted that the feed rate at z = 154 mm is about 50% higher than at z = 59 mm, but results in the same size.

The amount of incomplete melted and evaporated particles is increasing when the plasma is quenched closer to the torch exit (see Figure 5-12). This can be explained by a decreased residence time the precursor spends above the boiling point.

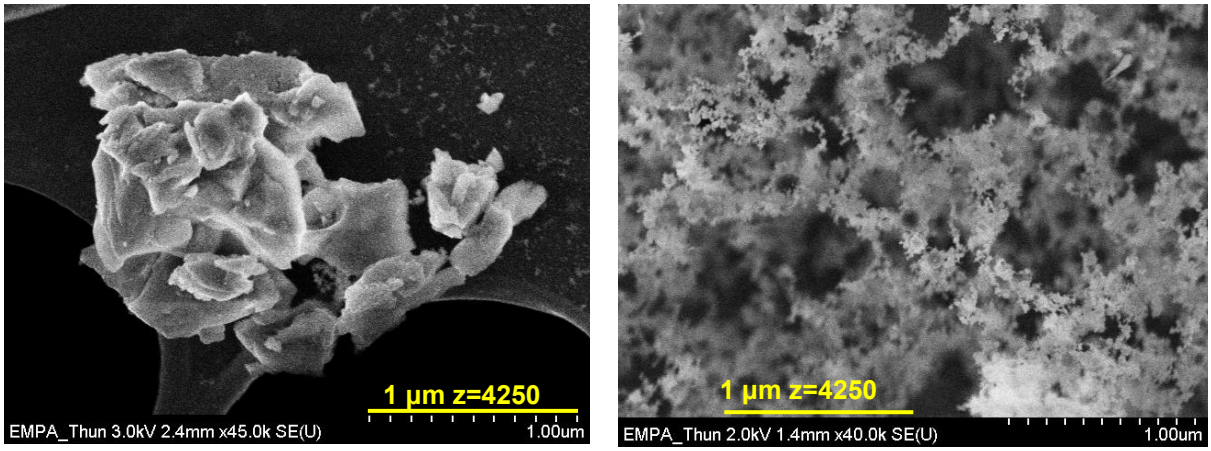

Figure 5-12: SEM images of Si nanoparticles synthesised when quenched at different heights. Left: 59 mm and 1.3 g.min^{-1}. Right: 159 mm and 1.9 g.min^{-1}. Process parameters: 3-12-80/6, 15.6 kW, 40 kPa, quenching: 8 x ϕ 1.5 mm, angled, extracted at z = 4250 mm.

As the step from the eight-nozzle design without angle to the eight-nozzle with angle resulted in less deflection of the particle flow, but in hardly any change in the SSA for the used process parameters, a funnel (section 4.2.3.2) has been placed on top of the eight-nozzle (ϕ 1.5 mm, angled). The aim of the funnel was to guide the particle laden plasma flow better than it was the case without funnel and thus allowing the synthesis of smaller nanoparticles with the same quench gas flow rate. Figure 5-13 shows the influence of such a funnel placed on top of the quench ring on the particle laden plasma flow.

Figure 5-13: left: Si loaded plasma quenched with 2.8 slpm Ar. Right: Si loaded plasma quenched with 56 slpm Ar. Plasma parameters: 3-12-80/6, 40 kPa, 15.6 kW plate power, 3.1 g.min^{-1} Si feed rate, quench ring at z = 121 mm (8 x ϕ 1.5 mm, 15° angle).

Figure 5-13 shows that, at least from an optical point of view, fewer particles are spread throughout the reactor. It was however not possible to completely avoid the particle dispersion around the quench design: the orange glow at the edges of the funnel is originating from particles.

In Figure 5-14, the results of the heat source model are shown, when the quenching is carried out with a funnel placed on top of the quench ring.

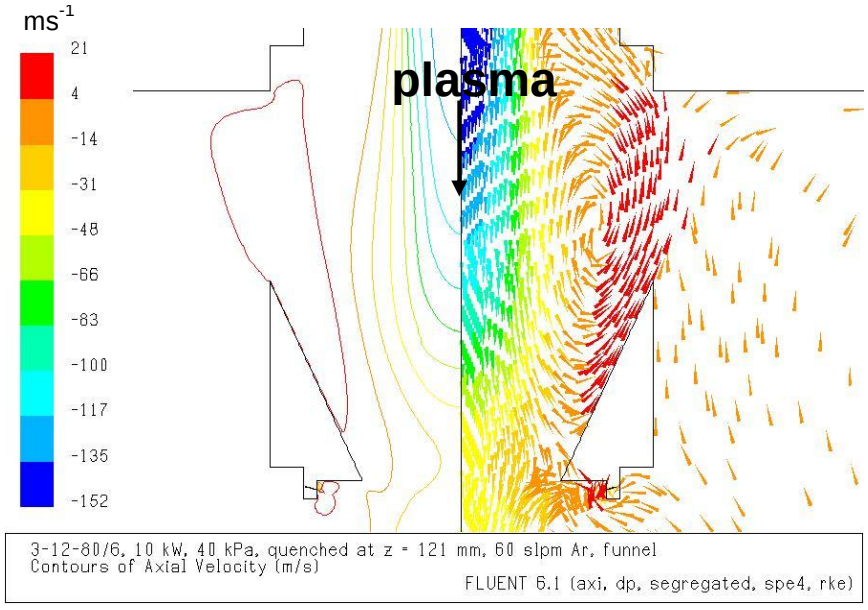

Figure 5-14: iso contours and vector representation of the axial velocity for the funnel design. Modelled parameters: 3-12-80/6, 10 kW, 40 kPa, quenched at z = 121 mm with 60 slpm Ar (surface equivalent 8 x ϕ 1.5 mm, angled 15 °). The white triangle represents the funnel.

The graphs represent different representations of the same phenomena: there is a recirculation positioned at the funnel wall. Some of the particles that get entrained in this recirculation flow are ejected at the edges, resulting in the situation which shown in the right image of Figure 5-13. These particles will finally flow around the funnel or get re-entrained. The other particles follow the plasma through the funnel and are not or just slightly diverted.

The results in Table 5-7 are obtained from experiments in which a funnel is placed on top of the eight-nozzle (angled) ring.

Table 5-7: results of BET measurements for the eight-nozzle (angled) ring design with funnel (see section 4.2.3) as a function of the quench gas flow rate. Experimental conditions: 3-12-80/6, plate power 15.6 kW, 40 kPa, quenched at z = 121 mm (8 x ϕ 1.5 mm, angled), injector position z = -65 mm.

Quench gas flow rate [slpm]	Feed rate [g.min^{-1}]	SSA [m^2.g^{-1}]	d_{BET} [nm]	d_{model} [nm]
2.8 Ar	2.0	96	27	47
2.8 Ar*	2.1	91	28	52
56 Ar	1.8	145	18	13
56 Ar*	1.8	118	22	36

* for comparison eight-nozzle angled without funnel, quenched at z = 121 mm

By carrying out the synthesis process with the funnel configuration, the SSA of the product could be increased by 23% as compared to the eight-nozzle angled system without the funnel for quench gas rates of 56 slpm Ar (Table 5-3)

Figure 5-15 shows two SEM images of nanoparticles synthesised the eight-nozzle (ϕ 1.5 mm, 15° angle) with and without funnel.

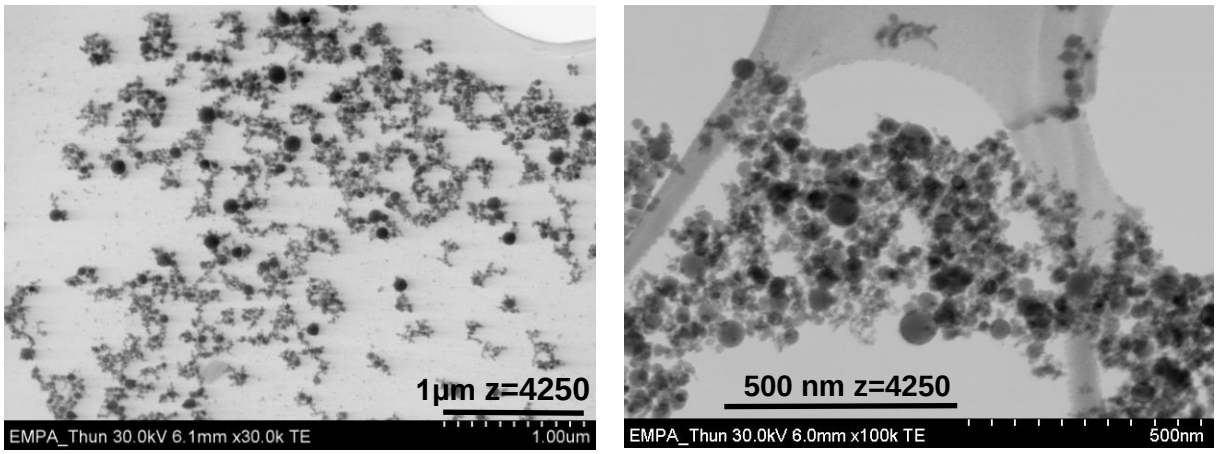

Figure 5-15: SEM image of the eight-nozzle angled design without funnel (left) and with funnel (right). Process parameters: 3-12-80/6, 15.6 kW, 40 kPa, quenched at z = 122 mm with 56 slpm Ar. Injector at z = -65 mm, sampled at z = 4250 mm. Feed rate: 1.8 g.min^{-1}.

The SEM image of the nanoparticles synthesised with the funnel design show smaller particles and a narrower distribution. The latter only has been identified from the images and not validated with measurements like photon correlation spectroscopy.

The samples collected from the sampling filter have been characterised by X-ray diffraction, see Figure 5-16.
The XRD spectrum shows the presence of pure crystalline Si. The feed rate did not influence the characteristics of the recorded XRD spectra. The crystallite size has not been determined with X-ray diffraction.

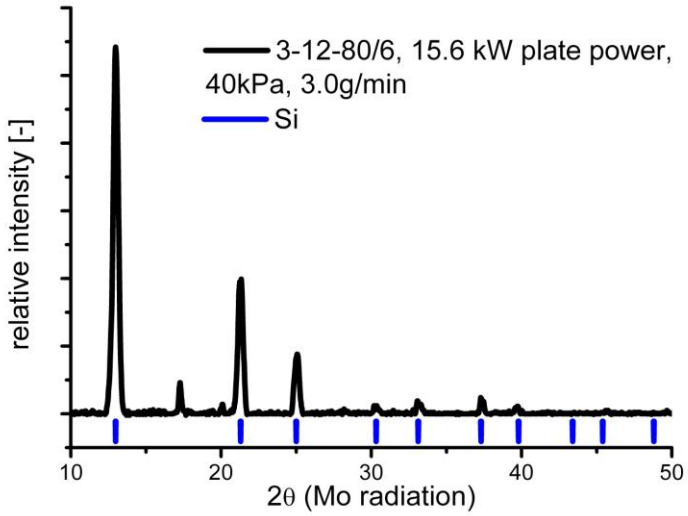

Figure 5-16: X-ray diffractogram of ICP synthesised Si nanoparticles. Process parameters: 3-12-80/6, 15.6 kW plate power, 40 kPa, quenched at z = 122 mm (8 x ϕ 1.5 mm, angled), feed rate 1.3 g.min^{-1} and quenched with 2.8 slpm Ar. (The small lines at the bottom represent the theoretical peak positions of cubic Si (JCPDS card 27-1402).

The reproducibility of the process is determined by several factors. The process instabilities on the final product were reduced as much as possible by taking samples from products which have been collected during 7.5 minutes of processing time. Process instabilities are for example the plasma instability (as shown by Boulos [165]). The cooling of the torch and RF generator and therefore the heat losses, are not always constant as a consequence of external influences (daily temperature, etc.) on the cooling water. Furthermore, there are instabilities in the precursor feed rate caused by the transport from feeder to injector inlet. The broad size distribution of the precursor results in slightly different precursor loading introduced in the plasma each time (the precursor feeder uses short pulses). Minor differences in the pressure caused by the clogging of the filters (automatic pressure correction by opening or closing of a valve), will have an effect on the process. Also the correct positioning of the quench system after substitution of another system is introducing errors. Furthermore, it is very difficult to obtain exactly the same anode current and anode voltage after a restart (plate power).The total effect of these process instabilities on the final product has been estimated to be around 15%.
Some of the BET analyses have been repeated in house and at the CEA (Saclay, France) for determining the reproducibility. The measured SSA's showed a maximal deviation of 12% per experiment. The main error in the BET measurements is caused by the sample preparation and extraction. Repetition of the same sample resulted in an error up to 3%, caused by inadequate removal or re-adsorption of water on the sample.
The assumptions behind the BET analysis result in differences between the SEM images and the BET measurement. But the problem is not solved by simply taking another sizing technique [185].

Summary of section 5.1.2
The trends of the particle growth modelling are in good agreement with the experiments, like an increased d_{pp} for an increased precursor feed rate, an increased (plate) power, and increased pressure, were found in both model and experiments. The predicted diameters are about 50% overestimated as compared to the experiments. Especially, the assumption of all monomers being present as seeds

results in an overestimation of the actual concentration, which will contribute to a larger diameter. Furthermore, the assumption of monodispersity will result in an overestimation of the particle size compared to the experiments. Because the results of the BET analysis are weight based and will favour the smaller particles as compared to techniques using volume based diameters.

The predicted improvement of the quenching design, going from a two-nozzle system to an eight-nozzle system with funnel, are also confirmed by the experiments [194]. Also the difference between the several designs can be seen as expected from the CFD model. By using the eight-nozzle angled system instead of the two-nozzle system the SSA could be increased from 90 to 145 $m^2.g^{-1}$. By optimising the quenching height even values up to 201 $m^2.g^{-1}$ could be achieved.
The higher SSA, was found when the quenching was carried out further away from the torch, where the plasma is colder.

The assumptions and limits of the BET analysis should be kept in mind; the particles are single spherical particles and the d_{BET} is based on number mean and will therefore take the presence of a few large unmelted or partial molten particles less into account on the average diameter.

5.1.3 Quenching with CH_4

Quenching of Si with an Ar/CH_4 mixture was carried out to investigate the quenching efficiency of such a mixture. The use of a molecular gas should consume more energy (especially when it decomposes) and will therefore enhance the quenching. The decomposition of CH_4, into C + 2 H_2, takes place at about 1100 K and requires about 100,000 $kJ.kg^{-1}$ (compared to c_p of Ar: 525 $kJ.kg^{-1}$), thus a strong quenching effect can be expected from quenching with CH_4.
Another additional effect from quenching with CH_4, could be the possible carburation of the Si into SiC (nano SiC is very interesting, for example to enhance the strength and toughness in (nano)composites [195]).
It has already been shown by Leparoux et al. [196] that synthesis of nano SiC is possible from in-situ carburation of Si by the ICP process. Guo et al. [45] added CH_4 together with the solid Si precursor while Hollabaugh et al. [197] injected the CH_4 in the plasma tail to $SiCl_4$ plasma and obtained mainly β-SiC, they did, however, not discuss the quenching effect.
The reactive plasma is not restricted to carbon containing species alone, also the addition of ammonia ([169]) for example is possible.

Figure 5-17 shows two photographs of CH_4 added to the plasma process and along with the carrier gas (left) and via the quenching gas (right).

As the CH_4 is introduced along with carrier gas, the CH_4 (probably visible as the green colour, emitted by the C_2 radicals, the so-called “Swan” bands, but this has to validated with spectroscopic means, e.g. optical emission spectroscopy) remains in the middle of the plasma. However, when the methane is introduced with the quenching gas, the green colour is only visible at the edges of the plasma. Also, a green colour is observed above the injection point of methane.

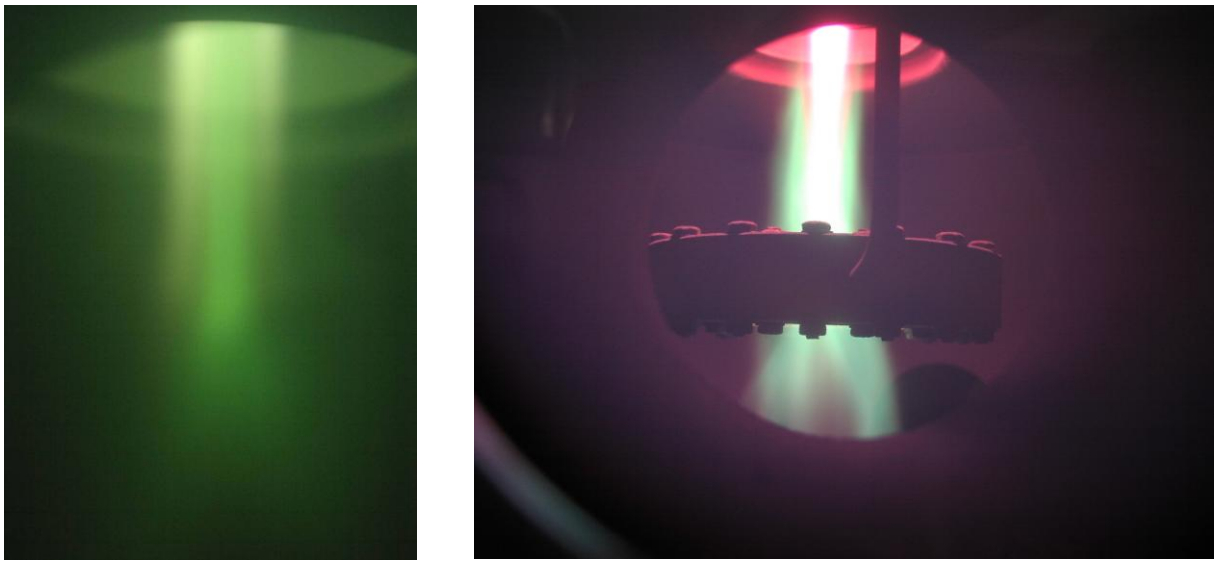

Figure 5-17: left: 2.4 slpm CH_4 introduced with the carrier gas. Process conditions: 9.6 (7.2/2.4 Ar/CH_4)-27-80/6, 40 kPa, 25 kW plate power. Right: 0.5 slpm CH_4 introduced in the quenching gas. Process conditions: 3-12-80/6, 40 kPa, 15.6 kW plate power, quenched at z = 121 mm (8 x ϕ 1.5 mm, angled).

The CFD model with N_2 as quench gas can explain the behaviour of the quench gas as is shown in Figure 5-18. In this figure only the regions having a component opposite to the plasma flow direction are shown. The model predicts that the quench gas, in this case N_2, flows upwards along the plasma gas at higher quench gas flow rates. Other modelling results show furthermore that this effect gets stronger with increasing quench gas flow rate.

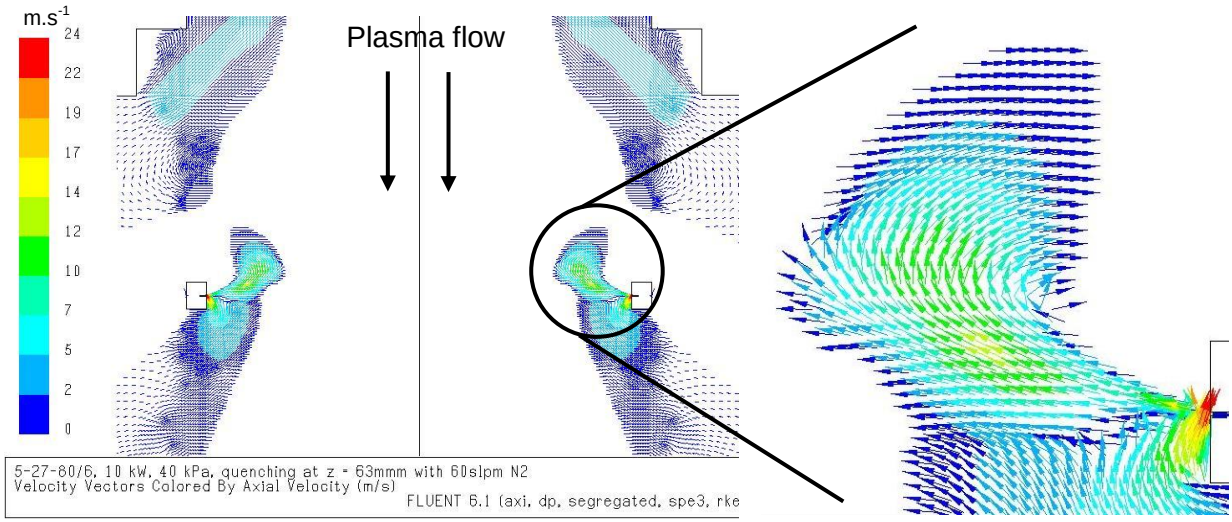

Figure 5-18: only vectors with a velocity component opposite to the plasma (top-down) are shown. Some vectors go from the precursor inlet upstream. Modelling (2D) conditions: 3-12-80/6, 40 kPa, 10 kW net power input, quenched at z = 63 mm (surface equivalent to 8 x 2 mm) with 60 slpm N_2.The two open rectangles represent the quenching system.

The produced powder was collected on the filter and characterised by SEM and XRD. The diagram shows that quenching of the Si vapour with an Ar/CH_4 mixture results in a partial carburisation of Si to SiC (Figure 5-19) The formed SiC compound is probably the low temperature stable (< 2000 K) β form, although the presence of α-SiC in the product can not be excluded from these results. It remains however questionable if the carburisation can solely be attributed to the CH_4 present in the

plane of quenching. Since some CH_4 was observed further upstream (see Figure 5-17 left photograph) and perhaps already reacts there. This point is not addressed in the work of Hollabaugh et al. [197], but this could have been an issue there as well.

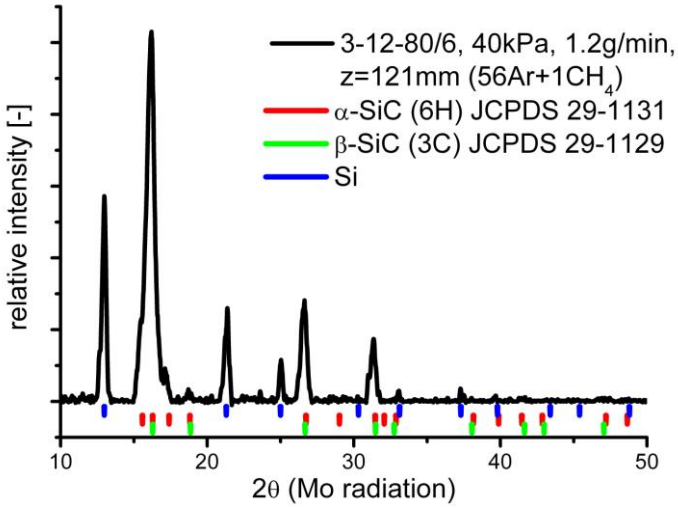

Figure 5-19: X-ray diffractogram of ICP synthesised Si nanoparticles quenched with an Ar / CH_4 mixture. Process parameters: 3-12-80/6, 40 kPa, 15.6 kW plate power, Si feed rate 1.2 g.min^{-1}, quenched at z = 121 mm (8 x ϕ 1.5 mm, angled) with 56/1 slpm Ar/CH_4.

The result of the BET measurements for the Ar/CH_4 experiment, with the process parameters used as described in Figure 5-19, amounts 110 m^2.g^{-1} (BET equivalent diameter of 17 nm assuming a specific density of 3.2).
Unfortunately, it was not possible to use the enthalpy probe to determine the quantitative effect of quenching with CH_4, because solid carbon, which is formed as a consequence of the CH_4 decomposition, would clog the tip of the enthalpy probe and therefore make the measurements impossible.

Figure 5-20 shows SEM pictures of the Si/SiC product sampled from the filter.

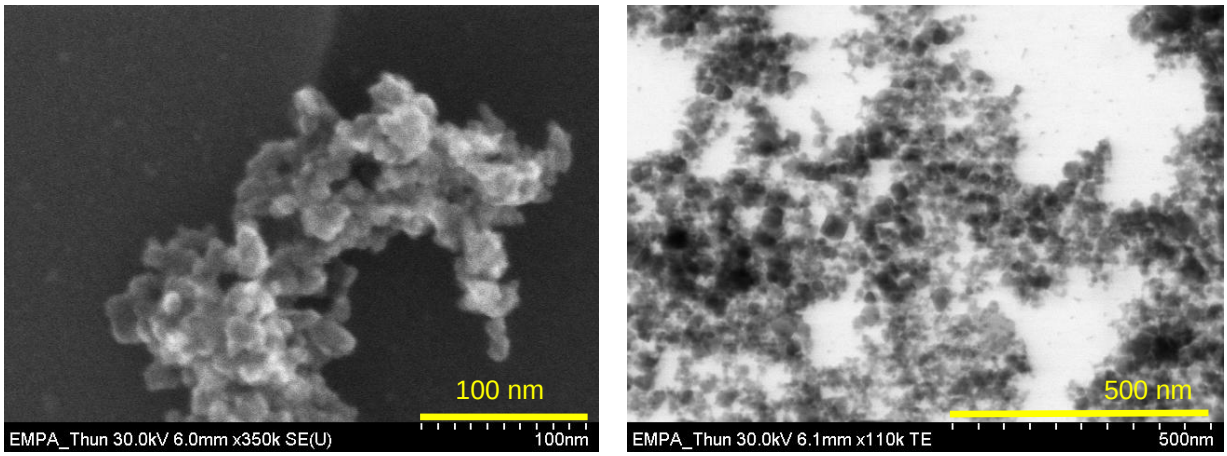

Figure 5-20: left: SEM image. Right: STEM image. Process parameters: 3-12-80/6, 15.6 kW, 40 kPa, quenched at z = 121 mm (8 x ϕ 1.5 mm, angled) with 56/1 slpm Ar/CH_4, feed rate 1.2 g.min^{-1}. Sampling position: z = 4250 mm.

Summary of section 5.1.3
The effect of the CH_4 in the quenching gas on the quenching efficiency could not be determined, because no measurements could be made with the enthalpy probe. The

addition of CH_4 results in the formation of soot, which will clog the entrance of the enthalpy probe and therefore make measurements impossible. It is however expected that the addition of CH_4 has a stronger cooling effect than Ar, because of the amount of energy required to decompose CH_4 is very large in comparison to the heat capacity of Ar.
By adding CH_4 to the quenching gas, it is possible to partially carburise Si into β-SiC, the presence of α-SiC can not be excluded. It is however not clear at the moment if the carburisation is caused by the CH_4 at the quenching plane and/or by CH_4 reacting further upstream.

5.2 Synthesis of tungsten carbide nanopowders

5.2.1 WC Precursor

The WC precursor of Ceratizit (see section 3.3.1.3) had a sphere like shape and a d_{10} of 0.7 µm and a d_{90} of 2.7 µm as determined by laser diffraction. To get an idea about the maximal quantity of WC that could be evaporated a "back of the envelope" calculation was performed. Since only a few data were available, the values of W were used; the heat of evaporation amounts 4480 $kJ.kg^{-1}$, while the heat of fusion amounts 195 $kJ.kg^{-1}$. For the evaporation of 1 kg of W about 5800 kJ is required. Assuming that a 10 kW net input in the plasma is completely available for the evaporation of the W, about 103 $g.min^{-1}$ can be evaporated. But, just like for Si, the energy losses caused by radiation plasma – particle interaction, etc., are not included, this means that actually much less than 10 kW is available for the evaporation process, resulting in an actual evaporation rate that is much lower than 103 $g.min^{-1}$. It looks peculiar that despite of the much higher boiling temperature more W can be vaporised with 10 kW than Si. This is only due to the fact that energy required to heat up the plasma to temperatures above the boiling point has not been taken into account.

5.2.2 Plasma experiments

The experiments were carried out under variation of other process parameters like quench gas flow rates, amount of methane, and precursor feed rate. The samples were characterised by electron microscopy, BET analysis, and X-ray diffraction.
Figure 5-21 shows three TEM images of the synthesised nano WC.

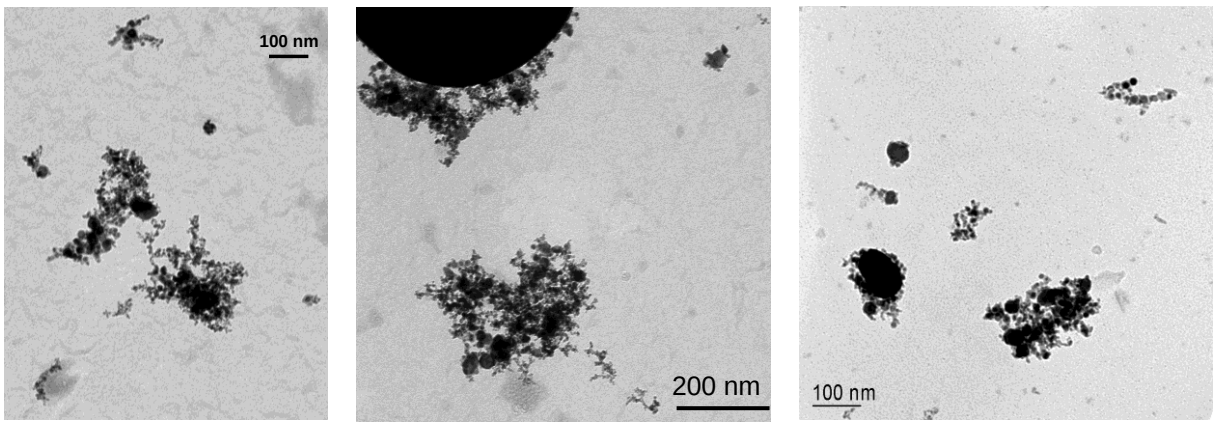

Figure 5-21: TEM pictures of synthesised nano WC. Process conditions: $1H_2$-6-80/6, 40 kPa, 30 kW plate power, feed rate 10 $g.min^{-1}$, quenched at z = 58 mm with 70 slpm Ar (2 x ϕ 4 mm). Samples extracted at z = 4250 mm.

The pictures show the presence of nanoparticles in the product, but also the presence of larger spherical particles.

The products have been characterised by XRD (Figure 5-22).

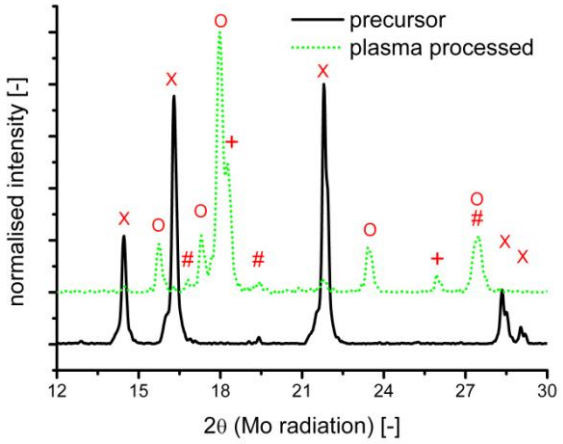

Figure 5-22: XRD spectra showing phase composition of precursor (WC CT-1.0) and plasma processed product. Process conditions: 9.6-4-80/6, 40 kPa, 30 kW plate power, feed rate 4 $g.min^{-1}$. Legend: x: WC, #: WC_{1-x}, O: W_2C, +: W.

The results of the XRD spectra show a carbon deficiency compared to the phase composition of the precursor. Besides WC, also WC_{1-x}, W_2C, and W are obtained in the product. The reason for this carbon deficiency is the reducing atmosphere of the plasma (Ar/H_2 mixture) and since WC is a line compound a small local deviation of the ideal W to C ratio already results in the formation of sub-stoichiometric phases and carbon (see Figure 2-6).

As the presence of sub-stoichiometric phases in the final product is not desired, the loss of carbon has to be compensated by the addition of a carbon containing species [198].
Figure 5-17 shows two photographs of the plasma as a carbon containing source is introduced along with the quench gas (left) and with the carrier gas (right). Figure 5-23 shows the XRD spectra of the synthesised products with different amounts of methane in the quenching gas.

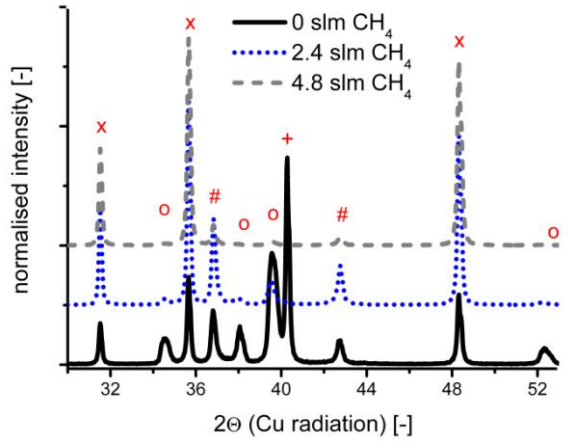

Figure 5-23: XRD spectra showing phase composition as a function of the methane flow rate. Process conditions: 9.6($Ar+CH_4$)-6-80/6, plate power 30 kW, 40 kPa, quenched at z = 58 mm with 70 slpm Ar (2 x ϕ 4 mm). Feed rates: 5.0 $g.min^{-1}$ for 0 slpm CH_4, 6.0 $g.min^{-1}$ for 2.4 slpm CH_4, and 6.7 $g.min^{-1}$ for 4.8 slpm CH_4. Legend: x: WC, #: WC_{1-x}, O: W_2C, +: W.

The XRD spectra show that the amount of sub-stoichiometric WC phases can be reduced by increasing the amount of methane in the carrier gas.
The phases have been quantified by using a Rietveld analysis and the results are summarised in Table 5-8.

Table 5-8: Rietveld analysis (error of less than 3%) of the synthesised product as a function of the CH_4 amount in the carrier gas. Plasma conditions: 9.6(Ar+CH_4)-27-80/6, 30 kW plate power, 40 kPa. Feed rate 5.0 – 6.7 g.min^{-1} WC.

Phase / CH_4	feed rate [g.min^{-1}]	WC	WC_{1-x}	W_2C	W
0 slpm	5.0	27	25	16	32
1.2 slpm	5.7	37	41	10	12
2.4 slpm	6.0	61	29	6	5
4.8 slpm	6.7	90	7	3	0

The trend found is an increasing WC content with increasing CH_4 flow rate, suggesting that a product consisting out of 100% WC can be obtained. It should however be noted that the presence of amorphous phases (free carbon for example) is not visible in the X-ray spectrum.
At 1.2, 2.4 and 4.8 slpm it is expected that free C is present in the product (W / $C_{methane}$ ratio 0.54, 0.29, and 0.16 respectively). TEM analysis revealed in case of 4.8 slpm CH_4, the deposition of a graphite coating on the surface of the "WC" nanoparticles (Figure 5-24). This coating can be used for the in-situ passivation of reactive particles with carbon. Although the addition of methane was aimed to the in-flight carburisation of the sub-stoichiometric phases, it demonstrates the ability of the ICP process to coat the nanoparticles in-situ.

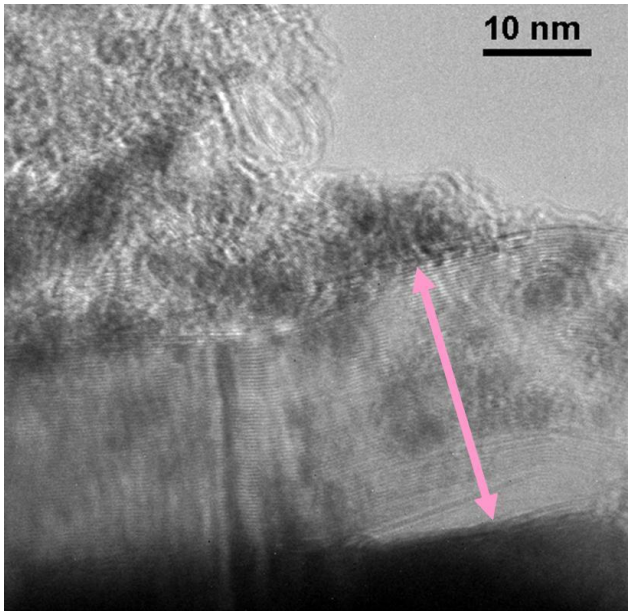

Figure 5-24: TEM image of ICP processed WC under addition of CH_4. The arrow indicated the presence of a graphite coating. Process conditions: 3Ar/0.5CH_4-4-80/6, plate power 30 kW, 40 kPa, quenched at z = 58 mm with 70 slpm Ar (2 x ϕ 4 mm).

Also experiments using a solid carbon source instead of a gaseous one, mixed (ball milling for 2 hours) with the precursor, were carried out. Figure 5-25 shows the crystalline phase composition after plasma processing (9.6-4-80/6, plate power

30 kW, 40 kPa, quenched at z = 58 mm with 70 slpm Ar (2 x ϕ 4 mm)) as a function of the added carbon content. 1 wt% C is equivalent to 0.1 slpm CH_4 at a feed rate of 5 $g.min^{-1}$ WC.

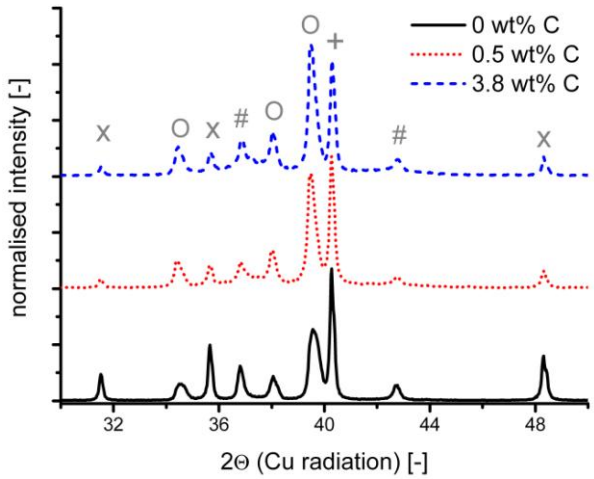

Figure 5-25: XRD spectra of plasma processed WC and carbon black as a function the carbon black amount. Process conditions: 9.6-4-80/6, plate power 30 kW, 40 kPa, quenched at z = 58 mm with 70 slpm Ar (2 x ϕ 4 mm). Feed rate mixture: 0% 6.0 $g.min^{-1}$, 0.5% 1.9 $g.min^{-1}$, and 3.8% 1.3 $g.min^{-1}$. Legend: x: WC, #: WC_{1-x}, O: W_2C, +: W.

The XRD spectra show that the intensity of the W_2C and WC_{1-x} signal are increasing and that of W is decreasing, when carbon black is added to the WC precursor. There is no effect on the WC intensity when the 0.5 and 3.8wt% WC/C mixtures are compared. A difference is found between 0wt% and the others; the intensities of the WC peaks are reduced in the WC/C mixtures.

The synthesis of WC nanoparticles from metallic tungsten mixed with carbon black as a precursor was investigated as well. Figure 5-26 compares the phase composition of WC and the product of a stoichiometric W/C mixture as determined by XRD.

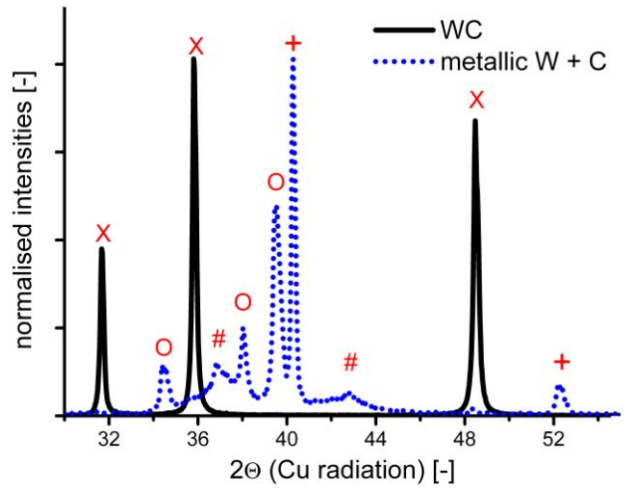

Figure 5-26: comparison between the XRD spectra of pure WC and the product of a metallic tungsten (Woka, 3µm) / carbon black (Cabot, Grade N134) mixture. The amount of carbon black is 6.1 wt%. Process conditions: 9.6-4-80/6, 30 kW plate power, 40 kPa, quenched at z = 58 mm with 70 slpm Ar (2 x ϕ 4 mm). Feed rate: 2.2 $g.min^{-1}$. Legend: x: WC, #: WC_{1-x}, O: W_2C, +: W.

Figure 5-26 shows that a partial carburisation of the metallic tungsten in a reactive plasma is possible. Although about 20% of the tungsten is carburised, hardly any WC is formed (1% determined by Rietveld analysis).

As already mentioned, quenching not only influences the particle growth, but also "freezes" the nanoparticles in a particular thermodynamic state. Therefore it is expected that the quenching may influence the phase composition of the synthesised product, especially in the W-C system. The XRD spectra of the product, as a function of the quench gas flow rate, are shown in Figure 5-27.

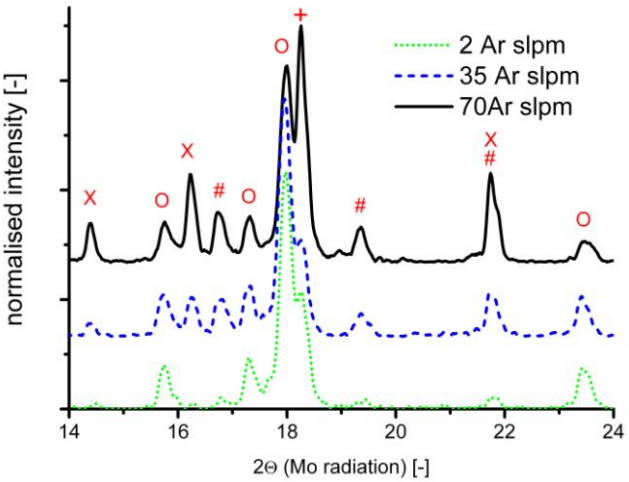

Figure 5-27: left: comparison between the phase compositions of the product as a function of the Ar quench gas rate. Process parameters: 9.6-5-80/6, 40kPa, 30 kW plate power, quenched at z = 58 mm, (2 x ϕ 4 mm). Feed rate: 2 slpm 4.0 g.min^{-1}, 35 slpm 6.0 g.min^{-1}, and 70 slpm 5.0 g.min^{-1}. Legend. x: WC, #: WC_{1-x}, O: W_2C, +: W.

Comparison of the XRD spectra shows that the quenching has an influence on the phase composition of the product. The dominant phase for non quenching conditions is W_2C. The amount of WC increases with increasing quench gas flow rate, whereas the W_2C decreases.
The quantitative phase composition as determined by Rietveld analysis is shown in Table 5-9.

Table 5-9: phase composition (in wt%) as a function quench gas flow rate determined by XRD. Process parameters: 9.6-4-80/6, 30 kW plate power, 40 kPa, quenched at z = 58 mm (2 x ϕ 4 mm)

phase / quench flow	Feed rate [g.min^{-1}]	WC	WC_{1-x}	W_2C	W
2 slpm Ar	4.0	4	14	64	18
35 slpm Ar	6.0	16	14	58	13
70 slpm Ar	5.0	27	25	16	32
70 slpm N_2	6.6	11	19	40	30

The results show that the amount of WC increases with increasing quench gas flow rate. Furthermore, there is a significant decrease of the amount of W_2C.
Quenching with N_2 results in a larger carbon deficiency of the products, as compared to quenching with the same gas flow rate of Ar. This is shown by the large amount of W_2C and W in the product. The presence of nitrides was not observed by X-ray diffraction. The effects as shown in Table 5-9 have to be investigated in more detail, because the "kinetics" have to be considered as well.

A point which has not been taken into consideration with respect to the quantitative determination of the phase composition by XRD, is the sensitivity to larger particles. As the larger particles have reflective planes, they will give a larger contribution to measured signal than the smaller particles.

This will be of major influence if there is an incomplete evaporation of the precursor particles. The addition of CH_4 or carbon black to the precursor will engrave this situation, because energy is required to decompose or evaporate the carbon containing species, leaving less energy for the evaporation of WC.

Summary of section 5.2.2

It is possible to make nanoparticles from high refractory materials like WC. The high temperature and reducing atmosphere of the plasma result in a carbon deficiency of the WC product. By using a reactive plasma, by addition of a carbon containing source to the precursor, the carbon deficiency of final phase composition can be reduced. A gaseous precursor is more beneficial for this objective than a solid precursor. But because of the large W / C ratio when methane is used, the formation of a film around the particles was observed. This, however, also opens the route to in-situ passivation and surface functionalisation of the synthesised nanoparticles, without needing a second process step.

The in-situ carburisation of metallic tungsten with carbon black did not result in a carburisation of W to WC. The XRD spectrum however reveals the presence of W_2C and WC_{1-x}.

Quenching of the particle loaded plasma flow with different quench gas rates and chemistry influences the final phase composition.

6 Conclusions

The heat source model, being used as a first approximation to describe the temperature and velocity profiles outside the torch, is well suited to predict the behaviour of the plasma qualitatively.
Also the quantitative agreement between the heat source model and the experiments (enthalpy probe measurements) is very satisfactory. The current model finds an efficiency of ~50% to values of 60% in literature for the same torch. In the efficiency of 50% are the losses of the coil cooling already included, which is not the case for the literature values.

The 2D extended field approach has shown that for the current process parameters (3-12-80/6, 13.56 MHz, 40 kPa, and 10 kW net power) the reflow caused by the EM field is absent. Thus the temperature and velocity profiles in the torch will resemble the profiles obtained by the heat source model.

The heat source model has been used to determine the optimal plasma gas composition for the nanoparticle synthesis. The composition that has been picked was 3-12-80/6. Factors like long residence times at high temperatures (evaporation), carrier gas flow rate for the particle injection, operation constraints, costs, etc. have been taken into account.

When the quench designs are modelled, the qualitative results of the heat source model remain very good. The optical appearance of the plasma is predicted very well, e.g. splitting of the plasma, pushing the plasma back into the torch at higher quench gas flow rates, presence of “hot” fingers, etc..
The two-nozzle (ϕ 4 mm) design showed a splitting of the plasma (3-12-80/6, 15.6 kW plate power, 40 kPa, and quenched at z = 121 mm) at 56 slpm, which results in undefined trajectories. By increasing the number of nozzles to eight (ϕ 2 mm), the plasma trajectories showed an improved behaviour. This effect was increased by reducing the nozzle diameter to ϕ 1.5 mm and adding an angle of 15°. A further improvement was introduction of a funnel on top of the quenchring.

With respect to the quantitative comparison it can be said that the heat source model overestimates the quench gas flow rate necessary to penetrate the plasma. These deviations can be explained by the errors of the enthalpy probe measurements, entrainment of cold gas enveloping the plasma jet, and the fluctuations of the plasma. However the most important error is caused by the model itself: description of the heat source, neglecting the influence of the EM field, boundary conditions (like wall temperature), absence of swirl component, absence of radiation, approximation of the gas properties, accuracy of modelled compared to real geometry, etc.. But despite these approximations and assumptions the model is able to describe the trends found in the experiments.

N_2 is a more effective quench gas than Ar for the same plasma gas flow rate, when immediate mixing and heat transfer are assumed, especially at high temperatures where the dissociation of N_2 requires extra energy. The advantage of using Ar instead N_2 quenching gas is its inertness.
A higher quenching efficiency can be obtained by quenching at higher temperatures, which has the disadvantage that more gas is required to reach the targeted temperature than quenching at lower temperatures.

The enthalpy probe measurements showed that a minimum amount of quench gas (between 30-40 slpm Ar and N_2) is required to obtain a partial penetration of the plasma (5-27-80/6, 40 kPa, 22.5 kW plate power, quenched at z = 63 mm with the 8 x ϕ 2 mm design). A complete penetration under the same conditions is obtained with 56 slpm N_2, more than 56 slpm is required for Ar.
There is a threshold value for the amount of quench gas above which the plasma gas will be deflected, resulting in uncontrolled trajectories. This value depends on several parameters, like nozzle number, diameter, and angle, quenching height.
The optimal quench design is a trade-off between the number of nozzles (homogeneity) and surface of the nozzle (momentum). When the total quench outlet surface was set to 2.51×10^{-5} m^2 (equivalent to 2 x ϕ 4 mm), the highest temperature reduction was obtained with a two-nozzle system, whereas the ring design resulted in the most homogeneous temperature profile. The best compromise will be the four- or five-nozzle design.
The optimal quench process for the nanoparticle synthesis depends on all these parameters, but is determined by the temperature that is targeted after quenching, which depends on the physical properties of the particles. Small particles are obtained by a fast temperature reduction below the sintering temperature (~60% of the melting point).

The 3D model is more accurate than the 2D axi-symmetric one, because the approximation of the single nozzles (3D) being a slot in the 2D model. The 3D model is able to describe features, like splitting of the plasma, presence of “hot” fingers.

The model describing the particle growth by coalescence and coagulation as described by Kruis [77] has been adapted to account for temperatures above the solidification point and has proved once again to be very useful. The trends found in the experiments with Si can be predicted qualitatively very well. The influence of the pressure, feed rate, power, and quenching height are described satisfactory.
The growth model also shows that the temperature reduction has a larger influence on the particle growth, than the dilution effect (concentration).
In order to obtain small nanoparticles; the applied power, pressure, and feed rate should be low (NB for the currently used quenching conditions: height and gas flow rate). Quenching at higher plate power should take place at higher z value, in order to be comparable with the conditions at lower plate power). These conditions are opposite to the conditions for the evaporation of many (and large) particles. The growth model also has shown that there is minimum in the particle size as a function of the quench gas flow, this also applies for the quench position. The position of this minimum depends on the used process parameters.

The combination of the growth model with the heat source model has shown that the particle size (3-12-80/6, 10 kW, 40 kPa, 2.0 $g.min^{-1}$, 60 slpm Ar, z = 121 mm) for an eight-nozzle design can be reduced from 51 nm to 37 nm by reducing the nozzle diameter from 2 to 1.5 mm, at the same number of nozzles and quench gas flow rate, and giving the nozzle an axial component of 15°. By simply reducing the nozzle diameter the particles size decrease from 51 to 47 nm. The introduction of an angle to the nozzle resulted in decrease of 10 nm to 41 nm. A funnel placed on top of the 8 x ϕ 1.5 mm, angled quench design reduced the diameter down to 14 nm.

Although the nanoparticle synthesis of Si using an ICP process combined with CFD and particle growth modelling has already been published in the 1990's, the current work goes into much further detail with respect to the quenching process (both theoretical and experimental) and uses a solid Si precursor instead of gaseous $SiCl_4$.

The SSA of the (experimentally) synthesised Si nanoparticles becomes larger with increasing quench gas flow rate, decreasing pressure, decreasing plate power, and decreasing feed rate, which is in agreement with particle growth model.
The SSA can be increased by improving the quench design. Without quenching, the SSA amounted 64 $m^2.g^{-1}$ or d_{BET} 40 nm at 3-12-80/6, 15.6 kW plate power, 40 kW, 2.6 $g.min^{-1}$, quenched at z = 121 mm. When a two-nozzle system was used at an almost similar feed (2.4 $g.min^{-1}$) and 56 slpm Ar, the SSA could be increased to 90 $m^2.g^{-1}$ or d_{BET} 29 nm. The replacement of a two-nozzle system by an eight-nozzle system resulted in smaller primary particles (107 $m^2.g^{-1}$ or d_{BET} 24 nm with 56 slpm Ar) and a smaller size distribution. When a feed rate of 1.8 $g.min^{-1}$ was quenched with 56 slpm a SSA of 123 $m^2.g^{-1}$ or d_{BET} 21 nm was obtained. The substitution of the ϕ 2 mm by the ϕ 1.5 mm, 15° angled nozzles, resulted in a SSA of 118 $m^2.g^{-1}$ or d_{BET} 22 nm (1.8 $g.min^{-1}$) and 135 $m^2.g^{-1}$ or d_{BET} 19 nm (1.4 $g.min^{-1}$) when quenched with 56 slpm Ar. The introduction of a funnel on top of the eight-nozzle system increased the SSA even further to 145 $m^2.g^{-1}$ or d_{BET} 18 nm at a feed rate of 1.8 $g.min^{-1}$.
Thus the quench designs as proposed by the CFD modelling have brought improvements in the experiments, as was predicted by the growth model at the hand of the modelled temperature and velocity profiles.
When the process parameters were used as described above using the 8 x ϕ 1.5 mm, angled design at z = 122 mm a decrease of the particle size with decreasing plate power was found: 109 $m^2.g^{-1}$ or d_{BET} 24 nm (1.3 $g.min^{-1}$, 18.5 kW) to 171 $m^2.g^{-1}$ or d_{BET} 15 nm (1.3 $g.min^{-1}$, 13.4 kW) over 135 $m^2.g^{-1}$ or d_{BET} 19 nm (1.4 $g.min^{-1}$, 15.6 kW).
The 8 x ϕ 1.5 mm, angled design resulted in a SSA of 201 $m^2.g^{-1}$ or d_{BET} 13 nm (3-12-80/6, 15.6 kW plate power, 40 kW, 1.9 $g.min^{-1}$, 56 slpm Ar) when the quenching took place at z = 159 mm.

SiC nanoparticles can be synthesised by reactive quenching (mixture of an inert gas and a carbon containing gas) of a Si loaded plasma gas flow. The product consisted out of a SiC and Si mixture (XRD). It is, however, not clear yet if the carburisation takes place at the quenching plane or further upstream (which means different plasma temperatures), since a part of the quenching gas is entrained in an upward flow and there contacts the Si loaded plasma flow. The heat source model also showed that some of the quench gas was getting upstream.

It is feasible to synthesise nanoparticles of high refractory materials by using the ICP process. Microscopic WC (0.7 – 2.7 µm), with a boiling point of 6000 K, has been transformed into nanoscopic WC. The synthesis of WC nanoparticles however, is more complicated than that of Si nanoparticles, because of the chemistry involved which is expressed in the formation of sub-stoichiometric WC phases in the product. The degree of carbon deficiency occurring during processing can be countered by creating a reactive plasma formed by the introduction of a carbon containing species. In this manner the WC content could be increased from 27% without the addition of methane to 90% for 4.8 slpm Ar, the tungsten metal content was reduced from 32% to 0%.

The phase composition of the synthesised product can also be influenced and guided by quenching, as has been demonstrated in the experiments with WC. In which the quench gas flow rate and quench gas composition have been identified as the major process parameters influencing the phase composition.
Increasing of the quench gas flow from 2.8 to 70 slpm Ar results in more WC, whereas the amount of W_2C was reduced from 64% to values below 20%.

By combining CFD, particle growth modelling, and experiments, a powerful tool has been created to optimise the ICP process for nanoparticle synthesis. These tools have been used for the development of the quenching design and optimising of the process parameters for the synthesis of silicon nanoparticles by means of ICP. The tools developed in this work are general and are by no means restricted to Si and/or the used process parameters.

7 Thoughts for future work

The recommendations for other issues that have not been dealt with or not treated in enough detail are mentioned below. These issues are mentioned because they would improve the models and/or experiments. They are listed under topics dealing with the modelling, equipment, experiments, and characterisation.

Modelling

As far as the modelling is concerned, the models could be improved by addition of new features. The heat source model for example can be improved by reshaping the heat source to show a better agreement with the skin depth or by, which is even better, incorporation of the electromagnetic (EM) field.

The effect of parameters, like the quench ring diameter and nozzle angle, on the quenching efficiency and particle growth should be investigated into more detail.

As the EM field is introduced, resulting in a better description of the temperature and velocity profiles in the torch, a particle evaporation model should be implemented, to get an idea about the maximal particle size and feed rate that can be evaporated. To make this evaporation realistic, the influence of the particles on the plasma temperature and the particle – particle interaction should be regarded, besides the Knudsen, the vaporisation, and variable properties effects.

The particle growth model can be extended by including supersaturation and nucleation (Kelvin diameter), distribution of the monomer concentration, and by using a multidisperse model.

Although all these modules and improvements already exist, they have never been combined into one complete model. Such a model would show the best compromises on for example for the working pressure; a high pressure is beneficial for the particle evaporation, but also results in a large particles.

Equipment

It would be very interesting to build a torch, which can be operated at different frequencies, built in such a way that the plasma can be observed. The particle trajectories could then be made visible with tracer particles. With this configuration the validation of the modelling results with respect to a vanishing reflow with increased frequency can be validated.

The equipment should be redesigned in order to obtain a high pressure in the temperature region above the boiling point, as this is beneficial for evaporation of large particles. As the temperature is getting below the boiling point, a low pressure regime is desired since this has a positive effect on the synthesis of small particles.

Such a configuration, consisting out of a high and low pressure region, could be built by introduction of an expansion nozzle through which the plasma gas has to flow.

Another redesigning would comprise the extension of the funnel below the quench ring, with holes in the funnel for the quench gas.

As the four-nozzle design is more efficient than the eight nozzles quench design (Table 4-7, page 93), but results in a more inhomogeneous temperature profile, a few thoughts should be spent on “cascade” quenching, in which second quench plane is created. These planes should be positioned in such a way that each of the four flows which is not cooled (see Figure 4-39, page 91) ends up in front of the nozzle of the next layer, thus the nozzles of the second layer should be shifted by 45° compared to the first layer.

Furthermore should the issue of the high quench gas consumption be tackled, by for instance using a gas recycler.

Experiments

The SiC product as synthesised by quenching of Si with an Ar/CH_4 mixture should be characterised further, to determine the exact phase composition with respect to α- and β-SiC. Furthermore should the reactive quenching in general get a closer look to find out if the reaction takes place at the quenching plane or at positions further upstream. A position further upstream means a higher temperature, which would mean that the reactive quenching solely result in a quench effect and does not introduce any chemistry. Unfortunately the chemistry will also be influenced by the kinetics, which will undoubtly increase the complexity of this theme.

Experiments with quenching of WC at different heights and quench rates should be carried out to find out which conditions result in a larger amount of WC in the product. These experiments should be carried out using feed rates, which allow the complete atomisation of WC.

In the article of Demetriou et al. [84] is described that the crystallisation rates of WC, W_2C, and WC_{1-x} changes with the cooling rate and thus the quenching process.

To control the amount of sub-stoichiometric phases in the synthesised product, it is also worthwhile substituting H_2 by another molecular gas (e.g. N_2) in the sheath gas, to weaken the reducing atmosphere.

As the ICP process is very versatile with respect to the (reactive) atmosphere and precursor choice, contemplations should be made on functionalising the nanoparticles by coating them or by the synthesis of (nano)composites. The nanoparticles could be covered with other particles to obtain for example catalytic active particles. The quench design could be used as the inlet for a second precursor to obtain a coating or a mixture of nanoparticles and to enhance the quenching effect.

The temperature profiles calculated by the CFD model, could be used to obtain the information required for the optimum injection height of a second precursor.

Characterisation

The in-line sampling extraction should be continued to track on the particle growth within the entire synthesis chamber (both radial and axial directions), to combine the samples with results of the particle growth model and on-line size distribution measurements, as described at the end of section 4.3.5 (page 108). The results of the on-line measurements can be compared with the results of the Powdershape software. This software, originally designed to calculate the size distribution of isolated particles by using image analysis, is currently under development to extract information from agglomerated particles [198].

Furthermore, the results of the XRD measurements could be used to determine the crystallite size.

As it is very difficult to differentiate between soft and hard agglomerates with SEM, other techniques like photo correlation spectroscopy (PCS) should be used. PCS measurements will also result in information on particle size distribution.

It is also very important to know how representative the (product) sample is with respect to the complete evaporated amount of precursor. Therefore also samples extracted from other positions (like walls) should be characterised.

8 Symbols and abbreviations

c1	material constant [-]
c2	material constant [-]
C_c	Cunningham correction factor [-]
c_p	specific heat [$J.kg^{-1}.K^{-1}$]
$CuK\alpha_1$	Copper radiation, $1.5406x10^{-10}$ [m]
d*	Kelvin diameter [m]
d_{10}	diameter at which 10 volume% is smaller [m]
d_{90}	diameter at which 10 volume% is larger [m]
d_{agg}	soft agglomerate diameter [m]
d_{BET}	BET equivalent diameter [m]
$d_{hard\ agg}$	hard agglomerate diameter [m]
d_{nozzle}	nozzle diameter [m]
d_p	particle diameter [m]
$d_{p,\ q}$	diameter only influenced by dilution effect [m]
$d_{p,\ T}$	diameter only influenced by temperature effect [m]
$d_{p,min}$	material constant [m]
d_{pp}	primary particle diameter [m]
E	electrical field strength [$V.m^{-1}$]
f	frequency [Hz]
I	current [A]
k	Boltzmann' constant $1.38x10^{-23}$ [$J.K^{-1}$]
Ma	Mach number [-]
$MoK\alpha_1$	Molybdenum radiation $0.7093x10^{-10}$ [m]
N	particle concentration per m^3 gas phase [$\#.m^{-3}$]
N'	particle concentration per kg gas phase [$\#.kg^{-1}$]
n	number of monomers [#]
n_p	number of primary particles per agglomerate [-]
p	pressure [Pa]
Q1	carrier gas flow [slpm]
Q2	central gas flow [slpm]
Q3	total sheath gas flow [slpm]
$Q3_m$	molecular sheath gas flow [slpm]
$Q3_n$	noble sheath gas flow [slpm]
R_s	specific gas constant [$J.kg^{-1}.K^{-1}$]
S	supersaturation ratio [-]
SSA	specific surface area [$m^2.g^{-1}$]
Stk_{50}	Stokes number [-]
T	temperature [K]
T_b	boiling point [K]
T_e	electron temperature [K]
T_h	heavy species temperature [K]
T_m	melting point [K]
v	velocity [$m.s^{-1}$]
v_{ax}	axial velocity [$m.s^{-1}$]
V	volume [m^3]
V	voltage [V]
z	axial distance, measured from torch exit [m]

β	collision frequency [$\#.s^{-1}$]
γ	ratio of the specific heats (C_p/C_v) [-]
δ_c	skin depth [m]
Δ	difference
θ	angle [-]
κ	thermal conductivity [$W.m^{-1}.K^{-1}$]
λ	mean free path length [m]
μ	viscosity [$kg.m^{-1}.s^{-1}$]
ξ_0	magnetic permeability $1.26x10^{-6}$ [$Hy.m^{-1}$]
ρ_g	gas phase density [$kg.m^{-3}$]
ρ_p	particle density [$kg.m^{-3}$]
σ	electric conductivity [$mho.m^{-1}$]
σ_c	collision diameter [m]
σ_s	surface tension [$J.m^{-2}$]
τ_c	characteristic collision time [s]
τ_s	characteristic sintering time [s]
ϕ	nozzle diameter [m]
v	molar volume [$m^3.mole^{-1}$]

#	number
1, 2, 3D	1, 2, 3 dimensional
AD	Aerosol Dynamics
a.m.u.	atomic mass unit
bdf	backward difference formula
BET	Brunauer Emmett Teller
C++	programming language
CFD	computational fluid dynamics
CVC	chemical vapour condensation
CVS	chemical vapour synthesis
DC	direct current
dpi	dots per inch
EDX	energy dispersive X-ray analysis
EM	electromagnetic
HR-SEM	high resolution scanning electron microscopy
HV	Vicker's hardness
ICG	inert gas condensation
ICP	inductively coupled plasma
LTE	local thermal equilibrium
mfp	mean free path
MHD	magnetic hydrodynamic
MS	mass spectrometer
pl	pathline (trajectory of massless particle)
pp	primary particle
qp	quench plane
RF	radio frequency
SEM	scanning electron microscopy
STEM	scanning transmission electron microscopy
TEM	transmission electron microscopy
XRD	X-ray diffraction

µW	microwave

9 References

[1] R. P. Feynman, "There's Plenty of Room at the Bottom - An Invitation to Enter a New Field of Physics", 1959, presentation at the California Institute of Technology.
[2] G. D. Ulrich, "Flame Synthesis of Fine Particles", Chemical and Engineering News **62** (1984), 22-29.
[3] M. C. Roco, "Nanoparticles and Nanotechnology Research", Journal of Nanoparticle Research **1** (1999), 1-6.
[4] R. Anselmann, "Nanoparticles and Nanolayers In Commercial Applications", Journal of Nanoparticle Research **3** (2001), 329-336.
[5] M. C. Roco, "Nanoscale Science and Engineering: Unifying and Transforming Tools", AIChE Journal **50** (2004), 891-897.
[6] O. Preining, "The physical nature of very, very small particles and its impact on their behaviour", Journal of Aerosol Science **29** (1998), 481-495.
[7] W. K. Maser et al., "Superconducting RNi_2B_2C (R = Y, Lu) Nanoparticles: Size Effects and Weak Links", Advanced Materials **9** (1997), 503-506.
[8] P. Buffat and J.-P. Borel, "Size effect on the melting temperature of gold particles", Physical Review A **13** (1976), 2287-2298.
[9] X. Y. Qin et al., "An experimental study on thermal diffusivity of nanocrystalline Ag", Nanostructured Materials **7** (1996), 383-391.
[10] B. Berger et al., "Synthesis, Characterization and Reactivity of Silicon Nano Particles for Pyrotechnical Applications", in *36th International Annual Conference of ICT combined with 32nd International Pyrotechnics Seminar*, edited by T. S. Fischer, D. W. S. Werbeagentur und Verlag GmbH, Karlsruhe, Germany (2005), 1-14.
[11] D. Y. H. Pui and D.-R. Chen, "Nanometer particles: A new frontier for multidisciplinary research", Journal of Aerosol Science **28** (1997), 539-544.
[12] I. Brigger et al., "Nanoparticles in cancer therapy and diagnosis", Advanced Drug Delivery Reviews **54** (2002), 631-651.
[13] F. E. Kruis et al., "Synthesis of nanoparticles in the gas phase for electronic, optical and magnetic applications - a review", Journal of Aerosol Science **29** (1998), 511-535.
[14] J. Grabis et al., "Coating of plasma-processed nanosized powders", Journal of the European Ceramic Society **24** (2004), 179-184.
[15] D. Vollath and D. V. Szabo, "Coated Nanoparticles: A New Way to Improved Nanocomposites", Journal of Nanoparticle Research **1** (1999), 235-242.
[16] D. P. Dufaux and R. L. Axelbaum, "Nanoscale unagglomerated nonoxide particles from a sodium coflow flame", Combustion and Flame **100** (1995), 350-358.
[17] R. A. Andrievski, "The synthesis and properties of nanocrystalline refractory compounds", Russian Chemical Reviews **63** (1994), 431-448.
[18] M. T. Swihart, "Vapor-phase synthesis of nanoparticles", Current Opinion in Colloid & Interface Science **8** (2003), 127-133.
[19] H. Hahn, "Gas phase synthesis of nanocrystalline materials", Nanostructured Materials **9** (1997), 3-12.
[20] S. E. Pratsinis and S. Vemury, "Particle formation in gases: a review", Powder Technology **88** (1996), 267-273.
[21] S. L. Girshick and C. P. Chiu, "Homogenous Nucleation of Particles from the Vapor Phase in Thermal Plasma Synthesis", Plasma Chemistry and Plasma Processing **9** (1989), 355-369.
[22] R. C. Flagan and M. M. Lunden, "Particle structure control in nanoparticle synthesis from the vapor phase", Materials Science and Engineering A **204** (1995), 113-124.
[23] S. E. Pratsinis, "Flame aerosol synthesis of ceramic powders", Progress in Energy and Combustion Science **24** (1998), 197-219.
[24] S. K. Friedlander, "Smoke, Dust, and Haze - Fundamentals of Aerosol Dynamics", Oxford University Press, New York (2000), isbn 0-19-512999-7.
[25] W. C. Hinds, "Aerosol technology - Properties, Behavior, and Measurement of Airborne Particles", John Wiley and Sons, New York (1998), isbn 0-471-19410-7.
[26] S. Tsantilis and S. E. Pratsinis, "Soft- and Hard-Agglomerate Aerosols Made at High Temperatures", Langmuir **20** (2004), 5933-5939.
[27] M. S. Wooldridge, "Gas-phase combustion synthesis of particles", Progress in Energy and Combustion Science **24** (1998), 63-87.
[28] C. G. Granqvist and R. A. Buhrman, "Ultrafine metal particles", Journal of Applied Physics **47** (1976), 2200-2219.

[29] D. Vollath and K. E. Sickafus, "Synthesis of nanosized ceramic nitride powders by microwave supported plasma reactions", Nanostructured Materials **2** (1993), 451-456.
[30] G. Skillas et al., "Simulation of particulates in a carbon black reactor", Journal of Nanoparticle Research **7** (2005), 15-27.
[31] G. Y. Zhao et al., "Preparation of tungsten and tungsten carbide submicron powders in a chlorine-hydrogen flame by the chemical vapor phase reaction", Journal of the Less-Common Metals **163** (1990), 269-280.
[32] A. Singhal et al., "Minimizing Aggregation Effects in Flame Synthesized Nanoparticles", Scripta Materialia **44** (2001), 2203-2207.
[33] K. Wegner et al., "Flame-nozzle synthesis of nanoparticles with closely controlled size, morphology and crystallinity", Materials Letters **55** (2002), 318-321.
[34] T. Johannessen et al., "Computational fluid-particle dynamics for the flame synthesis of alumina particles", Chemical Engineering Science **55** (2000), 177-191.
[35] N. Rao et al., "Nanoparticle Formation Using a Plasma Expansion Process", Plasma Chemistry and Plasma Processing **15** (1995), 581-606.
[36] F. Gitzhofer, "Induction plasma synthesis of ultrafine SiC", Pure and Applied Chemistry **68** (1996), 1113-1120.
[37] P. V. Ananthapadmanabhan et al., "Characterization of plasma-synthesized alumina", Journal of Alloys and Compounds **244** (1996), 70-74.
[38] Y. Sakka et al., "Synthesis and characterization of Fe and composite Fe-TiN nanoparticles by dc arc-plasma", Journal of Alloys and Compounds **346** (2002), 285–291.
[39] J. Karthikeyan et al., "Plasma spray synthesis of nanomaterial powders and deposits", Materials Science and Engineering A **238** (1997), 275-286.
[40] D. Vollath et al., "Synthesis and Properties of Ceramic Nanoparticles and Nanocomposites", Journal of the European Ceramic Society **17** (1997), 1317-1324.
[41] V. N. Troitskiy et al., "Synthesis and Characteristics of Ultra-Fine Superconducting Powders in the Nb-N, Nb-N-C, Nb-Ti-N-C systems", Journal of Nanoparticle Research **5** (2003), 521-528.
[42] P. H. Dundas and M. L. Thorpe, "Titanium dioxide production by plasma processing", Chemical Engineering Progress **66** (1970), 66-71.
[43] M. Sugasawa et al., "Synthesis of Y-Fe-O ultrafine particles using inductively coupled plasma", Journal of Aerosol Science **29** (1998), 675-686.
[44] S. L. Girshick et al., "Thermal plasma synthesis of ultrafine iron particles", Journal of Aerosol Science **24** (1993), 367-382.
[45] J. Y. Guo et al., "Induction plasma synthesis of ultrafine SiC powders from silicon and CH_4", Journal of Materials Science **30** (1995), 5589-5599.
[46] Y. Mizoguchi et al., "Synthesis of ultrafine particles and thin films of $BaFe_{12}O_{19}$ by the Spray-ICP technique", Nanostructured Materials **4** (1994), 591-596.
[47] G. Nutsch et al., "Nanoparticle Formation using an Inductively Coupled Radio Frequency Plasma", in *ISPC 13*, edited by C. K. Wu, Peking University Press, Bejing, China (1997), 1642-1647.
[48] E. Bouyer et al., "Thermal Plasma Processing of Nanostructured Si-based Ceramic Materials", Journal of Nanoparticle Research **3** (2001), 373-378.
[49] R. Kumar et al., "RF plasma processing of ultra-fine hydroxyaptite powders", Journal of Materials Processing Technology **113** (2001), 456-462.
[50] K. Akashi, "Progress in thermal plasma deposition of alloys and ceramic fine particles", Pure and Applied Chemistry **57** (1985), 1197-1206.
[51] S. Pirzada, "Method of Producing Nanoscale Powders by Quenching of Vapors", US 5788738 (2003).
[52] M. Boulos, "Plasma Synthesis of Metal Oxide Nanopowder and Apparatus Therefor", WO 2004/052778 (2003).
[53] T. Yoshida et al., "Characterization of a hybrid plasma ant its application to a chemical synthesis", Journal of Applied Physics **54** (1983), 640-646.
[54] P. C. Kong and Y. C. Lau, "Plasma synthesis of ceramic powders", Pure and Applied Chemistry **62** (1990), 1809-1816.
[55] T. B. Reed, "Induction-Coupled Plasma Torch", Journal of Applied Physics **32** (1961), 821-824.
[56] P. R. Taylor and S. A. Pirzada, "Thermal Plasma Processing of Materials: A Review", Advanced Performance Materials **1** (1994), 35-50.
[57] R. M. Young and E. Pfender, "Generation and behavior of fine Particles in Thermal Plasmas - A Review", Plasma Chemistry and Plasma Processing **5** (1985), 1-37.
[58] J.-F. Bilodeau and P. Proulx, "A mathematical model for ultrafine iron powder growth in a thermal plasma", Aerosol Science and Technology **24** (1996), 175-189.
[59] P. Fauchais and J.-M. Baronnet, "State of the art of plasma chemical synthesis of homogenous and heterogenous products", Pure and Applied Chemistry **52** (1980), 1669-1705.

[60] B. Waldie, "Review of Recent Work on Processing of Powders in High-Temperature Plasmas .1. Processing and Economic Studies", The Chemical Engineer (1972), 92-96.
[61] P. Fauchais et al., "Reactive Thermal Plasmas - Ultrafine Particle Synthesis and Coating Deposition", Surface and Coatings Technology **97** (1997), 66-78.
[62] M. I. Boulos, "Thermal Plasma Processing", IEEE Transactions on Plasma Science **19** (1991), 1078-1089.
[63] P. C. Kong and E. Pfender, "Plasmas Processes",in Carbide, Nitride and Boride Materials Synthesis and Processing edited by A. L. Weimer, Chapman & Hall, London (1997), isbn 0-412-54060-6.
[64] G. González et al., "synthesis and characterization of nanophase particles obtained by D.C. sputtering", Scripta Materialia **44** (2001), 1883–1887.
[65] Z. Márton et al., "A comparative study of size distribution of nanoparticles generated by laser ablation of graphite and tungsten", Materials Science and Engineering C **23** (2003), 225-228.
[66] N. Herlin-Boime et al., "Flame Temperature Effect on the Structure of SiC Nanoparticles Grown by Laser Pyrolysis", Journal of Nanoparticle Research **6** (2004), 63-70.
[67] K. Yamada, "Synthesis of tungsten carbide by dynamic shock compression of a tungsten–acetylene black powder mixture", Journal of Alloys and Compounds **305** (2000), 253-258.
[68] M. Omori, "Sintering, Consolidation, Reaction and Crystal Growth by the Spark Plasma System (SPS)", Materials Science and Engineering A **287** (2000), 183-188.
[69] Q. Wang et al., "Preparation and characterization of nanocrystalline powders of Cu–Zn alloy by wire electrical explosion method", Materials Science and Engineering A **307** (2001), 190–194.
[70] L. Zhang et al., "Synthesis of nanophase silver particles using an aerosol reactor", Journal of Aerosol Science **33** (2002), 1559-1575.
[71] T. Trindade et al., "Nanocrystalline Semiconductors: Synthesis, Properties, and Perspectives", Chemistry of Materials **13** (2001), 3843-3858.
[72] K. Nakaso et al., "Synthesis of non-agglomerated nanoparticles by an electrospray assisted chemical vapor deposition (ES-CVD) method", Journal of Aerosol Science **34** (2003), 869–881.
[73] Y.-S. Chang et al., "Synthesis and characterization of zinc titanate nano-crystal powders by sol–gel technique", Journal of Crystal Growth **243** (2002), 319-326.
[74] C. Araujo-Andrade et al., "Synthesis of nanocrystalline Si particles from a solid-state reaction during a ball-milling process", Scripta Materialia **49** (2003), 773–778.
[75] R. Elkalkouli et al., "mechanical and magnetic properties of nanocrystalline FeCo alloys produced by mechanical alloying", Nanostructured Materials **5** (1995), 733-743.
[76] J. Amouroux et al., "Calculation of silicon particles dynamics, heat and mass transfers in thermal plasmas. Effect of particles vaporization", High Temperature Material Processes **7** (2003), 93-105.
[77] F. E. Kruis et al., "A Simple Model for the Evolution of the Characteristics of Aggregate Particles Undergoing Coagulation and Sintering", Aerosol Science and Technology **19** (1993), 514-526.
[78] H. Wiggers et al., "Silicon Particle Formation by Pyrolysis of Silane in a Hot Wall Gasphase Reactor", Chemical Engineering & Technology **24** (2001), 261-264.
[79] B. Giesen et al., "Formation of Si-nanoparticles in a microwave reactor: Comparison between experiments and modelling", Journal of Nanoparticle Research **7** (2005), 29-41.
[80] M. Desilets et al., "Modelling of the reactive synthesis of ultra-fine powders in a thermal plasma reactor", Journal of Physics D: Applied Physics **30** (1997), 1951-1960.
[81] Z. Yao et al., "Nano-grained tungsten carbide-cobalt (WC/Co)", Company: Materials Modification, Inc., USA
[82] G. E. Spriggs, "A History of Fine Grained Hardmetal", International Journal of Refractory Metals and Hard Materials **13** (1995), 241-255.
[83] W. D. Schubert et al., "General Aspects and Limits of Conventional Ultrafine WC Powder Manufacture and Hard Metal Production", International Journal of Refractory Metals and Hard Materials **13** (1995), 281-296.
[84] M. D. Demetriou et al., "Kinetic modeling of phase selection during non-equilibrium solidification of a tungsten–carbon system", Acta Materialia **50** (2002), 1421-1432.
[85] X. L. Jiang et al., "Reactive deposition of tungsten and titanium carbides by induction plasma", Journal of Materials Science **30** (1995), 2325-2329.
[86] X. L. Jiang and M. I. Boulos, "Particle melting, flattening, and stacking behaviors in induction plasma deposition of tungsten", Transactions of Nonferrous Metals Society of China **11** (2001), 811-816.
[87] P. Linke et al., "Neue Technologie zur Herstellung von Wolframschmelzkarbid", Materialwissenschaft und Werkstofftechnik **34** (2003), 613-617. {in German}
[88] M. Boulos, "Plasma power can make better powders", Metal Powder Report **59** (2004), 16-21.
[89] M. I. Boulos et al., "Thermal Plasmas - Fundamentals and Applications", Plenum Press, New York (1994), isbn 0-306-44607-3.

[90] H. U. Eckert, "The Induction Arc: A State of the Art Review", High Temperature Science **6** (1974), 99-134.
[91] E. Pfender, "Thermal Plasma Technology: Where Do We Stand and Where Are We Going?" Plasma Chemistry and Plasma Processing **19** (1999), 1-31.
[92] H. Conrads and M. Schmidt, "Plasma generation and plasma sources", Plasma Sources Science and Technology **9** (2000), 441-454.
[93] M. I. Boulos, "The inductively coupled R.F. (radio frequency) plasma", Pure and Applied Chemistry **57** (1985), 1321-1352.
[94] M. I. Boulos, "The inductively coupled radio frequency plasma", High Temperature Material Processes **1** (1997), 17-39.
[95] J. Hopwood, "Review of inductively coupled plasmas for plasma processing", Plasma Sources Science and Technology **1** (1992), 109-116.
[96] D. Bernardi et al., "Three-dimensional effects in the modelling of ICPTs: Part I: Fluid dynamics and electromagnetics", The European Physical Journal D **25** (2003), 271 - 277.
[97] T. B. Reed, "Growth of Refractory Crystals Using the Induction Plasma Torch", Journal of Applied Physics **32** (1961), 2534-2535.
[98] J. D. Chase and L. J. Van Ruyven, "Plasma-grown rutile single crystals and their distinctive properties", Journal of Crystal Growth **5** (1969), 294-298.
[99] J. Mostaghimi et al., "Parametric Study of the Flow and temperature Fields in an Inductively Coupled r.f. Plasma Torch", Plasma Chemistry and Plasma Processing **4** (1984), 199-217.
[100] D. Allemand and R. M. Barnes, "A Study of Inductively Coupled Plasma Torch Configurations", Applied Spectroscopy **31** (1977), 434-443.
[101] G. Soucy et al., "Mixing Study of the Induction Plasma Reactor: Part I. Axial Injection Mode", Plasma Chemistry and Plasma Processing **14** (1994), 43-58.
[102] M. I. Boulos et al., "Effect of Swirl and confinement on the Flow and temperature fields in a Inductively Coupled r.f. Plasma", The Canadian Journal of Chemical Engineering **58** (1980), 367-375.
[103] G. Soucy et al., "Mixing Study of the Induction Plasma Reactor: Part II. Radial Injection Method", Plasma Chemistry and Plasma Processing **14** (1994), 59-71.
[104] D. Bernardi et al., "Three-dimensional effects in the modelling of ICPTs Part II: Induction coil and torch geometry", The European Physical Journal D **25** (2003), 279-285.
[105] S. Xue et al., "Effect of the Coil Angle in an Inductively Coupled plasma Torch: A Novel Two-Dimensional Model", Plasma Chemistry and Plasma Processing **23** (2003), 245-263.
[106] M. I. Boulos, "Flow and Temperature Fields in the Fire-Ball of an Inductively Coupled Plasma", IEEE Transactions on Plasma Science **4** (1976), 28-39.
[107] R. M. Barnes, "Temperature and velocity profiles and energy balances for an inductively coupled plasma discharge in nitrogen", Journal of Applied Physics **47** (1976), 3929-3934.
[108] R. M. Barnes et al., "Temperature and velocity distributions in an inductively coupled plasma", Spectrochimica Acta Part B: Atomic Spectroscopy **36** (1981), 81-101.
[109] N. N. Sesi et al., "Fundamental studies of mixed-gas inductively coupled plasmas", Spectrochimica Acta Part B: Atomic Spectroscopy **49** (1994), 1259-1282.
[110] M. Cai et al., "Computer simulation of argon - nitrogen and argon - oxygen inductively coupled plasmas", Spectrochimica Acta Part B: Atomic Spectroscopy **52** (1997), 369-386.
[111] H. Nishiyama et al., "The control of gas temperature and velocity fields of a RF induction thermal plasma by injecting secondary gas", Journal of Physics D: Applied Physics **29** (1996), 2634-2643.
[112] H. Nishiyama et al., "Functionalization of a Nonequilibrium RF Induction Plasma by Gas Mixtures", JSME International Journal, Series B **41** (1998), 502-510.
[113] M. Rahmane et al., "Diffusion phenomena of a cold gas in a thermal plasma jet stream", Plasma Chemistry and Plasma Processing **16** (1996), 169s-189s.
[114] M. Rahmane et al., "Mass transfer in induction plasma reactors", International Journal of Heat and Mass Transfer **37** (1994), 2035-2046.
[115] S. L. Girshick and W. Yu, "Radiofrequency Induction Plasmas at Atmospheric-Pressure - Mixtures of Hydrogen, Nitrogen, and Oxygen with Argon", Plasma Chemistry and Plasma Processing **10** (1990), 515-529.
[116] M. Désilets et al., "Mixing study in an Inductive Plasma Reactor: Comparison Between Model Calculations and Experimental Results", The Canadian Journal of Chemical Engineering **76** (1998), 707-716.
[117] S. H. Paik and E. Pfender, "Modeling of an Inductively Coupled Plasma at Reduced Pressures", Plasma Chemistry and Plasma Processing **10** (1990), 167-188.
[118] K. C. Paul and T. Sakuta, "Properties study of inductively coupled nitrogen plasmas and pressure effects on them", Electric Power Systems Research **56** (2000), 185-193.

[119] J. Mostaghimi et al., "A two-temperature model of the inductively coupled rf Plasma", Journal of Applied Physics **61** (1987), 1753-1760.
[120] Z. Njah et al., "Study of 3-D mixing of a cold jet with a transverse plasma stream", International Journal of Heat and Mass Transfer **36** (1993), 3897-3907.
[121] Z. Njah et al., "Mathematical-Modeling of the 3-D Mixing in an Induction Plasma Reactor", International Journal of Heat and Mass Transfer **36** (1993), 3909-3919.
[122] B. Davies and G. Soucy, "Experimental Study of the Heat and Mass Transfer in a High-Frequency Thermal Plasma Reactor", IEEE Transactions on Plasma Science **25** (1997), 1052-1057.
[123] P. Meubus, "Hydrogen Concentration Profiles and Velocity Distributions in a Reducing Argon/Hydrogen Plasma", The Canadian Journal of Chemical Engineering **52** (1974), 616-624.
[124] J. Mostaghimi and M. I. Boulos, "Effect of Frequency on Local Thermodynamic-Equilibrium Conditions in an Inductively Coupled Argon Plasma at Atmospheric-Pressure", Journal of Applied Physics **68** (1990), 2643-2648.
[125] M. Shigeta et al., "Computational simulation of a particle-laden RF inductively coupled plasma with seeded potassium", International Journal of Heat and Mass Transfer **47** (2004), 707-716.
[126] D. Vanden Abeele and G. Degrez, "Scaling laws and stability analysis for high-pressure inductively coupled plasma sources", (2003), 1-6.
[127] M. Rahmane et al., "Similarity analysis and scale-up criteria for thermal plasma jets", High Temperature Material Processes **2** (1991), 177-193.
[128] A. Merkhouf and M. I. Boulos, "Distributed energy analysis for an integrated radio frequency induction plasma system", Journal of Physics D: Applied Physics **33** (2000), 1581-1587.
[129] R. C. Miller and R. J. Ayen, "Temperature profiles and energy balances for an inductively coupled plasma torch", Journal of Applied Physics **40** (1969), 5260-5273.
[130] T. Johannessen, "Synthesis of Nano-Particles in Flames", The Aerosol Laboratory, Department of Chemical Engineering, Technical University of Denmark, Lyngby, Denmark (1999).
[131] K. Wegner and S. E. Pratsinis, "Nozzle-Quenching Process for Controlled Flame Synthesis of Titania Nanoparticles", AIChE Journal **49** (2003), 1667-1675.
[132] D. W. Sundström and R. L. DeMichiell, "Quenching Process for High Temperature Chemical Reactions", Industrial & engineering chemistry process design and development **10** (1971), 114-122.
[133] J. P. Hansen et al., "Synthesis of ZnO particles in a quench-cooled flame reactor", AIChE Journal **47** (2001), 2413-2418.
[134] B. C. Stratton et al., "Synthesis of Ozone at Atmospheric Pressure by a Quenched Induction-Coupled Plasma Torch", Plasma Chemistry and Plasma Processing **19** (1999), 191-216.
[135] S. V. Patankar, "Computational modeling of flow and heat transfer in industrial applications", International Journal of Heat and Fluid Flow **23** (2002), 222-231.
[136] P. Proulx and C. Trassy, "Better Plasma Process Control through CFD and Spectroscopic Modeling", in *Flucome 2000*, edited by A. Laneville, Sherbrooke, Canada (2000).
[137] V. N. Soshnikov and E. S. Trekhov, "The Theory of High-Frequency Vortex Discharges at High Pressure. I", High Temperature **4** (1966), 165-171.
[138] J. D. Chase, "Magnetic Pinch Effect in the Thermal rf Induction Plasma", Journal of Applied Physics **40** (1969), 318-325.
[139] J. Mostaghimi and M. I. Boulos, "Two-Dimension Electromagnetic Field Effects in Induction Plasma Modelling", Plasma Chemistry and Plasma Processing **9** (1989), 25-44.
[140] J. H. Park and S. H. Hong, "Numerical Analysis of Nitrogen-Mixed Argon Plasma Characteristics and Injected Particle Behavior in an ICP Torch for Ultrafine Powder synthesis", IEEE Transactions on Plasma Science **23** (1995), 4.
[141] S. Xue et al., "Extended-field electromagnetic model for inductively coupled plasma", Journal of Physics D: Applied Physics **34** (2001), 1897-1906.
[142] D. Bernardi et al., "Three-dimensional modelling of inductively coupled plasma torches", The European Physical Journal D **22** (2003), 119-125.
[143] M. Vardelle et al., "Influence of Injector Geometry on Particle Trajectories: Analysis of Particle Dynamics in the Injector and Plasma Jet", in *15th International Thermal Spray Conference - Thermal Spray: Meeting the Challenges of the 21st Century*, edited by C. Coddet, ASM International, Materials Park, OH 44073-0002, Nice, France (1998), **1**, 887-894.
[144] A. Vardelle et al., "Heat Generation and Particle Injection in a Thermal Plasma Torch", Plasma Chemistry and Plasma Processing **18** (1998), 551-574.
[145] M. D. Demetriou et al., "Numerical simulation of plasma heating of a composite powder particle", in *5th ASME/JSME Joint Thermal Engineering Conference*, San Diego, CA, USA (1999).
[146] M. Vardelle et al., "Controlling Particle Injection in Plasma Spraying", Journal of Thermal Spray Technology **10** (2001), 267-284.
[147] P. Proulx et al., "Plasma-particle interaction effects in induction plasma modeling under dense loading conditions", International Journal of Heat and Mass Transfer **28** (1985), 1327-1336.

[148] M. I. Boulos, "Heating of powders in the fire ball of an induction plasma", IEEE Transactions on Plasma Science **PS-6** (1978), 93-106.
[149] G. Thursfield and G. J. Davies, "Effect of Progress Variables on the Decomposition of Rhodonite in Induction Coupled Argon Plasmas", Transactions of the institution of chemical engineers **52** (1974), 237-247.
[150] P. Proulx et al., "Heating of powders in an r.f. inductively coupled plasma under dense loading coatings", Plasma Chemistry and Plasma Processing **7** (1987), 29-52.
[151] A. Schwenk et al., "Improved Nozzle Design of de-Laval-type Nozzles for the Atmospheric Plasma Spraying", in *ITSC 2004 Thermal Spray Solutions - Advances in Technology and Applications*, edited by DVS-TSS-IIW, DVS, Osaka, Japan (2004), 17-22.
[152] R. Ramasamy and V. Selvarajan, "Heat transfer to a single particle injected into a thermal plasma", Computational Materials Science **15** (1999), 265-274.
[153] B. Waldie, "Review of Recent Work on Processing of Powders in High-Temperature Plasmas .2. Particle Dynamics, Heat-Transfer and Mass-Transfer", The Chemical Engineer (1972), 188-193.
[154] E. Pfender, "Particle Behavior in Thermal Plasmas", Plasma Chemistry and Plasma Processing **9** (1989), 167s-194s.
[155] E. Pfender and Y. C. Lee, "Particle Dynamics and Particle and Mass Transfer in Thermal Plasmas. Part I. The Motion of a single Particle without Thermal effects", Plasma Chemistry and Plasma Processing **5** (1985)
[156] Y. C. Lee et al., "Particle Dynamics and Particle Heat and Mass Transfer in Thermal Plasmas. Part II. Particle Heat and Mass Transfer in Thermal Plasmas", Plasma Chemistry and Plasma Processing **5** (1985), 391-412.
[157] P. Proulx et al., "Radiative energy transfer in induction plasma modelling", International Journal of Heat and Mass Transfer **34** (1991), 2571-2579.
[158] A. Essoltani et al., "A combined convective, conductive and radiative heat transfer study for an evaporating metallic particle under plasma conditions", High Temperature Chemical Processes **2** (1993), 37-46.
[159] X. Chen et al., "Heat transfer to a particle under plasma conditions with vapor contamination from the particle", Plasma Chemistry and Plasma Processing **5** (1985), 119-141.
[160] D. Bernardi et al., "3-D numerical simulation of fully-coupled particle heating in ICPTs", The European Physical Journal D **28** (2004), 423-433.
[161] M. Shigeta et al., "Numerical investigation for nano-particle synthesis in an RF inductively coupled plasma", Thin Solid Films **457** (2004), 192-200.
[162] T. Johannessen and S. Koutsopoulos, "One-Step Flame Synthesis of an Active Pt/TiO_2 Catalyst for SO_2 Oxidation—A Possible Alternative to Traditional Methods for Parallel Screening", Journal of Catalysis **205** (2002), 404-408.
[163] J.-M. Baronnet, "Thermal plasma synthesis of nanometric ceramic powders", High Temperature Chemical Processes **1** (1992), 577-597.
[164] Borgiann.C et al., "Behaviour of Metal Oxides Injected into an Argon Inducgion Plasma", Combustion and Flame **13** (1969), 181-&.
[165] M. I. Boulos, "Visualization and Diagnostics of Thermal Plasma Flows", Journal of Visualization **4** (2001), 19-28.
[166] P. Proulx and J.-F. Bilodeau, "A model fur ultrafine powder production in a plasma reactor", Plasma Chemistry and Plasma Processing **11** (1991), 371-386.
[167] T. Ishigaki et al., "Controlling the synthesis of TaC nanopowders by injecting liquid precursor into RF induction plasma", Science and Technology of Advanced Materials **6** (2005), 111-118.
[168] S. V. Joshi et al., "Effect of Quenching Conditions on Particle Formation and Growth in Thermal Plasma Synthesis of Fine Powders", Plasma Chemistry and Plasma Processing **10** (1990), 339-358.
[169] G. Soucy et al., "Heat and Mass Transfer During In-Flight Nitridation of Molybdenum Disilicide Powder in an Induction Plasma Reactor", Materials Science and Engineering A **300** (2001), 226-234.
[170] R. J. Munz et al., "Application of transferred arcs to the production of nanoparticles", Pure and Applied Chemistry **71** (1999), 1889-1897.
[171] K. Baba et al., "Synthesis and properties of ultrafine AIN powder by rf plasma", Applied Physics Letters **54** (1989), 2309-2311.
[172] P. B. Pavlovic et al., "Thermal Plasma Synthesis of Ultrafine Si_3N_4 and SiC Ceramic Powders", Materials Science Forum **214** (1996), 205-214.
[173] R. Bandyopadhyaya et al., "Aerosol dynamics and the synthesis of fine solid particles", Powder Technology **139** (2004), 193-199.
[174] H. Muehlenweg et al., "Product engineering of gas-born nano-sited particles", Materials Science Forum **343-346** (2000), 941-948.

[175] A. Schild et al., "Simulation of nanoparticle production in premixed aerosol flow reactors by interfacing fluid mechanics and particle dynamics", Journal of Nanoparticle Research **1** (1999), 305-315.
[176] R. S. Windeler et al., "Production of nanometer-sized metal oxide particles by gasphase reaction in a free jet. II: particle sizer and neck formation - Comparison with theory", Aerosol Science and Technology **27** (1997), 191-205.
[177] M. Rahmane et al., "Analysis of the enthalpy probe technique for thermal plasma diagnostics", Review of Scientific Instruments **66** (1995), 3424-3431.
[178] M. Leparoux and S. Siegmann, "Development of a filtration unit with a by-pass sampling system for nanoparticle collection", in *Filtech Europa 2003 - International Conference and Exhibition Filtration and Separation Technology*, Düsseldorf, Germany (2003), **2**, II-242 - II-248.
[179] D. L. Johnson et al., "Nanoparticle synthesis apparatus and method", US 5665277 (1997).
[180] R. A. Dobbins and C. M. Megaridis, "Morphology of flame-generated soot as determinates by thermophoretic sampling", Langmuir **3** (1987), 254-259.
[181] M. Choi et al., "Measurements of Silica Aggregate Particle Growth Using Light Scattering and Thermophoretic Sampling in a Coflow Diffusion Flame", Journal of Nanoparticle Research **1** (1999), 169-183.
[182] C. Janzen et al., "Size analysis in low-pressure nanoparticle reactors: comparison of particle mass spectrometry with in situ probing transmission electron microscopy", Journal of Aerosol Science **33** (2002), 833-841.
[183] A. Jillavenkatesa and J. F. Kelly, "Nanopowder Characterization: Challenges and Future Directions", Journal of Nanoparticle Research **4** (2002), 463-468.
[184] C. Bernhardt, "Particle Size Analysis—Problems and Possibilities in the Fine and Ultrafine Range", Journal of Materials Synthesis and Processing **8** (2000), 213-221.
[185] A. Rawle, "Basic principles of particle size analysis", Malvern Instruments Limited, UK.
[186] S. Brunauer et al., "Adsorption of Gases in Multimolecular Layers", Journal of the American Chemical Society **60** (1938), 309-319.
[187] M. Dvorak and M. Birchler, "Method and device for conveying dosed quantities of a fine-grained bulk material", WO 03/029762 (2003).
[188] H. Schmid et al., "New Dimensions of Nano-Particle Size- and Shape -Characterisation", in *Partec 2004 - International Congress for Particle Technology*, edited by S. E. Pratsinis *et al.*, Nürnberg, GER (2004), 26.5.
[189] A. B. Murphy and C. J. Arundell, "Transport-Coefficients of Argon, Nitrogen, Oxygen, Argon-Nitrogen, and Argon-Oxygen Plasmas", Plasma Chemistry and Plasma Processing **14** (1994), 451-490.
[190] Private communications. R. Bolot, Laboratoire d'Études et de Recherches sur les Matériaux, les Plasmas et les Surfaces (LERMPS), Université de Technologie de Belfort-Montbeliard, France.
[191] Private communications. M.I. Boulos, Département de génie chimique, Faculté de génie, Université de Sherbrooke, Canada.
[192] C. Schreuders et al., "Quenching Design for Plasma Synthesis of Nanoparticles", in *16th International Plansee Seminar 2005 - Powder Metallurgical High Performance Materials*, edited by G. Kneringer *et al.*, RWF Werbegesellschafft m.b.H., Reutte, Austria (2005), **2**, 45-50.
[193] P. Buchner et al., "Diagnostics of an RF Plasma Flash Evaporation Process Using the Monochromatic Imaging Technique", Plasma Chemistry and Plasma Processing **21** (2001), 1-21.
[194] C. Schreuders et al., "Influence of the quenching process on thermal plasma synthesis of engineered nanoparticles", in *Fifth World Congress on Particle Technology*, Omnipress, Orlando, Florida (2006), 1.6.
[195] Š. Kavecký et al., "Silicon carbide powder synthesis by chemical vapour deposition from silane/acetylene reaction system", Journal of the European Ceramic Society **20** (1997), 1939-1946.
[196] M. Leparoux et al., "Induction plasma synthesis of carbide nanopowders", Advanced Engineering Materials **7** (2005), 349-353.
[197] C. M. Hollabaugh et al., "R.F.-plasma system for the production of ultrafine, ultrapure silicon carbide powder", Journal of Materials Science **18** (1983), 3190-3194.
[198] C. Schreuders et al., "Nanosized tungsten carbide powder produced by thermal plasma", in *Partec 2004 - International Congress for Particle Technology*, edited by S. E. Pratsinis *et al.*, NuernbergMesse GmbH, Nürnberg, GER (2004), 16.4.

Appendices

A Kruis model

The differential equations that have to be solved are:

$$\frac{dN}{dt} = -\frac{1}{2} * \beta * N^2 \text{ with } N = \frac{n}{V} \quad \frac{[\#]}{[\mathrm{m}^3]} \text{ and } N' = \frac{n}{V} * \frac{1}{\rho} = \frac{n}{V} * \frac{V}{M} \quad \frac{[\#]}{[m^3]} \cdot \frac{[m^3]}{[kg]} = \frac{[\#]}{[kg]}$$

In which N denotes particle concentration [#.m^{-3}], t time [s], β collision frequency [m^3.#$^{-1}$.s^{-1}], n number of particles [#], V gas volume [m^3], N' particle concentration [#.kg^{-1}], ρ density [kg.m^{-3}], and M molar weight [kg.mole^{-1}]

Substitution of N by n/V results in

$$\frac{d\left(\frac{n}{V}\right)}{dt} = \frac{1}{V} * \frac{dn}{dt} + n * \frac{d\left(\frac{1}{V}\right)}{dt} = -\frac{1}{2} * \beta * \left(\frac{n}{V}\right)^2$$

As the volume of the reactor remains constant the term with $d\left(\frac{1}{V}\right)$ equals zero:

$$\frac{d\left(\frac{n}{V}\right)}{dt} = \frac{1}{V} * \frac{dn}{dt} = -\frac{1}{2} * \beta * \left(\frac{n}{V}\right)^2$$

Multiplication of the left hand side by M/M results in

$$\frac{M}{V} * \frac{d\left(\frac{n}{M}\right)}{dt} = -\frac{1}{2} * \beta * \left(\frac{n}{V}\right)^2$$

Substituting M/V by ρ and n/M by N'

$$\frac{dN'}{dt} = -\frac{1}{2} * \frac{\beta}{\rho} * \left(\frac{n}{V}\right)^2$$

Multiplication of the right hand side by M^2/M^2 results in

$$\frac{dN'}{dt} = -\frac{1}{2} * \frac{\beta}{\rho} * \frac{n^2}{V^2} * \frac{M^2}{M^2} = -\frac{1}{2} * \frac{\beta}{\rho} * \frac{n^2}{M^2} * \frac{M^2}{V^2}$$

Substituting M/V by ρ and n/M by N'

$$\frac{dN'}{dt} = -\frac{1}{2} * \frac{\beta}{\rho} * N'^2 * \rho^2 = -\frac{1}{2} * \beta * N'^2 * \rho$$

In the same manner

$$\frac{da}{dt} = -\frac{1}{N} * \frac{dN}{dt} * a - \frac{1}{\tau} * (a - a_s) \quad \text{becomes} \quad \frac{da}{dt} = -\frac{1}{N'} * \frac{dN'}{dt} * a - \frac{1}{\tau} * (a - a_s)$$

In which a denotes surface area of an aggregate [m^2], a_s surface area of a completely fused (spherical) aggregate [m^2], and τ characteristic sintering time [s].

$$\frac{dv}{dt} = -\frac{1}{N} * \frac{dN}{dt} * v \quad \text{becomes} \quad \frac{dv}{dt} = -\frac{1}{N'} * \frac{dN'}{dt} * v$$

In which v denotes volume of the aggregate [m^3].

The results of the current model have been validated with the original Kruis model [77]. Figure A-0-1 to Figure A-0-3 compare the current data with the original results. A good agreement between the literature and the current data is found. The differences are caused by errors in determining the values from the Kruis' paper and the uncertainty in the calculation of the gas viscosity.

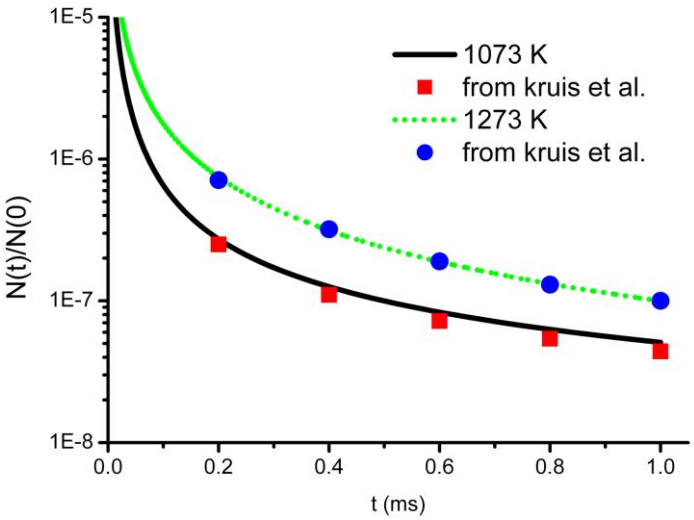

Figure A-0-1: the current monomer concentration to initial monomer concentration plotted as function of time for 1073 K (black solid line) and 1273 K (green dotted line). The single points represent the values as found in the Kruis model [77].

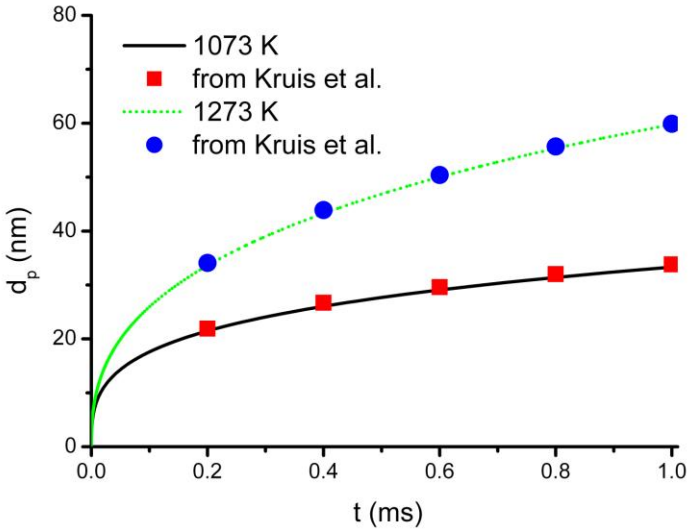

Figure A-0-2: the primary particle growth plotted as function of time for 1073 K (black solid line) and 1273 K (green dotted line). The single points represent the values as found in the Kruis model [77].

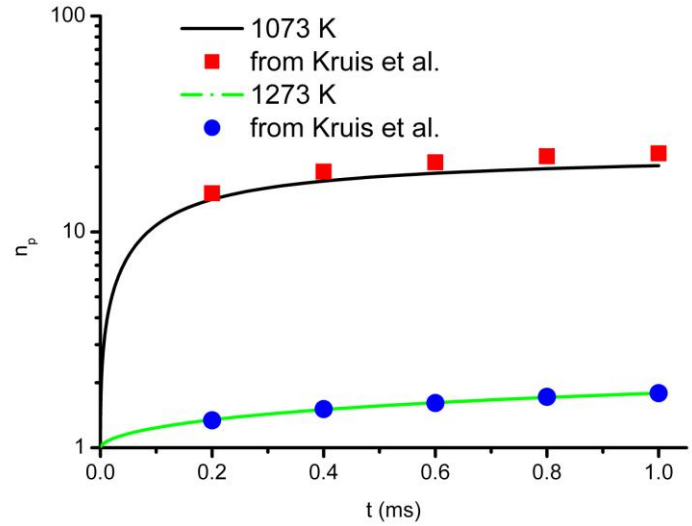

Figure A-0-3 the number of primary particles per agglomerate plotted as function of time for 1073 K (black solid line) and 1273 K (green dotted line). The single points represent the values as found in the Kruis model [77].

a	surface area of an aggregate [m^2]
a_s	surface area of a completely fused (spherical) aggregate [m^2]
M	molar weight [$kg.mole^{-1}$]
N	particle concentration [$\#.m^{-3}$]
N'	particle concentration [$\#.kg^{-1}$]
n	number of particles [#]
t	time [s]
V	gas volume [m^3]
v	volume of the aggregate [m^3]
β	collision frequency [$m^3.\#^{-1}.s^{-1}$]
ρ	density [$kg.m^{-3}$]
τ	characteristic sintering time [s]

List of publications

Articles

M. Leparoux, C. Schreuders, J.-W. Shin and St. Siegmann: Induction plasma synthesis of carbide nanopowders, Advanced Engineering Materials, 7 (2005), 349-353

Conferences

C. Schreuders, M. Leparoux, J.-W. Shin, M. Dvorak, St. Siegmann, “Nanosized tungsten carbide powder produced by thermal plasma”, Partec 2004 - International Congress for Particle Technology, Nürnberg, Germany, March 16-18 2004, proceedings.

C. Schreuders, M. Leparoux, J.-W Shin, H. Miyazoe, St. Siegmann, “Quenching design for plasma synthesis of nanoparticles”, 16th Plansee Conference, Reutte, Austria, May 30 – June 03 2005, proceedings.

C. Schreuders, M. Leparoux, St. Siegmann,”Influence of the quenching process on thermal plasma synthesis of engineered nanoparticles”, Fifth world congress on particle technology, Orlando, USA, April 23-26 2006, proceedings.

J.-W. Shin, H. Miyazoe, C. Schreuders, M. Leparoux, S. Siegmann, J.-L. Dorier, C. Hollenstein, “In-situ process monitoring for plasma synthesis of alumina nanoparticles”, Fifth world congress on particle technology, Orlando, USA, April 23-26 2006, proceedings.

H. Schmid, M. Dvorak, M., G. Bürki, M. Leparoux, St. Siegmann, C. Schreuders, “New Dimensions of Nano-Particle Size- and Shape –Characterisation”, Partec 2004 - International Congress for Particle Technology, Nürnberg, Germany, March 16-18 2004, proceedings.

H. Miyazoe, J.-W.Shin, M. Leparoux, C. Schreuders, K. Terashima, St. Siegmann, “Monitoring of Al2O3 nano-powder synthesis by inductively coupled thermal plasma” The 15th Symposium of The Materials Research Society of Japan, Tokyo, Japan, December 23-24 2004.

B. Berger, B. Haas, S. Vaucher, M. Leparoux, M. Dvorak, C. Schreuders, “Synthesis, Characterization and reactivity if silicon nano particles for pyrotechnical applications”, 36th International Annual Conference of ICT combined with 32nd International Pyrotechnics Seminar, Karlsruhe, Germany, June 28 - July 1 2005, proceedings.

M. Leparoux, C. Schreuders, St. Siegmann, M. Dvorak:Production de nanopoudres par procédé plasma - Maîtrise des risques d'exposition, Colloque SF2M – Poudres et Matériaux Frittés 2005, Cherbourg, France, May 18-20 2005, proceedings.

M. Leparoux, H. Miyazoe, C. Schreuders, J.-W. Shin, St. Siegmann: Production de nanopoudres par procédé plasma - Synthèse et caractérisation in-situ du procédé,

Colloque SF2M – Poudres et Matériaux Frittés 2005, Cherbourg, France, May 18-20 2005, proceedings.

Posters

J. H. Walther, C. Schreuders, S. Tsantilis, P. Koumoutsakos, M. Leparoux, S. E. Pratsinis, "Fundamental Research on Ceramic Nanoparticles: Understanding Nanoparticle Formation", Nanofair, St. Gallen, Switzerland, September 9-11 2003.

W.J. Stark, F. O. Ernst, J.-. Grunwaldt, S. Hannemann, C. Schreuders, R. Strobel, K.Wegner, A. Baiker, M. Leparoux, S. E. Pratsinis, "Fundamental Research on Ceramic Nanoparticles: Nanoparticle Production", Nanofair, St. Gallen, Switzerland, September 9-11 2003.

C. Schreuders, M. Leparoux, M. Dvorak, J.-W. Shin, St. Siegmann, "Nanosized carbide and metallic powders processed by inductively coupled thermal plasma", 12th Workshop Plasma Technology, Technische Universität Ilmenau, Ilmenau, Germany, September 23-24 2004, proceedings.

H. Schmid, M. Dvorak, C. Schreuders, G. Bürki, M. Leparoux, St. Siegmann, "Image analysis using fractal dimension - A powerful tool for nano-powder characterization" 7th international Conference on Nanostructured Materials "NANO 2004", Wiesbaden, Germany, June 20-24 2004, proceedings.

St. Siegmann, M. Leparoux, C. Schreuders, J.-W. Shin, L. Rohr: Quenching the Inductively Coupled Thermal Plasma for Nanoparticle Synthesis, ISPC17, Toronto, Canada, August 7-12 2005, proceedings.

H. Miyazoe, K. Terashima, J.-W.Shin, C. Schreuders, M. Leparoux, St. Siegmann, "Inductively coupled thermal plasma processing: Al2O3 nano-powder synthesis" Nanoarchitectonics Workshop 2005 Tsukuba, Japan, March 3-4 2005.

C. Schreuders, M. Leparoux, St. Siegmann,"Influence of the quenching process on thermal plasma synthesis of engineered nanoparticles", Fifth world congress on particle technology, Orlando, USA, April 23-26 2006.

Other

Patent

V. Hopfe, G. Mäder, D. Rogler, C. Schreuders, „Verfahren und Vorrichtung zur Grossflächigen Beschichtung von Substraten bei Atmosphärendruckbedingungen", Patent number: DE10239875, date of publication 24-03-2004 or „Process and apparatus for coating of large area of substrates under atmospheric pressure", Patent number: EP1394283, 2004-03-03

Conferences

V. Hopfe, R. Liske, D. Rogler, G. Mäder, C. Schreuders, „Atmospheric Pressure Microwave CVD for Barrier Layers on Steel Sheets", International Conference on Metallurgical Coatings and Thin Films (ICMCTF 2003), San Diego, USA, April 28 – May 02 2003.

I. Dani, V. Hopfe, D. Rogler, G. Mäder, C. Schreuders, K. Landes, E. Theophile, M. Dzulko, R. Spitzl, „Influence of Plasma Source on Atmospheric Pressure PECVD Process Characteristics“, 16th International Symposium on Plasma Chemistry, Taormina, Italy, June 22-27 2003.

G. Mäder, F. Präßler, C. Schreuders, V. Hopfe, „Atmosphärendruck Plasma-CVD – Einfluss verschiedener Plasmagaseinspeisungen und Düsengeometrien auf die Schichtabscheidung“, Fluent users conference, Bingen, Germany, 24-25 September 2003

Summary:
An important step in the synthesis of nanoparticles by means of an inductively coupled plasma (ICP) process is quenching, which is the fast controlled cooling of the plasma gas. As quenching is influencing the temperature and velocity profiles, it is also affecting the particle size, size distribution, and phase composition of the product.
In this work, the effect of several quench parameters, like nozzle number, nozzle diameter, quench gas flow rate, etc., on the final particle size has been investigated both theoretically and experimentally.
The influence of the quench and other process parameters (plate power, pressure, gas flow rates, …) on the plasma's temperature and velocity profiles has been modelled using CFD and validated with experimental results. The particle size was modelled using a particle growth model and has been compared to results obtained from experiments with silicon. The effect of quenching on the product chemistry has been demonstrated for tungsten carbide.

Key words: inductively coupled plasma (ICP), quenching, nanoparticles, silicon (Si)

Sommaire:
Une étape importante de la synthèse de nanoparticules par plasma inductif est la trempe de la phase gazeuse. Cette trempe modifie les profiles de température et de vitesse des gaz, et donc la distribution de taille des particules produites ainsi que leur composition cristallographique.
Cette étude théorique et expérimentale démontre ces effets sur les propriétés des particules en fonction de paramètres de trempe, tels que la géométrie de l'anneau de trempe, le nombre d'injecteurs et le flux de gaz.
Les profiles de température et de vitesse du plasma ont été modélisés par CFD puis validés expérimentalement en fonction de paramètres de procédé, tels que la puissance de couplage, la pression du réacteur, les flux de gaz du plasma. La croissance des particules a aussi été modélisée, puis comparée à des résultats expérimentaux sur la synthèse de nanopoudres de silicium. L'influence de la trempe sur la formation de différentes phases cristallines a été démontrée sur le carbure de tungstène.

Mots-clés: plasma inductif, trempe, particules nanométriques, silicium (Si)